Circumnuclear Gas in Radio AGN Revealed by Molecular Absorption

INAUGURAL-DISSERTATION
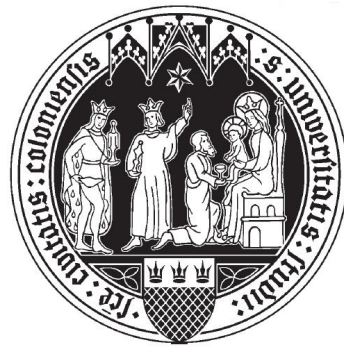
vorgelegt von

Dongjin Kim

aus Seoul, Republik Korea

Köln, 2021

To my dear grandmother
who showed me what love is

Abstract

Active galactic nuclei (AGN) are among the most powerful energy sources in the Universe. The radio jet outflows triggered by AGN activity are supposed to play an important role in galaxy formation and evolution. However, our knowledge about the different types of radio jets and their influence on their host galaxies (i.e., radio jet feedback) is still limited. As a matter reservoir in the vicinity of the central engine, the circumnuclear gas is the key to study different accretion environments and the process of radio jet feedback in radio AGN. Although radio AGN tend to be gas-poor and distant, observations of molecular absorption lines against bright continuum radio jets facilitate the detection of this circumnuclear gas, independent from their cosmological distance. Moreover, spectral line VLBI observations towards molecular absorption lines provide a unique tool to study the small-scale ($< \mathrm{pc}$) structure of the circumnuclear gas, which might be related to AGN fueling and feedback processes. By taking such advantages, this thesis aims to shed more light on the physical connection between the central portions of radio jets and their surrounding medium in radio AGN.

The **first chapter** of this thesis briefly introduces the current understanding of AGN and touches on some remaining open questions. **Chapter 2** briefly describes relevant observing tools for absorption line studies and principles of radio observations. **Chapter 3** presents attempts to find molecular absorption lines towards 41 radio AGN with the 100-m Effelsberg and 30-m IRAM single dish telescopes. Although strong radio frequency interference and standing waves in the observed spectra resulted in a rather low detection rate, we detected molecular absorption in 3 AGN, and the $22\,\mathrm{GHz}$ H_2O maser line in 2 AGN. Diagnostics using the molecular absorption and maser lines show different kinematics of the circumnuclear gas in the Seyfert galaxy NGC 3079 and in the radio-loud AGN NGC 1052. As a new approach to overcome technical hindrances from single-dish absorption studies, an interferometric absorption line study was conducted using the NOEMA interferometer. These results are presented in **Chapter 4**. The copious molecular absorption lines detected in 3C 293 and 4C 31.04 demonstrate the excellence of the interferometric array in absorption line observations towards radio AGN with bright continuum jets. In particular, the physical and chemical properties constrained by the detected molecular absorption lines better clarify the physical origin of the obscuring gas, and provide a diagnostics of radio jet feedback on the circumnuclear gas in the restarted (3C 293) and young (4C 31.04) radio AGN.

In order to reach even smaller angular and spatial scales of the circumnuclear gas in radio AGN, high-resolution Very Long Baseline Interferometry (VLBI) observations were conducted towards OH absorption lines. **Chapter 5** presents VLBI observations towards OH absorption lines at 6 GHz in the Seyfert galaxy NGC 3079 using the European VLBI Network (EVN). The still putative radio jet feedback was confirmed by the detection of spatially resolved OH absorption lines on the continuum jets. The blue-shifted OH absorption on the propagating jet component indicates jet-ISM interaction and a resultant molecular outflow at a distance of a few pc from the central engine. An increasing jet luminosity and decelerated jet motion show the impact of jet-ISM interaction on jet evolution. **Chapter 6** presents High Sensitivity Array (HSA) and EVN observations towards two distinct radio-loud AGN Cygnus A and NGC 4261. The 6 GHz and 13 GHz excited OH absorption lines were searched to test the unified scheme and different accretion environments in Cygnus A (HERG and FR II) and NGC 4261 (LERG and FR I). The 13 GHz OH absorption lines detected in front of the jet, but not on the counter-jet in Cygnus A contradict the classical scenario of an obscuring torus, which covers the counter-jet, but not the jet. The red-shifted and compact OH cloud in front of the jet might indicate fueling gas falling into the central engine. In contrast to this, no OH absorption was seen in NGC 4261 despite previous detection of 6 GHz OH absorption. Several scenarios are discussed to explain the lack of OH absorption in NGC 4261.

Chapter 7 summarizes the implications of molecular absorption line studies towards radio AGN from the ongoing work and addresses some remaining questions. The absorption studies presented in this thesis provide new insights on the circumnuclear gas in the observed radio AGN, constraining their physical and chemical properties down to sub-parsec scales and near the jet-launching region. With planned imaging arrays of higher sensitivity and extended spectral coverage, future absorption line VLBI studies have a great potential to reveal even more details on the physical and geometrical properties of the circumnuclear gas and on the interaction between inflow and outflow of matter within the central regions of radio galaxies.

Zusammenfassung

Aktive galaktische Kerne (Active Galactic Nuclei, AGN) gehören zu den stärksten Energiequellen im Universum. Die Ausflüsse von Radio-Jets, die durch Aktivität von AGN entstehen, spielen eine wichtige Rolle bei der Entstehung und Entwicklung von Galaxien. Allerdings ist die Entstehung verschiedener Typen von Radio-Jets und deren Einfluss auf die AGN-Host-Galaxien (Feedback von Radio-Jets) bisher wenig erforscht. Das den AGN umgebende (zirkum-nukleare) Gas dient als Masse-Reservoir für den zentralen Motor des AGN und ist der Schlüssel zur Erforschung verschiedener Szenarien von Akkretion und des Prozesses für Feedback von Radio-Jets in Radio-AGN. Obwohl Radio-AGN gas-arm und weit entfernt sind, erlauben Beobachtungen molekularer Absorptionslinien in Jets, die hell im Radio-Kontinuum sind, die Detektion von zirkum-nuklearem Gas in Radio-AGN, unabhängig der kosmologischen Entfernung. Außerdem liefern Beobachtungen von Spektrallinien mit VLBI (Very-Long-Baseline-Interferometry) von molekularer Absorption einen einzigartigen Blick auf die Struktur des zirkum-nuklearen Gases auf kleinen Skalen ($< pc$), das mit dem Antrieb des AGN und Feedback-Prozessen in Verbindung stehen könnte. Diese Arbeit zielt darauf ab, die Vorteile dieser Beobachtungen einzusetzen, um die physikalische Verbindung zwischen Radio-Jets und deren Umgebung in Radio-AGN zu offenbaren.

Im ersten Kapitel dieser Arbeit wird der Leser in den aktuellen Forschungsstand und die noch offenen Fragen zu AGN eingeführt. **Kapitel 2** erklärt knapp die Beobachtungstechniken und Grundlagen von radioastronomischen Beobachtungen. In **Kapitel 3** werden Studien von zu Absorptionslinien mit dem 100-m-Effelsberg-Teleskop und dem 30-m-IRAM-Teleskop in 41 radio-hellen AGN präsentiert. Obwohl starkes RFI (Radio-Frequency-Interference) und stehende Wellen in den beobachteten Spektren zu einer eher niedrigen Detektionsrate führten, haben wir molekulare Absorption in 3 AGN detektiert, sowie eine H_2O-Maser-Line bei 22 GHz in 2 AGN. Mithilfe verschiedener diagnostischer Methoden anhand der molekularen Absorptionslinien konnten unterschiedliche Kinematiken des zirkum-nuklearen Gases in der Seyfert-Galaxie NGC 3079 und in dem radio-lauten AGN NGC 1052 festgestellt werden. Um die technischen Schwierigkeiten bei Beobachtungen mit einzelnen Teleskopen zu vermeiden, wurde als neuer Ansatz eine Studie zu Absorptionslinien mit dem NOEMA-Interferometer durchgeführt, deren Ergebnisse in **Kapitel 4** zu finden sind. Die zahlreichen molekularen Absorptionslinien, die in 3C 293 und 4C 31.04 entdeckt wurden, zeigen die hervorragende Leistung der interferometrischen Anordnung bei

der Beobachtung von Absorptionslinien in Radio-AGN mit hellen Kontinuumsjets. Insbesondere zeigen die physikalischen und chemischen Eigenschaften, die durch die Studien von molekularer Absorption bestimmt wurden, den physikalischen Ursprung des Gases und weisen auf den Einfluss des Radio-Jets auf das zirkum-nukleare Gas in den neu gestarteten (3C 293) und jungen (4C 31.04) Radio-AGN hin.

Um noch kleinere Winkel- und räumliche Skalen des zirkum-nuklearen Gases in Radio-AGN untersuchen zu können, wurden sehr langer Basislinieninterferometry (VLBI)-Beobachtungen von OH-Absorptionslinien bei hoher Auflösung durchgeführt. In **Kapitel 5** werden VLBI-Beobachtungen mit dem EVN (European VLBI Network) von OH-Absorptionslinien in der Seyfert-Galaxie NGC 3079 bei 6 GHz präsentiert. Mutmaßliches Radio-Jet-Feedback wurde nachgewiesen durch die Entdeckung räumlich aufgelösten OH-Absorptionslinien in den Kontinuum-Jets. Die blauverschobenen OH-Absorptionslinien in der propagierenden Jet-Komponente weisen auf eine Interaktion zwischen Jet und ISM (Interstellar Medium) und einen daraus resultierenden molekularen Ausfluss bei einer Distanz von wenigen Parsec zum zentralen Motor hin. Die steigende Helligkeit und die verlangsamte Bewegung des Jets deuten auf die Wirkung der Interaktion zwischen Jet und ISM auf die Entwicklung des Jets hin. **Kapitel 6** zeigt die Beobachtungen von Hochempfindliches Array (HSA) und dem EVN bei zwei ausgeprägten, radio-lauten AGN, Cygnus A und NGC 4261. Die Beobachtungen von angeregten OH-Absorptionslinien bei 6 GHz und 13 GHz wurden benutzt, um das "Unified Scheme" und verschiedene Akkretions-Umgebungen von Cygnus A (HERG und FR II) und NGC 4261 (LERG und FR I) zu prüfen. Absorptionslinien von OH bei 13 GHz in Cygnus A, die vor dem Jet, aber nicht im Counter-Jet gefunden wurden, widersprechen dem klassischen Bild eines Torus, der den zentralen Motor verdeckt, aber nicht im Counter-Jet zu finden ist. Die rotverschobene und kompakte OH-Wolke vor dem Jet, die in Richtung des zentralen Motors fällt, könnte als Treibstoff für diesen dienen. Im Gegensatz dazu wurde keine OH-Absorption in NGC 4261 detektiert, trotz der früheren Detektion von OH-Absorption bei 6 GHz. Verschiedene Szenarien werden diskutiert, um die Nicht-Detektionen der OH-Absorptionslinien in NGC 4261 zu erklären.

Kapitel 7 fasst ich die Implikationen der Studien zu molekularen Absorptionslinien in Radio-AGN zusammen, im Hinblick auf die laufende Forschung und die weiterhin offenen Fragen. Die in dieser Arbeit präsentierten Studien von Absorption bieten einen neuen Blick auf das zirkum-nukleare Gas in Radio-AGN. Dadurch wurden die physikalischen und chemischen Eigenschaften auf mikroskopischen (sub-Parsec) Skalen und in der Nähe der Region des startenden Jets beschränkt. Mit zukünftigen Interferometern mit hoher Empfindlichkeit könnte man mit weiteren VLBI-Studien zu Absorptionslinien mehr über die physikalischen und geometrischen Eigenschaften

des zirkum-nuklearen Gases und der Interaktion von Ein- und Ausströmen der Materie innerhalb zentraler Regionen der Radiogalaxien offenbaren.

Contents

List of Figures

List of Tables

Chapter 1

Introduction

Abstract A supermassive black hole (SMBH) in the center of galaxies attracts surrounding matter and forms a matter accreting system. Active Galactic Nuclei (AGN) are the SMBHs in an active accretion phase, and they show strong emission over the entire electromagnetic spectrum. This chapter reviews the current knowledge on the structure, classification, and outflows of AGN revealed by multi-wavelength studies. In particular, the feedback and fueling processes of AGN are addressed from the perspective of radio activity with remaining open questions.

1.1 Active galactic nuclei

1.1.1 Discovery

In the 1930s, remarkably bright optical emission was detected from the center of certain spiral galaxies. Seyfert (1943) reported very broad (3600-8500 $\mathrm{km s^{-1}}$) ionized emission in the galactic nuclei of those peculiar galaxies. The luminosity of the ionized emission was even comparable to the entire light emitted by the host galaxies. The discovery of these Seyfert galaxies alluded a "central engine", which radiates more efficiently than typical stellar nuclei of galaxies. An indirect evidence for the putative central engine also arose with the discovery of a luminous central radio source in some galaxies. In the late 1950s, radio sky surveys identified hundreds of bright radio sources (Edge et al. 1959; Bennett 1962). Soon after, some radio sources were identified as the counterparts of the extremely bright optical sources in the galactic nuclei (Matthews & Sandage 1963). This finding posed a possibility of a common physical process responsible for the luminous optical and radio emissions in galaxies, but a plausible explanation for the putative central engine was not yet clear. Salpeter (1964) proposed a massive accretion system as the source of the luminous extragalactic optical and radio emissions. Later, Lynden-Bell & Rees (1971) suggested a supermassive black hole (SMBH), forming a massive accretion system in galaxies. This hypothesis is widely accepted today by accumulating evidence for the presence of SMBHs in the center of galaxies and our improved understanding
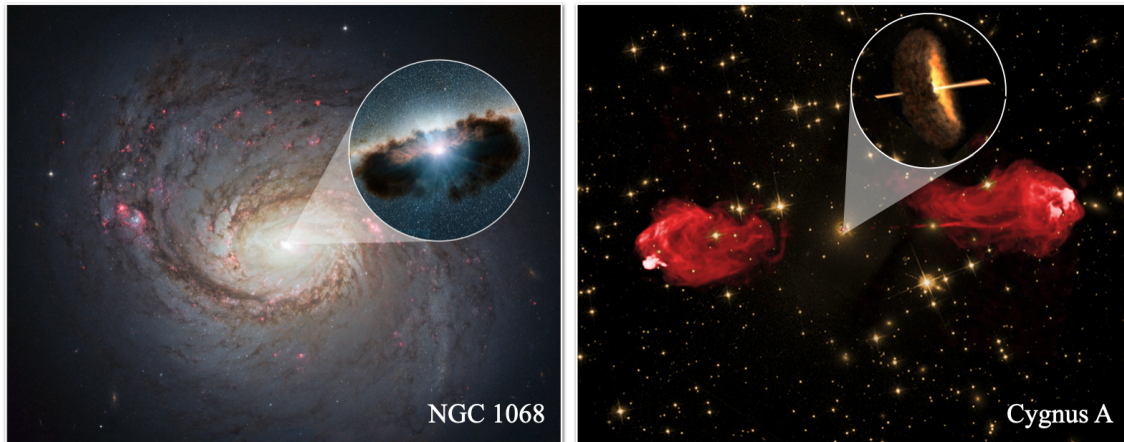
FIGURE 1.1: Manifestations of AGN at optical and radio wavelengths. The location of the AGN is shown as an insert. **Left**: The Seyfert galaxy NGC 1068 harbors a bright optical core within which the AGN resides. **Right**: Cyngus A is a representative radio AGN characterized through extended two-sided radio jets and lobes. Radio (red) and optical (yellow) images are overlaid to show the radio jet structure from the galactic nucleus. Image credits: NASA/STSiC/JPL-Caltech/NSF/NRAO/AUI/VLA/SOFIA/Lynette Cook.

of the accretion process in various astrophysical systems. In particular, SMBHs in an active accretion phase are termed as Active Galactic Nuclei (AGN) through their prominent and highly variable emission seen over the full electromagnetic spectrum. Fig. 1.1 shows two representative AGN identified at optical (NGC 1068) and radio (Cygnus A) wavelengths, respectively. As our view on AGN expand over the past decades from the optical to a broader range of the electromagnetic spectrum, new discoveries have been made. One of the most intriguing findings in the recent studies of AGN is a tight correlation between the SMBH masses and the physical properties of their host galaxies (Ferrarese & Merritt 2000; Ferrarese & Ford 2005; Fiore et al. 2017). Accumulating observational evidence suggests a coevolution of the SMBHs and galaxies, but the underlying physical mechanism is still controversial (Kormendy & Ho 2013, and references therein). AGN feedback led by the energetic AGN outflows is thought to play an important role in the evolution of the SMBHs and their host galaxies, regulating the accretion and star formation rates. However, the scope of AGN feedback on the host galaxy and its influence on the growth of the SMBH mass have not been yet clearly assessed (Cicone et al. 2018; Gaspari et al. 2020). Regarding this matter, the key is to quantify different types of AGN activities, and evaluate their impact on the host galaxies. As a general introduction, the following section describes the different structures and outflows found in AGN.

1.1.2   Structure

Despite a still incomplete understanding of AGN, there has been a broad consensus on their basic structure (see Fig. 1.2). The observational features of each sub-structure of an AGN allow us to characterize the AGN activities, accretion modes, and environments. This subsection briefly describes the observational features and theoretical understanding on the underlying structural/physical components.
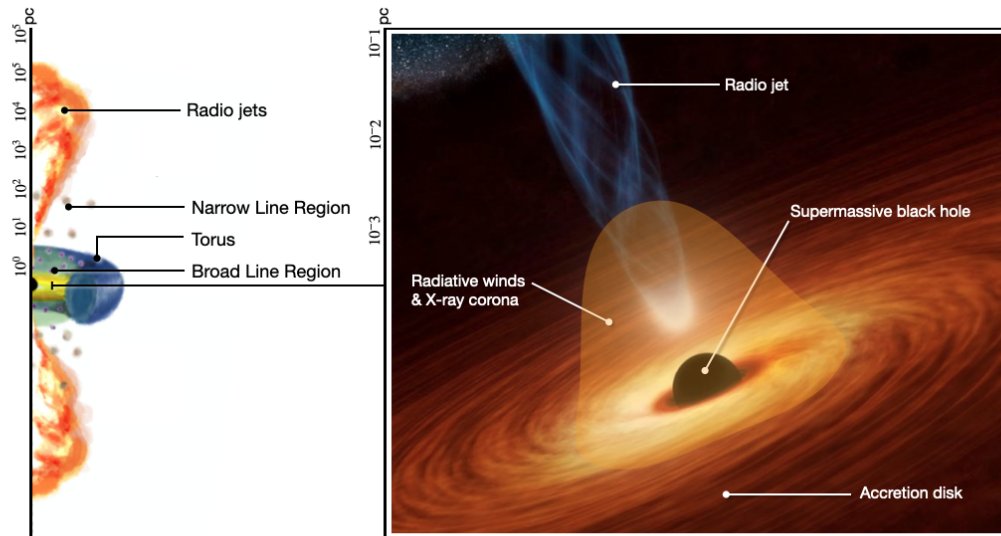
FIGURE 1.2: **Left**: Schematic view of the sub-structure of AGN from pc to Mpc scales. The BLR is located in the innermost region, and the torus partially obscures the BLR. The NLR and radio jet extend over the spatial scale of the torus. **Right**: The structure of an AGN on sub-pc scales. It includes, the SMBH, accretion disk, X-ray corona, radiative winds and radio jet. Image credit: MIT Kavli institute.

- **Supermassive blackhole (SMBH)**: A massive black hole in the center of galaxies seems to be essential to form an accretion system. The presence of a SMBH in the Milky Way galaxy has been proven by the peculiar orbital motion of stellar components (Genzel et al. 1997). In other galaxies, diagnostics using the ionized emission lines, stellar velocity dispersion in the bulge, Keplerian motion of the megamaser disk, and direct B shadow detection, measure the masses of the SMBHs in the range of 10^6 - 10^{10} $L_\odot$ (Peterson et al. 2004; Nelson et al. 2004; Kuo et al. 2011; Event Horizon Telescope Collaboration et al. 2019). Either matter accretion or SMBH mergers can lead to SMBH mass growth (Kulkarni & Loeb 2012; Shankar et al. 2013). The SMBH growth models based on the continuity equations well describe the local Black-Hole Mass Function (BHMF) by assuming an accretion dominated SMBH growth (Small & Blandford 1992; Shankar et al. 2013). The SMBH mass, spin, and accretion

rate characterize the intrinsic properties of AGN. A rotating SMBH has an angular momentum a ($a = cJ_{\mathrm{BH}}/GM_{BH}^2$ and $0 \leq a \leq 1$), where G is the gravitational constant and c is the speed of light. The spacetime of rotating Black Holes (BHs) is described by the Kerr metric (Kerr 1963), which predicts the formation of an ergosphere, where a test particle can extract the spin energy of the rotating BH. According to the jet formation model proposed by Blandford & Znajek (1977), the magnetic extraction of the spin energy in rotating SMBHs can power relativistic plasma jets. Several authors have attempted to relate the SMBH spins and jet properties, but more evidence will be needed to establish the spin-jet correlation (Narayan & McClintock 2012; Russell et al. 2013; Reynolds 2020). In the local Universe, AGN with powerful radio jets tend to harbor high mass SMBHs with a low accretion rate. Contrary, optically luminous AGN harbor less massive SMBHs with a high accretion rate (see Fig. 1.9) (Heckman & Best 2014).

- **Accretion disk**: Matter accretion onto a SMBH forms a rotating disk. The friction in this accretion disk converts the potential energy of the accreting matter to heat and radiation. This causes a fueling flow to the SMBHs. The temperature of the accretion disk ranges from 10^5 to 10^6 K, and its black-body radiation is sometimes observable as a Big Blue Bump (BBB) in the optical and at UV wavelengths (Barvainis 1993; Bonning et al. 2006). The luminosity of an accretion disk is given by $L_{\mathrm{acc}} = \eta \dot{M} c^2$, where $\dot{M}$ is the accretion rate, and η is the energy-mass conversion ratio. η is estimated to be around 0.1. Theoretically, a rotating SMBH can enhance the energy-mass conversion rate up to 0.3 (Kerr 1963; Thorne 1974). The radiative pressure produced by scattered light limits the accretion luminosity by preventing further matter accretion. This is called the Eddington luminosity L_{edd}, which is given by

$$L_{\mathrm{edd}} = \frac{4\pi G M_{\mathrm{BH}} m_p c}{\sigma_T} \qquad (1.1)$$

where G, M_{BH}, m_p, c, and σ_T are the gravitational constant, SMBH mass, proton mass, speed of light, and Thompson cross section for the election scattering, respectively. The Eddington luminosity in units of solar luminosity ($L_\odot$) is

$$L_{\mathrm{edd}} \sim 3.3 \cdot 10^4 (M_{\mathrm{BH}}/M_\odot) L_\odot. \qquad (1.2)$$

For instance, the Eddington luminosity of an AGN with a SMBH mass of $M_{\mathrm{BH}} \sim 10^{7-8} M_\odot$ is about $L_{\mathrm{edd}} \sim 10^{12-13} L_\odot$, which is comparable with the luminosity of typical field galaxies. The Eddington ratio ($\lambda_{\mathrm{edd}} = L_{\mathrm{acc}}/L_{\mathrm{edd}}$) is commonly used to quantify the degree of the accretion rate of AGN. Theoretical
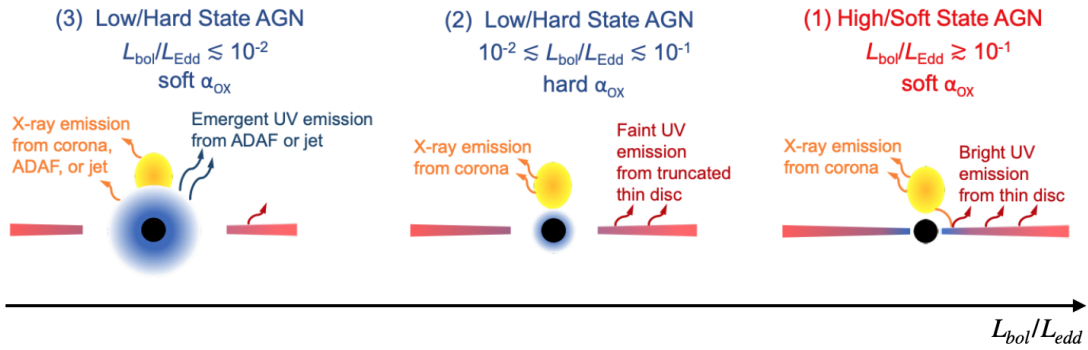
FIGURE 1.3: The geometry of the accretion disks in different Eddington regimes. For high Eddington ratios, accretion disks are thin, and show high energy X-ray emission. For low Eddington ratios, accretion disks are thick, and truncated by Advection Dominated Accretion Flow (ADAF). The figure is taken from Ruan et al. (2019).

studies suggest that the Eddington ratio can be used to characterize the two distinct forms of accretion disks (thick vs. thin) and accretion flows (cold vs. hot) (Yuan & Narayan 2014, and references therein). Fig. 1.3 shows the geometry of accretion disk systems over ranges in Eddington ratio. Hot gas accretion forms advection dominated accretion flows (ADAFs), with a truncated thin disk in the innermost region. Hot accretion flows are usually radiatively inefficient and have low Eddington ratios ($\lambda_{edd} \leq 0.01$) (Narayan & Yi 1994). Contrary, cold gas accretion forms a standard thin accretion disk, which is radiatively more efficient and leads to a large Eddington ratio ($\lambda_{edd} \geq 0.01$) (Shakura & Sunyaev 1973).

- **X-ray corona**: Bright X-ray emission is a typical property of an AGN. Fig. 1.4 sketches X-ray features at energy level from 1 to a few hundreds keV with their locations. Optical and UV photons in the accretion disk are up-scattered to X-ray by inverse Compton scattering of the hot electrons in a corona. This forms a primary X-ray source (Titarchuk 1994; Haardt et al. 1997). The observed power-law X-ray spectra are described by the spectral index α ($I_f \propto f^{-a}$, where I_f is the X-ray flux and f is the frequency) and the photon index Γ ($\Gamma = \alpha+1$). The photon index, Γ is in the range of 1.5-2.5, and tends to be steeper in AGN with high Eddington ratios (Page et al. 2005; Shemmer et al. 2008; Tortosa et al. 2018). The primary X-ray emission can be reflected by the accretion disk or molecular torus. If a reflector is Compton thick ($N_H \geq 10^{24} cm^{-2}$), the iron Kα line becomes visible at 6-7 keV. The reflection efficiency increases from 1 to 30 keV, which forms the so called Compton hump. The optical depth and electron temperature of the X-ray corona determine the high energy rollover (50–300 keV) (Tortosa et al. 2018). A soft X-ray (≥ 2 keV) excess is prevalent in
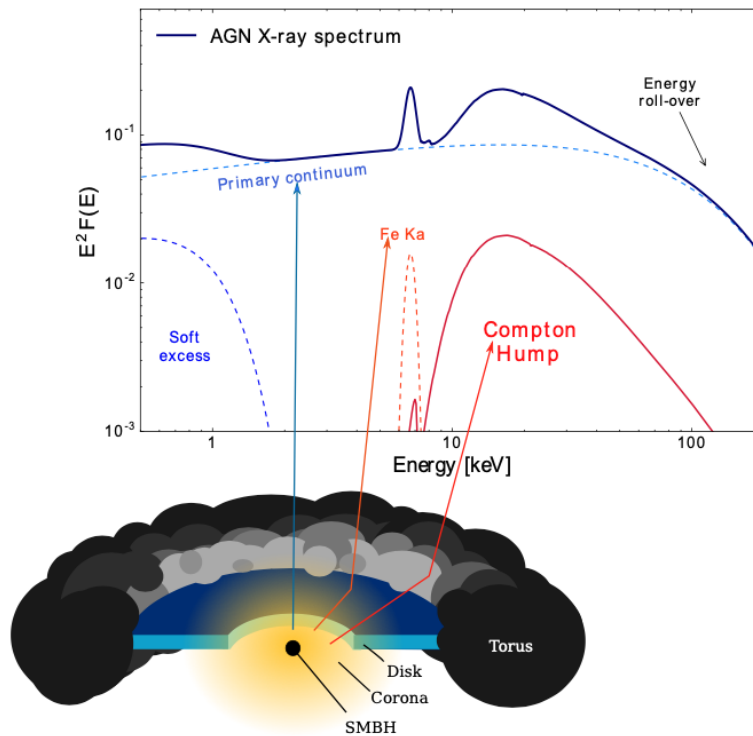
FIGURE 1.4: Spectral decomposition of the innermost region of AGN. The location of the individual X-ray feature in the spectrum is marked with arrows. The primary X-ray emission comes from the X-ray corona. The reflected X-ray emissions result in the Fe line and the Compton hump. The location of the soft emission is not marked due to its unclear origin. The figure is taken from Baronchelli (2020).

AGN. Thermal Comptonization or blurred ionized reflection models have been suggested to reconstruct the soft X-ray excess in AGN, but its origin is still under debate (Blandford & Payne 1982; Crummy et al. 2006; Petrucci et al. 2018).

- **Broad-line region (BLR)**: Ionized emission lines appear via the permitted atomic transitions of H, C, Mg and Fe at optical wavelength in AGN. The emitting region close to the central engine (within sub-pc scale) shows orbiting velocities of about a few thousands $\mathrm{km\,s^{-1}}$, and it is termed as the Broad-Line Region (BLR). For instance, spatially resolved BLR clouds in the quasar 3C273 show a spatial extent of 0.03 to 0.12 pc with a line width of $2700\,\mathrm{km\,s^{-1}}$ (Gravity Collaboration et al. 2018). The BLR can be obscured by a dusty structure in the core region. For high-luminosity AGN, the presence of the BLR discriminates between obscured (Type 2) and unobscured (Type 1) AGN. According to the disk-wind scenario, the BLR may not exist in low-luminosity AGN (i.e., low accretion rates) (Elitzur & Ho 2009; Elitzur et al. 2014).
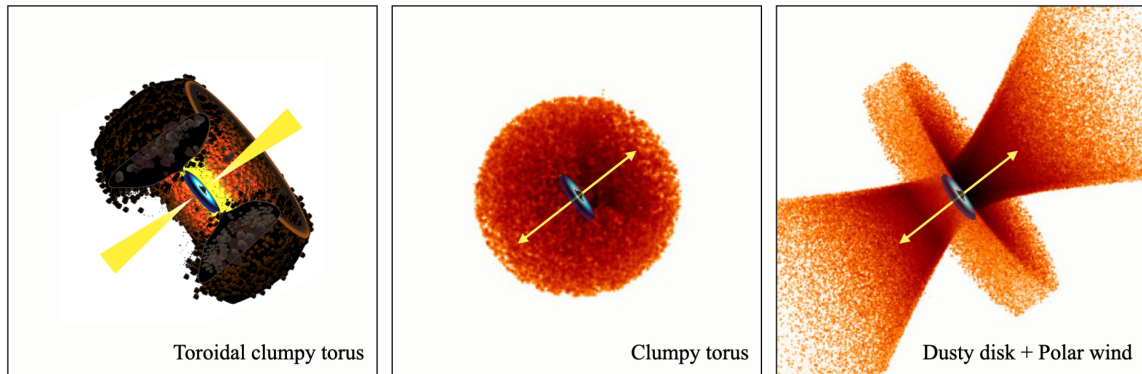
FIGURE 1.5: Various torus models, explaining the obscuring structure in AGN. **Left**: A classical toroidal torus, which is composed of clumpy clouds. Image credits: Bill Saxton, NRAO/AUI/NSF. **Middle**: A spherical clumpy torus model. The obscuration of the BLR is determined by the filling factor and distribution of the clumpy clouds. **Right**: A torus model consisting of a dusty disk and polar wind. The middle and right figures are taken from Stalevski et al. (2019)

- **Torus**: An infrared bump in the Spectral Energy Distribution (SED) of AGN indicates a heated dusty structure in the vicinity of the central engine. The Unified model of AGN postulates a toroidal dusty structure that can obscure the innermost region of AGN, such as the accretion disk, X-ray corona, and BLR (Antonucci 1993). If the torus are not spherically symmetric and inhomogeneous, the inclination of an AGN towards our line of sight can be a critical parameter, constraining the appearance of the AGN. The biconical ionized emission and the reflected emission of the BLR seen in the polarized light support the presence of an obscuring structure in AGN (Antonucci & Miller 1985; Nagao et al. 2004). Reflected or absorbed X-ray emissions also indicate a compact dusty structure surrounding the innermost region of AGN. However, the physical origin and properties of the torus still are poorly understood. Numerical models based on infrared reverberation mappings and SED analysis suggest a parsec scale clumpy cloud instead of a continuous toroidal structure as the source of infrared emission in AGN (Nenkova et al. 2008; Hönig et al. 2010). Recent high-resolution observations using infrared interferometry reveal a significant contribution of the polar dust infrared emission (Asmus et al. 2016; Asmus 2019). For example, Fig. 1.5 shows several models, which describe the infrared emission of the obscured Type 2 AGN Circinus. A torus model consisting of a dusty disk and polar wind provides the best fit to the observed mid-infrared interferometric data (Stalevski et al. 2019). On the other hand, infrared observations show the absence of a torus in low-luminosity AGN (van der Wolk et al. 2010; Trump et al. 2011). These results challenge simple models for the origin of the dusty structure in AGN.

- **Narrow-line region (NLR)**: Ionized emission lines in AGN extend up to a few hundred pc from the central engine. The line widths are about a few hundred $km\,s^{-1}$. In the optical, the NLR is not obscured by a putative torus due to its large spatial extent. In some cases, the NLR extends up to several kpc showing a conical or bipolar structure (Sun et al. 2018; Storchi-Bergmann et al. 2018). For example, Fig. 1.6 shows the NLR in the Seyfert galaxy Mrk 573. The $H\alpha$ emission extends over a few hundred pc. The NLR is an important probe for studying the interaction of the AGN with its host galaxy. A spatial correlation between the NLR and the radio jet is attributed to the jet-driven ionization induced by Jet-ISM interactions (Wang et al. 2011; Williams et al. 2017).

- **Low-Ionization Nuclear Emission-Line Region (LINER)**: Low-ionization emission lines are detected in the nuclear region of very low-luminosity AGN (Ho et al. 2014). The Baldwin-Phillips-Terlevich (BPT) diagram using the emission line ratios of $S\,[II]/H\alpha$ and $O\,[III]/H\beta$ separates ionized emission from the star-formation, LINER, and AGN (Baldwin et al. 1981). Various ionization mechanisms have been suggested to explain the origin of LINER, which include a low luminosity AGN, shock excitation, and late-type stellar population (Ho & Peng 2001; Ho et al. 2014; Belfiore et al. 2016). Spatially resolved ionized emission in Seyfert AGN show that the NLR is surrounded by the LINER-like ionized emission (see Fig. 1.6). A transitional region between the NLR and LINER is likely to be affected by radio jets or AGN outflows (Ma et al. 2021).
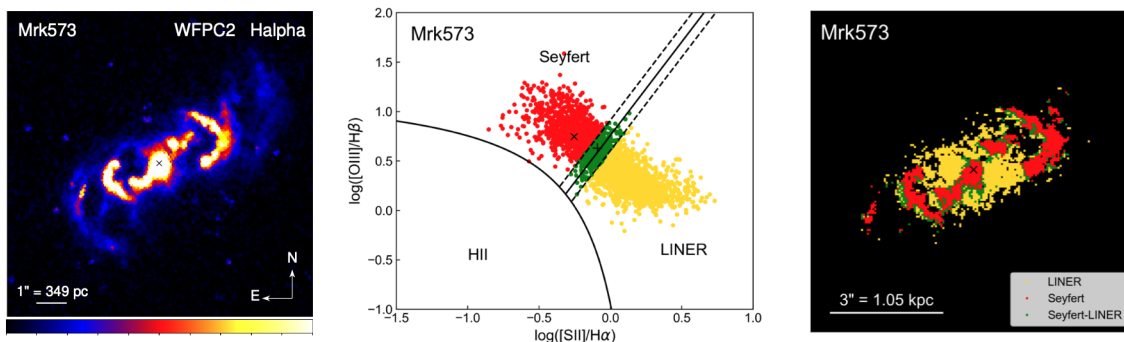
FIGURE 1.6: Spatial distribution of the NLR and LINER in the Seyfert galaxy Mrk 573. **Left**: The NLR of Mrk 573 seen in $H\alpha$ emission. **Middle**: The BPT diagram of Mrk 573. Red and yellow dots represent the ionized emission from the AGN activity and LINER, respectively. Green dots denote a transitional line between the AGN and LINER. **Right**: Spatial distribution of the AGN and LINER ionized emission lines. Ionized emission from the AGN activity is surrounded by the LINER. The transitional ionized line in the middle panel (green) appears at the edge of the AGN feature. The figures are taken from Ma et al. (2021).

1.1.3   AGN outflows

AGN release a significant amount of energy via strong outflows. The AGN outflows are driven by the radiative winds and kinetic radio jets. Fig. 1.7 shows the signatures of the radiative (left) and kinetic (right) outflows of AGN. Two distinct forms of outflows are caused by different physical mechanisms, and thus are one of the important features to characterise AGN. In the following I describe theoretical models and observational properties of the radiative and kinematic AGN outflows.
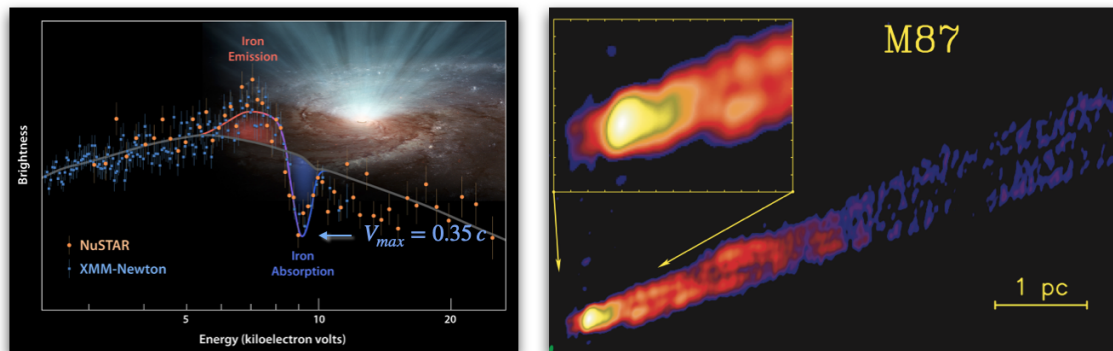
FIGURE 1.7: **Left**: Radiative wind in the BALQSO PDS 456. Highly blue-shifted absorption indicates a sub-relativistic outflow. Image credit: NASA/JPL-Caltech/Keele Univ. **Right**: Radio jet outflow in M 87. A highly collimated radio jet is accelerated to relativistic speeds. The figure is taken from Kovalev et al. (2007)

- **Radiative winds**: A broad absorption feature is seen against the UV or optical continuum emission in Quasi-Stellar Objects (QSOs). A highly blue-shifted line profile indicates sub-relativistic outflows ($\sim$0.3 c) on the surface of the accretion disk (Reeves et al. 2003; Tombesi et al. 2010; Gofford et al. 2011). About 40 % of QSOs exhibit such strong radiative disk winds, and they are termed as Broad Absorption Line Quasars (BALQSOs) (Ganguly & Brotherton 2008; Allen et al. 2011). In most AGN, the Eddington ratio of AGN is less than 1, and hence the radiative pressure of accreting matter is not sufficient to halt its accretion flow against the gravitational force of the SMBH. Apparently, an additional force is required to explain the sub-relativistic outflows observed in BALQSOs. Several models have been proposed as the physical mechanism of the radiative winds in BALQSOs, which include a magnetocentrifugal wind (Blandford & Payne 1982), thermal pressure (Woods et al. 1996), and a line-driven wind (Murray et al. 1995; Nomura et al. 2020). Among them, the spectral line driven wind model is the most favored model due to its reliable physical conditions. According to the line-driven wind model, the low opacity of spectral lines helps to extract the momentum of the radiation field in the vicinity of the accretion disk. Consequently, the radiative pressure of spectral lines can be a few orders

of magnitude stronger than the radiation force induced by electron scattering. Therefore, the radiation force is capable of driving a sub-relativistic outflow, overcoming the SMBH's gravity at the surface of the accretion disk. Strong radiative winds can quench the star formation of the host galaxy by expelling the ambient medium (Fabian 2012, and references therein). There has been much effort to find the signature of strong radiative winds in the nearby Seyfert galaxies as a low-luminosity version of BALQSOs. Relatively weak or moderate outflows are rarely found in nearby Seyfert galaxies, and they are termed as mini-BAL QSO (Giustini et al. 2011; Kaastra et al. 2014).

- **Kinetic radio jet**: A highly collimated relativistic radio jet appears in AGN, which are hosted by massive elliptical galaxies. The spatial extent of the radio jet ranges from AU to Mpc scales. The radio jet consists of the compact radio core, collimated jet, and extended lobe structures. The physical mechanisms of the jet formation are explained by two major models, which are the Blandford-Znajek (BZ) and Blandford-Payne (BP) (Blandford & Znajek 1977; Blandford & Payne 1982) model. The magnetic field energy accumulated by the differential rotations of the rotating SMBH (BZ model) or accretion disk (BP model) drives jet formation and accelerates the jet up to relativistic speeds. High-resolution VLBI observations of the base of radio jets indicate that the BP and BZ processes are not exclusive; instead, they might coexist in the process of jet formation (Boccardi et al. 2016; Baczko et al. 2019). Magnetohydrodynamic processes are thought to drive jet acceleration gradually over the distance of 10^2 - $10^6 \, r_g$ where r_g is the Schwarzschild radius of the SMBH (Asada et al. 2014; Boccardi et al. 2017). Luminous radio emission of the jet is ascribed to the synchrotron radiation of relativistic electrons (Burbidge 1956). The radio jets are classified by their structural differences and power. For instance, the Fanaroff-Riley classification (i.e., FR I and FR II) categorizes luminous radio jets by their shape of the extended structures (Fanaroff & Riley 1974). FR I type radio jets have a bright core and diffuse lobe structure. Contrary, FR II type radio jets are characterized by an edge brightened lobe structure. In particular, FR II sources have much higher luminosity than FR I sources. AGN harboring relatively small scale radio jets ($<1 \, \mathrm{Kpc}$) also exist. These compact radio sources are termed as Compact Symmetric Objects (CSOs), and their spectral features subdivide CSOs into the High Frequency Peakers (HFP) and Gigahertz Peaked Spectrum (GPS) sources. They are supposed to represent young progenitors of the extended radio jets or frustrated versions of the extended radio jets caused by interactions with a dense ambient interstellar medium (ISM) (An & Baan 2012, and references therein).

1.1.4   Classification

Classifications based on the observational properties of AGN have resulted in more than 50 sub-classes (Padovani et al. 2017). Such a complicated classification system does not properly reflect the intrinsic properties of AGN. Instead of listing all the sub-classes of AGN, it is more worthwhile to consider only a few critical criteria, which differentiate the overall AGN populations. These criteria are **i) radio-loudness, ii) accretion rate (i.e., Eddington ratio)**, and **iii) amount of obscuration**. Fig. 1.9 shows how the AGN can be divided into the sub-classes by these criteria. The first two criteria are related to the intrinsic properties of AGN. Radio-loudness and degree of accretion are direct observational probes, indicating the state of outflows and accretion of AGN. The radio-loudness parameter is defined by $R=(L_{\mathrm{radio}}/L_{\mathrm{opt}})$, where L_{radio} is the radio luminosity at $5\,\mathrm{GHz}$ and L_{opt} is the optical luminosity at $4400\,\mathring{A}$ (Kellermann et al. 1989; Ho 2002). $R=10$ is commonly used as the boundary between radio-loud and radio-quiet classes. Radio-loud AGN are hosted by giant elliptical galaxies harboring massive SMBHs. Radio-quiet AGN are dominantly hosted by spiral galaxies having less massive SMBHs. The Eddington ratio or line ratio of the ionized lines are dimensionless quantities, which are useful to compare the degree of accretion among different types of AGN. Based on the degree of accretion, both radio-loud and quiet AGN are further divided into two distinct sub-classes. Radio-loud AGN are classified into High Excitation Radio Galaxies (HERGs) and Low Excitation Radio Galaxies (LERGs) with the excitation index (see Fig. 1.13). For radio-quiet AGN, Seyfert and Low-Ionization Nuclear Emission-line Region (LINERs) are the counterparts of the HERGs and LERGs, respectively.
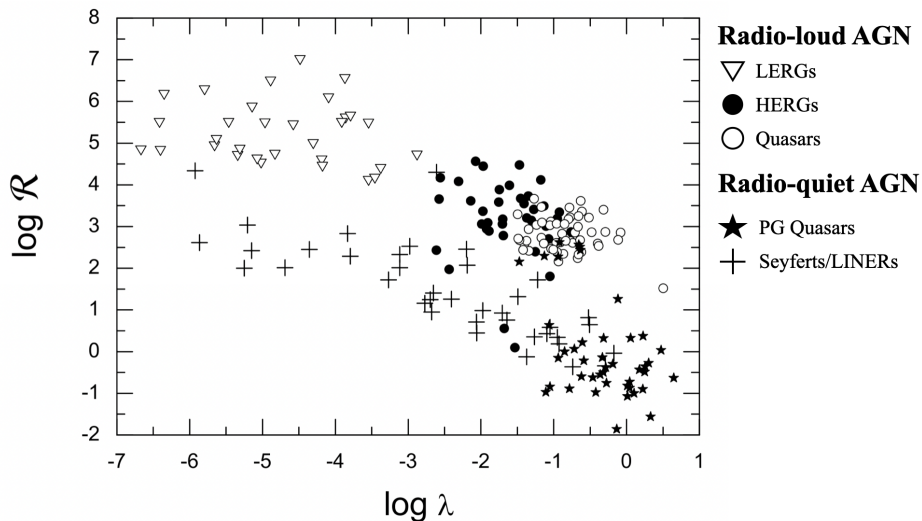
FIGURE 1.8: Radio loudness (R) versus Eddington ratio (λ) of AGN. Types of AGN are marked with different symbols on the right corner. The figure is taken from Sikora et al. (2007).
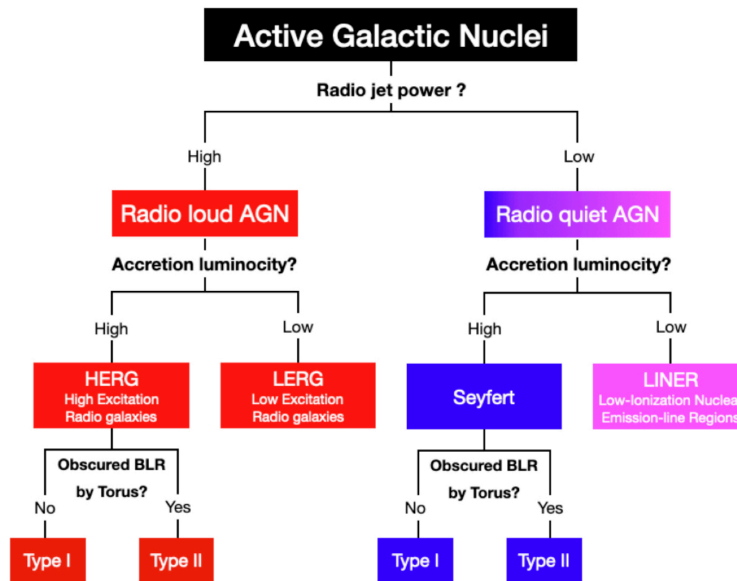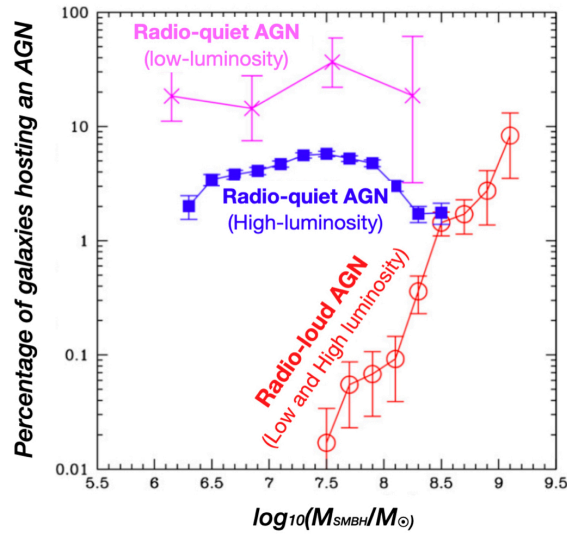
FIGURE 1.9: **Top**: The fraction of different types of AGN depending on the SMBH masses. **Bottom**: Classification of AGN based on the radio power, accretion luminosity, and obscuration of the BLR. The right figure is taken from Alexander & Hickox (2012).

The Eddington ratios have a mutual relation with the radio-loudness. Radio sources with powerful radio jets tend to have low Eddington ratios. This trend is found over a broad range of Eddington ratios (Ho 2002; Sikora et al. 2007; Chiaberge & Marconi 2011). An inverse correlation between the Eddington ratio and radio-loudness implies a physical connection between the accretion and radio jet outflow in AGN. However, the radio-loudness extends over a few orders of magnitude for a given Eddington ratio, including different types of AGN (see Fig. 1.8). Therefore, both radio-loudness and Eddington ratios are crucial factors to explain the subdivision of AGN.

On the other hand, different viewing angles towards AGN are also an important factor in the classification of AGN. Antonucci (1993) attributed the various appearances of AGN to a selective obscuration effect depending on our viewing angle towards an AGN. AGN consist of several sub-structures and they are not spherical symmetric. The accretion disk is close to a flat disk, and the collimated radio jet has a thin cylindrical structure. Also, relativistic beaming effects of the jet cause different jet properties depending on the observer's viewing angle. Consequently, the classification of AGN depends on both their intrinsic properties and our viewing angles. The unified model of AGN postulates a toroidal structure, obscuring the inner region of AGN. The torus intuitively explains the presence or non-presence of the BLR in AGN with an angle dependent obscuration effect. This paradigm is called the unified model of AGN, and it has been the basis of the AGN studies over the past decades. An important point is that the unified model of AGN does not explain the origin of all different AGN sub-classes. The unified model only explains the subdivision of intrinsically identical or analogous AGN populations. Therefore, the role of the unified model is located in the lowest layer in the hierarchic AGN classification system. Fig. 1.10 depicts the classification of the AGN populations.
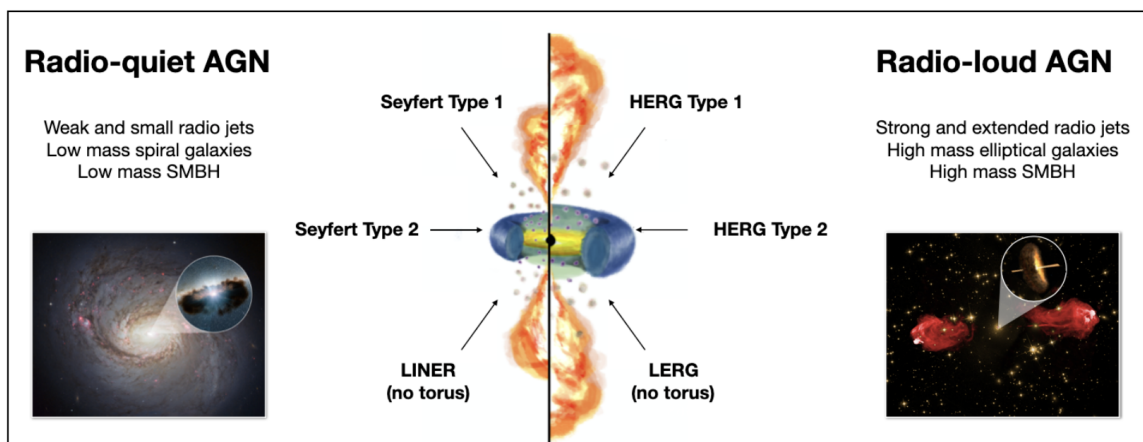
FIGURE 1.10: Illustration of the radio-loud and quiet AGN with their general properties. Image credits: NASA/STSiC/JPL-Caltech/NSF/NRAO/AUI/VLA/SOFIA/Lynette Cook.

1.2 AGN feedback and fueling

AGN outflows deposit a significant amount of energy into the surroundings (see §1.1.3). For instance, the radiative winds of AGN present in QSOs at high redshifts quench the star-formation by expelling the cold ambient medium. While the extended radio jets are relatively dominant in low-luminosity AGN at low redshifts. The radio jets suppress the cooling flows of the intergalactic medium (Best & Heckman 2012; Heckman & Best 2014, and references therein). These different forms of the AGN feedback are physically linked to the fueling flow. Therefore, a comprehensive study of the fueling and feedback processes of AGN is important to understand the relation between AGN and galaxies. In particular, this section describes these issues for AGN with radio jet outflows.

1.2.1 Mechanical feedback

As a radio jet is accelerated up to relativistic speeds, kinetic energy is dominant in the jet. The propagation of the radio jets lasts until the jet deposits all its kinetic energy into the surroundings. The radio jet is extending up to a few hundred kpc scales. This is a typical form of the radio jet feedback found in radio-loud AGN. In this process, the radio jets expels and heats the ambient medium. Combined X-ray and radio studies show a clear heating process caused by the radio jet propagation (McNamara & Nulsen 2007, 2012, and references therein). X-ray cavities and shock fronts coincide with the radio jet lobes (see Fig. 1.11). The total kinetic power of AGN jets is estimated using the suppressed X-ray surface brightness in the cavity (Bîrzan et al. 2008). The kinetic energy of the radio jets suppresses the cooling process of hot ambient gas. This could prevent the formation of cold molecular gas and suppress star formation in galaxies. Consequently, the growth of massive galaxies is hampered (Ciotti et al. 2017). In terms of the energy budget and the scale of influence, the radio jet is likely to be the primary heating source in massive galaxies.

Over the past decades, radio-quiet AGN have received less attention with regard to radio jet feedback due to their relatively low radiation power and small scale radio jets. However, the kinetic power of radio jets could be an order of magnitude higher than its radiation power (i.e., synchrotron radiation) (McNamara & Nulsen 2007). Despite the small spatial extent of the jets, the nuclear region of radio-quiet AGN is filled with a denser gas than radio-loud AGN, and thus even weak radio jets might also heat, expel, and shock the circumnuclear gas on kpc scales. Indeed, numerical simulations of the radio jet feedback show that low-power radio jets are more efficiently coupled with the surroundings than powerful radio jets found in radio-loud AGN (Mukherjee et al. 2016, 2018b). In their model, the powerful radio jets pass through the ambient ISM without strong interactions, but the lower power radio jets
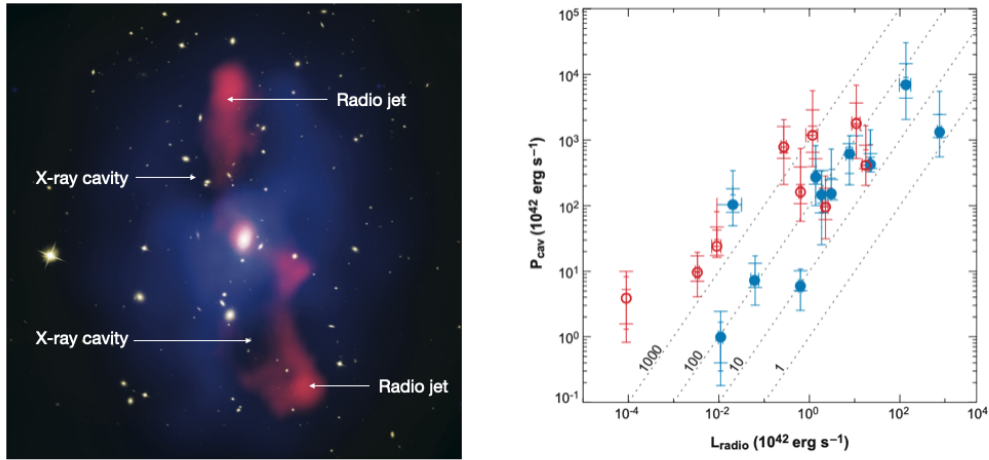
FIGURE 1.11: **Left**: Superposed images of Hubble optical (background), Chandra X-ray (blue) and the VLA radio (red) observations of the cluster MS0735.6+7421. The X-ray image shows two cavities that are filled with the radio lobes. **Right**: Comparison between the radiative and kinetic power of the radio jets. Solid blue and open red dots represent empty X-ray and radio-filled cavities of radio AGN. The total radio luminosity was measured with the VLA from 10 MHz to 10 GHz. The figures are taken from McNamara & Nulsen (2007)

more efficiently disrupt the surrounding gas as the jets are coupled with the ambient medium. The impact of radio jet feedback on radio-quiet AGN could be significant on sub-galactic scales within a few kpc (see Fig. 1.12). Shocks induced by jet-ISM interaction can expel or compress the ambient ISM. Consequently, the star formation efficiency can be suppressed or enhanced (Alatalo et al. 2015; Oosterloo et al. 2017). This new insight brings a strong implication to understanding the scope of the radio jet feedback. The most pressing task is to find the signature of radio jet feedback in the innermost region of radio-quiet AGN. Density, kinematics, and chemical properties of the ISM interacting with radio jets can provide observational constraints to prove the presence of the radio jet feedback in radio-quiet AGN. ALMA observations show a possible jet-driven molecular outflow within the central few hundred pc of radio-quiet AGN (i.e., Seyfert galaxies). However, the connection between the jet and molecular outflows are unclear due to insufficient angular resolutions. (Oosterloo et al. 2017; Alonso-Herrero et al. 2018; Fernández-Ontiveros et al. 2020a). Alternatively, high-resolution observations towards molecular absorption lines against radio jets can help to scrutinize the molecular gas on sub-pc scales (Morganti et al. 2003, 2005, 2013; Aditya & Kanekar 2018).

1.2.2 Fueling flow

A fueling flow triggers the AGN outflows, and also determines the form of AGN feedback. For example, the powerful radio jet is mostly found in AGN with low
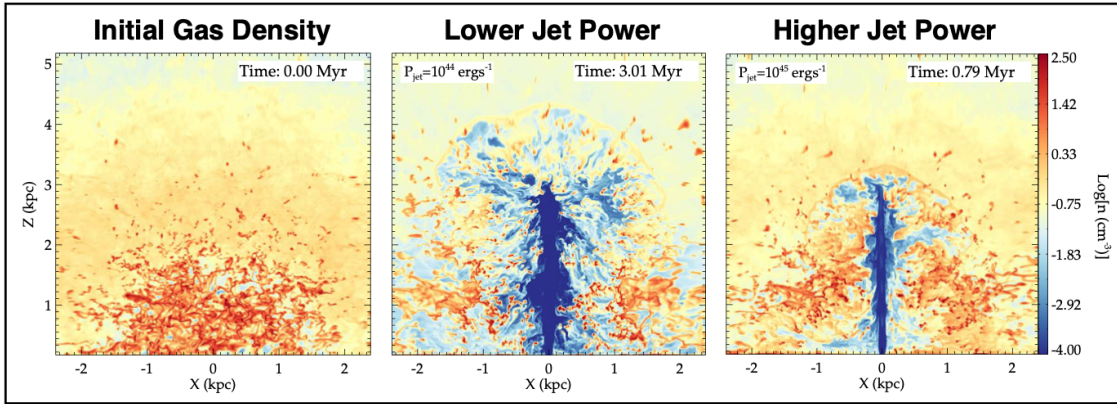
FIGURE 1.12: The impact of the radio jet feedback with different jet power. The left panel shows the initial gas density. Middle and right panels show the variation of gas density by the propagation of the low and high power jets, respectively. The color scale indicates the gas density. The figure is taken from Mukherjee et al. (2018b)

Eddington ratios (i.e., radio-loud AGN). As it is noticed in §1.1.4, radio-loud AGN are classified into HERGs and LERGs via the excitation index or the Eddington ratio (see Fig. 1.13). Apparently, different types of fueling flows are likely to be present in HERGs and LERGs, respectively (Buttiglione et al. 2010; Best & Heckman 2012). A natural explanation on the bimodality of the radio-loud AGN is a higher accretion rate in HERGs compared to LERGs. The presence of cold gas in AGN can enhance the Eddington ratio. Fueling cold gas leads to high accretion rates via a radiatively-efficient thin accretion disk, while fueling hot gas results in relatively low accretion rates, forming a radiatively-inefficient thick disk. Without external supply of cold gas by galaxy mergers or interactions, most radio-loud AGN are supposed to be enshrouded by a hot atmosphere. In such a case, the fueling process is led by hot gas, cooled by the intergalactic medium. The Bondi accretion model describes the amount of accretion led by hot gas (Bondi 1952). The Bondi accretion rate is

$$M_{bondi} = 4\pi\lambda \left(GM_{\text{SMBH}}\right)^2 \rho/c_s^3, \qquad (1.3)$$

where λ is the scaling coefficient, and G is the gravitational constant, M_{SMBH} is the SMBH mass, c_s is the adiabatic sound speed of the gas, and ρ is the gas density. Within the Bondi radius ($R_B = GM_{\text{SMBH}}/c_s^2$), the accretion flow follows the Bondi solution. Allen et al. (2006) shows a tight correlation between the jet power of the low luminosity radio AGN and the Bondi accretion rate. However, the hot accretion model has been questioned due to several simplifying assumptions in the Bondi accretion model, such as spherically symmetric and adiabatic accretion flows with unperturbed and steady initial conditions. Also, the jet power of the most luminous radio AGN cannot be explained well enough by the accretion rate estimated with the Bondi accretion model (McNamara et al. 2011). An accretion rate higher than
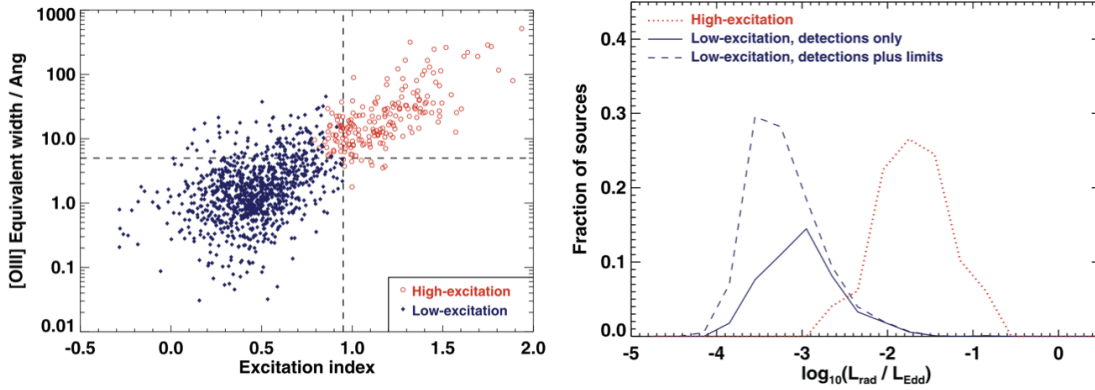
FIGURE 1.13: **Left**: The distribution of HERGs and LERGs on the [O III] equivalent width versus excitation index plane (Buttiglione et al. 2010). It shows a clear dichotomy between HERGs and LERGs. **Right**: The fraction of HERGs and LERGs versus the Eddington ratio measured with the [O III] luminosity. For LERGs, the dashed line indicates the maximal distribution calculated using either measurements of, or 3σ upper limit to, the [O III] luminosity. The solid line indicates the subset of these which are measurements rather than limits. The source samples are limited to z < 0.1. The figures are taken from Best & Heckman (2012).

the typical Bondi accretion rate is also required to explain secular HERGs, which have no signature of gas supply from recent gas-rich galaxy mergers or stripping. The Chaotic Cold Accretion (CCA) model has been considered as a more realistic fueling process present in radio-loud AGN (Gaspari et al. 2015, 2017). The CCA suggests a strong cooling process of the hot atmosphere induced by growing thermal instabilities and collisions between condensed gas blobs. The three-dimensional adaptive mesh refinement simulations of the accretion process, including realistic physics such as heating, cooling and turbulence, show an enhanced accretion rate by two orders of magnitude higher than the Bondi accretion rate (Gaspari et al. 2013). The presence of cold gas in the nuclear region of radio-loud AGN has been reported via molecular absorption line observations (Tremblay et al. 2016; Nagai et al. 2019; Kameno et al. 2020; Rose et al. 2020). However, the limited angular resolutions (a few tens of pc) prevent to resolve a fueling flow in the vicinity of the central engine. High-resolution spectral line VLBI observations are needed to test the prediction of the CCA model in HERGs and LERGs on scales of pc and sub-pc scales.

1.3   Motivation and outline of this thesis

Relativistic plasma jet from AGN, which can be observed at radio wavelengths, is one of the most interesting astrophysical phenomena. Our understanding of the radio jet has significantly improved over the last decades in both theoretical and observational aspects. However, the nature of different types of radio jets and the physical connection with their host galaxies are still controversially discussed. Regarding these issues, an immediate ambient medium (i.e., circumnuclear gas) of radio jets is a key probe which can discriminate accretion models responsible for different radio jet properties and reveal the influence of radio jets on their surroundings. For these reasons, much effort has been devoted to characterizing the physical and chemical properties of the circumnuclear gas in radio AGN. However, biased AGN samples and rather coarse angular resolutions have limited observational studies using molecular emission lines.

To better constrain the circumnuclear gas properties in different types of radio AGN, this thesis attempts to study the circumnuclear gas by using molecular absorption observations against the continuum emission of radio jets. Bright continuum radio jets in the nuclear region of radio AGN allow us to detect even rare molecular species in absorption. Moreover, spectral-line VLBI observations towards molecular absorption lines can spatially resolve a small scale (<sub-pc) structure or kinematics of the circumnuclear gas near the jet launching region. Such high-resolution observations are crucial to reveal the onset of radio jet feedback or the fate of a fueling flow in the vicinity of the central engine.

Despite the advantages of absorption line studies, only a handful of radio AGN has been identified as a molecular absorption system. Moreover, the physical origin of the obscuring gas in known absorption systems are ambiguous. This motivated me to conduct a comprehensive molecular absorption line study for radio AGN using state-of-art radio facilities, including single-dish, interferometer, and VLBI arrays. The strategy of this research is to find new molecular absorption systems for a large number of radio AGN via single-dish observations. Follow-up spectral line observations using a high-sensitivity connected array aim at detecting various molecular species to constrain the physical and chemical properties of the obscuring gas. Finally, for an absorption system with peculiar absorption features, such as broad line widths or larger Doppler shift velocities, spectral line VLBI observations aim at resolving the molecular absorber in front of the continuum jet and clarify its physical connection with AGN fueling or feedback processes. Below I summarize the content of the chapters of this thesis.

- **Chapter 2** introduces the observational tools used for the molecular absorption line studies presented in this thesis. Basic principles and measurements in radio observations are described for various radio facilities, such as a single-dish telescope, connected interferometry, and VLBI. The data reduction and imaging processes for interferometric observations are also briefly addressed.

- **Chapter 3** presents the 100m Effelsberg and IRAM 30m telescope surveys of molecular absorption lines toward a sample of radio AGN. This is a pilot study to find molecular absorption systems suited for follow-up spectral line high-resolution VLBI observations. The survey results and the capability of single-dish telescopes for absorption line observations are discussed.

- **Chapter 4** presents a 3 mm spectral line survey towards the radio AGN 3C293 and 4C31.04 using the NOEMA interferometer. This is a follow-up study for the confirmed molecular absorption systems in the single-dish surveys from Chapter 3. Various molecular species have been newly detected in absorption. Diagnostics using different molecule species characterize the chemical properties of the kpc scale nuclear disk of 3C293 and 4C31.04.

- **Chapter 5** presents the high-resolution VLBI observations of the radio-quiet AGN NGC 3079. The circumnuclear OH gas and radio jet of NGC 3079 is spatially resolved on a sub-pc scale via high-sensitive EVN observations. The kinematics and location of the 6 GHz OH absorption lines and radio jet show the impact of jet-ISM interaction on the circumnuclear gas and radio jet.

- **Chapter 6** addresses the observations of OH gas in the innermost region of the radio-loud AGN Cygnus A. High sensitive array (HSA) VLBI observations at 13 GHz detect a putative fueling flow or a molecular torus in the core region of Cygnus A. The kinematics and the origin of excited OH molecular clouds are discussed in the context of AGN fueling and the unified scheme of AGN.

- **Chapter 7** summarizes the main findings achieved in this thesis. Ongoing observation programs and an outlook on future works are also addressed.

Chapter 2

Radio observations

Abstract AGN radiate over the entire electromagnetic spectrum. However, AGN emission at optical wavelengths is easily obscured because the ISM is optically thick in the central region of the galaxy. Radio observations are less affected by obscuration of dust and the ISM. Observations using radio interferometry in the mm bands enable us to reveal the most important physical phenomena in the innermost region of AGN with the highest resolution. This chapter outlines observational tools and techniques to study AGN at radio wavelengths.

2.1   Single-dish telescopes

A single-dish telescope is a fundamental tool in radio astronomy to detect radio emission from celestial objects. The first parabolic radio telescope built by Reber (1944) observed radio emission at 160 MHz (1.9 m in wavelength) with an angular resolution of about 12 degrees. In the early days, receiver technology was able to observe only at long wavelengths (a few meters), and this limited the angular resolution of early radio telescopes to a few degrees ($\Theta_{res}=\lambda/D$, where λ is the observing wavelength, and D is the aperture size). As the receiver capabilities have been improving over the past decades, modern radio telescopes now cover a much broader range of wavelengths from a few meters to sub-mm. Depending on the main scientific applications, different telescope structures (e.g., mount, reflector, and geometry) or receiver systems (single or multiple pixels) are adopted. Nevertheless, most radio telescopes have similar sub-systems using the same basic principles. Thus, getting a glimpse of a modern radio telescope system is beneficial for understanding the process of radio observations. Fig. 2.1 shows a schematic view of the Gregorian type Sardinia Radio Telescope (SRT). Its main sub-systems are present in Fig. 2.2. The pathway of the received radio signal is divided into three steps. First, the filled aperture reflects the radio signal to a focal plane. Then, the front-end filters and amplifies a specific range of wavelengths of the radio signal. Lastly, the processed radio signal is digitized and recorded in the back-end system. A more detailed description of each step is described below.
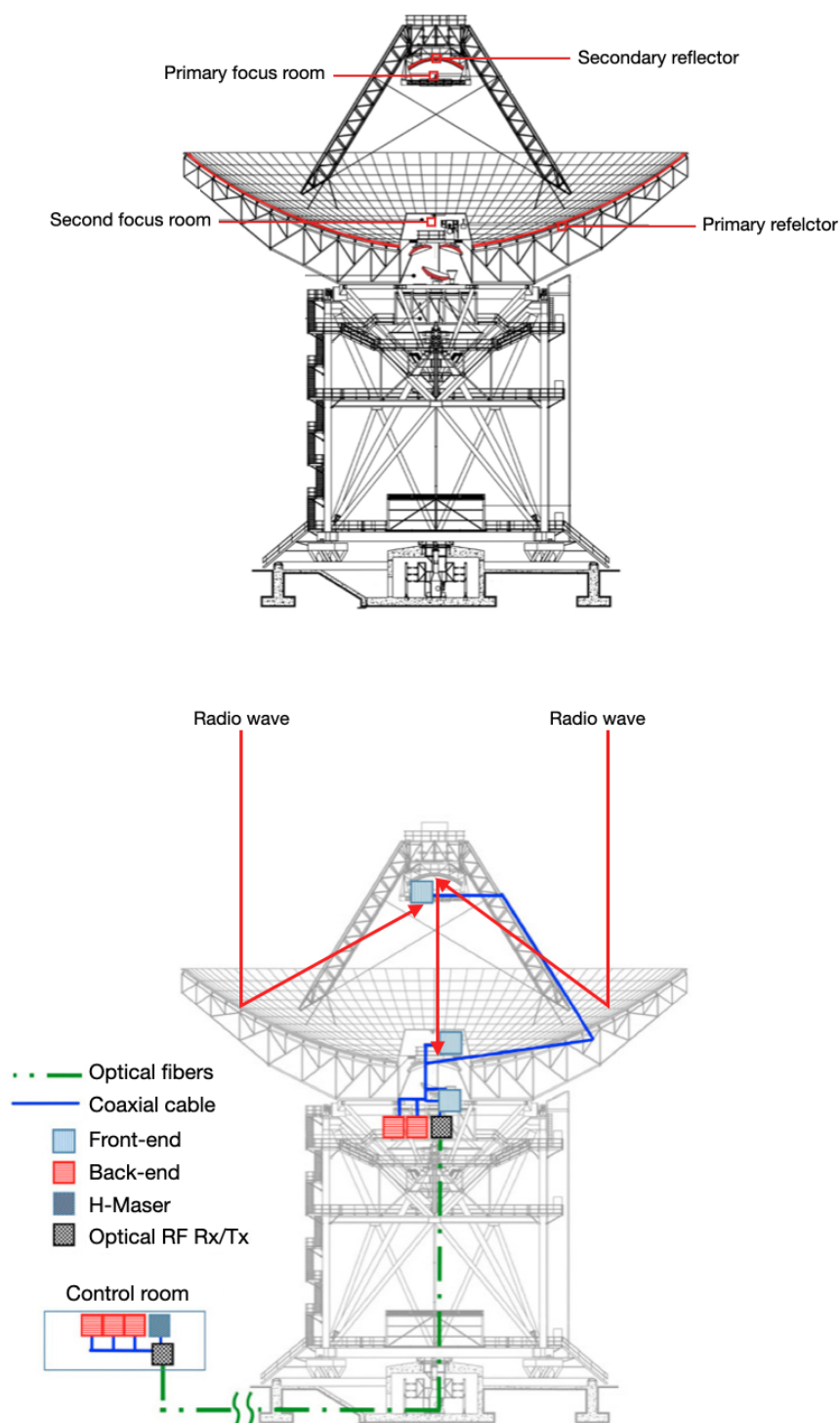
FIGURE 2.1: Top: A schematic view of a radio telescope, here as an example the 64 m Sardinia radio telescope. The Gregorian system has two focal planes. Low and high frequency receivers are positioned at the primary and second focus rooms, respectively. Bottom: The signal paths of the incoming radio signals. The red solid line indicates the signal path from the sky to the front-end. The blue solid line traces the signal path from the front-end to the back-end. The green dotted line marks the signal path from the back-end to the digital recording system in the control room. The figures are taken from Bolli et al. (2015).

2.1.1   Signal paths

- **Antenna and focal plane**: In the Gregorian system, the primary aperture reflects the incoming radio signals to the prime focal plane. A sub-reflector behind the prime focus reflects the collected radio signals to the second focal plane. Radio receivers are located either at the prime or second focal plane. Low frequency observations are relatively tolerant for an inaccurate focal point compared to high-frequency observations, and hence low-frequency receivers are also often located at the prime focal plane. The second focal plane has much longer focal length than the prime focal plane, which helps minimize the sidelobe and deviations of the focal point. Thus, the second focal plane is favored for high-frequency observations. For a large telescope, the temperature or gravity can cause deformations of the primary aperture. It can significantly degrade the surface accuracy of the radio telescope. If the amount of deformation is too large, actuators can be attached to the primary aperture to adjust the surface panels of the primary aperture. Alternatively, the variation of the antenna gain is measured by observing radio sources at different elevations, and applied in the calibration process.

- **Front-end**: The received radio signal induces a voltage oscillation on the feed horns located at the focal plane. The feed horn response is highly sensitive to a specific frequency range. Orthomode Transducers (OMT) split the received signal into two circular (right and left) or linear (vertical and horizontal) polarizations. In principle, single-dish telescopes are single-pixel imagers, but a multiple beam system using an array of feed horns and receivers can scan a large area of the sky at the same time with multiple pixels. The radio signal received at the feed horn is filtered by a band-pass filter and proceeds to a mixer. An intermediate frequency signal generated by a local oscillator is mixed with the radio signal. For VLBI observations, an accurate timing signal from a hydrogen maser is used to phase-lock the signal at the mixing stage. The mixer lowers the frequency of the original radio signal (down-conversion). The products of the mixer are the upper and lower sidebands. The frequency of the local oscillator determines the spectral window. Thus, available local oscillator frequencies must be considered in advance for spectral line observations. The Low-Noise Amplifier (LNA) attached to the mixer amplifies the radio signal. The feeds and LNAs are cooled-down at a few tens of Kelvin. The receiver cooling is done via liquid nitrogen to minimize the thermal noise. The temperature of the receiver room is cooled and monitored during the observing time. The processed radio signal proceeds to the back-end system via coaxial cables (see Fig. 2.2).
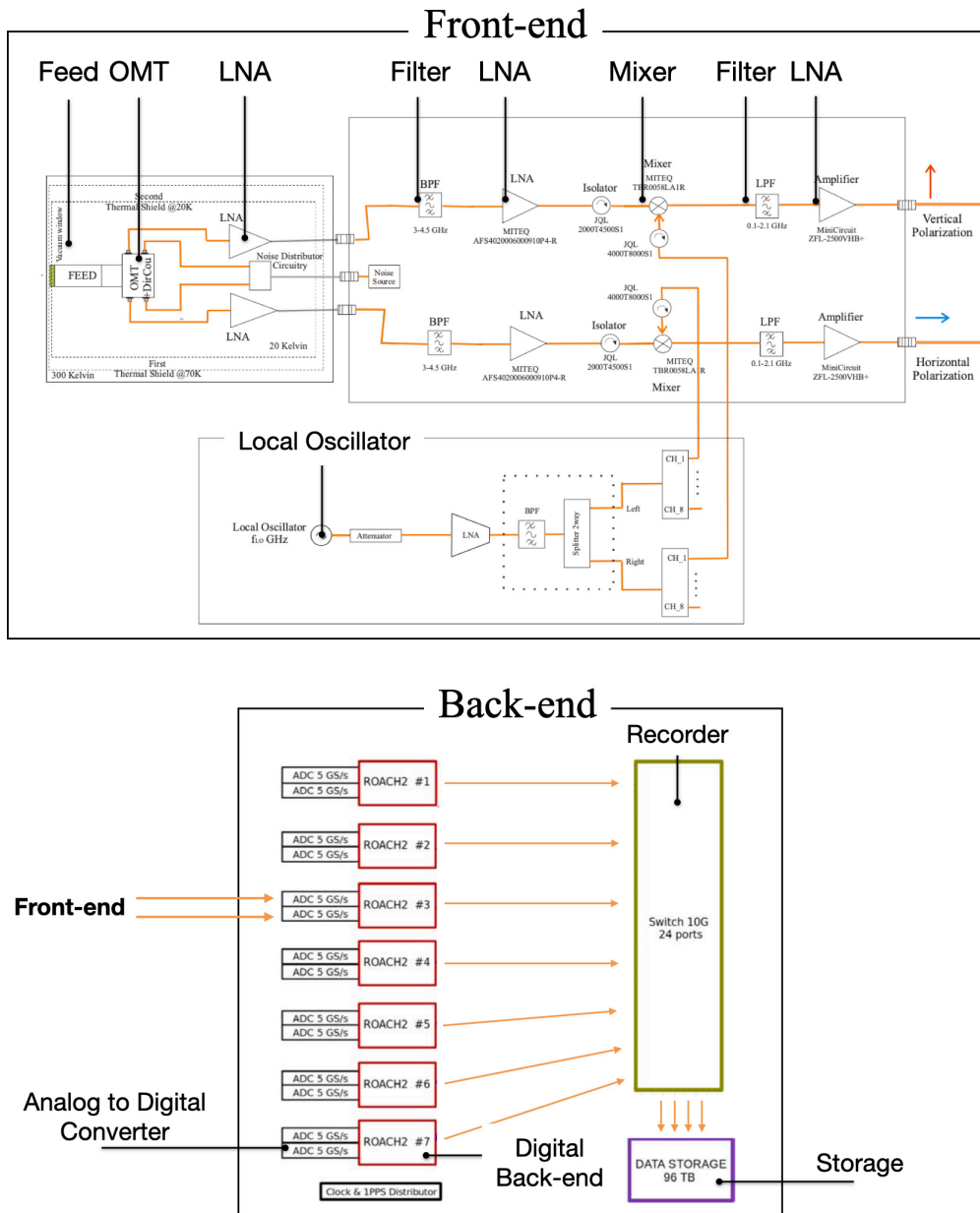
FIGURE 2.2: The path of the radio signal over the front-end and back-end systems in the 64 m Sardinia radio telescope. The front-end amplifies, filters, and down-converts the received radio signal. The radio signal is processed separately for each polarization. The power of the radio signal is measured, digitized, and recorded in the back-end system. The figures are taken from Valente et al. (2016) and Melis et al. (2018).

- **Back-end**: The back-end digitizes and records the processed radio signals in the front-end. A square-law detector squares the voltage oscillations, and the attached integrator eventually provides the power of the radio signal. A modern digital back-end system also serves as a spectrometer. A Fourier transform of the time series data yields a radio spectrum for the spectral window. The digital back-end system sets the spectral window, bandwidth, and the number of the channels to record. According to the Nyquist–Shannon sampling theorem (Shannon 1949), at least two times higher sampling frequency than the frequency of the target signal is necessary to preserve the information of the original signal in the sampled data. The raw data output from the back-end system is converted to Flexible Image Transport System (FITS) format, which commonly has compatibility with data reduction softwares in radio astronomy. In VLBI observations, the observed data are recorded by a specialized recording system to process the observation data from different radio telescopes in the correlator center. The Mark 4, 5, and 6 VLBI data recording systems, developed by Haystack Observatory[1], are commonly used for this purpose. The observed VLBI data are labeled with highly stable and accurate time information, referring to a phase stable local oscillator such as the hydrogen maser frequency standard.

2.1.2 Single-dish observations

The purpose of single-dish observations is to measure the brightness temperatures of radio sources. The radio source can emit continuum, spectral lines, or both. The diffraction limit of the primary aperture determines the angular resolution of the radio telescopes, which is the minimum size of the sampling area on the sky in single-dish observations. Ideally, a circular aperture forms a diffraction pattern, and its bright central region is called the Airy disk. The angular size of the Airy disk (θ) represents the diffraction limit $\theta = 1.22\,\lambda/\mathrm{D}$, where λ is the observing wavelength and D is the aperture size. The Full Width at Half Maximum (FWHM) is the angular size between the two points where the Airy disk is half of the maximum amplitude, which is a measure of the angular resolution of radio telescopes. The FWHM of a Gaussian beam is approximately $\theta = 1.02\,\lambda/\mathrm{D}$. The solid angle of radio telescopes is given by $\theta^2/4\pi$ in the units of radian. The effective aperture of radio telescopes, A_{eff} is usually smaller than the ideal geometric aperture size ($A_{geo} = \pi\mathrm{D}^2$). The effective solid angle of the radio telescopes is

$$\Omega_{SD} = \frac{\lambda^2}{4\pi A_e}. \tag{2.1}$$

---

[1]https://www.haystack.mit.edu/
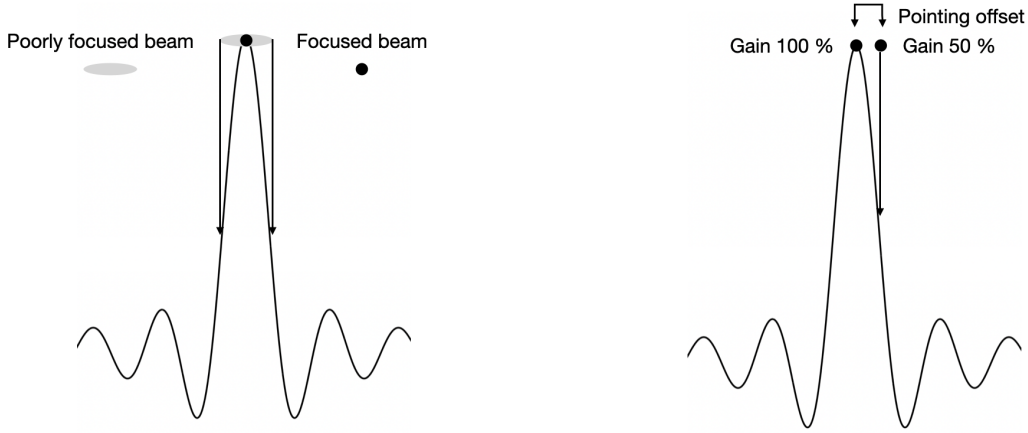
FIGURE 2.3: The effect of poor focus and pointing in the gain of the radio telescopes. For a point-like source, a poor focus blurs the response of the beam. A pointing offset locates the target source at the side of the beam, where the gain is lower than at the peak.

Single-dish observations measure the surface brightness I_ν ($\mathrm{W\,m^{-2}\,Hz^{-1}\,sr^{-1}}$) on the sky integrated over the effective solid angle of radio telescopes. The flux density of a radio source is defined via:

$$S_\nu\,(\mathrm{W\,m^{-2}\,Hz^{-1}}) = \int_{\Omega_{\mathrm{SD}}} I_\nu d\Omega. \tag{2.2}$$

A conventional unit measuring the flux density of radio sources is Jansky ($1\,\mathrm{Jy} = 10^{-26}$ $\mathrm{W\,m^{-2}\,Hz^{-1}}$). The observed flux density is translated to the brightness temperature (T_{B}) by assuming a blackbody radiation of the radio source. Although many radio sources are not ideal blackbody radiators, the brightness temperature is commonly used for the comparison of various radio sources. The relation between flux density and brightness temperature is

$$S_\nu = \frac{2k\nu^2}{c^2} T_{\mathrm{B}} \int_{\Omega_{SD}} d\Omega, \tag{2.3}$$

where S_ν, k, ν, c, T_{B}, are the flux density, Boltzmann constant, observing frequency, speed of light, and brightness temperature, respectively. The beam efficiency is affected by the relative angular size between the target source and beam. The antenna efficiency (A_{eff}) reflects those factors, and simply relates the temperature and flux density of the target source. Therefore, the actual measurement from single-dish observations of the radio source is the antenna temperature:

$$T_{\mathrm{A}} = \frac{A_{\mathrm{eff}}}{2k} S_\nu = G \cdot S_\nu, \tag{2.4}$$

where S_ν is the flux density of the source, and G is the gain factor. The physical meaning of the T_{A} is the convolution between the sky brightness of the source and

the beam pattern of the radio telescopes. The gain factor is given in the units of K/Jy, and it represents the sensitivity of radio telescopes. A large aperture size, high surface accuracy of the aperture, and low observing frequencies are factors that can increase the gain factor of radio telescopes. The surface efficiency η_s is given by

$$\eta_s = \exp\left[-\left(\frac{4\pi\sigma}{\lambda}\right)^2\right], \tag{2.5}$$

where the σ is the rms surface error, and λ is the observing wavelengths (Ruze 1966). According to this Ruze equation, the deformation of the aperture induced by gravity degrades the surface efficiency. In practice, the surface efficiency is a function of the elevation of radio telescopes. For radio telescopes equipped with an active surface system, the increased surface errors can be compensated by using actuators attached to the aperture. Otherwise, the variation of the surface efficiency should be taken into account in the data reduction process. To obtain the expected gain factor, accurate pointing and focus of the beam are necessary. A relative position offset between source position and telescope beam significantly degrades the gain factor on the target source (see Fig. 2.3).

Radio observations towards blank sky yield the so called system temperature

$$T_{\mathrm{sys}} = T_{\mathrm{rx}} + T_{\mathrm{amt}} + T_{\mathrm{bg}} + T_{\mathrm{spill}} + T_{\mathrm{loss}} + T_{\mathrm{sw}}, \tag{2.6}$$

which include all thermal noise sources irrelevant to the temperature of the target source, such as the receiver (T_{rx}), atmosphere (T_{amt}), galactic background (T_{bg}), thermal sources captured by side-lobes (T_{spill}), instrumental loss (T_{loss}). Observations of a very bright continuum source may also induce a standing wave (T_{sw}). The response of the radio telescope to a radio source is temperature T_{sou}, which is the summation of the system temperature and the antenna temperature of the source ($T_{\mathrm{sou}}{=}T_{sys} + T_{\mathrm{Ant}}$). However, the temperature is not directly measured in Kelvin. The raw output from the back-end system is **counts** (i.e., analog to digital units, ADU). Therefore, it should be properly scaled to the units of temperature. The chopper wheel method using cold and hot loads measures the scale between the counts and antenna temperature (Penzias & Burrus 1973; Kutner & Ulich 1981). The counts scale to a temperature scale also can be measured with a switched noise diode of known temperature.

In the following, I explain the chopper wheel method in detail. The back-end outputs for the different emission sources are
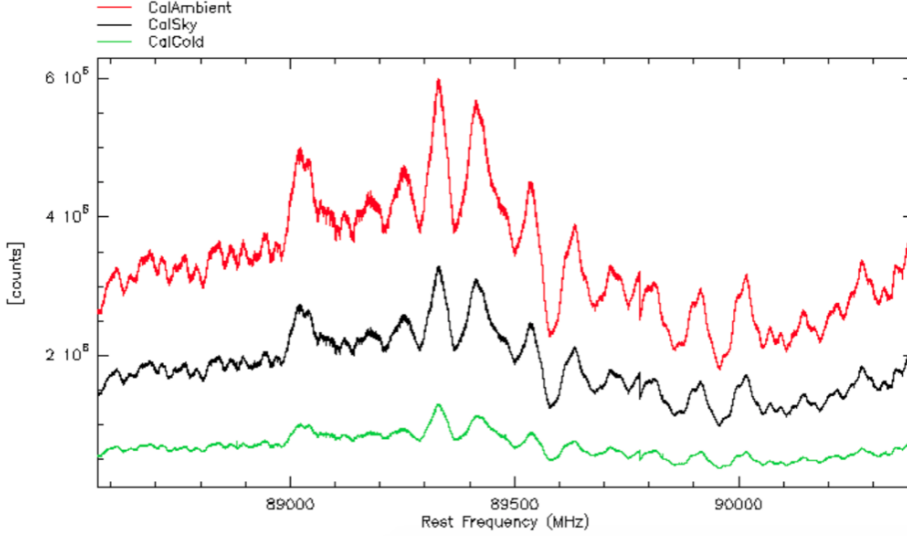
FIGURE 2.4: The example of the back-end outputs of the IRAM 30-m radio telescope for different calibration sources as a function of frequency. The back-end outputs are unstable over the frequency channels. Red and green solid lines show the back-end outputs from cold and hot loads. The black solid line indicates the back-end output for the blank sky. The counts are used to measure the scale factor and the system temperature of the radio telescope.

$$C_{load} \cdot k = (T_{rx} + T_{load}), \tag{2.7}$$

$$C_{sky} \cdot k = (T_{rx} + T_{emi}) = T_{sys}, \tag{2.8}$$

$$C_{source} \cdot k = (T_{rx} + T_{emi} + F_{eff} \cdot e^{-\tau} \cdot T_{Ant}^*), \tag{2.9}$$

where C and T are the counts and temperature from different sources, k is the scale factor, F_{eff} is the beam efficiency, and $e^{-\tau}$ is the atmospheric attenuation. Counts measurements from the hot and cold loads are used to obtain the scale factor k

$$k = \frac{T_{hot} - T_{cold}}{C_{hot} - C_{cold}}. \tag{2.10}$$

Observation of the blank sky gives the system temperature. Fig. 2.4 shows the back-end outputs of the 30-m IRAM telescope over the spectral window for 3 different calibration loads. The back-end outputs are unstable over the frequency axis. Calibration of the frequency dependent T_{sys} and scale factor k is an important issue in spectral line observations (Winkel et al. 2012). A subtraction of the counts between the target source (C_{on}) and the blank sky close to the source (C_{off}) gives the antenna temperature of the source T_{Ant}

$$T_{Ant} = \Delta T = T_{On} - T_{Off} = k \times (C_{source} - C_{sky}) \tag{2.11}$$

$$T_{Ant} = T_{sys} \times \frac{(C_{source} - C_{sky})}{C_{sky}}. \tag{2.12}$$

Several switching methods are used to obtain the antenna temperature of the source T_{Ant}. The position switching method uses the T_A of the blank sky. It is available for both continuum and spectral line observations, but doubles the observing time. Also, a standing wave (T_{sw}) induced by a bright continuum source cannot be removed by the position switching method. The frequency switching method subtracts T_A between two different spectral ranges, and is only applicable to spectral line observations. The beam switching method using T_A measurements in two independent beams saves observing time, but an additional calibration is necessary to calibrate the different instrumental gain between the two beams. The corrections of the atmospheric attenuation and beam efficiency (F_{eff}) of the telescope yield the intrinsic antenna temperature of the target source

$$T_{Ant}^* = T_{Ant} \times \frac{e^\tau}{F_{eff}}. \tag{2.13}$$

The sensitivity of radio telescopes is given by

$$\sigma_T = \frac{\kappa \cdot T_{\mathrm{sys}}}{\sqrt{\Delta\nu\Delta t}} \tag{2.14}$$

where κ is the noise coefficient, $\Delta\nu$ is the bandwidth, Δt is the total observing time. For instance, $\kappa = \sqrt{2}$ for switching observations due to a half integration time on the source.

2.2   Radio interferometry

After the first radio sky survey using single-dish telescopes (Edge et al. 1959; Bennett 1962), subsequent efforts to find the optical counterparts of the detected radio sources raised the demand for high angular resolution radio observations. At a given wavelength, the angular resolution can be improved by enlarging the aperture size of the telescope, but the cost would become excessive to build a steerable single-dish radio telescope larger than 100-m. As a new approach to attain higher angular resolutions, much work has been devoted to the development of radio interferometer, which uses two or more single-dish telescopes. In the 1960s, the successful demonstration of the aperture synthesis technique revolutionized radio astronomy and added the capability of radio interferometry. Today, radio interferometers, such as the VLA[2] offer a wide range of angular resolutions by changing the configuration of the (up to 27) radio telescopes. This section describes the key principle of the aperture synthesis and data reduction process to reconstruct radio images from interferometric observations. The content follows the overview provided by Thompson et al. (2017).
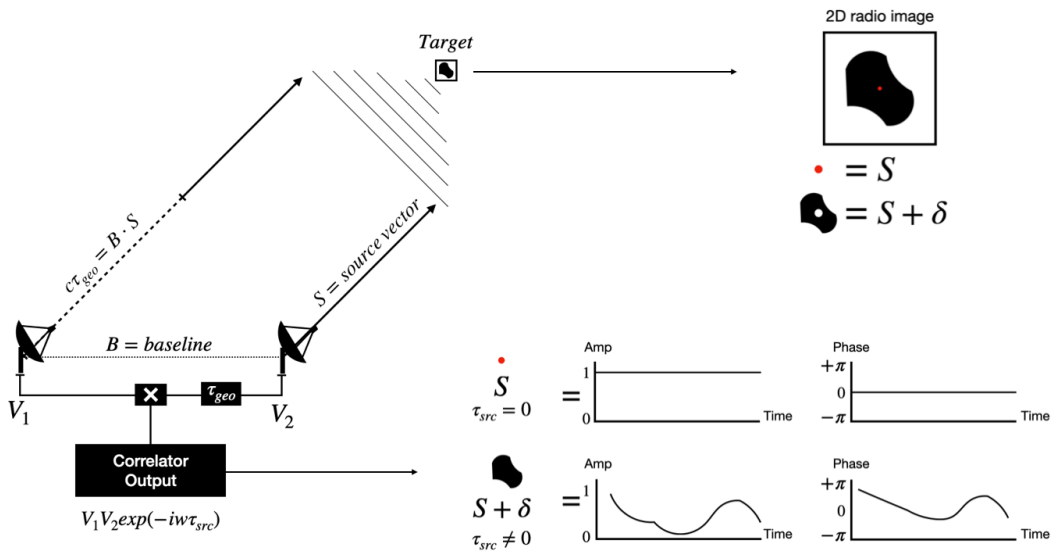
FIGURE 2.5: **Left**: Structure of a basic interferometer. Radio signals observed by two separated radio telescopes are multiplied and integrated with delay compensations. The output is a correlation function. Right (top): 2D radio image of the target source. A geometric delay between two stations is compensated by the point source at the coordinate **S**. Right (bottom): Correlator outputs for the radio image. A residual delay is 0 for the point source at **S**. Accordingly, the amplitude and phase of the correlation function are 1 and 0, respectively. The amplitude and phase are constant over time. Contrary, a residual delay for the radio source at the coordinate **S** + δ is not 0. The residual delay caused by the source structure induces variation of the amplitude and phase of the correlation function.

---

[2]https://science.nrao.edu/facilities/vla/docs/manuals/oss/performance/resolution

2.2.1   Aperture synthesis

The simplest radio interferometer consists of two spatially separated radio telescopes. The arrival time of the incoming radio signal at the two stations is different. The recording system of the radio telescope allows us to synchronize two radio signals from different stations by compensating for the time delay of the radio signals. For the synchronized radio signals, the correlator measures their correlation functions (i.e., visibility). This is the basic measurement output of radio interferometry. The principle of the aperture synthesis is to translate the measured visibility samples to the two-dimensional sky brightness distribution of the radio source. If the delay compensation is complete, one might cast doubt on the meaning of the correlation function for the two identical radio signals. The answer is that the delay compensation is performed towards the infinitesimal point source located at source vector $\mathbf{S}$, which points to the (phase) center of the brightness distribution. For instance, the geometric time delay (τ_g) between two stations towards a radio source vector $\mathbf{S}$ is

$$\tau_\mathrm{g} = \frac{\mathbf{S} \cdot \mathbf{b}}{c}, \tag{2.15}$$

where $\mathbf{b}$ is the baseline vector, and c is the speed of light. After the delay compensation for τ_g, the two-dimensional radio emission at $\mathbf{S} + \delta$ induces a residual delay τ_src, which is given by

$$\tau_\mathrm{src} = \frac{\delta \cdot \mathbf{b}}{c}. \tag{2.16}$$

A residual delay related to the source structure is translated to the baseline dependent visibility function through the correlation process. The measured visibility samples are used to reconstruct the true image of the radio source. Fig.2.5 illustrates the correlation outputs of a two-element interferometer for a point-like and a two-dimensional brightness distribution of the source. The visibility (i.e., correlation) function for the residual delay is

$$V_1 V_2^* = V_1 \exp(iwt) V_2 \exp[-iw(t + \tau_\mathrm{src})] = V_1 V_2 \exp(-iw\tau_\mathrm{src}), \tag{2.17}$$

where V_i is the amplitude of the radio signal at telescope i, w is the wave number ($2\pi\nu$), t is the time, τ_src is the delay induced by the radio emission at source vector $\mathbf{S} + \delta$. In practice, the output of the correlator (i.e., visibility) is the correlation function response for the two-dimensional intensity distribution of the radio source $I(\delta)$. The source power received by the two-element interferometer is $V_1(\delta) V_2(\delta) = A_N(\delta) I(\delta)$, where $A_N(\delta)$ is the normalized power pattern of the interferometer. The observed visibility of the source from interferometric observations is the Fourier transform of the intensity distribution. It can be written as:

$$V_{1,2} = \int A_N(\delta)I(\delta)\exp(-iw\tau_{\text{src}})d\delta \tag{2.18}$$

$$V_{1,2} = \int A_N(\delta)I(\delta)\exp(\frac{-2\pi i\delta \cdot \mathbf{b_{1,2}}}{\lambda})d\delta \tag{2.19}$$

The rectangular coordinate system commonly used in synthesis imaging consists of the direction cosines u, v, and w, where u and v are perpendicular to direction to the source, and u points towards the source vector. This denotes the baseline vector as

$$b = ue_u + ve_v + we_w \tag{2.20}$$

e_u, e_v, and e_w are the unit vectors. The vector of an arbitrary position of the two-dimensional radio image is $\delta = xe_u + ye_v$. This is so called the tangential approximation assuming $w=0$. The spatial frequencies $u_\lambda=u/\lambda$ and $v_\lambda=v/\lambda$ denote the length of the projected baseline towards the source vector $\mathbf{S}$ in the units of wave number. Consequently, the visibility function from interferometric observations is

$$V(u,v) = \int\int A_N(x,y)I(x,y)\exp[-2\pi i(ux+vy)]dxdy \tag{2.21}$$
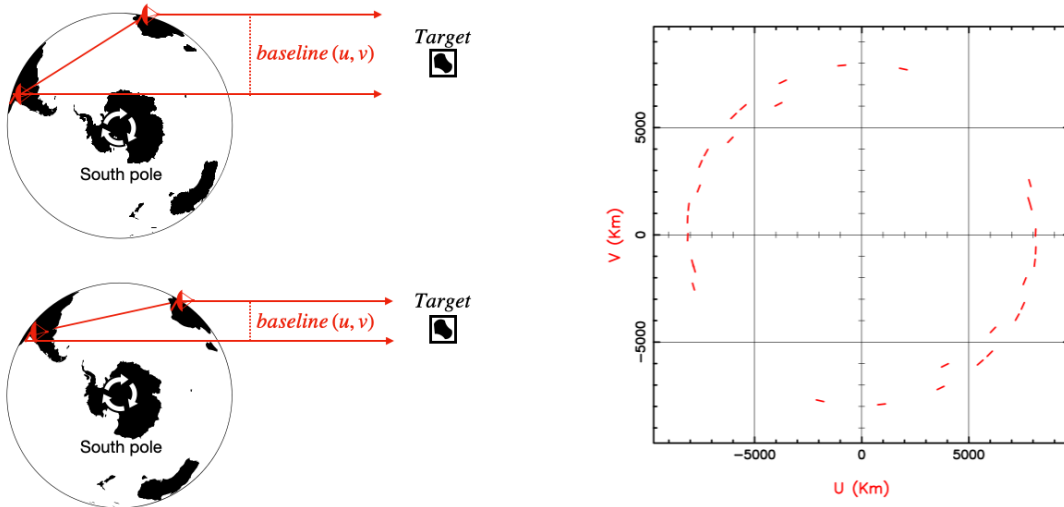
FIGURE 2.6: **Left**: The projected baseline length in the two-element interferometer is changing by the Earth rotation. **Right**: UV space of the target source filled with interferometric observations. The red dotted line indicates the projected UV distances for a pair of radio telescopes.

The Earth rotation helps sample the visibility of the radio source by changing the length of the projected baseline (see Fig. 2.6). The number of visibility sample increases with the number of antenna ($N_{vis}=N(N+1)/2$, where N is the number of

antenna). According to the *van-Cittert Zernike theorem*, the sky brightness distribution of the radio source is the inverse Fourier transform of the sampled visibility function. Therefore, we obtain the intrinsic sky brightness distribution (Eq. 2.22) from interferometric observations.

$$A_N(x, y)I(x, y) = \int \int V(u, v) \exp[2\pi i(ux + vy)] du dv \qquad (2.22)$$

2.2.2 Deconvolution

The normalized power pattern of the interferometer $A_N(x, y)$ (i.e., Synthesized beam) is a Gaussian beam in the ideal case. In practice, interferometric observations only partially fill the UV space. Thus the dirty beam pattern (i.e., Fourier transformation of the UV-coverage) corrupts the intrinsic intensity distribution $I(x, y)$. Fig.2.7 shows the effect of convolution of the dirty beam with the true image. Various deconvolution algorithms have been developed to reconstruct the true image from the dirty (i.e., convolved) images. The CLEAN algorithm uses an iterative process, subtracting the convolved Point Spread Function (PSF) from the peak position of the dirty map. Some variant clean algorithms have also been suggested (Högbom 1974; Clark 1980). The Maximum Entropy Method (MEM) uses the Bayesian statistic to determine pixels and amplitudes for deconvolution (Cornwell & Evans 1985; Narayan & Nityananda 1986). The Adaptive Scale Pixel (ASP) fits the dirty image with Gaussian components in various scales, and models visibilities corresponding to the Gaussian components. Iterative Gaussian fittings also yield good approximations to the true image (Bhatnagar & Cornwell 2004).
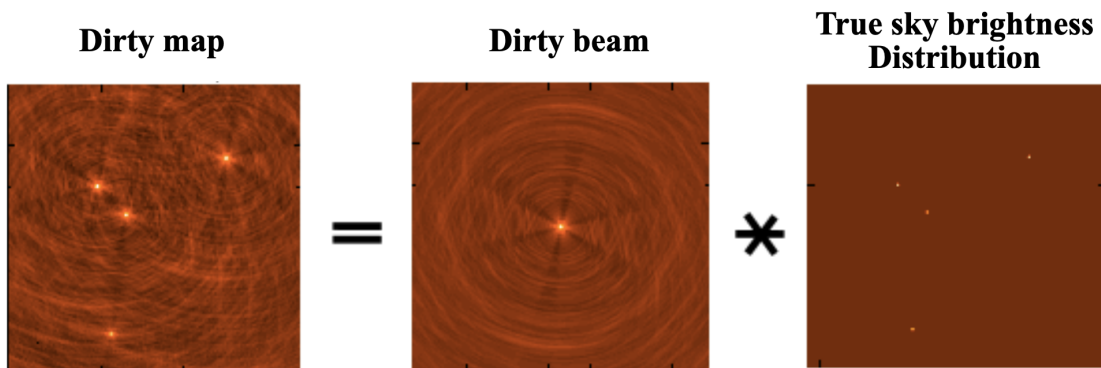
FIGURE 2.7: **Left**: Convolution of the true image and the dirty beam. **Middle**: Dirty beam obtained from the Fourier transformation of the UV-coverage. **Right**: The true sky brightness distribution of the source. Figures are taken from the CASA webpage (https://casa.nrao.edu/casadocs/).

2.2.3   Connected interferometer and VLBI

With the successful installation of connected interferometers, the demand even for higher angular resolutions led to the development of the VLBI, which uses a baseline length of more than a few hundred kilometers. As described in §2.2.1, the sampled visibility is only meaningful when two separated stations are synchronized to the same wave-front towards the source vector **S**. Time delay compensations among distant VLBI stations are technically demanding due to different atmospheric conditions and ambiguous delay factors. Hence, additional techniques and calibration processes are necessary for the realization of a VLBI system.

A connected array consists of a tens of radio telescopes separated by a few kilometers, and the stations are physically connected with coaxial cables. The delay compensation of connected arrays is made by adding an instrumental delay to each station with respect to a reference station. The similar atmospheric condition for all the stations helps to keep the synchronization during the observing time with a small variation in phase and delay. Intervening scans on a bright radio source are used to calibrate the phase fluctuations. Consequently, the correlation model for a connected interferometer is relatively simple compared to the one used by VLBI. Harsh weather conditions and more extended array configurations further increase phase fluctuations, but more frequent phase calibrations can solve this issue. If the target source is bright enough, phase calibration can be made directly using the target source without an intervening calibrator. This is called self-calibration.

On the other hand, VLBI stations are spread over more than a few hundred kilometers. Hence, data independently recorded at each station need to refer to a local hydrogen maser frequency standard, which adds accurate time stamps to the recorded data. All data are transferred to a correlator center to obtain the visibility samples on the target source. The first step in the correlation of VLBI data is to determine the relative delay offsets between the stations. This process is called **fringe search**. An elaborate correlation model is needed to compensate for delays and delay rates among VLBI stations. The proper delay and delay rates parameters are determined by searching for the highest amplitude of the correlation function. For this purpose, all VLBI observations must include a few scans towards a bright and compact radio source. The bright radio source serves as a fringe finder in the correlation process. If a fringe is detected at a baseline, it works as a visibility sampler for the target radio source. The delay and phase fluctuations during the observing time are typically larger than for connected arrays due to different regional conditions. These residual delay and phase variations are compensated using calibration sources. The latter steps for VLBI imaging are similar for the connected arrays.

2.2.4   Calibration and imaging interferometric data

The amplitudes of the visibility samples measured by interferometric observations should be calibrated to a physical scale for synthesis imaging. The relation between the measured (V'_{ij}) and true (V^*_{ij}) visibility between station i and j is given by

$$V'_{ij}(t) = A_i A^*_j V^*_{ij}(t) + \epsilon_{ij}(t), \qquad (2.23)$$

where A_i and A_j are the station-based complex antenna gains and $\epsilon_{ij}(t)$ is additive noise. Phase and amplitude calibrations estimate proper complex gains to derive the true visibility of the source. In principle, inverse Fourier transformation of the calibrated visibilities yields the radio image. However, visibility samples obtained from interferometric observations are discrete and only partially fill the Fourier space (i.e., $u-v$ space). Accordingly, sophisticated imaging methods (i.e., deconvolution) are required to reconstruct the most likely image of the true sky brightness distribution of the radio source. The basic steps for calibrations and imaging of the interferometric data are briefly outlined below:

- **Correlation**: A correlator synchronizes, multiplies and integrates the recorded radio signals from the spatially separated interferometry stations to obtain visibility samples. Once the data arrives at the correlation center, the correlator play back and processes the recorded data. The geometric delay and the delay rates between each pair of stations are compensated by using a correlation model and a fringe finder. Accurate delay and delay rate parameters are searched, tracking the peak amplitude of the correlation functions of the fringe finder. As the next step, the correlator multiplies and integrates the radio signals from the target source with the optimal delay and delay rate parameters obtained from the fringe finder. This process is done in the complex plane to get both the real and imaginary parts of the correlation function. To get the correlation function over the different frequency channels (i.e., frequency), a Fourier transform is applied for the time series voltage data. The order of Fourier transform in the correlation process defines the type of correlators. The XF–type correlator performs the correlation first, and the FX-type correlator performs the Fourier transform first. Most modern correlators are of FX-type due to its simpler structure than the XF-type. Time integration increases the SNR of the visibility as long as the visibility phase is stable over the integration time. The integration time is limited when the accumulated phase error exceeds 1 radian. Atmospheric turbulence and residual clock-offsets shorten the maximum accumulation time. The final product of the correlation is the visibility, which is the profound measurement of interferometric observations for imaging.

- **Phase calibration**: The correlator would compensate for the delay and delay rate of the radio signals by using the fringe finder. Nevertheless, unexpected atmospheric turbulence and instrumental errors could lead to a residual delay and delay rate on the visibility of the target source. The tracking of the residual delay during the observing time is crucial to use the visibility samples for imaging. The purpose of the phase calibration (i.e., fringe fitting) is to keep the delay compensations for each pair of stations by measuring the residual delay and delay rate with the phase of visibility samples. The residual delay and delay rate errors appear in the phase of the cross-power spectrum as a linear function of frequency and time, respectively. The phase induced by the residual delay τ_r is

$$\phi\left(t, \nu\right) = 2\pi\nu\tau_r. \tag{2.24}$$

A linear fitting of the phase shifts over time and frequency measures the residual delay and delay rate. The relation between phase shifts and residual delay and delay rate is

$$\Delta\phi\left(t, \nu\right) = \phi_0 + \left(\frac{\partial\phi}{\partial\nu}\Delta\nu + \frac{\partial\phi}{\partial t}\Delta t\right). \tag{2.25}$$

Fringe fitting also can be done with a bright spectral line source assuming a small residual delay over the spectral window of the line. The phase shift measurement over the time yields the delay rate. A point-like radio source is suited for the phase calibration due to the lack of phase fluctuation originating from the source structure.

- **Amplitude calibration**: The Fourier transform of the correlator outputs yields the cross-power spectrum. In the correlation process, integration over frequency and time reduces uncorrelated noise signals $(T_{sys,i}T_{sys,j})$, but maintains the correlated signal $(T_{Ant,i}T_{Ant,j})$. Hence, the signal-to-noise ratio (SNR) of the cross-power spectrum $(R_{i,j})$ is given by

$$R_{i,j} = \eta\sqrt{\frac{T_{Ant,i}exp(\tau_i)T_{Ant,j}exp(\tau_j)}{T_{sys,i}T_{sys,j}}}\sqrt{2\Delta\nu\Delta t}, \tag{2.26}$$

where η is the efficiency factor associated with digitization losses (η=0.88 for 2 bit sampling), $exp(\tau)$ is the compensation of the atmospheric attenuation, $\Delta\nu$ is the bandwidth of each channel, and Δt is the integration time. The SNRs of the cross-power spectrum $(R_{i,j})$ are translated to the flux density of the visibility $(S_{i,j})$ by applying the system temperature T_{sys} and gain factor (G_i) of the

individual stations. The correlated flux density relates to the cross correlation coefficient $R_{i,j}$ as follows:

$$S_{i,j} = R_{i,j}\sqrt{\frac{T_{sys,i}T_{sys,j}}{G_i \; G_j}}, \qquad (2.27)$$

System temperatures and elevation dependent gain factors are measured at each station, and are used for the amplitude calibration.

- **Self-calibration**: The phase and amplitude calibrations do not completely recover the true complex gain of the visibility data. A residual error in the complex gain is the main factor that corrupts or distorts the reconstructed image. The self-calibration method makes use of the closure phase and closure amplitude to minimize the complex gain error. The closure phase is the summation of the visibility phases from a set of three baselines of three stations, and the closure amplitude is the fraction of the visibility amplitudes from a set of four baselines of four stations. The closure quantities are good observable of interferometric observations, which represent the true phase information of the source and the fraction of the antenna based gains. The self-calibration method uses a least squares solution between a reliable source model and the observed data to estimate reliable complex gain values (Cornwell & Wilkinson 1981). For an interferometry with N telescopes, the number of closure phase and amplitude are $C_{phase}=(N-1)(N-2)/2$ and $C_{amp}=N(N-3)/2$, respectively. Therefore, a large number of stations is highly beneficial to establish a reliable source model via self-calibration.

- **Imaging**: According to the *van-Cittert Zernike theorem*, the calibrated visibility samples can be translated into the two-dimensional sky brightness distribution of the target source via inverse Fourier transformation. Nonetheless, the conversion is not straightforward in most cases because the visibility samples only partially fill the UV plane and the SNR of the visibility samples is not uniform. The UV-spacing determines the normalized power pattern of the interferometer (i.e., synthesized beam). Consequently, a direct inverse Fourier transform of the incomplete visibility samples results in the so called dirty image, which is corrupted by a dirty synthesized beam. An important step in interferometric imaging is to reduce the effect of the dirty synthesized beam on the dirty image. This process is called **deconvolution**. Different deconvolution algorithms have been suggested for synthetic imaging as described §2.2.2. In the CLEAN imaging process, point sources are selected and convolved with the dirty synthesized beam. Then, the convolved image is subtracted from the dirty

map. The clean process makes it easy to find real emission features, removing fake components induced by the dirty synthesized beam. The clean is repeated until no apparent point component is found on the dirty map. The final product of the clean imaging is the convolution between the identified point components and a Gaussian beam, which has the same angular resolution as the central part of the dirty beam.

2.3 Spectral line observations

As quantum systems, atomic or molecular gas have discrete energy levels, and a transition between two energy levels can lead to an emission or absorption line. The rest frequency of the transition is $\nu = \Delta E / h$, where ΔE is the energy gap between two energy levels, and h is the Planck constant. Numerous atomic and molecular lines are located at radio wavelengths. Hence, radio observations are suited for studying atomic and molecular gas in various astrophysical environments. In particular, this subsection describes spectral line observations towards AGN, including calibration and imaging processes.

2.3.1 Spectral lines from AGN

The dense gas in the central region (from a few pc to kpc scales) of an AGN is termed circumnuclear gas. Molecular thermal emission lines have been used to study the impact of AGN activities on the physical properties of the circumnuclear gas. For instance, the UV radiation of AGN creates the photo-dissociation region (PDRs), which then leads to an increase of the abundance of HCN and CN and ionized species (HCO$^+$ and CO$^+$) (Izumi et al. 2016; Imanishi et al. 2020). Shock waves induced by AGN outflows enhance abundances of molecules such as SiO, CH$_3$OH, and HNCO (García-Burillo et al. 2010, 2014; Martín et al. 2015). A Doppler shifted velocity of the spectral emission line also can identify and trace gas outflow or inflow features in AGN (Cicone et al. 2014; Harrison et al. 2018).

Despite their usefulness, molecular thermal emission lines are barely detectable in radio-loud AGN due to their large distances and a small amount of gas. However, the circumnuclear gas in radio-loud AGN can be detected in absorption when a bright background continuum source is present in the core of the AGN (Liszt & Lucas 2004; Combes et al. 2019). Furthermore, spectral line VLBI observations using the absorption lines against radio jets provide a few orders of magnitudes higher angular resolution than studies using molecular thermal emission lines. Spatially resolved gas distribution and kinematics in the innermost region of AGN is promising to reveal the

AGN fueling and feedback processes (Carilli et al. 2019). Fig. 2.8 depicts the location of molecular thermal emission and absorption lines in the core of radio-loud AGN.
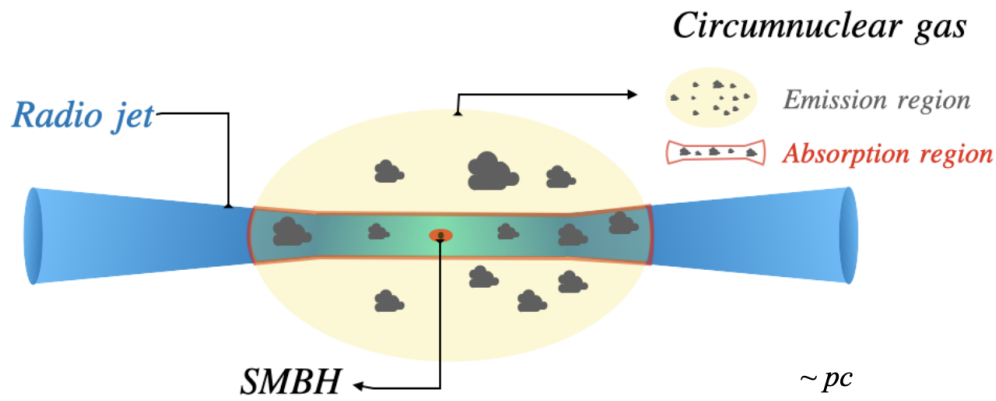
FIGURE 2.8: A schematic view of the innermost region of an AGN. A clumpy ambient medium surrounds the central engine and the radio jet. The location of molecular emission and absorption lines are sketched for illustration. Inflow or outflow of a gaseous medium can be studied via molecular absorption observations.

An amplified non-thermal emission line is also an important probe to study the circumnuclear gas in AGN. Molecular gas with an inverted level-population is the site of molecular Microwave Amplification by Stimulated Emission of Radiation (Maser). The inverted level-population is formed by external collisional or radiation pumping (Elitzur 1992). As it is named, the maser lines are highly amplified by stimulated emissions. H_2O and OH are well-known masing molecules. Maser clouds are characterized with high brightness temperatures (sometimes $>10^9 K$) and compact sizes (a sub-pc scale) by high-resolution VLBI observations.

Maser have been found in about 150 AGN, and are mostly hosted by Seyfert galaxies (Lo 2005, and references therein). In Seyfert galaxies, maser disks are located at the outer regions of the accretion disks within the sub-pc scale. Therefore, masers are key probes to study the gas kinematics in the vicinity of the SMBH. Maser disks in AGN have been used to measure the SMBH masses in AGN (Miyoshi et al. 1995; Gao et al. 2017). Maser emission is very rare in radio-loud AGN, which are hosted by elliptical galaxies. The line profile of the maser lines detected in radio AGN differs from the typical disk maser found in Seyfert galaxies. A shock maser driven by jet-ISM interactions (i.e., jet maser) has been suggested to explain the nature of maser in radio-loud AGN (Claussen et al. 1998; Wagner 2013). Fig. 2.9 shows a representative disk and jet maser in radio-quiet (NGC 4258) and radio-loud (NGC 1052) AGN, respectively.
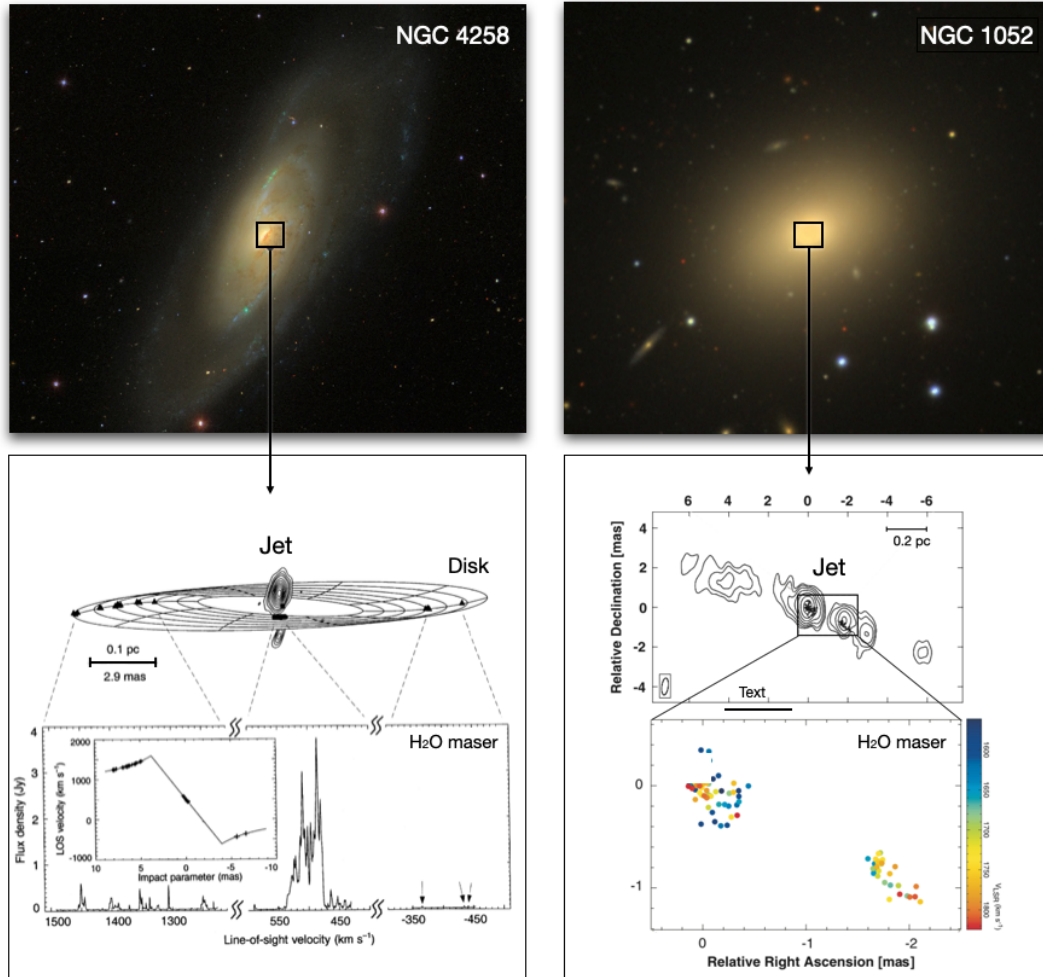
FIGURE 2.9: Examples for water maser emission in AGN. **Left**: H_2O maser in the radio-quiet AGN NGC 4258. The spatial distribution of the maser indicates a sub-pc scale warped disk. The radio jet is perpendicular to the maser disk. **Right**: H_2O maser in the radio-loud AGN NGC 1052. Aligned maser spots with the radio jet imply shock driven maser. The figures are taken from Herrnstein et al. (1999); Sawada-Satoh et al. (2008). Image credit: Sloan Digital Sky Survey

2.3.2   Observations and data reduction

Spectral line studies require additional steps in the observations and data reduction compared to continuum observations. First, frequency setup is important to locate the target transition on the observing spectral window. The observing frequency is determined by the rest frequency of the target transition and redshift of the target source. However, the sky frequency of the target transition needs to be accurately estimated if the available spectral window is narrow. For example, relative motions between the telescope and target source lead to Doppler shifts of the spectral line in the frequency domain. Most single-dish telescope support the Doppler tracking to compensate the Doppler shifts with respect to the reference velocity frame during

observations. On the other hand, radio interferometers use the topocentric reference velocity frame. Hence, the Doppler correction should be performed against a proper reference velocity frame in the calibration process. The kinematical Local Standard of Rest (LSR) frame is favored for galactic sources. However, the heliocentric velocity frame is preferred for extragalactic sources due to a simple frequency conversion with the optical redshift of the target source.

An accurate bandpass calibration is necessary for spectral line observations. For emission lines without a bright background continuum source, a prior gain correction over the frequency axis is sufficient to get a flat baseline in the spectral window. On the other hand, absorption line observations against a bright continuum source require additional bandpass calibrations. This is because the continuum emission affects bandpass shapes, and induces standing waves on the baseline. A bandpass calibration using a nearby bright continuum source and subsequent polynomial and sinusoidal baselines fittings help to get a flat baseline. However, oscillating baseline patterns often remain in the spectrum, and this hampers the identification of weak absorption lines. In such a case, interferometric observations are highly beneficial for removing standing waves in the spectrum. The correlation process of radio interferometric data effectively eliminates uncorrelated signals, such as standing waves and local RFI. Hence, radio interferometers are particularly suitable for absorption line observations.

In interferometric observations, the imaging process of spectral emission and absorption lines are different. For bright emission lines, the channel of the emission peak is used for the fringe fitting, but absorption lines use the continuum emission outside of the absorption region for the fringe fitting (see Fig. Fig. 2.10). Thus, the maximum achievable bandwidth is preferred for absorption line imaging. If the emission line or the continuum background of the absorption line are too faint to perform fringe fitting, a nearby bright continuum source can be used for the phase calibration. After the phase calibration, the imaging process is straightforward for spectral emission lines. After the Doppler correction, all spectral channels with an emission feature are imaged through an iterative deconvolution and self-calibration processes. For imaging absorption lines, the continuum emission needs to be subtracted. The continuum subtraction can be made either in the UV domain or image domain. The continuum subtraction in the UV domain is favored for high signal-to-noise UV data. A high-fidelity continuum image model should be established to subtract continuum in the image domain. The data reduction of interferometric observation data is conducted by using the imaging software Astronomical Image Processing System (AIPS) and the Difmap. Fig. 2.10 shows the block diagram of the detailed calibration processes for imaging spectral emission and absorption lines data with description for each step.
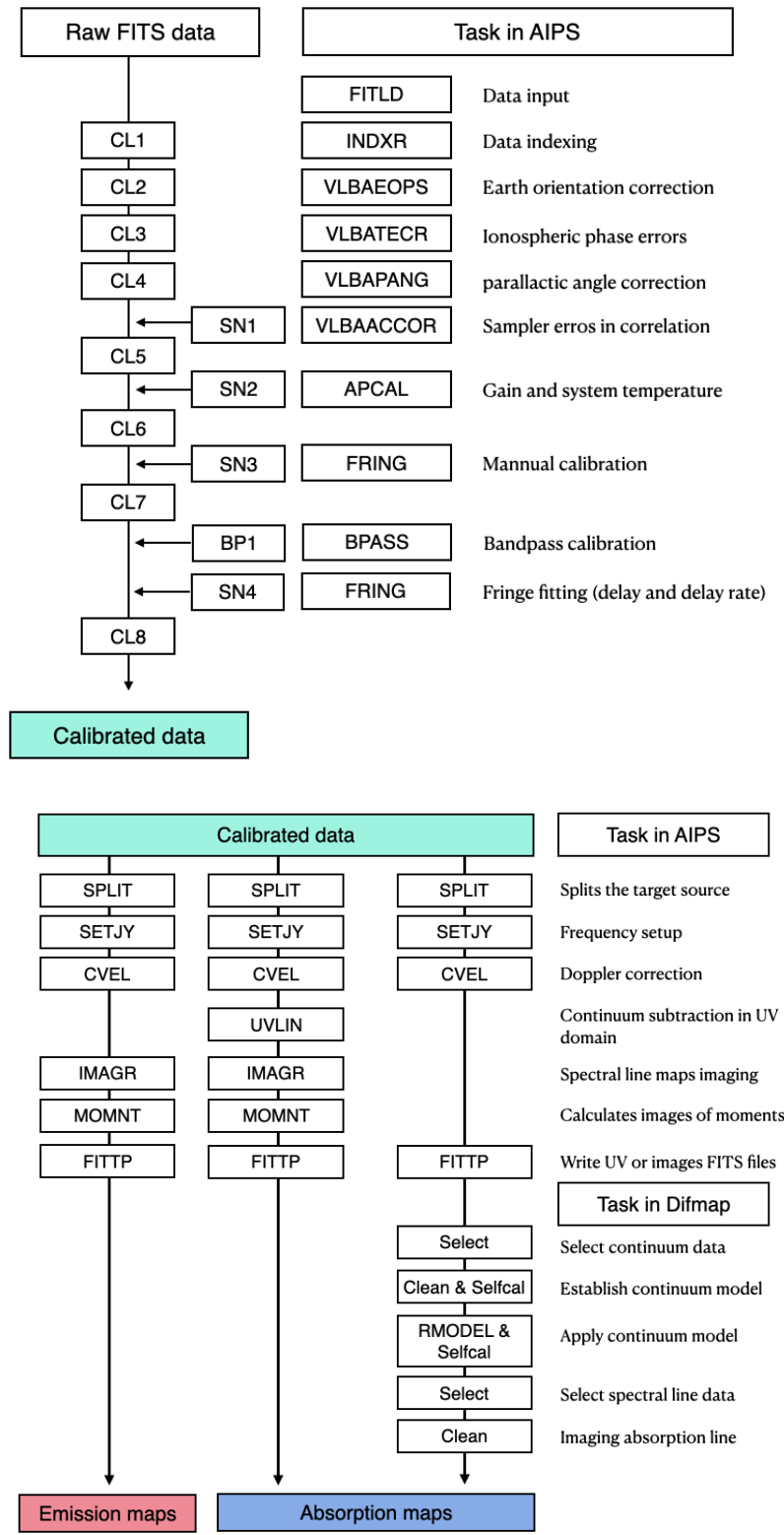
FIGURE 2.10: **Top**: A priory calibration process of VLBI data in AIPS. **Bottom**: Different calibration routes for imaging spectral line data. The left route shows the imaging process of spectral emission line data without continuum emission. The middle and right routes show the imaging process of molecular absorption lines with different continuum subtraction methods in UV and image domain, respectively.

Imaging spectral line data yields a three dimensional image cube. The third axis contains information for the velocity. Different integration methods along the velocity axis yield momentum maps. The moment maps represent total intensity (moment 0), intensity-weighted velocity (moment 1), and intensity-weighted velocity dispersion (moment 2). Each moment map is obtained by

$$
\begin{aligned}
Moment\ 0 &= \Delta v \sum_{i=1}^{N_{chan}} S_\nu\left(\alpha, \delta, \nu_i\right) \\
Moment\ 1 &= \frac{\sum_{i=1}^{N_{chan}} \nu_i S_\nu\left(\alpha, \delta, \nu_i\right)}{\sum_{i=1}^{N_{chan}} S_\nu\left(\alpha, \delta, \nu_i\right)} \\
Moment\ 2 &= \sqrt{\frac{\sum_{i=1}^{N_{chan}} \left(\nu_i - \overline{\nu}\left(\alpha, \delta\right)\right)^2 S_\nu\left(\alpha, \delta, \nu_i\right)}{\sum_{i=1}^{N_{chan}} S_\nu\left(\alpha, \delta, \nu_i\right)}}
\end{aligned}
\tag{2.28}
$$

where S_ν is the channel map, ν is the velocity, and $\overline{\nu}$ is the mean velocity. Fig. 2.11 shows the moment maps of CO emission lines in NGC 613 as an example.
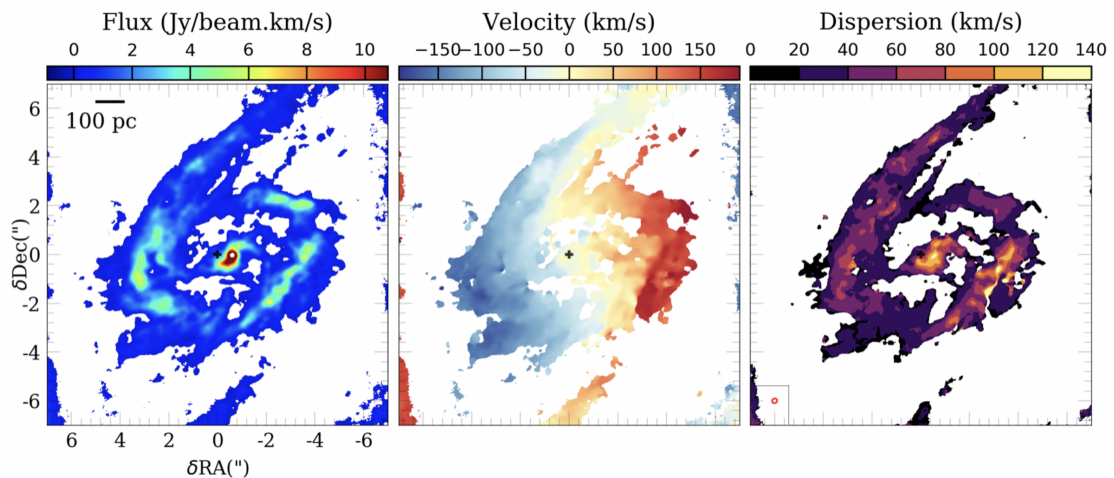
FIGURE 2.11: CO (J=3-2) moment maps of NGC 613. Moment maps are shown in order of moment 0, moment 1, and moment 2 from left to right. The figure is taken from Audibert et al. (2019).

Chapter 3

Single-dish molecular absorption line surveys

Abstract This chapter presents molecular absorption line pilot-surveys towards a sample of pre-selected radio AGN. OH, HCN, and HCO$^+$ lines were searched using the 100-m Effelsberg and 30-m IRAM telescopes at cm- and mm-wavelengths. The main goal of this study is to search for molecular absorption in front of the bright radio jets in AGN via single-dish spectroscopy. This is also a preparatory study for follow-up absorption line VLBI studies. In total 41 radio AGN were observed and molecular absorption lines were detected in 3 sources. Radio Frequency Interference (RFI) and standing waves present in the spectral line observations are the most likely causes for the low detection rates. The characteristics of the detected absorption line systems and their physical origins are discussed.

FIGURE 3.1: Two single-dish radio telescopes used in the molecular absorption line surveys. **Left**: The 100-m Effelsberg telescope operated by the Max Planck Institut für Radioastronomie (MPIfR), Germany (Credit: MPIFR). **Right**: The 30-m IRAM telescope operated by the Institut de Radioastronomie Millimétrique (IRAM), France at the Pico Veleta site in Spain.

3.1 Introduction

3.1.1 Motivation

Molecular absorption lines occur when continuum emission passes through the intervening interstellar medium (ISM). Studies using molecular absorption lines allow us to measure the physical quantities of the molecular gas in great detail complementing studies based on emission line observations (Combes 2008). Various molecular species are detectable in absorption regardless of their cosmological distance when a bright background continuum source (e.g., radio jet emission from AGN) is present. In contrast, emission line detection is more limited by the sensitivity of the observing telescope. One of the most useful applications using the absorption technique is to study the circumnuclear gas in radio AGN. The circumnuclear gas in radio AGN is of particular interest as it fuels the central engine, and influences the jet occurrence and propagation. In general, radio AGN are hosted by elliptical galaxies, and their circumnuclear gas is barely detectable via molecular emission lines due to their small gas content and large distance. However, their bright radio jets provide means to detect the circumnuclear gas via absorption.

Several molecular absorption line surveys of radio AGN have been carried out in the past, but the detection rates for the CO and OH ground transitions are rather low (Baan et al. 1992; Drinkwater et al. 1996). The lack of CO gas in radio AGN or high excitation temperatures caused by the strong continuum of radio AGN were suggested to explain the low detection rates in absorption surveys Maloney et al. (1994). An advanced absorption line survey using alternative molecular species or transitions from higher energy levels might enhance the detection rates. For instance, molecular emission line studies towards nearby AGN show higher abundances of certain molecular species in their circumnuclear region, such as HCN and HCO$^+$ (Usero et al. 2004; Kohno et al. 2008; Riechers et al. 2010). Indeed, HCN and HCO$^+$ lines have been detected in absorption from radio AGN with relatively higher absorption depths than other molecular species (Nagai et al. 2019; Kameno et al. 2020; Rose et al. 2020). Also, absorption surveys using rotationally excited OH transitions show higher detection rates than surveys using ground OH transitions (Impellizzeri 2008). However absorption surveys using HCN, HCO$^+$, and excited OH transitions are still rare, and hence only a handful of molecular absorption systems are known. This motivates us searching for HCN, HCO$^+$ and excited OH absorption lines in a well-selected sample of radio AGN. In this study, the 100-m Effelsberg and 30-m IRAM telescopes were used to search for molecular absorption in the cm-band for excited OH and in the mm-band for HCN and HCO$^+$.

3.1.2   Source selection and target transitions

We selected radio AGN candidates suitable for molecular absorption line surveys. Basic source selection criteria are flux limits ($S \geq 150\,\mathrm{mJy}$ at $6\,\mathrm{GHz}$) or ($S \geq 200\,\mathrm{mJy}$ at $13\,\mathrm{GHz}$), observable sky frequencies for the target transitions, previous detection of H I absorption, and compact ($\sim100\,\mathrm{pc}$) jet structure in VLBI images. With these selection criteria, we extensively searched the literature and relevant data bases. In particular, compact symmetric objects (CSO) and Gigahertz Peak Spectrum (GPS) sources were favored in source selection due to their adequate physical conditions for absorption line detection (O'Dea 1998; Fanti 2009; Collier et al. 2018). CSO and GPS are characterized by a small size (< 1 kpc), a young radio jet, and a mm-bright continuum. The anti-correlation between the neutral hydrogen column density and the radio source size indicates a higher gas content in compact CSO/GPS sources than in 'normal' FR-type radio galaxies (Pihlström et al. 2003). In statistical studies, CSO and GPS sources show much higher detection rates of H I absorption compared to other radio galaxies (Gupta et al. 2006; Curran et al. 2017). Thus, we preferentially selected CSO and GPS sources. However, we also included normal radio AGN with known H I or molecular absorption lines to constrain more detailed physical properties of the obscuring gas via our absorption study.

As target transitions, we selected rotational lines of HCN and HCO⁺ and hyperfine lines of excited OH. The optical depth of a molecular absorption line is given by:

$$\int \tau d\nu \propto \frac{\mathrm{N_J}}{\mathrm{T_{ex}}}\mu^2, \tag{3.1}$$

where τ is the optical depth, $\mathrm{N_J}$ is the column density of the molecule at energy level J, μ is the dipole moment of the molecule, and $\mathrm{T_{ex}}$ is the excitation temperature. The abundance of HCN is lower than CO ($\mathrm{N_{HCN}}/\mathrm{N_{CO}} = 10^{-2} \sim 10^{-5}$) (Tielens 2010), but its higher dipole moment ($\mu = 2.98$) than CO ($\mu = 0.11$) makes it a suitable tracer for detecting molecular gas in absorption. HCO⁺ ($\mu = 3.80$) also has high dipole moment. Thus, we used the rotational lines of HCN and HCO⁺ as the main tracers for our absorption line surveys. A high excitation temperature in the nuclear region of AGN could lower the optical depth of HCN and HCO⁺ absorption lines. Hence, we also included the rotationally-excited OH transitions at cm wavelengths as the target transitions. The energy levels of rotationally excited-state are about a few hundred Kelvin, which tolerate absorption line detection from a warm and excited molecular gas in the innermost region of radio AGN.

3.2 Absorption line survey using the 100-m Effelsberg telescope

3.2.1 Observations

Effelsberg observations were carried out on 11 Dec. 2018, 13-14 May, and 15-17 Dec. 2019. Target transitions are the excited OH $^2\Pi_{3/2}$, $J = 5/2, J = 7/2$, $J = 9/2$ (6.0307/6.0351 GHz, 13.3436/13.4414 GHz, 23.8176/23.8266 GHz), HCN $J = 1 - 0$ (88.6316 GHz), and HCO$^+$ $J = 1 - 0$ (89.1885 GHz) lines. The S45 and S14 receivers were used to observe the OH, HCN, and HCO$^+$ lines at the frequency range of 4-9 GHz and 18-26 GHz, respectively. The samples and target molecules are listed on Table. 3.1. We used four back-ends at each polarization, which are WFF1/WFF2 (channel width: 38 kHz, bandwidth: 2.5 GHz) and WFF3/WFF4 (channel width: 3 kHz, bandwidth: 0.2 GHz). Pointing was made for each target, and the focus was redetermined every two hours. The spectral line observations were made using the position-switching method. The integration time was 120 s towards the on and the off positions in each scan. The angular separation between the on and off position was 200 arcsec along the azimuthal direction. The observed data consist of 2 min scans on the target source. An integration time per source ranges from 20 to 60 min depending on the continuum flux density of the target source. When the target source shows a spectral line feature, its nearby continuum source was observed to discriminate between real features and artifacts, such as RFI and ghost lines from instruments.

3.2.2 Data reduction

The data reduction was performed with the Continuum and Line Analysis Single-dish Software (CLASS[1]). The corrupted scans were flagged, and the remaining scans were integrated over time and frequency. The Hanning smoothing method, which takes three adjacent channels for smoothing, was applied to improve the signal to noise ratio of the spectra. The velocities in the spectra were calculated, referring to the heliocentric reference frame. Radio Frequency Interference (RFI) and standing waves were severe throughout the spectral window, and they often induced absorption or emission like artifacts. Fig. 3.2 shows the time variable RFI features and standing waves in the spectral window of the S45 receiver. Those suspicious features were discriminated from the real emission or absorption lines by checking the presence of the line in scans at different times and polarization at the same frequency window. When the suspicious feature was not stationary over time or any strong RFI feature was present near the expected line frequency, the line was not considered as a molecular

---

[1]https://www.iram.fr/IRAMFR/GILDAS

line from the target source. If the rms level in a certain spectral range abnormally increased in some scans, those spectral windows were marked as the RFI regions and shaded in the spectra.

TABLE 3.1: Source list of the Effelsberg absorption line survey.

Name	Position (J2000)		Redshift	Target[a]	Note[b]
	RA	Dec	z	Molecule	
NGC 315	00:57:48.80	30:21:08.0	0.0200	OH	HI abs
B0108+388	01:11:37.31	39:06:28.1	0.6690	OH	HI abs
J0203+1134	02:03:46.65	11:34:45.4	3.6100	HCN	-
NGC 1052	02:41:04.79	-08:15:20.7	0.0049	OH	HI abs
B0240-060	02:43:12.46	-05:50:55.3	1.8000	OH	HI abs
3C84	03:19:48.16	41:30:42.1	0.0175	OH	HI abs
J0321+1221	03:21:53.10	12:21:13.9	2.6600	HCN	-
4C76.03	04:10:45.61	76:56:45.3	0.5983	OH	HI abs
3C120	04:33:11.10	05:21:15.6	0.0335	OH	HI abs
J0642+6758	06:42:04.25	67:58:35.6	3.1770	HCN	-
J0646+4451	06:46:32.02	44:51:16.5	3.4080	HCN	-
B0651+410	06:55:10.02	41:00:10.1	0.0200	OH	HI abs
J0836-2016	08:36:39.21	-20:16:59.5	2.7500	HCN	HI abs
J0905+4850	09:05:27.46	48:50:49.9	2.6860	HCN	-
NGC 3079	10:01:57.80	55:40:47.2	0.0038	OH	HI abs
3C236	10:06:01.70	34:54:10.0	0.0994	OH	HI abs
B1015+359	10:18:11.00	35:42:40.0	1.2290	OH	-
NGC 3894	11:48:50.35	59:24:56.3	0.0108	OH	HI abs
B1215+303	12:17:52.08	30:07:00.0	0.1300	OH	-
NGC 4261	12:19:23.20	05:49:31.0	0.0073	OH	HI abs
3C273	12:29:06.70	02:03:08.6	0.1583	OH	-
MRK 231	12:56:14.20	56:52:25.0	0.0415	OH	HI abs
4C12.50	13:47:33.35	12:17:24.2	0.1212	OH	HI abs
3C293	13:52:17.80	31:26:46.0	0.0452	OH	HI abs
B1355+441	13:57:40.60	43:53:59.0	0.6460	OH	-
B1404+286	14:07:00.40	28:27:15.0	0.0770	OH	-
B1504+374	15:06:09.50	37:30:51.0	0.6734	OH	HI abs
4C33.38	16:02:07.20	33:26:53.0	1.1000	OH	HI abs
J1625+4134	16:25:57.67	41:34:40.6	2.5500	HCN	-
NGC 6251	16:32:32.00	82:32:16.0	0.0200	OH	HI abs
4C39.49	16:53:52.20	39:45:36.6	0.0330	OH	-
UGC11035	17:54:29.41	32:53:14.2	0.0254	OH	-
J1850+2825	18:50:27.59	28:25:13.1	2.5600	HCN	-
J2050+3127	20:50:51.13	31:27:27.3	3.1800	HCN	-
J2139+1423	21:39:01.30	14:23:35.9	2.4300	HCN	-
3C452	22:45:48.77	39:41:15.9	0.0811	OH	HI abs
J2355+4950	23:55:09.40	49:50:08.0	0.2400	OH	HI abs

Notes.: [a]Target molecule. [b]Previous detection of 21 cm HI absorption line in the literature.
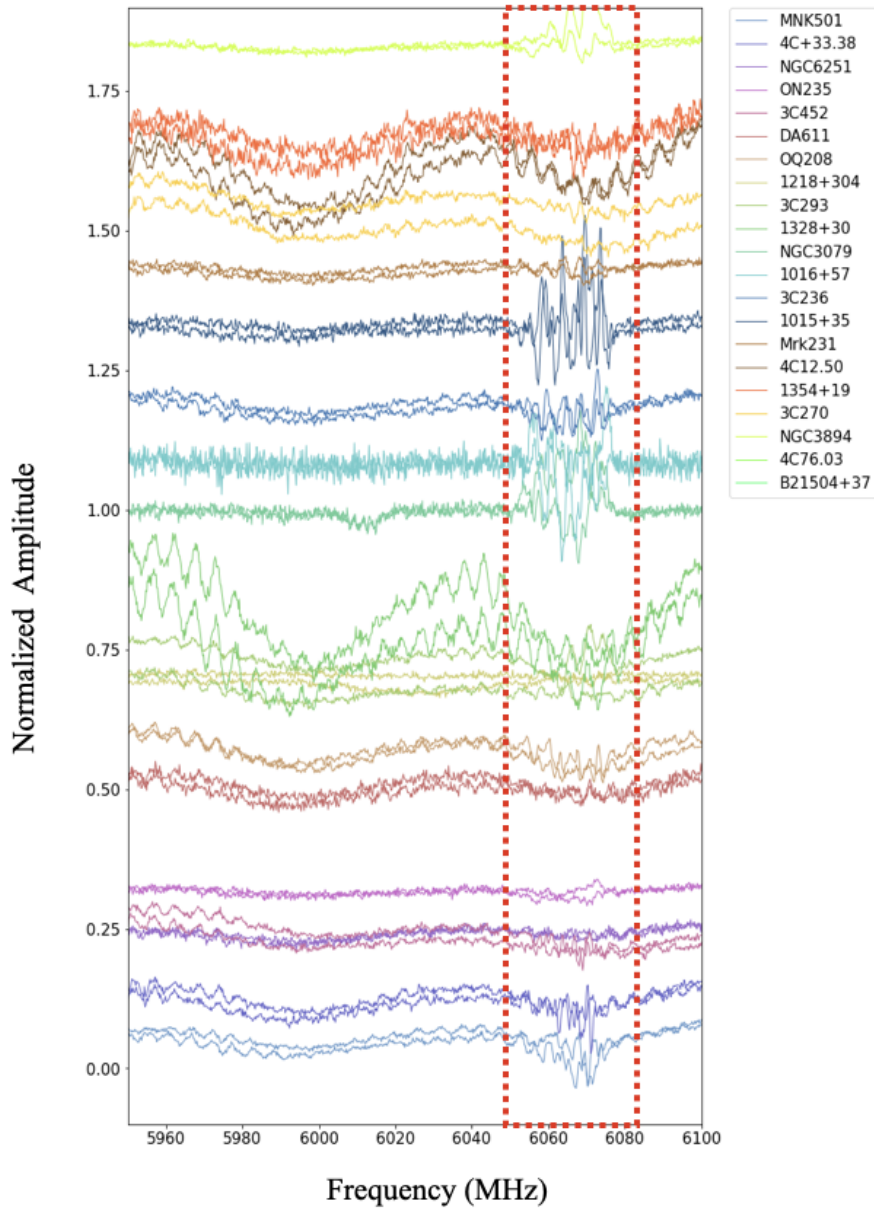
FIGURE 3.2: RFI and standing waves in the spectral window of the S45 receiver. Amplitudes of the spectra are normalized and shifted for a better visual inspection. The amplitude of standing waves is proportional to the continuum flux density. Red dotted square marks the time variable RFI features seen for many sources at a certain spectral window.

Despite elaborate baseline fittings, a wobbling baseline was the critical issue in identifying molecular absorption features in the spectra. Fig. 3.3 shows the exemplary cases of the baseline fittings for the spectra of NGC 1052 and NGC 3079. The baseline of the spectra was flattened via polynomial fitting. For the spectra with regular sinusoidal waves, the baseline ripples were removed by sinusoidal baseline fittings. Such ripples are thought to be induced by standing waves or imperfect gain and system temperature calibrations. The reflection between the secondary reflector and feeds cause the standing waves (Popping & Braun 2008).
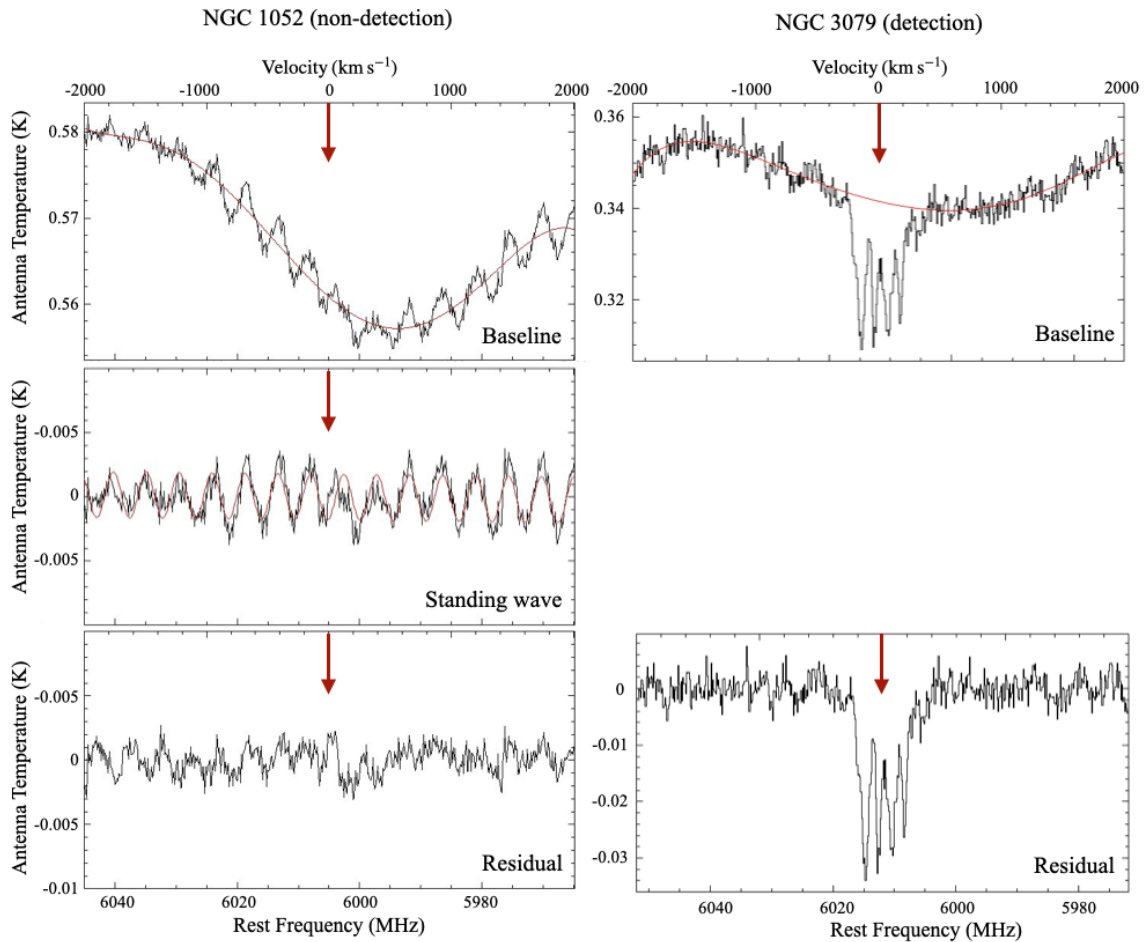
FIGURE 3.3: **Left**: Polynomial and sinusoidal baseline fittings and the residual spectra of NGC 1052. **Right**: Polynomial baseline fitting for NGC 3079. The expected location of OH transitions are marked with the red arrow.

The wavelength of a standing wave is described by c/2D, where c is the speed of light, and D is the distance between the feed and the secondary reflector (i.e., focal length). The focal length of the 100-m Effelsberg telescope is about ~30 m, (Holst et al. 2012), which is supposed to result in a standing wave wavelength of 5 MHz. This value is consistent with the wavelength of the standing wave (5.23 MHz) measured in the 6 GHz spectrum of NGC 1052. (see left middle panel in Fig. 3.3). Internal reflections on other structural elements of the dish (secondary focus housing, transition between inner and outer mesh, support legs, etc.) most likely are responsible for the broader baseline ripples present in the observed spectra. In most cases, baseline fittings are imperfect and still remain some ripples in the spectra.

3.2.3 Results

Fig. 3.7 and Fig. 3.8 show the spectra of the observed radio AGN, and the results of the absorption line survey are summarized in Table 3.3 and Table 3.4. Velocities of the target transition are given with respect to the systemic velocity of the target source. In our single-dish absorption line survey, we obtained low-detection rates (2/37). Severe RFI and standing waves were the main hindrances in identifying absorption features in the observed spectra. RFI was mitigated at the high frequency observations using the S14 receiver, but the standing waves were still a critical issue. Nevertheless, we detected OH absorption and H_2O maser emission lines in NGC 3079 and NGC 1052.

Fig. 3.4 shows the line profile of the OH absorption and H_2O maser emission in NGC 3079. The composite OH absorption lines in NGC 3079 were separated into four Gaussian components. The fitting results are present in Fig. 3.5, and the fitting parameters are given in Table. 3.2. The rest frequencies of 6 GHz Λ-doubling OH absorption lines are separated about 5 MHz, and it matches well with the frequency separation between the two former Gaussian components and the two latter Gaussian components. Therefore, the composite OH absorption line intrinsically represents two OH transitions and velocity components (hereafter C1 and C2). The C1 and C2 components are blue-shifted about $29 \, \text{km} \, \text{s}^{-1}$ and $130 \, \text{km} \, \text{s}^{-1}$ with respect to the systemic velocity, respectively. The C1 also has a 55 % broader line width (FWHM: $80 \, \text{km} \, \text{s}^{-1}$) than the C1 (FWHM: $45 \, \text{km} \, \text{s}^{-1}$). Such a feature is seen in both 6.035 GHz and 6.030 GHz OH absorption lines. In the comparison of the 6 GHz OH absorption and the 22 GHz H_2O maser emission lines, strong absorption and emission features commonly appear around a blue-shifted velocity of $130 \, \text{km} \, \text{s}^{-1}$, but only OH absorption feature is present near the systemic velocity.

23 GHz Λ-doubling OH absorption lines were detected for the first time in NGC 1052. Fig. 3.6 shows the 23 GHz OH absorption lines. Two 23 GHz OH transitions at 23.8176 GHz and 23.8266 GHz are separated by 9 MHz, but they were not resolved in velocity domain due to a broad line width. The absorption depth is about 2 % of the continuum flux density. The composite line is characterized by a red-shifted line centroid of $230 \, \text{km} \, \text{s}^{-1}$ with a line width of $188 \, \text{km} \, \text{s}^{-1}$. The 23 GHz OH absorption and 22 GHz H_2O maser emission line detected in NGC 1052 shows a very similar line profile with a broad single line. 6 GHz OH absorption lines were also searched towards NGC 1052, but strong continuum emission at 6 GHz corrupted the baseline shape. Fig. 3.3 shows the raw and baseline fitted spectra of NGC 1052 at 6 GHz. The upper limit of the 6 GHz OH absorption is 0.06 % (3σ) of the continuum flux density, which is much lower than the absorption peak of the 23 GHz OH absorption line.
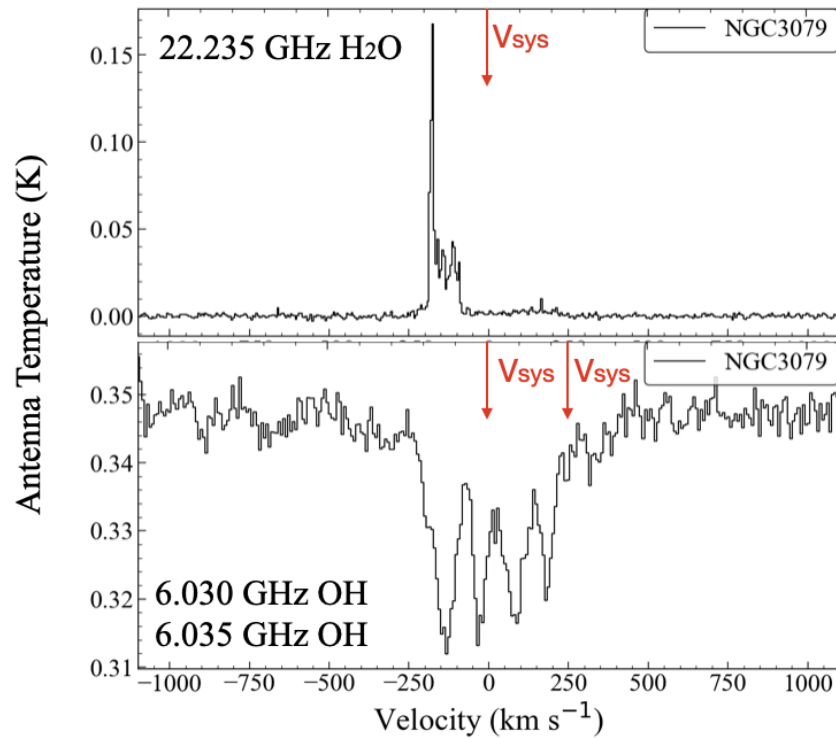
FIGURE 3.4: 22.235 GHz H_2O maser emission and 6.035/6.030 GHz OH absorption lines detected in NGC 3079. The location of spectral lines at the systemic velocity of NGC 3079 is marked with the red arrow.
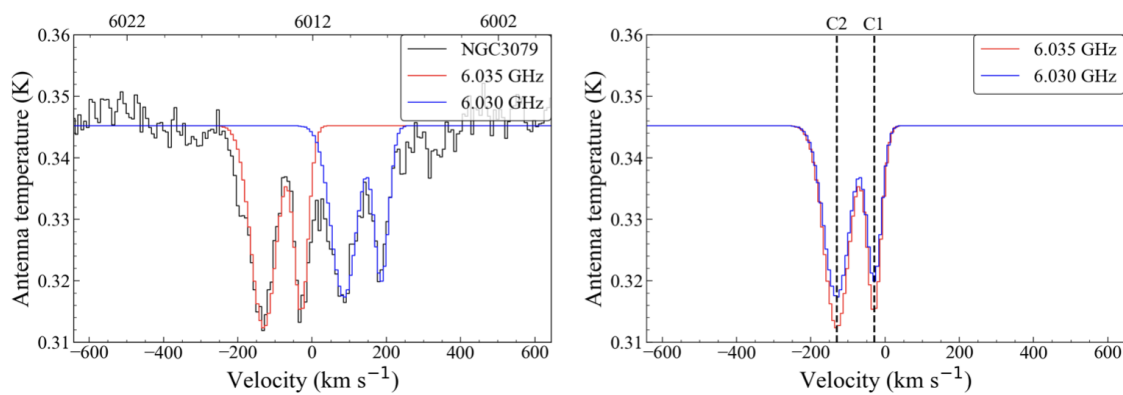
FIGURE 3.5: **Left**: Four Gaussian components overlaid on the 6 GHz OH absorption lines in NGC 3079. Gaussian components of 6.030 GHz and 6.035 GHz OH transitions are marked with blue and red, respectively. **Right**: Superposed Gaussian components of the 6.030 GHz and 6.035 GHz OH absorption lines.
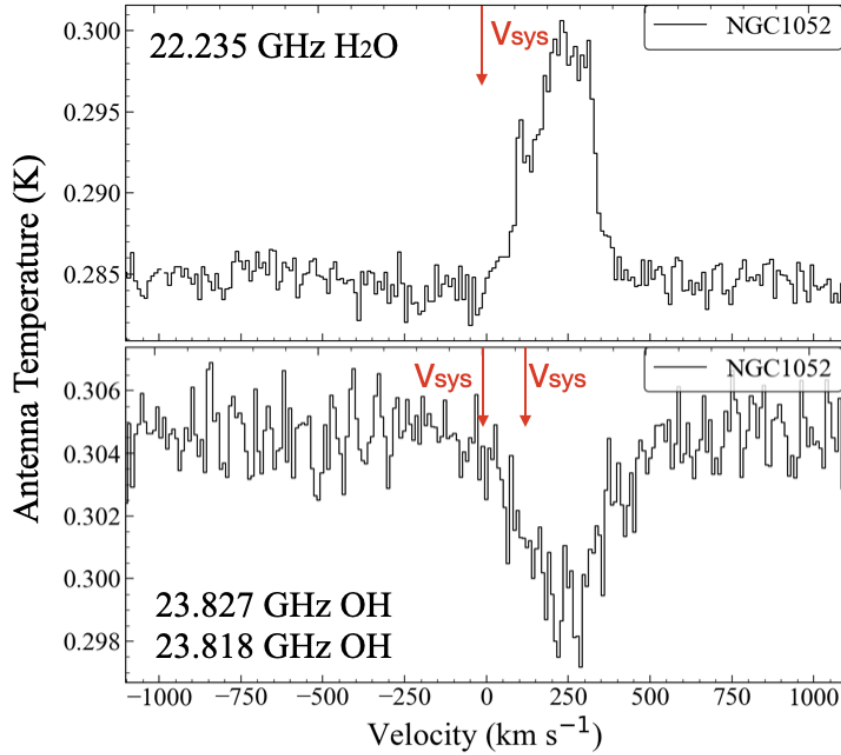
FIGURE 3.6: 22.235 GHz H_2O maser emission and 23.826/23.817 GHz OH absorption lines detected in NGC 1052. Red arrow indicates the systemic velocity of the AGN.

TABLE 3.2: Line parameters of OH absorption in NGC 3079 and NGC 1052.

Target	Comp	OH transition[a]	Freq[b] (MHz)	ΔV^{c} (km s^{-1})	V_0^{d} (km s^{-1})	$\int \tau dv^{e}$ (10^{-2} km s^{-1})
	C1$_{6035}$	$^2\Pi_{3/2}$, $J = 5/2\,F = 2-2$	6012.1	44.7	-29	427.5
NGC 3079	C2$_{6035}$	$^2\Pi_{3/2}$, $J = 5/2\,F = 2-2$	6012.1	80.0	-130	844.1
	C1$_{6030}$	$^2\Pi_{3/2}$, $J = 5/2\,F = 3-3$	6007.8	44.7	-29	354.2
	C2$_{6030}$	$^2\Pi_{3/2}$, $J = 5/2\,F = 3-3$	6007.8	80.0	-130	712.5
NGC 1052		$^2\Pi_{3/2}$, $J = 9/2\,F = 5-5$	23709.7	188	230	620.5
		$^2\Pi_{3/2}$, $J = 9/2\,F = 4-4$	23700.8			

Notes.: [a]Quantum numbers of the transition. [b]Sky frequency of the target transition. [c]Line width (FWHM) . [d] Doppler velocity [e] Integrated optical depth.

TABLE 3.3: Results of the absorption line survey at 4-9 GHz.

Source	OH transition[a]	Freq[b] (MHz)	ΔV[c] (km s^{-1})	Flux[d] (mJy)	rms[e] (mJy)	$\int \tau d\nu$[f] (10^{-2} km s^{-1})	Note[g]
NGC 315	$^2\Pi_{3/2}$, $J = 5/2$	5917	7.7	526	2.9	< 13.0	ripple
B0108+388	$^2\Pi_{3/2}$, $J = 7/2$	8053	5.7	364	8.8	< 42.9	RFI
NGC 1052	$^2\Pi_{3/2}$, $J = 5/2$	6005	7.6	671	1.2	< 4.3	ripple
B0240-060	$^2\Pi_{3/2}$, $J = 7/2$	4800	9.5	133	2.9	< 64.6	RFI
4C76.03	$^2\Pi_{3/2}$, $J = 7/2$	8410	5.4	816	9.3	< 18.9	RFI
NGC 3079	$^2\Pi_{3/2}$, $J = 5/2$	6012	7.6	217	1.3	2338.3	Detection
3C236	$^2\Pi_{3/2}$, $J = 5/2$	5490	8.3	781	4.6	< 14.8	RFI
B1015+359	$^2\Pi_{3/2}$, $J = 7/2$	6030	7.6	425	2.6	< 14.1	
NGC 3894	$^2\Pi_{3/2}$, $J = 5/2$	5971	7.7	297	1.3	< 9.9	ripple
B1215+303	$^2\Pi_{3/2}$, $J = 5/2$	5341	8.6	285	1.1	< 10.2	
NGC 4261	$^2\Pi_{3/2}$, $J = 5/2$	5991	7.6	651	2.6	< 9.0	ripple
MRK 231	$^2\Pi_{3/2}$, $J = 5/2$	5795	7.9	350	2.3	< 15.8	
4C12.50	$^2\Pi_{3/2}$, $J = 5/2$	5383	8.5	1647	7.3	< 11.4	ripple
3C293	$^2\Pi_{3/2}$, $J = 5/2$	5774	7.9	919	2.8	< 7.3	ripple
B1355+441	$^2\Pi_{3/2}$, $J = 7/2$	8166	5.6	156	1.3	< 14.6	RFI
B1404+286	$^2\Pi_{3/2}$, $J = 5/2$	5603	8.2	1012	5.6	< 13.7	ripple
B1504+374	$^2\Pi_{3/2}$, $J = 7/2$	8049	5.7	320	1.2	< 6.2	ripple
4C33.38	$^2\Pi_{3/2}$, $J = 7/2$	6400	7.1	883	5.8	< 14.2	RFI
NGC6251	$^2\Pi_{3/2}$, $J = 5/2$	5917	7.7	455	1.9	< 9.5	
4C39.49	$^2\Pi_{3/2}$, $J = 5/2$	5842	7.8	768	3.0	< 9.1	ripple
3C452	$^2\Pi_{3/2}$, $J = 5/2$	5582	8.2	516	1.5	< 7.2	ripple
J2355+4950	$^2\Pi_{3/2}$, $J = 5/2$	4867	9.4	663	2.5	< 10.7	

Notes.: [a] Quantum numbers of the transition. [b] Sky frequency of the target transition. [c] Velocity resolution. [d] Continuum flux. [e] Noise level. [f] constrained optical depths for the target transition. [g] Constrained integrated optical depths.

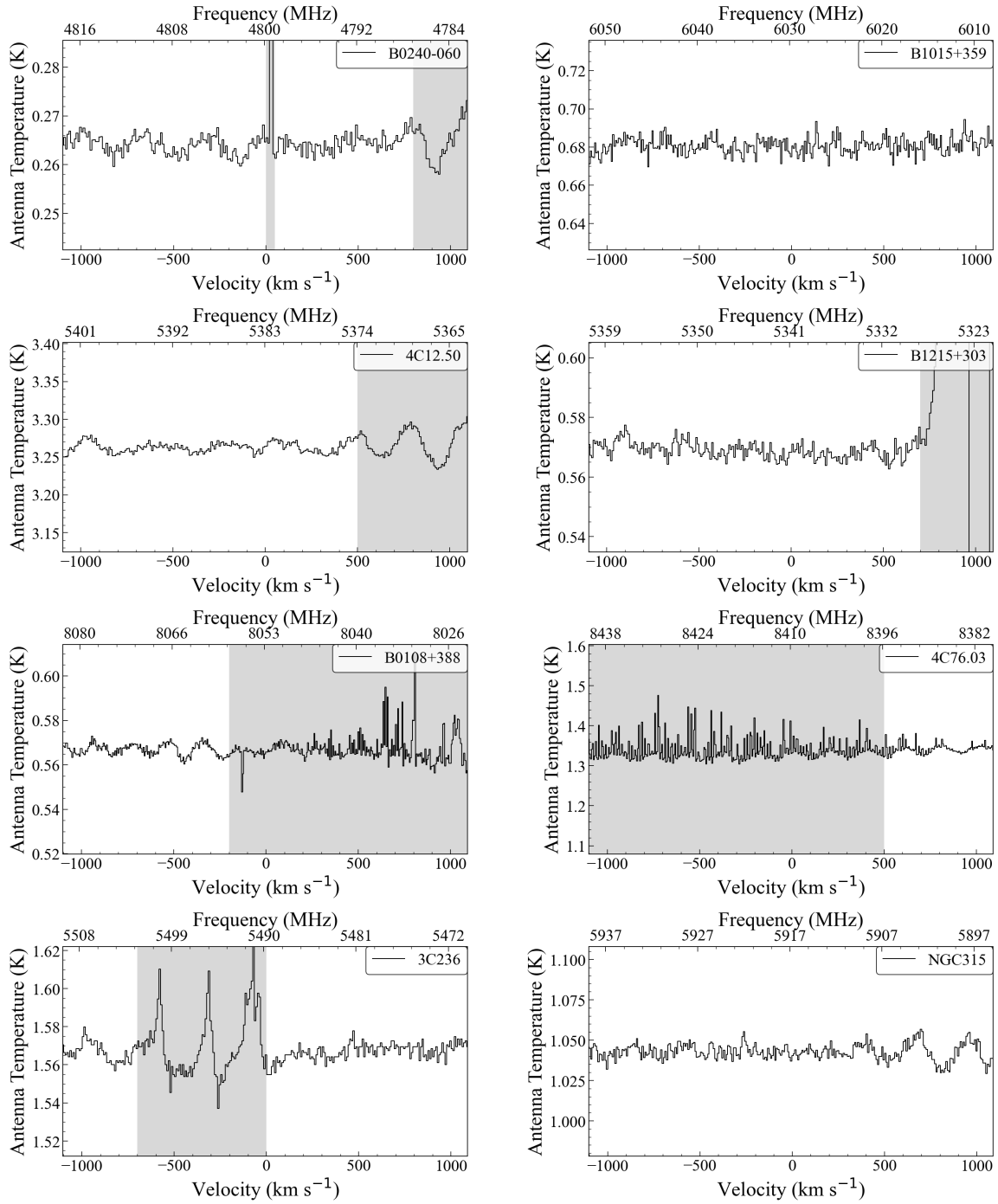FIGURE 3.7: Spectra of the radio AGN observed with the S45 receiver of the Effelsberg telescope at 6 cm. The amplitude is the antenna temperature. Horizontal axis indicates Doppler velocity of the expected absorption line with respect to the heliocentric velocity of the target source. Shaded regions indicate spectral channels, where RFI features appear.

FIGURE 3.7: continued.

FIGURE 3.7: continued.

TABLE 3.4: Results of the absorption line survey at 18-26 GHz.

Source	Transition[a]	Freq[b] (MHz)	ΔV[c] (km s^{-1})	Flux [d] (mJy)	rms [e] (mJy)	$\int \tau dv$ [f] (10^{-2} km s^{-1})
NGC 315	OH $^2\Pi_{3/2}$, $J = 9/2$	23359	9.8	298	6.7	< 68.6
NGC 1052	OH $^2\Pi_{3/2}$, $J = 9/2$	23710	9.6	1726	3.3	617.3
3C84	OH $^2\Pi_{3/2}$, $J = 9/2$	23417	9.8	22908	17.6	< 2.3
3C120	OH $^2\Pi_{3/2}$, $J = 9/2$	23054	9.9	4950	17.1	< 10.3
B0651+410	OH $^2\Pi_{3/2}$, $J = 9/2$	23359	9.8	1177	10.1	< 25.7
NGC 3079	OH $^2\Pi_{3/2}$, $J = 9/2$	23737	9.6	-	6.0	-
3C273	OH $^2\Pi_{3/2}$, $J = 9/2$	20570	11.1	6248	29.0	< 15.6
3C293	OH $^2\Pi_{3/2}$, $J = 9/2$	22796	10.0	149	7.7	< 170.1
UGC11035	OH $^2\Pi_{3/2}$, $J = 9/2$	23236	9.8	475	10.9	< 70.1
3C452	OH $^2\Pi_{3/2}$, $J = 9/2$	22041	10.4	567	3.0	< 16.8
J0203+1134	HCN $J = 1 - 0$	19226	11.9	106	2.7	< 92.9
	HCO$^+$ $J = 1 - 0$	19347				
J0321+1221	HCN $J = 1 - 0$	24216	9.4	376	3.8	< 28.9
	HCO$^+$ $J = 1 - 0$	24368				
J0642+6758	HCN $J = 1 - 0$	21219	10.8	85	2.6	< 103.1
	HCO$^+$ $J = 1 - 0$	21352				
J0646+4451	HCN $J = 1 - 0$	20107	11.4	589	4.4	< 26.0
	HCO$^+$ $J = 1 - 0$	20233				
J0836-2016	HCN $J = 1 - 0$	23635	9.7	185	5.2	< 85.0
	HCO$^+$ $J = 1 - 0$	23784				
J0905+4850	HCN $J = 1 - 0$	24046	9.5	522	10.2	< 57.7
	HCO$^+$ $J = 1 - 0$	24197				
J1625+4134	HCN $J = 1 - 0$	24967	9.2	726	4.4	< 16.8
	HCO$^+$ $J = 1 - 0$	25124				
J1850+2825	HCN $J = 1 - 0$	24897	9.2	567	7.0	< 34.7
	HCO$^+$ $J = 1 - 0$	25053				
J2050+3127	HCN $J = 1 - 0$	21204	10.8	199	2.2	< 36.9
	HCO$^+$ $J = 1 - 0$	21337				
J2139+1423	HCN $J = 1 - 0$	25840	8.9	1038	5.4	< 14.0
	HCO$^+$ $J = 1 - 0$	26002				

Notes.: [a]Quantum numbers of the transition. [b]Sky frequency of the target transition. [c]Velocity resolution of the spectral channel. [d] Continuum flux of the source. [e] Noise level of the channel. [f] Constrained optical depths for the target transition.

FIGURE 3.8: The spectra of the radio AGN observed with the S14 receiver at 1.3 cm of the Effelsberg telescope. The amplitude is the antenna temperature. Horizontal axis indicates Doppler velocity of the expected absorption line with respect to the heliocentric velocity of the target source. Shaded regions indicate spectral channels, where RFI features appear.
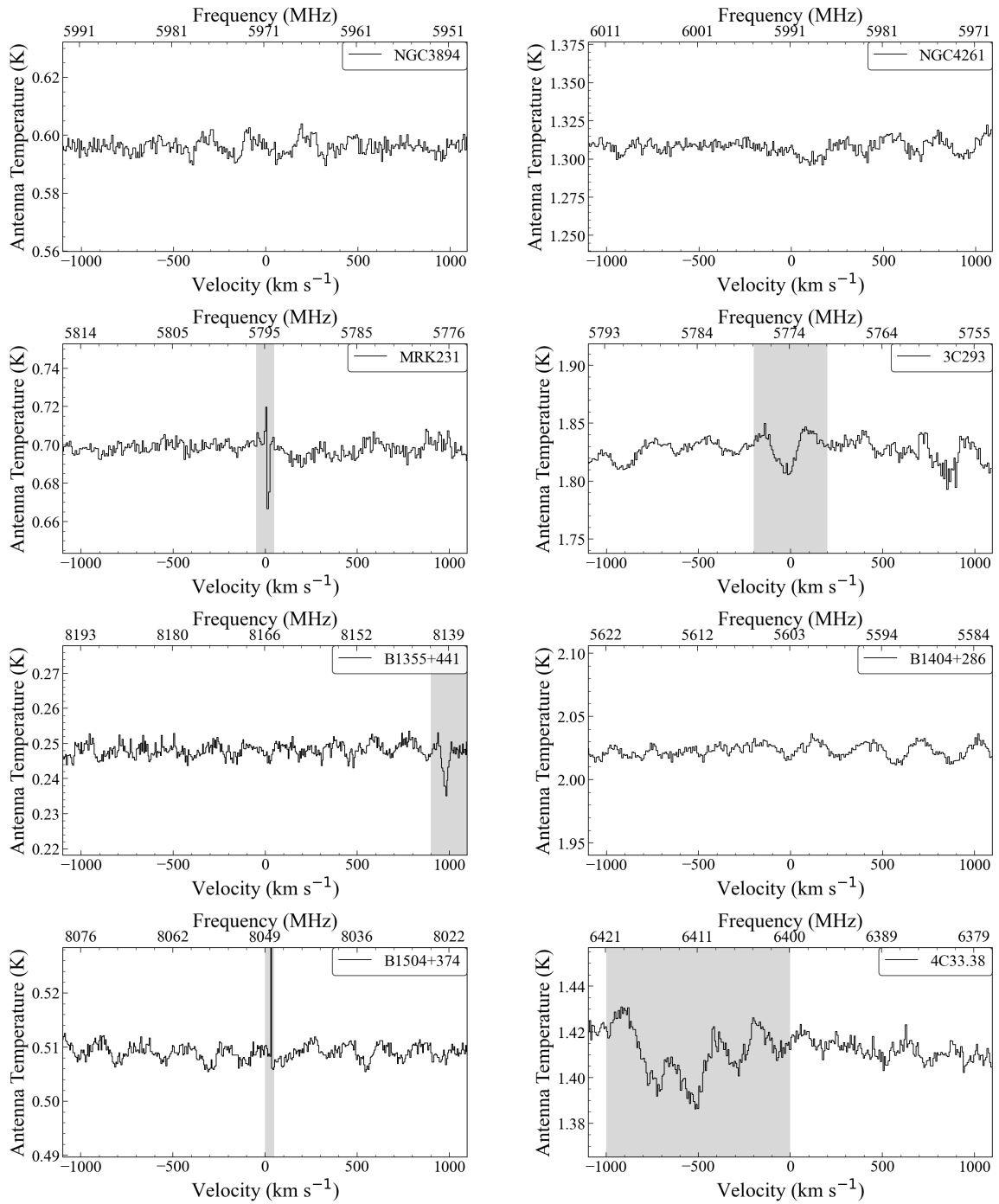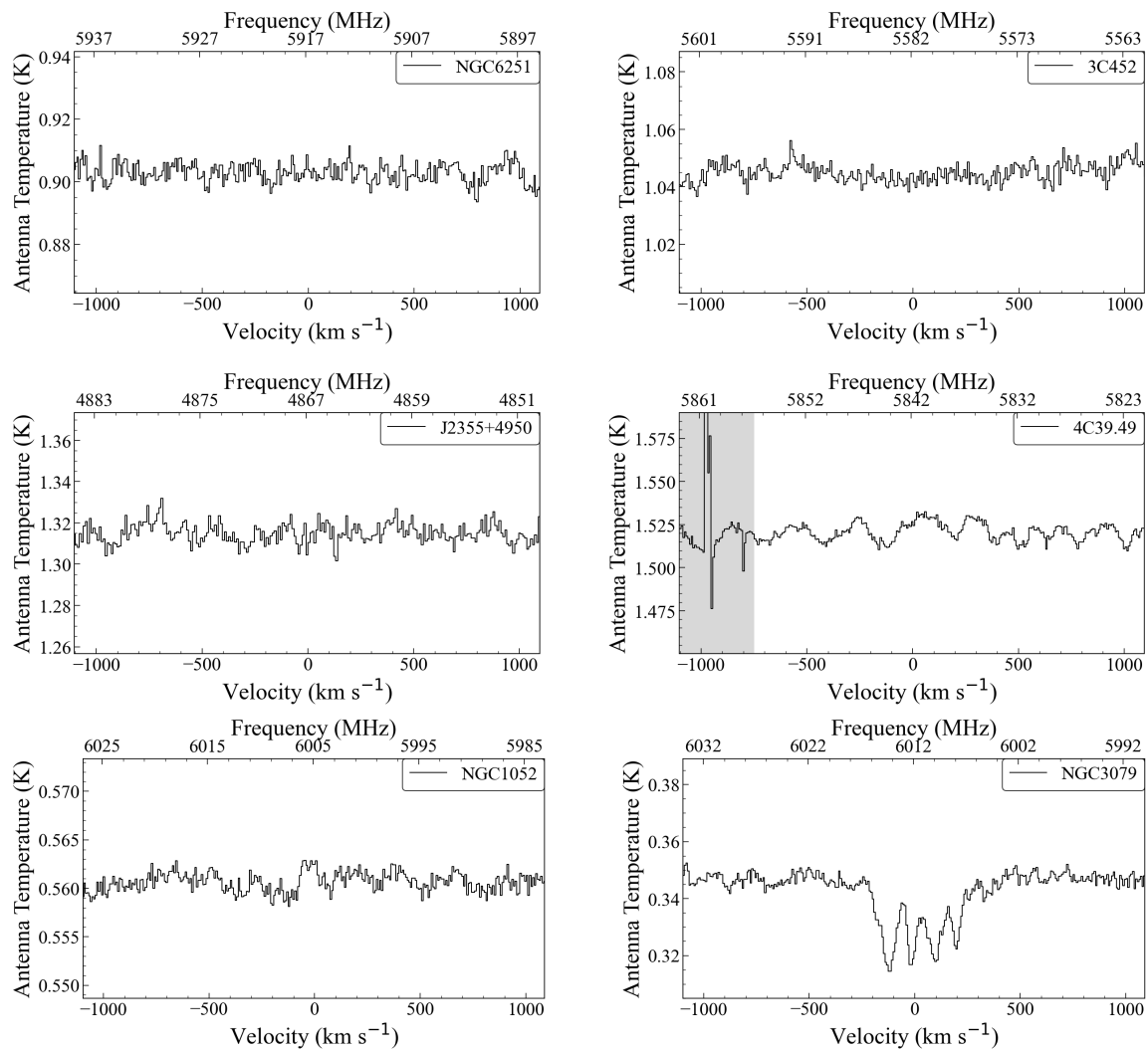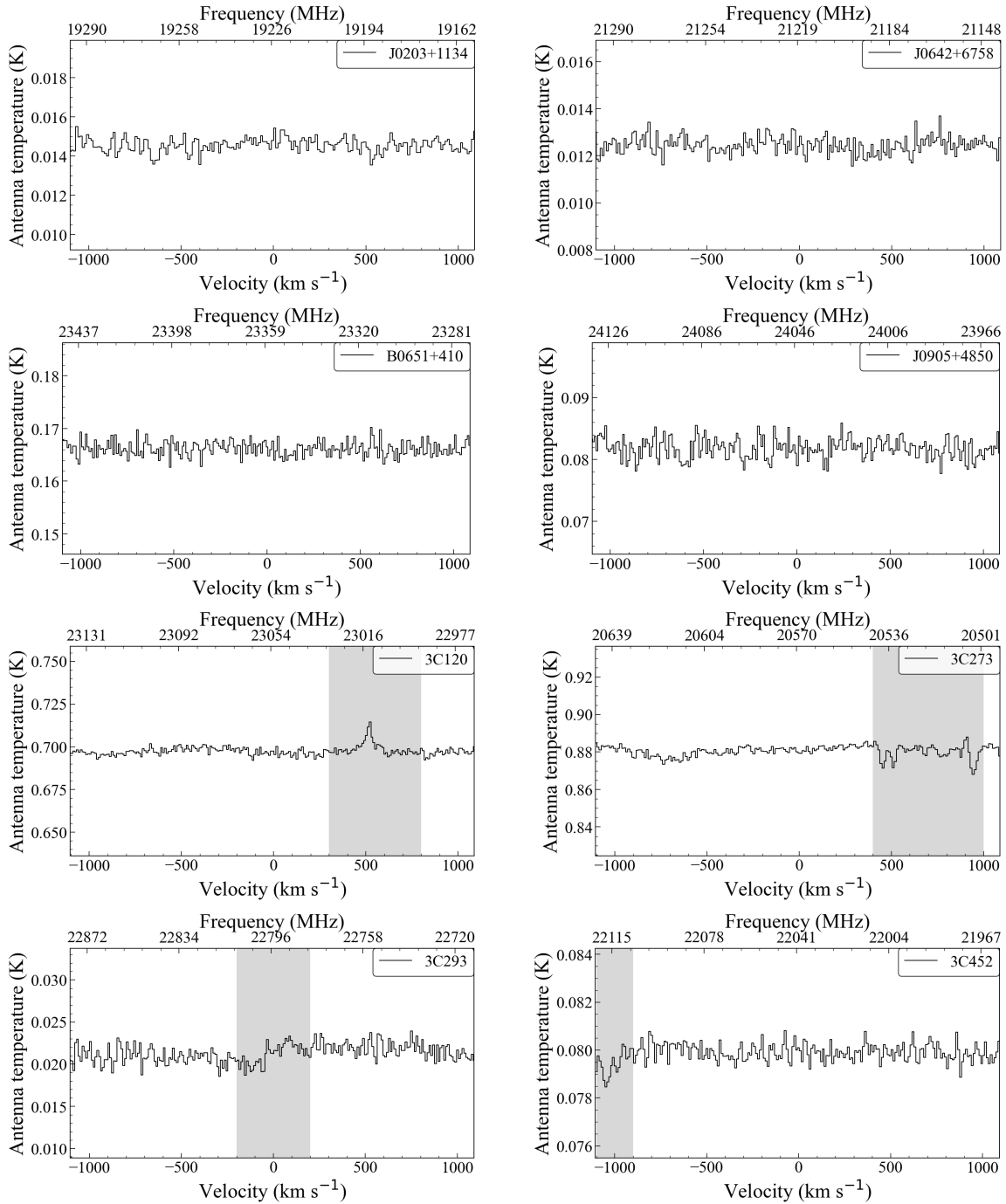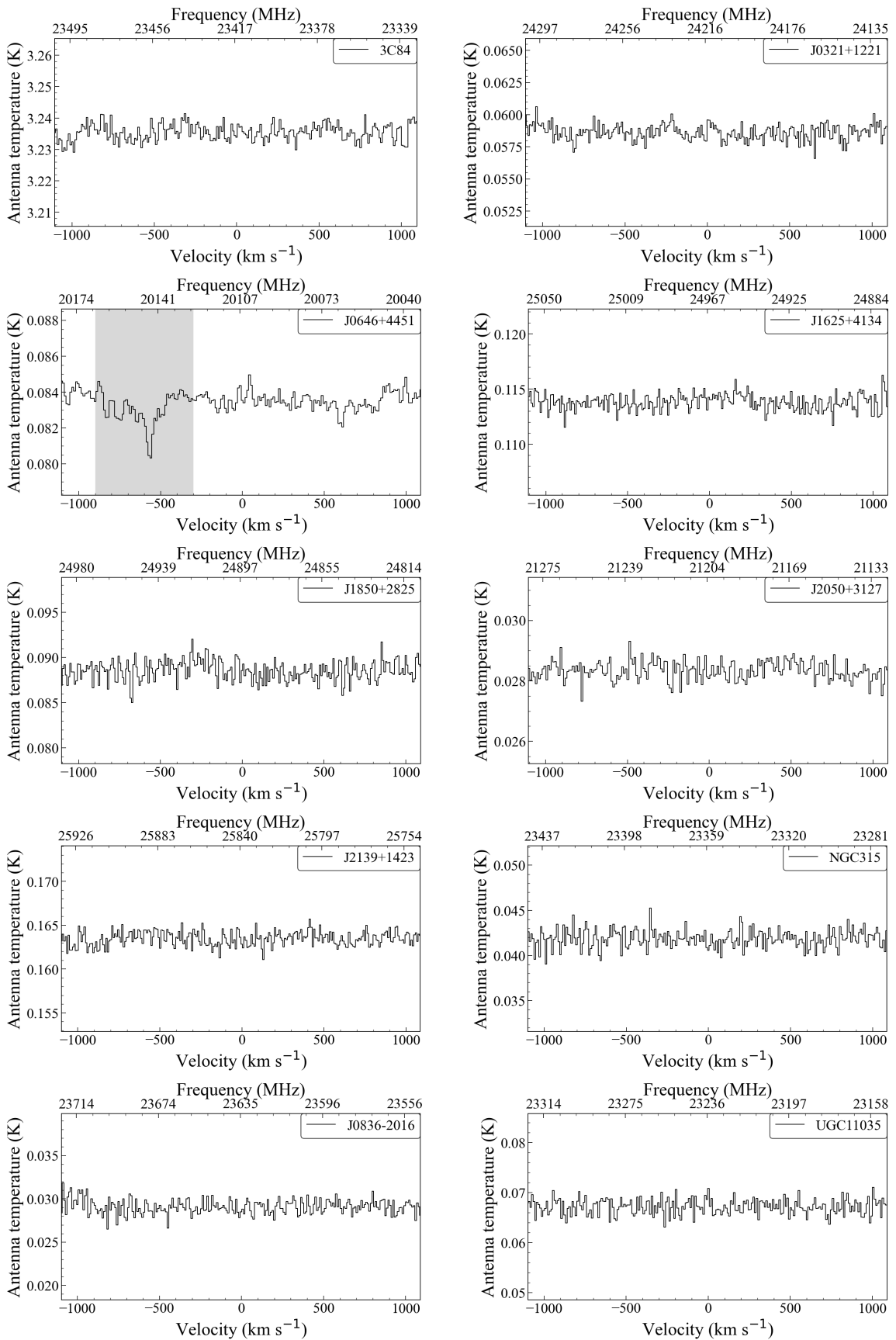
FIGURE 3.8: continued.

3.2.4 Discussion

NGC 3079 and NGC 1052 have distinct radio jet properties and environments. A low power radio jet resides in the nuclear region of the Seyfert galaxy NGC 3079. VLBI observations show an inclined radio jet with respect to the circumnuclear disk (Middelberg et al. 2007). 1.6 GHz OH absorption lines have been detected in NGC 3079, but its kinematics and physical origin is not yet clear (Hagiwara et al. 2004). Excited 6 GHz OH absorption lines were separated into two Gaussian components C1 and C2. Interestingly, the C2 component has a deeper absorption depth with broader line width than the C1 component. A shock induced by the Jet-ISM interaction compresses the ambient medium, and it can increase the local density and velocity dispersion of the interacting medium. If the C2 component would originate from ISM interacting with the propagating jet, the observed broad line profile of the C2 component could be interpreted as the result of Jet-ISM interaction. To test this scenario, it is crucial to spatially resolve the C1 and C2 components via high-resolution VLBI observations. A follow-up VLBI study towards the C1 and C2 components will be presented in Chap. 5.

NGC 1052 is an FR type I radio AGN hosted by a massive elliptical galaxy. A substantial amount of circumnuclear gas has been detected in NGC 1052 (Kameno et al. 2020). VLBI observations of the radio jet and 22 GHz H_2O maser show an aligned spatial distribution of the H_2O clouds with the radio jet, but it is not yet clear whether the H_2O maser clouds are directly interacting with the radio jet or just surrounding the jet (Sawada-Satoh et al. 2008). The 23 GHz OH absorption and 22 GHz H_2O maser emission lines detected with the 100-m Effelsberg show similarities in line profile and Doppler velocity, which implies the same physical origin of the OH and H_2O clouds. To clarify the physical connection between the 22 GHz H_2O maser and 23 GHz OH absorption, it is important to constrain the physical properties of the obscuring gas via further absorption line observations. The 13 GHz OH absorption lines were also detected in NGC 1052 in previous VLBI observations (Impellizzeri 2008), but the 6 GHz OH absorption line was not detected. The strong standing waves induced by the bright radio jet at 6 GHz are likely burying the relatively weak 6 GHz OH absorption feature in the spectra. Alternatively, a high excitation temperature of the OH clouds could result in a lower optical depth of the 6 GHz OH lines than the 23 GHz OH lines. The red-shifted peak velocity ($\sim230\,\mathrm{km\,s^{-1}}$) indicates a fueling flow towards the central engine. A further measurement of the opacity distribution and the velocity gradients along the radio jet would help to discern the origin of the OH absorption line in NGC 1052.

3.3 Absorption line survey using the 30-m IRAM telescope

3.3.1 Observations and data reduction

The molecular absorption line survey was made with the IRAM 30-m telescope from Jun. 2019 to Jul. 2019. In total 9 compact AGN were observed to search for HCN J=1-0, 2-1, 3-2 and HCO$^+$ J=1-0, 2-1, 3-2 transitions at rest frequencies 88.6318, 177.2611, 265.8861 GHz, 89.188, 178.3750, and 267.5576 GHz, respectively. The observing time was about 3-4 hr per source, including on and off positions in position switching mode. In total 40 hr was spent for the absorption line survey. The Eight MIxer Receiver (EMIR) receiver was used at four frequency bands (E0: 73-117 GHz, E1: 125-184 GHz, E2: 202-274 GHz, and E3: 277-350 GHz). The Fourier Transform Spectrometer (FTS) back-end recorded the spectral line data, providing a frequency resolution of 2 MHz with up to 7.7 GHz bandwidth per IF. The 30-m IRAM telescope offers dual-band observation mode, which can observe two frequency bands simultaneously among the four available frequency bands (e.g., E0+E1, E0+E2, or E1+E3). By taking advantage of the dual-band mode, we searched for multiple HCN and HCO$^+$ transitions at two frequency bands, simultaneously. The configuration of the dual-band mode was made, considering the sky frequencies of the target transitions. Spectral line data were obtained from the two perpendicular linear polarized feeds. Position-switching observations were made using the wobbler switching mode. A short switching time ($\sim$1 s) of the wobbler switching mode minimizes the variations in gain and bandpass shape during the position switching process. Wobbler sub-scans were integrated for 30 s, and the sub-scans were recorded every 5 min. The source sample and receiver configuration of the IRAM observations are listed in Table 3.5.

For the source selection, bright continuum sources at mm wavelengths were selected with a flux limit ($S \geq 150$ mJy at 86 GHz) in addition to the source selection criteria of the Effelsberg absorption line survey (see §3.1.2). Bandpass and gain calibrations over the spectral channels were performed in the beginning of each observation session. The chopper wheel method was used for the gain and system temperature measurements. Pointing and focus calibrations were made using a nearby planet or bright continuum source. The data reduction was performed using the CLASS[2] package. First, bad scans were flagged. Then sub-scans at different times, and polarization were integrated to increase sensitivity. A velocity resolution of $\sim$10 km s^{-1} was obtained using the Hanning smoothing method. RFI was not a serious issue at mm wavelengths, but ghost emission or absorption like features were found in the

---

[2]https://www.iram.fr/IRAMFR/GILDAS

TABLE 3.5: Source list and target transitions of the IRAM absorption survey.

Source	Obs date	Position (J2000)		Redshift	Rest frequency[a]	Receiver[b]
		R.A.	Dec.	(z)	HCN/HCO$^+$ (GHz)	(Band-mm)
NGC 1052	15-June-2019	02:41:04.79	-08:15:20.7	0.005	88.631/89.188	E0-3mm
					265.886/267.557	E2-2mm
4C 76.03	06-June-2019	04:10:45.61	76:56:45.3	0.559	177.261/178.375	E0-3mm
					265.886/267.557	E1-2mm
3C 216	14-July-2019	09:09:33.49	42:53:46.5	0.669	177.261/178.375	E0-3mm
					265.886/267.557	E1-2mm
3C 236	10-June-2019	10:06:01.70	34:54:10.0	0.101	88.631/89.188	E0-3mm
3C 270	10-June-2019	12:19:23.20	05:49:31.0	0.007	88.631/89.188	E0-3mm
					265.886/267.557	E2-1mm
3C 293	14-July-2019	13:52:17.80	31:26:46.0	0.045	88.631/89.188	E0-3mm
OQ 208	17-June-2019	14:07:00.39	28:27:14.7	0.077	88.631/89.188	E0-3mm
					177.261/178.375	E1-2mm
Cygnus A	22-July-2019	19:59:28.35	40:44:02.0	0.056	88.631/89.188	E0-3mm
					265.886/267.557	E2-1mm
PKS 2127+04	21-July-2019	21:30:32.87	05:02:17.5	0.990	177.261/178.375	E0-3mm
					265.886/267.557	E1-2mm

Notes.: [a]Rest frequencies of the target transitions. [b]Frequency band of the Emir receiver (E0: 73-117 GHz, E1: 125-184 GHz, E2: 202-274 GHz, and E3: 277-350 GHz).

spectra. These artifacts caused by the instrument were excluded by comparing the spectral line features in different polarizations or sub-scans at different times. Standing waves in the spectrum of strong continuum sources were removed by using either the sinusoidal baseline fitting or the wavelet fitting method (Shao & Griffiths 2007) in CLASS. Calibrated data were saved with a local format, and the data was exported to the Flexible Image Transport System (FITS) format for further data analysis. The continuum flux densities and noise levels were measured after the baseline fitting.

3.3.2 Results

Fig. 3.9 shows the spectra of 9 radio AGN observed with the 30-m IRAM telescope. The observational results are summarized in Table 3.6. Among 9 sources, 8 sources were detected in continuum, except OQ 208. The achieved mean noise levels (1σ) are 0.16 K, 0.21 K, and 0.23 K at 3 mm, 2 mm, and 1 mm, which correspond 3 %, 10 %, and 8 % of the continuum flux densities. At all frequency ranges, RFI signals were barely seen in the spectra, but standing waves were present in bright continuum sources, such as NGC 1052, 3C 216, and Cygnus A. Fig. 3.10 shows the 3 mm spectrum of NGC 1052 as an example. Wobbling baselines degraded the spectral line sensitivity. Molecular absorption lines were only detected in 3C 293, and no clear absorption line was confirmed in the spectra of 7 sources.

TABLE 3.6: Results of the absorption line survey at 80-260 GHz.

Source	Transition[a]	Freq[b] (GHz)	ΔV[c] (km s^{-1})	T_{ant}[d] (10^{-2} K)	rms[e] (10^{-2} K)	T_{rms}/T_{ant} [f] %	$\int \tau dv$[g] (10^{-2} km s^{-1})
NGC 1052	HCN $J = 1 - 0$	88.199	10.6	18.92	0.20	1.1	< 34
	HCO$^+$ $J = 1 - 0$	88.753					
	HCN $J = 3 - 2$	264.590	9.9	3.08	0.21	6.8	< 227
	HCO$^+$ $J = 3 - 2$	266.253					
4C 76.03	HCN $J = 2 - 1$	113.702	9.7	5.42	0.22	4.1	< 126
	HCO$^+$ $J = 2 - 1$	114.416					
	HCN $J = 3 - 2$	170.549	9.9	2.24	0.24	10.7	< 384
	HCO$^+$ $J = 3 - 2$	171.622					
3C 216	HCN $J = 2 - 1$	106.208	9.9	8.39	0.16	1.9	< 58
	HCO$^+$ $J = 2 - 1$	106.875					
	HCN $J = 3 - 2$	159.309	9.9	5.14	0.21	4.1	< 129
	HCO$^+$ $J = 3 - 2$	160.310					
3C 236	HCN $J = 1 - 0$	80.500	10.1	3.92	0.09	2.3	< 72
	HCO$^+$ $J = 1 - 0$	81.006					
3C 270	HCN $J = 1 - 0$	88.015	9.9	4.87	0.16	3.3	< 103
	HCO$^+$ $J = 1 - 0$	88.568					
	HCN $J = 3 - 2$	264.038	9.9	3.60	0.22	6.1	< 200
	HCO$^+$ $J = 3 - 2$	265.698					
3C 293	HCN $J = 1 - 0$	84.814	10.3	3.67	0.15	4.1	3936
	HCO$^+$ $J = 1 - 0$	85.347					6195
	HNC $J = 1 - 0$	86.762					1493
OQ 208	HCN $J = 1 - 0$	82.294	9.9	< 0.41	0.17		-
	HCO$^+$ $J = 1 - 0$	82.812					
	HCN $J = 2 - 1$	164.588	9.9	< 0.75	0.25		-
	HCO$^+$ $J = 2 - 0$	165.622					
CYGNUS A	HCN $J = 1 - 0$	83.931	9.9	16.65	0.14	0.8	< 25
	HCO$^+$ $J = 1 - 0$	84.458					
	HCN $J = 3 - 2$	251.786	9.9	2.57	0.25	9.7	< 342
	HCO$^+$ $J = 3 - 2$	253.369					
PKS 2127+04	HCN $J = 2 - 1$	89.076	9.8	1.78	0.12	6.7	< 221
	HCO$^+$ $J = 2 - 1$	89.636					
	HCN $J = 3 - 2$	133.611	10.0	0.91	0.15	16.5	< 682
	HCO$^+$ $J = 3 - 2$	134.451					

Notes.: [a]Quantum numbers of the transition. [b]Sky frequency of the target transition. [c]Velocity resolution of the spectral channel. [d] Antenna temperature. [e] Noise level (1σ) of the channel. [f] Ratios between the continuum and noise. [g] Constrained optical depths for the target transition.
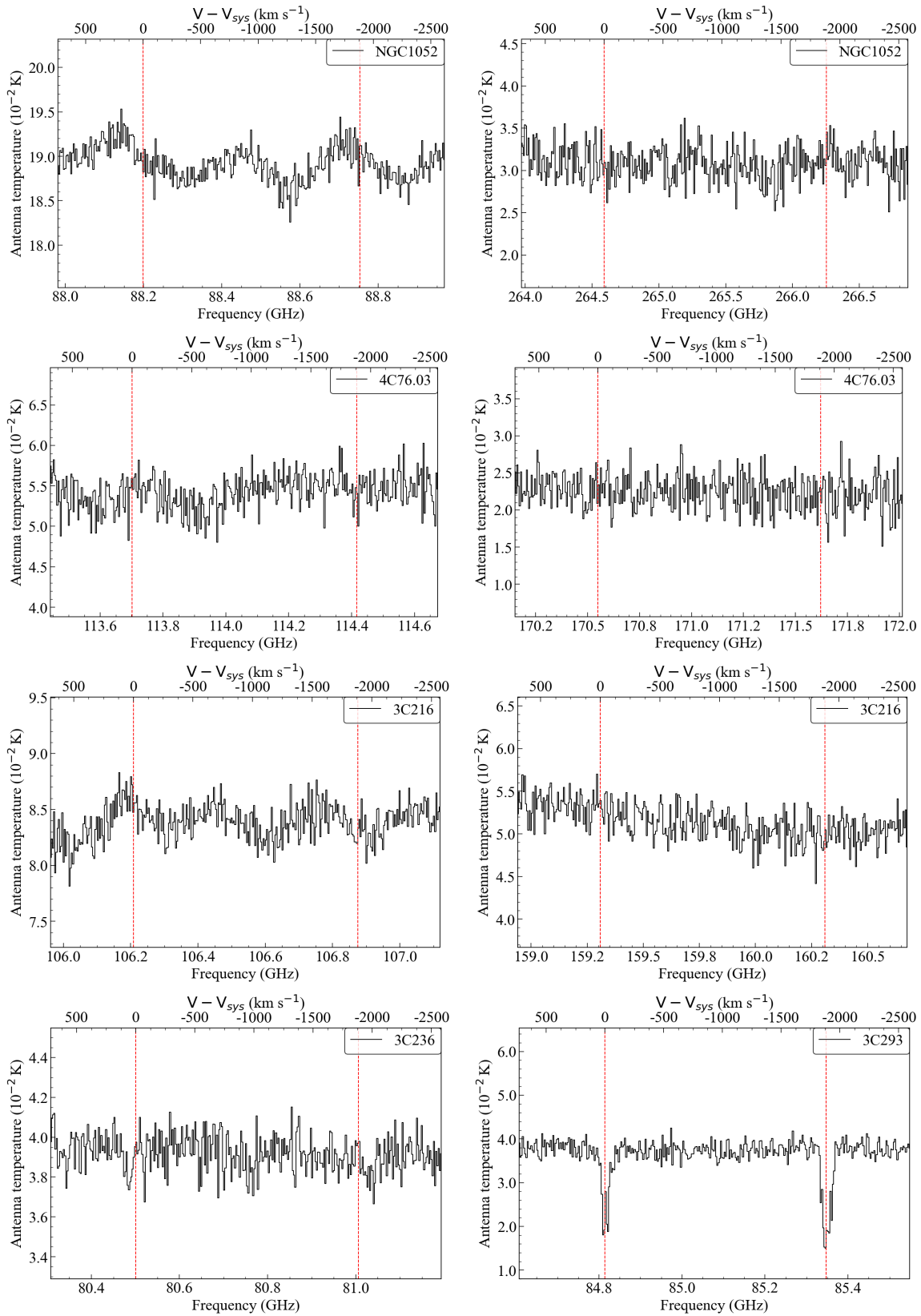
FIGURE 3.9: Spectra of the sources observed with the 30-m IRAM radio telescope. The sky frequencies of the target HCN and HCO$^+$ transitions are marked by the red dotted lines. The velocity axis is presented for the HCN transition at the systemic velocity of the target. The systemic velocity was calculated with the heliocentric reference frame. The amplitude is normalized for a better visual inspection. The velocity resolution in the spectra is $\sim$10 km s^{-1}.

FIGURE 3.9: continued.

FIGURE 3.10: 3 mm spectrum of NGC 1052. Standing waves are present over the entire spectral window.

FIGURE 3.11: Comparison of the 3 mm radio spectra of Cygnus A and MWC 349. **Top:** Spectra from horizontal polarization. **Bottom:** Spectra from vertical polarization. Two suspicious absorption features in Cygnus A are marked with the red arrows and also appear in the comparison spectrum of MWC 349.

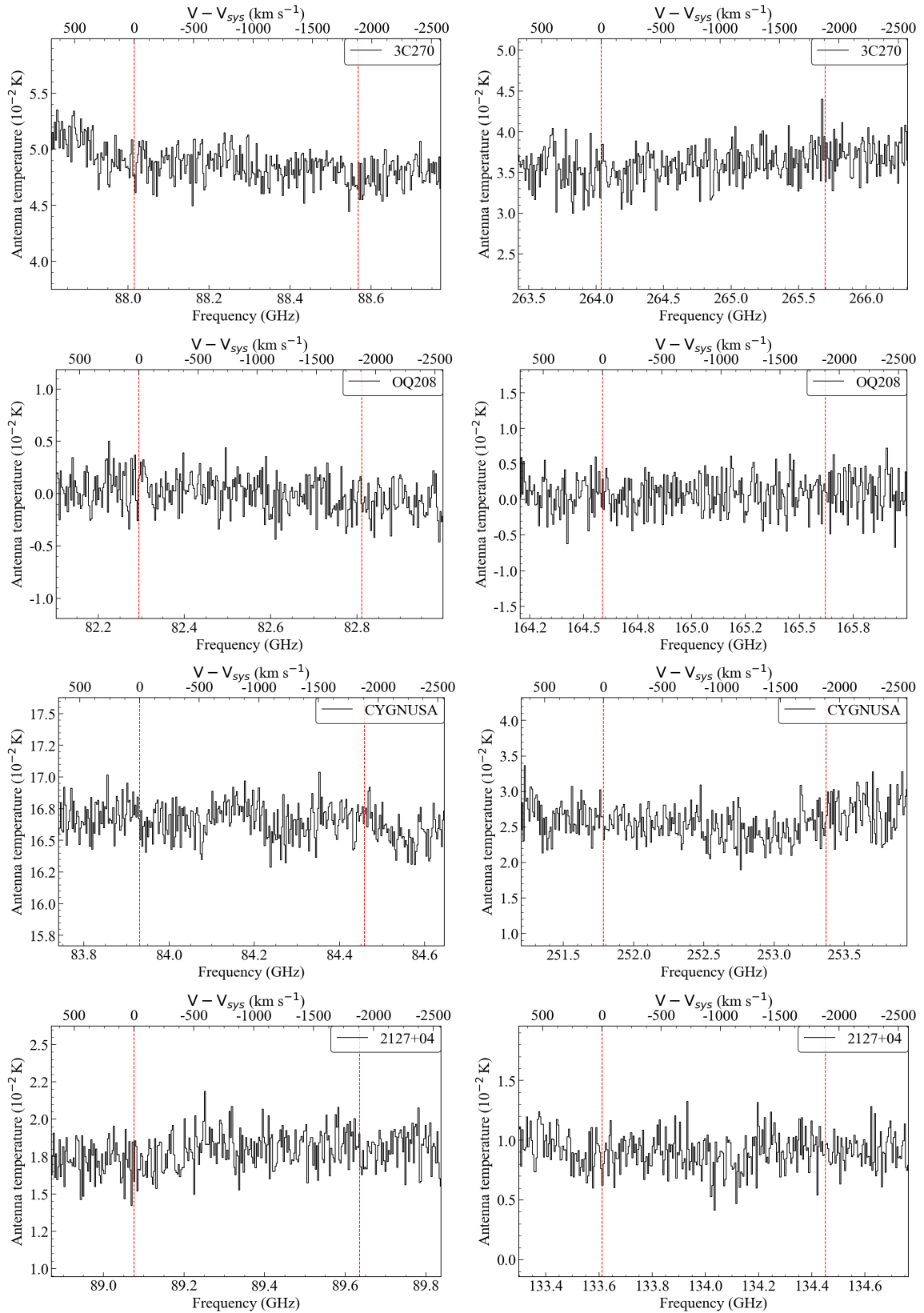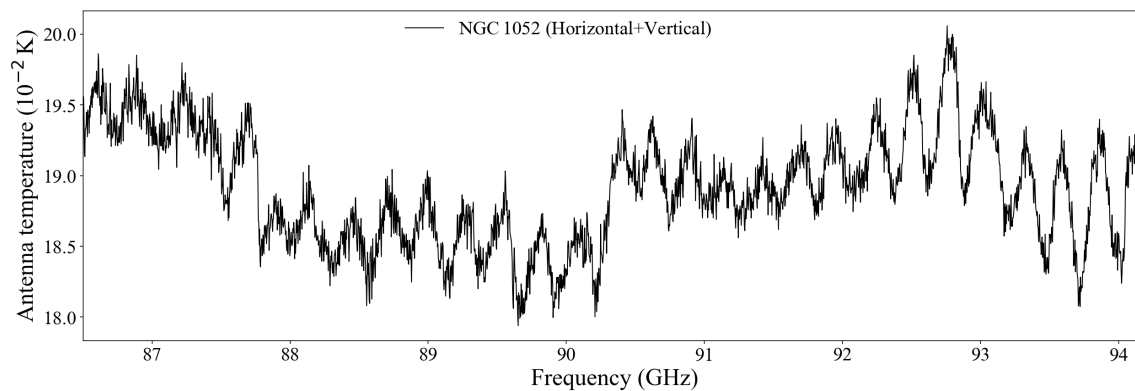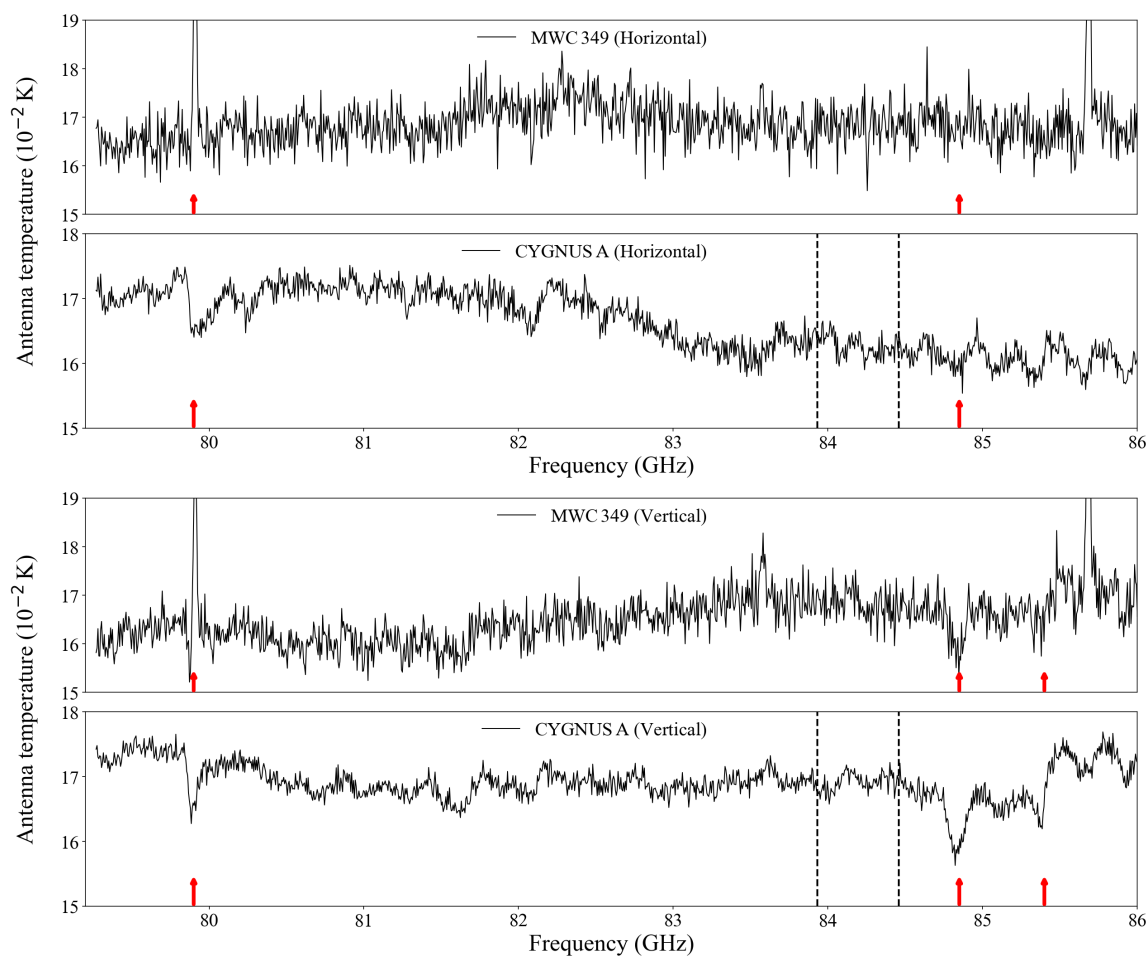Several suspicious absorption features were found in Cygnus A (see Fig. 3.11), but they were not confirmed as real absorption lines. The absorption features were located around 79.90 GHz and 84.85 GHz. No spike like features were identified in scans at different times. Some absorption features were detected in both polarizations, but their sky frequencies were far from the expected HCN J=1-0 (83.931 GHz) and HCO$^+$ J=1-0 (84.458 GHz) transitions. To validate the absorption features detected in Cygnus A, we observed the nearby continuum source MWC 349 with the same IF configuration. The continuum flux density of MWC 349 is comparable to Cygnus A, and hence it is suited for testing any instrumental effects that can cause fake spectral features in the spectrum. Fig. 3.11 shows the comparison of the spectra with the same spectral window. The location of the suspicious absorption lines are marked with the red arrows. MWC 349 also shows emission and absorption features around 79.90 GHz and 84.85 GHz. Thus, we conclude that the two suspicious absorption lines in Cygnus A originate from the instrument and are not real. This result demonstrates the importance of a nearby calibrator to validate suspicious absorption lines detected in single-dish observations.

Among 8 sources, clear molecular absorption lines were detected in 3C 293. Fig. 3.12 shows the HCO$^+$ J=1-0, HCN J=1-0, and HCN J=1-0 absorption lines detected in 3C 293. No emission feature is found in the spectra. The HCO$^+$ J=1-0 line shows a deeper absorption depth than the HCN J=1-0 and HNC J=1-0 lines. The peak absorption depth of HCO$^+$ J=1-0 line exceeds 60 % of the continuum flux density. All absorption features are found in the velocity range of 20-60 km s^{-1}. The absorption lines were fitted with two Gaussian components, and the fitting results are listed in Table. 3.7. Two red-shifted narrow peaks at 19 km s^{-1} and 54 km s^{-1} are consistent in the HCN J=1-0 and HNC J=1-0 lines. The two peaks seem to be present in the HCO$^+$ J=1-0 line, but they are blended due to more broader line widths than the HCN J=1-0 and HNC J=1-0 lines.

We estimated the kinetic temperature of the obscuring gas by using the relation between kinetic temperature and relative intensity of HCN/HNC lines suggested by Hacar et al. (2020) (see §4.3.4). By replacing the line intensities to the integrated optical depths, we obtained a kinetic temperature of 26 ±2.5 K. Assuming Local Thermodynamic Equilibrium (LTE) condition, the column density of the obscuring HCN, HNC, and HCO$^+$ molecules were calculated using the estimated kinetic temperature as the excitation temperature, and the results are listed in Table. 3.7. Details for the column density calculation is described in Appendix A. With the estimated column densities, the abundance ratios of N(HCN)/N(HCO$^+$) and N(HCN)/N(HNC) are 0.79 and 2.89.
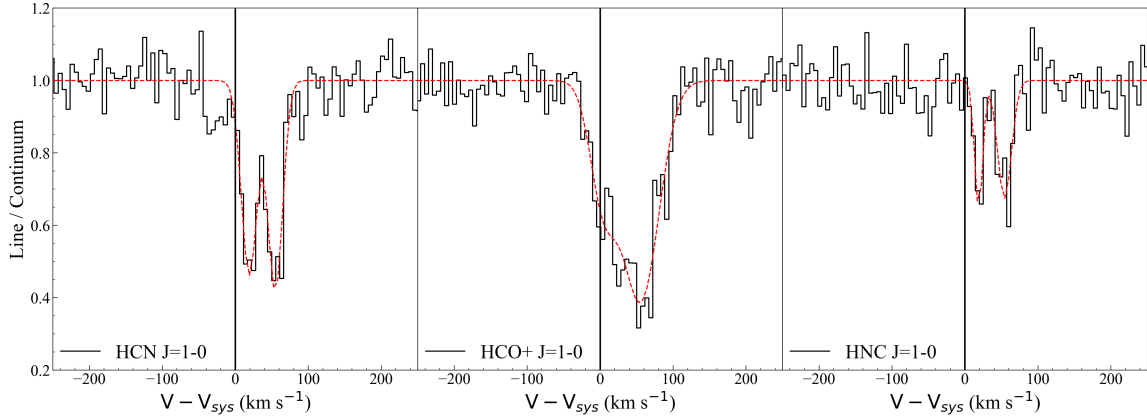
FIGURE 3.12: HCN, HCO$^+$, and HNC absorption lines detected in 3C 293. The red dotted lines show the Gaussian fitting models. Black vertical lines mark the systemic velocity of 3C 293.

TABLE 3.7: Molecular absorption lines detected in 3C 293.

Transition[a]	Frequency[b] (MHz)	ΔV[c] (km s^{-1})	V_0[d] (km s^{-1})	$\int \tau d\nu$[e] (10^{-3} km s^{-1})	Column Density[f] (10^{12} cm^{-2})
HCN $J = 1 - 0$	84814	25.5/23.9	19.2/54.8	3936	2954
HCO$^+$ $J = 1 - 0$	85347	42.5/59.7	4.0/55.2	6195	3747
HNC $J = 1 - 0$	86762	13.3/22.5	18.9/54.3	1493	1025

Notes.: [a]Quantum numbers of the transition. [b]Sky frequency of the target transition. [c]Line width (FWHM). [d] Doppler velocity [e] Integrated optical depth. [f]Column Density of the molecules assuming T$_{ex}$=26 K

3.3.3 Discussion

This section summarizes results from previous absorption line observations for individual sources. The physical properties of the putative molecular absorbers are discuss with regard to the new IRAM 30-m observations.

- **3C 293** is a low-luminosity AGN at z=0.045 with a pair of radio lobes on different scale (Alam et al. 2015). The inner radio lobe (~2 kpc) is misaligned from the outer radio lobe (~200 kpc) (Beswick et al. 2004). A nearby (~30 kpc) companion galaxy and dust lanes observed at optical wavelengths indicate a recent merger event (Floyd et al. 2006). A broad blue-shifted H I absorption line has been detected and spatially resolved via VLBI observations (Mahony et al. 2013; Schulz et al. 2021). A jet-driven outflow has been suggested to explain a highly blue-shifted H I absorption extending up to $1400 \, \mathrm{km \, s^{-1}}$, but the corresponding molecular outflow has not been reported. The molecular absorption lines detected in this study are narrow (FWHM~$20\text{-}30 \, \mathrm{km \, s^{-1}}$) and red-shifted about $19\text{-}55 \, \mathrm{km \, s^{-1}}$. Labiano et al. (2014) imaged a warped CO molecular disk, obscuring the continuum emission, and detected CO J=1-0 and J=2-1 absorption lines against the background continuum (see Fig 3.13). The line profile of the CO absorption lines are consistent with the HCN, HNC, and HCO$^+$ absorption lines detected with the IRAM 30-m telescope. For instance, the two peaks of the CO J=2-1 absorption are separated by $40 \, \mathrm{km \, s^{-1}}$ with FWHM~$20\text{-}30 \, \mathrm{km \, s^{-1}}$. At 1 mm, the background emission was spatially resolved into the core and jet components, which were separated by about 1.5 arcsec along the east-west direction. Contrary to the main absorption feature from the core component, the absorption against the jet component was blue-shifted by about $100 \, \mathrm{km \, s^{-1}}$ with respect to the systemic velocity. A faint CO absorption feature was detected at $200 \, \mathrm{km \, s^{-1}}$, but the corresponding absorption features were not detected in the HCN, HNC, and HCO$^+$ lines. This is likely due to the insufficient spectral line sensitivity of our IRAM observations. The large beam size of the IRAM 30-m telescope did not resolved the core and jet components, and thus the weak absorption feature towards the jet component could be buried or blurred by the strong absorption feature towards the core component. Comparison with the CO absorption lines indicates that the HCN, HNC, and HCO$^+$ absorption lines in 3C 293 originate in the galactic disk of 3C 293. Follow-up high-resolution observations are desirable to detect weaker absorption features, which are currently blended with the strong absorption feature. A more detailed discussion for the physical and chemical properties of the molecular absorbers is presented in Chapter 4.
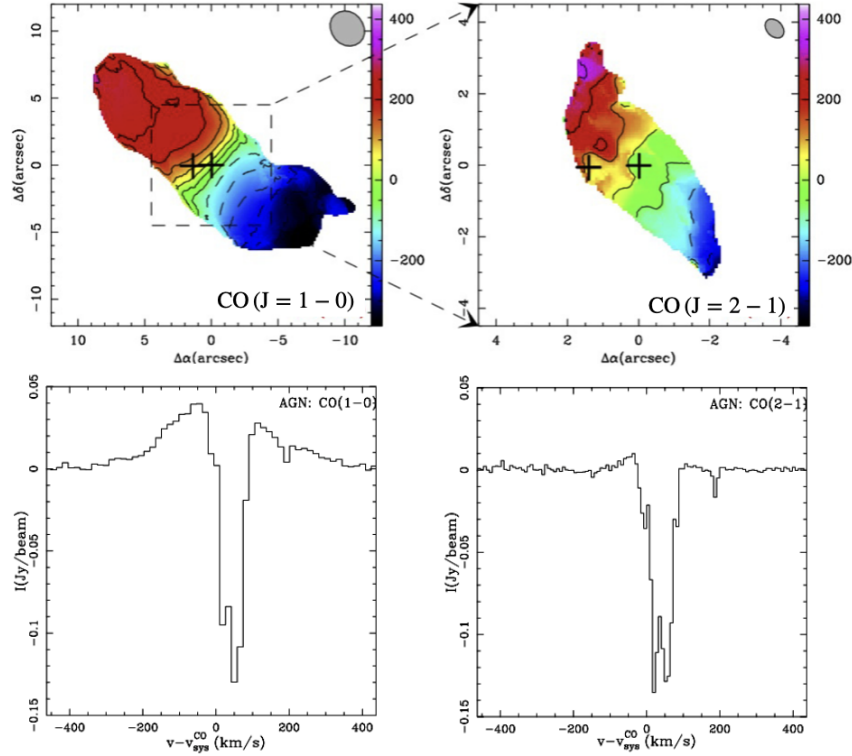
FIGURE 3.13: **Top**: Moment 1 maps of CO J=1-0 and J=2-1 emission from the circumnu-
clear disk in 3C 293. The location of continuum emission is marked with the black cross.
Bottom: Absorption spectra of CO J=1-0 and J=2-1 transitions against the background
continuum emission from the radio jet. The figures are taken from Labiano et al. (2014)

- **NGC 1052** is one of the closest young radio galaxies at z = 0.0049 ($\sim$20 Mpc,
  Tully et al. 2013), and is classified as a low-luminosity AGN ($L_{\rm bol} \sim 7 \cdot 10^{42}$
  erg s^{-1}; (Reb et al. 2018)) with a low accretion rate ($\log (L_{\rm bol}/L_{\rm edd}) = -3.4$;
  (Fernández-Ontiveros et al. 2019)). VLBI observations show prominent two-
  sided radio jets, which are oriented close to the plane of the sky (Baczko et al.
  2016, 2019). From studies over a wide wavelength range the presence of dense
  gas which is surrounding the nucleus is revealed. X-ray observations indicate a
  high nuclear hydrogen column density of $N_{\rm H} \sim 10^{22-23}$ cm^{-2} (Hernández-García
  et al. 2014). An emission gap between jet and counter-jet is explained by strong
  free-free absorption (FFA) from dense ionized material surrounding the core re-
  gion (Kadler et al. 2004). The observations of molecular absorption lines (e.g.,
  HI/OH/HCN/HCO$^+$) on arcsecond scales and towards the unresolved nucleus
  mark dense molecular gas obscuring either central engine and/or the inner jets.
  Their broad ($\sim 500\,$km s^{-1}) and blended (narrow and broad) line profiles point
  towards a complex nature of the obscuring gas (Liszt & Lucas 2004; Kameno
  et al. 2020). Mid-infrared interferometry observations detected a compact dust
  structure, but could not resolve scales smaller than $\sim 5\,$mas (0.5 pc) (Fernández-
  Ontiveros et al. 2019). Earlier VLBI observations of the molecular absorption

lines at cm-λ (OH at 5 & 2 cm; (Impellizzeri 2008)) and more recently also at 3 mm (HCN/HCO⁺) show absorption down to the 2 mas scale (Sawada-Satoh et al. 2019). The latter suggests absorption in front of the counter-jet with absorption depths of 10-15 %, but is still limited by low SNR. Spectral line observations at mm wavelengths are particularly important to find new molecular absorption lines accessible via mm-VLBI observations. HCN and HCO⁺ absorption lines detected at 1 mm with ALMA (see Fig. 3.14) show absorption depths of 10-15 % (Kameno et al. 2020). If the excitation temperature is only a few K, deeper absorption depths are expected for the HCN and HCO⁺ lines at 3 mm. The new IRAM 30-m observations reached a noise level of 1 % for the continuum level, but unexpectedly no clear absorption feature was found in the spectrum. Liszt & Lucas (2004) detected HCN and HCO⁺ absorption at 3 mm with the PdBI, and the absorption depths reached to 3-5 % of the continuum level. The previous absorption line observations using the KVN and the PdBI have much smaller beam size than the IRAM 30-m telescope. Thus, we attribute the non-detection to the beam dilution effect or the prominent standing waves (see Fig. 3.10). Alternatively, excited molecular clouds with high excitation temperatures might result in higher optical depths for HCN and HCO⁺ absorption lines at 1 mm than those at 3 mm
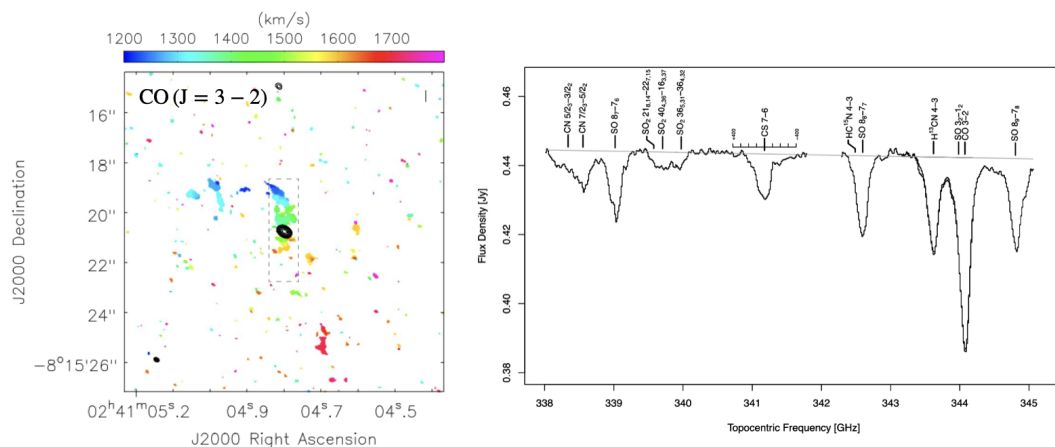
FIGURE 3.14: **Left**: Moment 1 map of CO J=3-2 emission from the circumnuclear disk in NGC 1052. The location of continuum emission is marked with the black contour. **Right**: Molecular absorption lines detected against the continuum radio jet at 1 mm. The figures are taken from Kameno et al. (2020)

- **3C 270 (NGC 4261)** is one of the prime candidates to investigate in more detail the spatial structure of the circumnuclear disk or torus on sub-parsec scales. Optical HST imaging shows a 100 pc scale disk of gas and dust in the nuclear region (Jaffe et al. 1993). Previous VLBI observations indicate strong evidence for obscuring matter in front of the VLBI core and inner jet. Multi-frequency VLBI maps show a two-sided jet with a pc-scale emission gap between

jet and counter-jet (Haga et al. 2015). The presence of significant free-free absorption from ionized gas in front of the counter-jet is thought to cause this emission gap (Jones et al. 2001). Various absorption lines (H I, OH, and CO) have been detected at both cm- and mm-wavelengths (Jaffe & McNamara 1994). The broad line width (up to $400 \, \text{km s}^{-1}$, see Fig. 3.15) implies that the obscuring gas is under strong gravitational influence from the SMBH or comes from a very turbulent environment. At 6 GHz, jet, core and counter-jet are bright enough to allow for absorption line VLBI, using excited OH, which was previously detected by Impellizzeri (2008). A 22 GHz H_2O maser line was detected in NGC 4261, but it has not been imaged with VLBI so far (Wagner 2013). A rotating CO disk has been imaged via ALMA observations (Boizelle et al. 2021), thus our non-detections of HCN and HCO⁺ absorption lines at 3 mm and 1 mm are likely due to the insufficient sensitivity rather than a lack of HCN and HCO⁺ molecular gas in the circumnuclear region of NGC 4261.
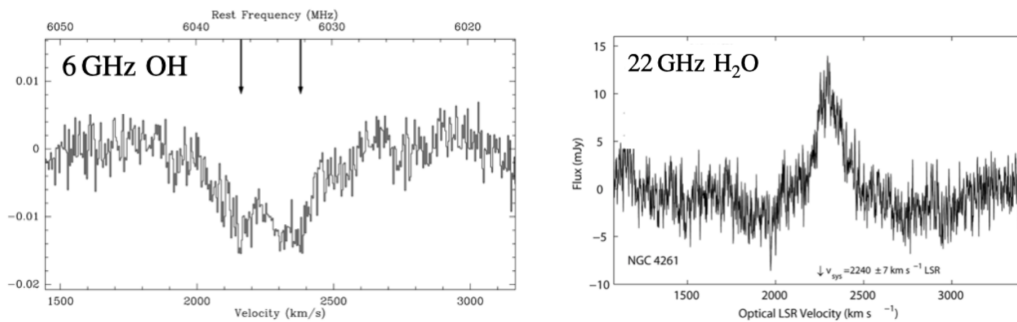

FIGURE 3.15: **Left**: 6 GHz OH absorption lines detected by the 100-m Effelsberg telescope. **Right**: 22 GHz H_2O maser line detected by the 100-m Effelsberg telescope. The figures are taken from Impellizzeri (2008); Wagner (2013).

- **Cygnus A** is a representative radio-loud AGN at z=0.056 (Stockton et al. 1994). Detailed descriptions for the source properties and previous absorption line studies are present in §6.1. Spectral line observations at 3 mm and 1 mm detected strong continuum emission with suspicious absorption features at 3 mm. Comparison of spectra from two polarizations and nearby continuum sources indicates that the detected absorption features are not real. To obtain flat baselines and avoid ghost spectral line like features, interferometric absorption line observations are highly desirable.

- **4C 76.03** is a CSS radio galaxy at z=0.5985 (O'Dea et al. 1991). VLBI observations show an asymmetric two-sided radio jet within sub-kpc scale at 5 GHz (Dallacasa et al. 2013). The flux density of the western jet is 7 times higher than the eastern jet (see left panel in Fig. 3.16). The radio core has an inverted spectral index (a=∼-0.5). Contrary, radio lobes have a steep spectral index

(a=>0.5). H I observations using the Westerbork Synthesis Radio Telescope (WSRT) detected both red-shifted ($315\,\mathrm{km\,s^{-1}}$) and blue-shifted ($-275\,\mathrm{km\,s^{-1}}$) absorption features (Vermeulen et al. 2003), but their spatial distribution and physical origin are not yet clear due to lack of high-resolution observations towards the H I absorption feature. HCN and HCO$^+$ J=2-1 and J=3-2 transitions were searched at $3\,\mathrm{mm}$ and $2\,\mathrm{mm}$, but no absorption was detected.

FIGURE 3.16: **Left**: $5\,\mathrm{GHz}$ VLBI continuum image of 4C 76.03. **Right**: $1.4\,\mathrm{GHz}$ H I absorption observed with The WSRT. Figures are taken from Dallacasa et al. (2013); Vermeulen et al. (2003)

- **3C 216** is a CSS source at z=0.67 with weak ionization levels in the optical spectrum (Gelderman & Whittle 1994; Lawrence et al. 1996). Fig. 3.17 shows the $5\,\mathrm{GHz}$ VLBI continuum image and $21\,\mathrm{cm}$ H I absorption line in 3C 216. A broad (FWHM: $280\,\mathrm{km\,s^{-1}}$) red-shifted ($+86\,\mathrm{km\,s^{-1}}$) H I absorption line was detected using the WSRT (Pihlström et al. 1999). The author suggests jet-ISM interaction as the origin of the broad H I absorption feature. A sharp bending jet structure towards a southwest lobe, and high rotation measure in polarization observations also support the jet-ISM interaction scenario in 3C 216 (Venturi et al. 1993; Venturi & Taylor 1999). The $5\,\mathrm{GHz}$ VLBI image shows a bending structure separated by $140\,\mathrm{mas}$ from the radio core. Estimated viewing angle is rather small ($<19°$) (Paragi et al. 2000). Strong continuum emission was detected at $2\,\mathrm{mm}$ from our IRAM observations, but no absorption features were found. Standing waves induced by the continuum emission degraded the spectral line sensitivity. Follow-up interferometric absorption line observations are necessary to remove the effect of standing waves.

- **3C 236** is a LERG at z=0.1 (Buttiglione et al. 2010). Very extended (a few Mpc) and compact (sub-kpc) radio jets are present, and they are supposed to trace different cycles of the jet outflow (Schilizzi et al. 2001). An H I absorption line has been detected against the radio jet (van Gorkom et al. 1989). VLBI observations show spatially resolved H I absorption line at the southeast
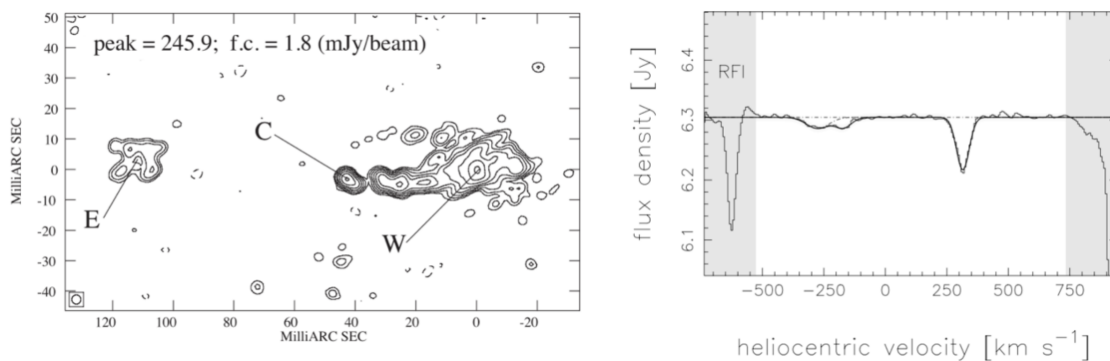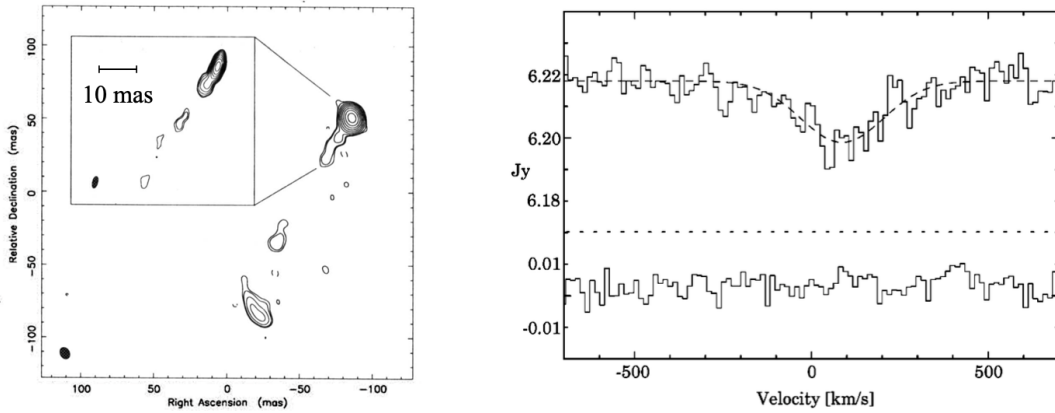
FIGURE 3.17: **Left**: 5 GHz VLBI continuum image of 3C 216. **Right**: 1.4 GHz H I absorption observed with The WSRT. Figures are taken from Pihlström et al. (1999); Paragi et al. (2000)

radio lobe, which is interpreted as a signature of jet-ISM interaction (Schulz et al. 2018). HCN and HCO⁺ J=1-0 transitions were searched at 3 mm, but no absorption was detected.

- **OQ 208** is a CSO source at redshift z=0.1. Optical observations show strong Balmer lines like typical Seyfert type-1 galaxies. Two compact lobes are spatially resolved by VLBI observations and a kinematic age of 255 yr was estimated (Wu et al. 2013). A dense ambient medium partially obscures the lobe structure at low-frequencies by free-free absorption or synchrotron self-absorption (Fanti 2009). The disturbed lobe structure suggests jet-ISM interaction in OQ 208. The blue-shifted (-1200 km s^{-1}) H I absorption feature indicates gas outflows driven by AGN feedback (Morganti et al. 2005). IRAM observations at 1 mm and 2 mm did not detect continuum and spectral line emission of OQ 208. Absorption line observations at mm wavelength for OQ 208 are inadequate due to its faint continuum emission.

- **PKS 2127+04** is a radio galaxy at redshift z=0.99 (Stickel et al. 1994). The convex radio spectra, peaking at a few GHz, show a bright continuum flux at mm wavelengths. VLBI observations revealed a double jet structure separated by 300 pc in the NW–SE direction (Stanghellini et al. 1997). H I and OH line observations were attempted, but absorption lines were not detected (Grasha et al. 2019). Continuum emission of PKS 2127+04 was detected at 1 mm and 2 mm, but absorption lines were not detected.

3.4   Conclusion

We carried out molecular absorption line surveys towards 41 radio AGN from cm to mm wavelengths using the 100-m Effelsberg and 30-m IRAM telescopes. As a result, the cm absorption line survey detected 6 GHz OH absorption and 22 GHz H_2O maser lines in NGC 3079 and 23 GHz OH absorption and 22 GHz H_2O maser lines in NGC 1052. mm absorption line survey detected HCN, HCO$^+$, and HNC absorption lines in 3C 293. The 6 GHz OH absorption lines in NGC 3079 show two separated absorption components blue-shifted about $29\,\mathrm{km\,s^{-1}}$ and $130\,\mathrm{km\,s^{-1}}$ with respect to the systemic velocity ($V_{sys}{=}1147\,\mathrm{km\,s^{-1}}$, see §5.3.2). The blue-shifted feature at $130\,\mathrm{km\,s^{-1}}$ might originate either from outflowing gas driven by the jet-ISM interaction or from intervening gas in the circumnuclear disk. The distinct line profiles between 22 GHz H_2O maser and 6 GHz OH absorption in NGC 3079 indicate their different physical origins. On the other hand, the 23 GHz OH absorption and 22 GHz H_2O maser lines detected in NGC 1052 are red-shifted at $250\,\mathrm{km\,s^{-1}}$ with a broad single feature. Their similar line profile implies similar location of the OH absorption and H_2O maser lines near the central engine. Further high-resolution observations are required to better determine and/or discriminate between different location scenarios for the absorption lines detected in NGC 3079 and NGC 1052. The 3 mm HCN, HCO$^+$, and HCN absorption lines detected in 3C 293 show a similar line centroid and line profile as the CO absorption line. The obscuring gas is most likely to be part of a warped circumnuclear disk in 3C 293.

We attribute the low-detection rates in the single-dish absorption line surveys presented here mainly to technical limitations such as non-optimal spectral baselines, standing waves (of similar bandwidth than the expected absorption features) and RFI. Despite extensive efforts to obtain flat baselines, residual errors from baseline fittings and instruments degraded the sensitivity of the spectral line observations. To yield higher detection rates, absorption line surveys using radio interferometers (higher sensitivity, flatter spectral baselines) are therefore more desirable. For subarcsecond resolution and a further reduced beam dilution, VLBI observations towards the molecular absorption lines could play a key-role to discern the nature of the obscuring gas.

Chapter 4

Interferometric molecular absorption line survey

Abstract As a follow-up study of the single-dish absorption surveys, this chapter presents an absorption line survey towards two radio AGN using the NOrthern Extended Millimeter Array (NOEMA). This line survey detected various molecular species in the radio AGN $3C\,293$ and $4C\,31.04$ over a spectral window of $15\,\mathrm{GHz}$ at $3\,\mathrm{mm}$. Spectroscopy using molecular absorption lines clarifies detailed physical and chemical properties of the circumnuclear gas. These measurements clarify the origin of the obscuring gas and a physical connection between the radio jet and the obscuring gas in $3C\,293$ and $4C\,31.04$.

FIGURE 4.1: The NOEMA interferometer operated by IRAM, France. 15-m x 11 antennas are in operation in 2021, and 12 antennas are planned to be in operation. (Credit: IRAM)

4.1   Introduction

The previously described single-dish absorption line surveys resulted in low detection rates due to technical hindrances, such as standing waves, RFI, and beam dilution effects. These obstacles can be effectively avoided by interferometric observations using an array of single-dish telescopes. For instance, the cross-power spectrum obtained from the correlation process removes standing waves caused by the individual antennas. The small beam size of a radio interferometer helps to detect a faint absorption feature, providing a higher filling factor. In particular, interferometric observations at mm wavelengths are beneficial for avoiding RFI signals. In this context, spectral line scans towards known molecular absorption systems are suited for demonstrating the advantages of interferometric absorption line observations. More importantly, newly detectable molecular species via absorption technique provide a unique opportunity to study chemical and physical properties of the circumnuclear gas in radio AGN. NOEMA is one the most advanced mm-interferometers, which is situated on the Plateau de Bure at 2550-m altitude in the French Alps. Currently, NOEMA consists of eleven 15-m single-dish telescopes. The observing wavelength of the dual-polarization receiver ranges from 1 to 3 mm. The wide bandwidth of the NOEMA ($\sim$ 7.8 GHz) allows to search for $H^{13}CN$, $H^{13}CO^+$, SiO, C_2H, HCN, HCO^+, HNC, and N_2H^+ transitions at 3 mm, simultaneously. By taking such advantages of NOEMA, we were aiming at the detection of various molecular species via absorption.

The target sources 3C 293 (z=0.0448±0.000025, V_{sys}=13434±8 km s^{-1} (Labiano et al. 2014)) and 4 C31.04 (z=0.0602±0.0002, V_{sys}=18047±60 km s^{-1} (García-Burillo et al. 2007)) are young radio AGN with SMBH masses of $\sim$1.41 $\times$ $10^8 M_\odot$ and $\leq$1.44 $\times$ $10^8 M_\odot$, respectively (Giroletti et al. 2003; Willett et al. 2010; Kuźmicz et al. 2017). The gas content in their nuclear region was estimated to be M(H$_2$) $\sim$2.2 $\times$ $10^{10} M_\odot$ for 3C 293 and M(H$_2$) $\sim$0.5-5.0 $\times$ $10^{10} M_\odot$ for 4C31.04 via molecular line observations (Labiano et al. 2014; García-Burillo et al. 2007). These values are significantly higher than typical gas content (M(H$_2$) $\sim$10^7 - $10^8 M_\odot$) found in nearby radio galaxies (Lees et al. 1991; Ocaña Flaquer et al. 2010). A recent galaxy merger or an interaction event is supposed to supply gas for AGN fueling, and trigger the radio jet activities (Emonts et al. 2016; Zovaro et al. 2019). H I absorption line observations indicate putative gas outflows via blue-shifted features in both galaxies. A broad blue-shifted absorption feature is extending up to 1400 km s^{-1} in 3C 293. 4C 31.04 shows moderate blue-shifted H I absorption around 130 km s^{-1}. Deep CO and HCN absorption lines detected at 3 mm make them prime candidates for high-sensitivity absorption line surveys at mm wavelengths (Labiano et al. 2014; García-Burillo et al. 2007).

4.2 Observations and data reduction

3C 293 and 4C 31.04 were observed with NOEMA on 1 Jan. 2020 and 24 May. 2020 to search for molecular absorption lines at 3 mm. Table. 4.1 summarizes the observing parameters of these NOEMA observations. The array configurations C (Baseline length: 20 - 192 m) and D (Baseline length: 42.3 - 452 m) were used for 3C 293 and 4C 31.04, respectively. Phase fluctuations on a short time scale (a few seconds) were calibrated via the real-time correction process during the observations. The spectral line data were obtained through the wide-band correlator PolyFiX, using 7.7 GHz bandwidth per side-band. To search for molecular absorption lines over a wide spectral window, both USB and LSB were used in each polarization feed (Vertical or Horizontal). At 3 mm a spectral window of 15 GHz was searched with a 2 MHz spectral resolution. The velocity resolution for the spectral lines at 3 mm is about ~6 km s^{-1}. Bandpass calibrators 3C 273 and 3C 454.3 were observed in the beginning of the observations. Nearby calibrators 1308+326 and 0109+224 were observed regularly for phase and gain calibrations. They were also used to test the possible contamination of RFI signals or artificial spectral line features from instruments. At the end of the observation session, the standard flux calibrator MWC349 was observed. The data reduction was performed with the Continuum and Line Interferometer Calibration (CLIC[1]) software. The data reduction process includes bandpass, phase, and amplitude calibrations. Long-term variations of phase and amplitude were corrected with the phase calibrator. A self-calibration was performed on 4C 31.04 to increase the signal to noise ratio on the target source. Self-calibration was not performed to 3C 293 as its continuum emission was resolved in C configuration. Channel smoothing and continuum imaging were made with the Astronomical Image Processing System (AIPS) package [2]. Spectral line data were extracted by using the AIPS task POSSM. Spectral index and baseline fittings were conducted by manually written scripts in Python. All velocities in the spectra were calculated, referring to the heliocentric reference frame.

TABLE 4.1: Configuration of NOEMA observations.

Target	Obs date (dd.mm.yyyy)	Array	Beam size (arcsec)	Spectral window (LSB/USB, GHz)	Resolution (MHz)
3C 293	01-01-2020	10C	1.48 x 3.08	82.5-90.0/98.0-105.5	2
4C 31.04	24-05-2020	10D	3.84 x 3.26	81.5-89.0/96.5-104.0	2

---

[1] https://www.iram.fr/IRAMFR/GILDAS/

[2] http://www.aips.nrao.edu

4.3 Results

4.3.1 Continuum emission of 3C 293 and 4C 31.04

Fig. 4.2 shows the continuum images of 3C 293 and 4C 31.04 observed with NOEMA. High-resolution VLBI images of the continuum emission are also presented for reference (Giroletti et al. 2003; Beswick et al. 2004).

Continuum map of 3C 293: 3C 293 appears partially resolved along the east-west direction with the NOEMA beam. The elongated continuum image is consistent with the previous 3 mm continuum map obtained with the Atacama Large Millimeter Array (ALMA) (Labiano et al. 2014). The peak flux density of the radio core is ~213 mJy at 82.4 GHz, and it decreases with increasing frequency with a spectral index of α=–0.7±0.1 (I(ν) $\propto \nu^{\alpha}$, where I is the flux density and ν is the frequency). The observed flux density is slightly lower than a previous flux measurement (234 mJy) at 115 GHz Labiano et al. (2014). High-resolution cm-VLBI observations show two continuum components separated about 1.3″ (Beswick et al. 2004) (see Fig. 4.2). At 3 mm, the separation angle between the radio core and the extended jet component was measured using the Gaussian model fitting method in Difmap. The measured separation angle 1.26″ is consistent with the VLBI results.

Continuum map of 4C 31.04: 4C 31.04 was not resolved with the NOMEA observations. The continuum flux density is 206 mJy at 80.9 GHz, which is ~30 % higher than previous flux density measurement at 84 GHz (~160 mJy) García-Burillo et al. (2007). It shows a more steep spectrum with a spectral index of α=–1.0±0.1 compared to 3C 293. The VLBI images at cm-wavelengths show a young radio jet, extending about 200 pc. The western jet shows extended diffuse emission, whereas the eastern jet is relatively bright and compact. A compact radio core is located in the middle of the two radio lobes. Clearly, the beam size of the NOEMA observations was too large to resolve the compact radio jet. The western jet shows extended diffuse emission, whereas the eastern jet is relatively bright and compact.

TABLE 4.2: Results of the circular Gaussian fitting on the continuum images.

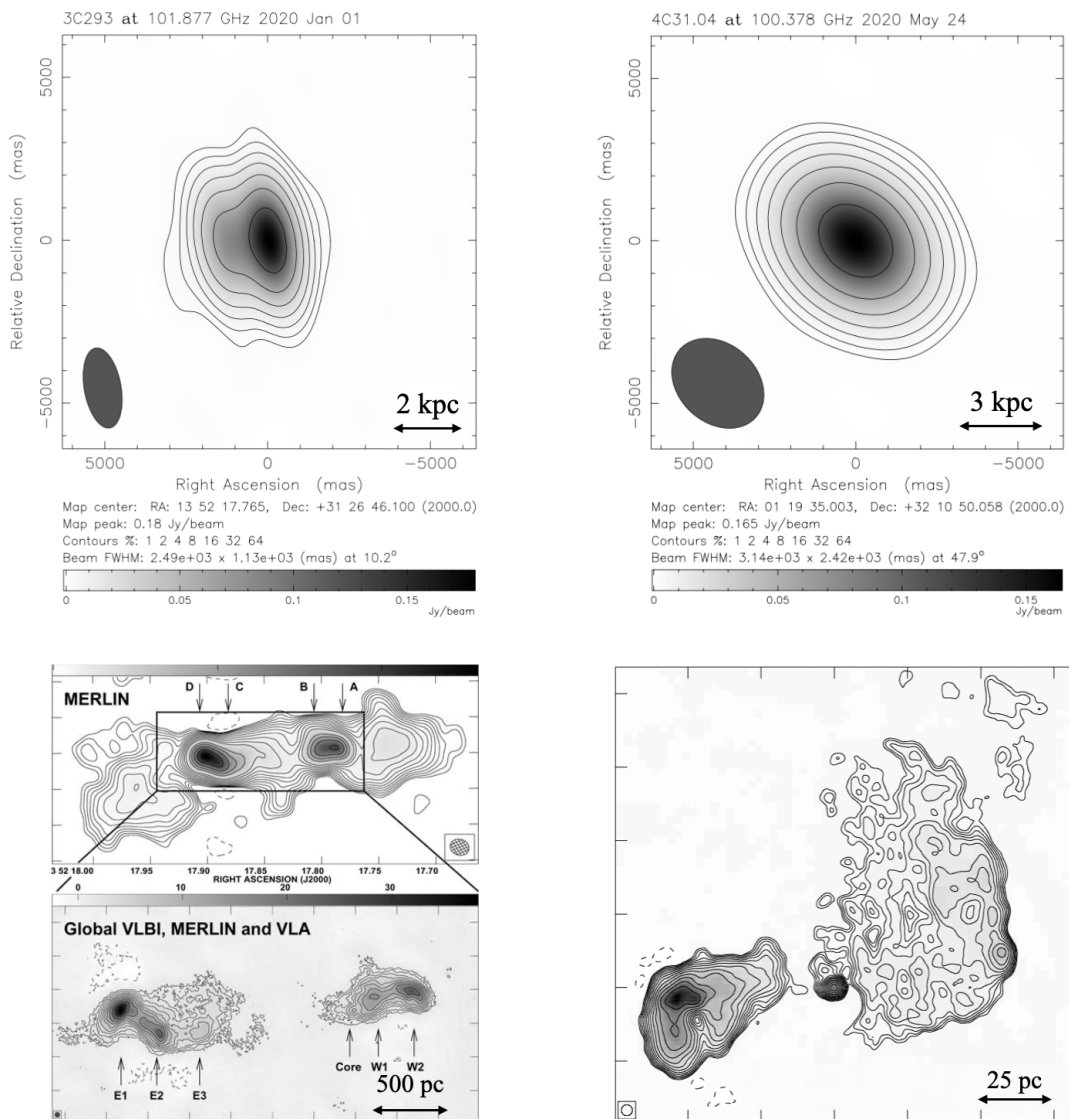| Target	Center freq (GHz)	Component	Flux (mJy)	Model	Size (arcsec)	Peak position (RA/DEC) (arcsec)
3C 293	101.9	core	189.0 ±0.2	gaussian	0.4 x 0.4	(0/0)
	101.9	jet	85.9 ±0.2	gaussian	0.6 x 0.6	(1.26/0)
4C 31.04	100.3	core	165.3 ±0.2	gaussian	0.2 x 0.2	(0/0)

FIGURE 4.2: **Top**: 3 mm continuum image of 3C 293 (left) and 4C 31.04 (right) observed with NOEMA. The linear scale and beam size are labeled on the bottom. **Bottom left**: 1.3 GHz VLBI maps of 3C 293 observed with the MERLIN and global VLBI array. **Bottom right**: 5 GHz VLBI image of 4C 31.04 observed with the VLBA. VLBI images are taken from Beswick et al. (2004); Giroletti et al. (2003).

4.3.2   Molecular absorption lines in 3C 293 and 4C 31.04

Fig. 4.3 and 4.4 show the 15 GHz wide radio spectra of 3C 293 and 4C 31.04 observed with NOEMA at 3 mm. The rms noise level is uniform over the upper and lower side bands. Achieved spectral line sensitivities are 0.7 mJy and 1.1 mJy at a spectral resolution of 4 MHz for 3C 293 and 4C 31.04, respectively. Continuum flux densities of 3C 293 and 4C 31.04 are 213-180 mJy and 205-160 mJy. Therefore, sensitivity for absorption line detection is 0.3-0.6 % of the continuum level. We detected $H^{13}CN$, $H^{13}CO^+$, SiO, C_2H, HCN, HCO^+, HNC, N_2H^+, and ^{13}CO lines in 3C 293, and C_2H, HCN, HCO^+, HNC, and ^{13}CO lines in 4C 31.04. The parameters of the detected molecular absorption lines are listed in Table. 4.3. Since the absorption lines in 4C 31.04 are much broader ($\sim$150 km s^{-1}) than the spectral resolution ($\sim$7 km s^{-1}), the Hanning smoothing method was applied to identify a buried absorption feature.

TABLE 4.3: List of molecular absorption lines detected in 3C 293 and 4C 31.04.

Target	Transition[a]	Frequency[b] (MHz)	ΔV[c] (km s^{-1})	V_0[d] (km s^{-1})	V_{res}[e] (km s^{-1})	$\int \tau dv$[f] (10^{-2} km s^{-1})
3C 293	$H^{13}CN$	82636.6	-73	22	7.3	183
	$H^{13}CO^+$	83033.2	-79	24	7.2	480
	SiO J=2-1	83121.9	-79	27	7.2	285
	C_2H N=1-0 J=3/2-1/2	83571.7	-	19	7.2	669
	C_2H N=1-0 J=1/2-1/2	83653.1	-86	60	7.2	326
	HCN J=1-0	84830.2	-134	56	7.1	5523
	HCO^+ J=1-0	85363.0	-154	31	7.0	9613
	HNC J=1-0	86774.8	-76	65	6.9	1964
	N_2H^+ J=1-0	89177.3	-87	25	6.7	559
	^{13}CO J=1-0	105474.6	-89	64	5.7	320
4C 31.04	$H^{13}CN$	82636.6	-	-	14.7	<60
	$H^{13}CO^+$	83033.2	-	-	14.6	<36
	SiO J=2-1	83121.9	-	-	14.6	<32
	C_2H N=1-0 J=3/2-1/2	83571.7	220	-118	14.6	161
	C_2H N=1-0 J=1/2-1/2	83653.1	-	-	14.5	<38
	HCN J=1-0	84830.2	281	-115	14.3	2203
	HCO^+ J=1-0	85363.0	283	-124	14.3	3720
	HNC J=1-0	86774.8	280	-139	14	573
	N_2H^+ J=1-0	89177.3	-	-	13.6	<35
	^{13}CO J=1-0	105474.6	211	-133	-11.5	377

Notes.: [a] Quantum numbers of the transition. [b] Sky frequency of the target transition. [c] Full Width at Zero Power (FWZP). [d] Doppler velocity. [e] Velocity resolution. [f] Integrated optical depth.
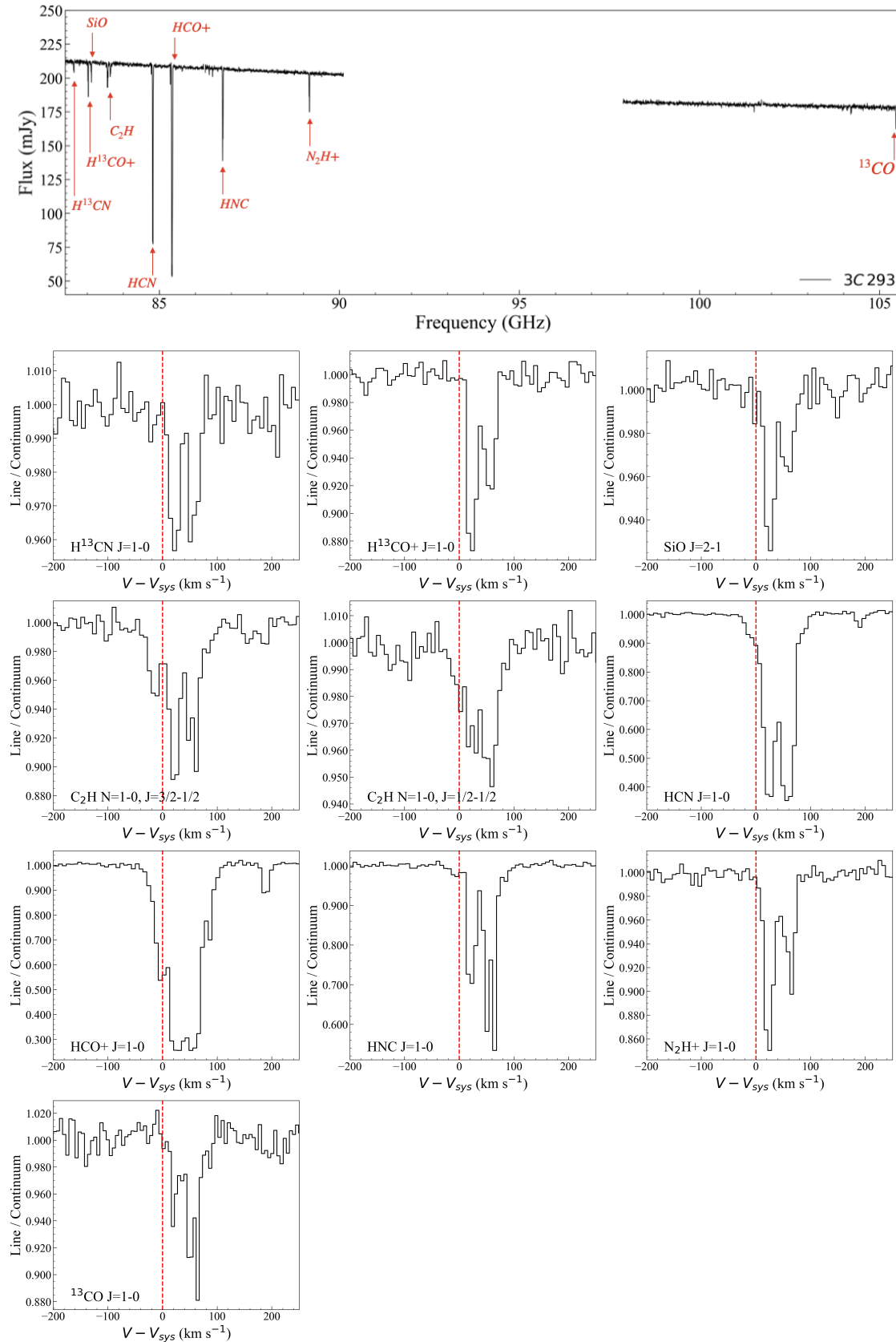
FIGURE 4.3: **Top:** 3 mm radio spectrum of 3C 293 observed with the NOMEA. **Bottom:** Individual spectra of the molecular absorption as denoted in the bottom of each panel. The amplitudes are normalized. The location of the systemic velocity is marked with the red dotted line.
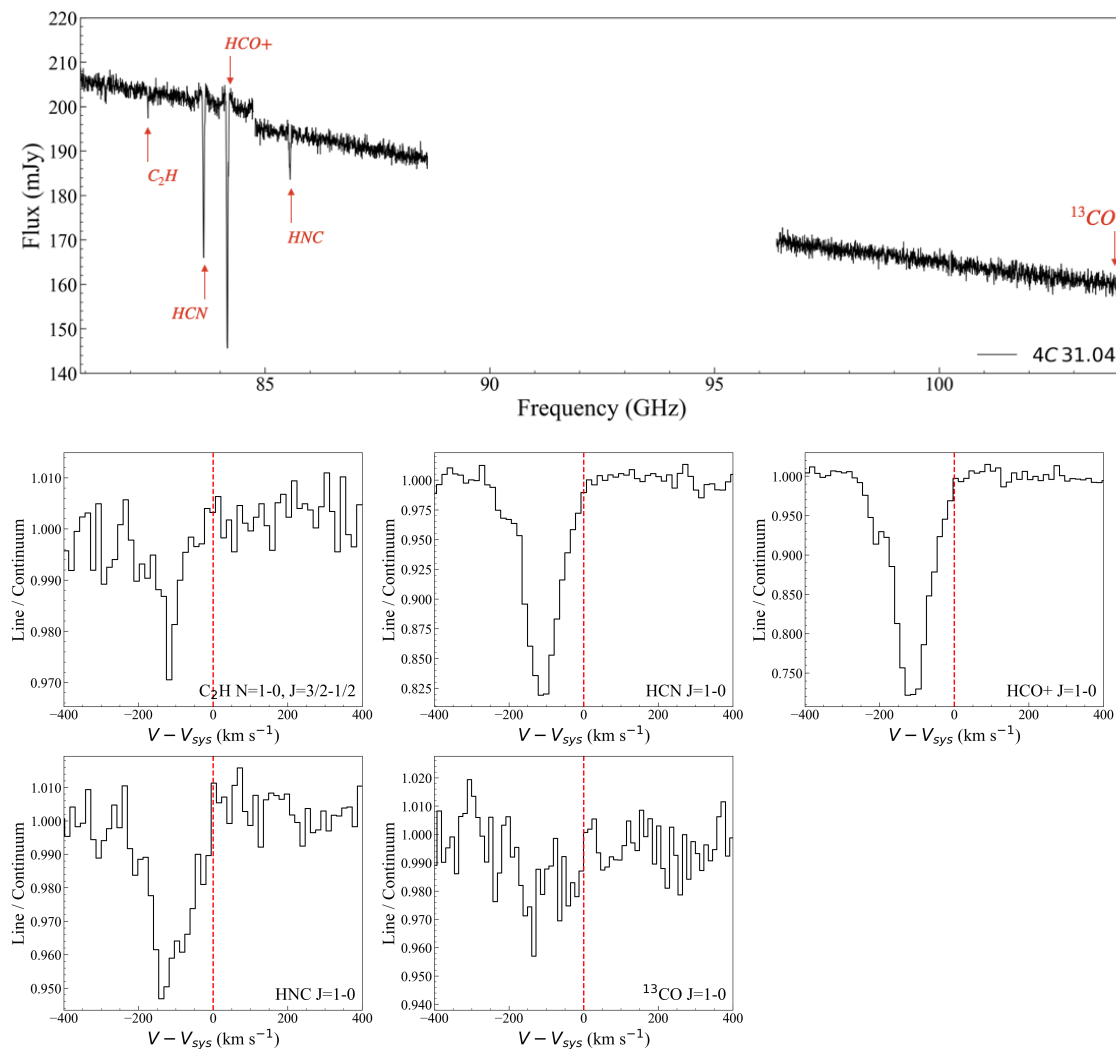
FIGURE 4.4: **Top:** 3 mm radio spectrum of 4C 39.01 observed with the NOMEA. **Bottom:** Individual spectra of the molecular absorption as denoted in the bottom of each panel. The amplitudes are normalized. The location of the systemic velocity is marked with the red dotted line.

4.3.3 Kinematics of molecular absorption lines

The spectra of the detected molecular absorption lines are presented in the bottom panels of Fig. 4.3 and 4.4. The molecular absorption lines in 3C 293 were red-shifted by about $50\,\mathrm{km\,s^{-1}}$ with respect to the systemic velocity. The line profiles show composite features rather than a single velocity component. Two narrow peaks were commonly found in several absorption lines at Doppler velocities around $25\,\mathrm{km\,s^{-1}}$ and $60\,\mathrm{km\,s^{-1}}$. $H^{13}CO^+$, SiO, and N_2H^+ lines peak at $25\,\mathrm{km\,s^{-1}}$, whereas ^{13}CO, HNC lines peak at $60\,\mathrm{km\,s^{-1}}$. In previous H I VLBI observations, broad absorption extending up to a few hundreds $\mathrm{km\,s^{-1}}$ was seen (Mahony et al. 2013). However, we did not detect any blue-shifted features corresponding to the H I absorption.

4C 31.04 absorption lines were blue-shifted about $150\,\mathrm{km\,s^{-1}}$ relative to the systemic velocity, and have much broader line widths and lower absorption depths compared to those in 3C 293. In this source, the Doppler velocities and line widths are consistent with the H I absorption line, but the narrow absorption feature found in H I observations was not found in molecular absorption lines (Conway 1996).

4.3.4 Physical quantities of the molecular absorbers

We derived the physical and chemical properties of the molecular absorbers by using absorption lines of different molecular species. In the following we describe the methodologies to measure physical quantities of the molecular absorbers in 3C 293 and 4C 31.04.

Kinetic temperature: The kinetic temperature of gas determines the physical properties of the ISM, such as gas pressure, sound speed, and fragmentation scale of gas (Larson 1985). The chemical reactions of certain molecular species also depend on the kinetic temperature (van Dishoeck 2018). Thus, an accurate kinetic temperature measurement is important to characterize the ISM property. A statistical study using a large sample of molecular gas suggests that HCN and HNC molecules can be used as a chemical thermometer for the molecular ISM (Hacar et al. 2020). With the HCN/HNC intensity ratio, the kinetic temperature of the molecular gas is given by

$$T_{kin}(K) = 10 \times \left[\frac{I(\mathrm{HCN})}{I(\mathrm{HNC})} \right] \text{ if } \left(\frac{I(\mathrm{HCN})}{I(\mathrm{HNC})} \right) \leq 4. \tag{4.1}$$

Integrated optical depths measured by HCN and HNC absorption lines can replace the HCN and HNC intensities in the Eq. 4.1. Using the optical depth measurements listed in Table. 4.3, we obtained a kinetic temperature of $28 \pm 2.5\,\mathrm{K}$ and $38 \pm 2.5\,\mathrm{K}$ for 3C 293 and 4C 31.04, respectively. For a low ($\leq 40\,\mathrm{K}$) temperature estimated by Eq.4.1, the expected error is less than $5\,\mathrm{K}$ (Hacar et al. 2020).

Hyperfine line: At $3\,mm$, in total 6 hyperfine C_2H transitions exist (Endres et al. 2016). Assuming LTE conditions, the relative line strengths among hyperfine lines can be calculated. Table. 4.4 shows the list of hyperfine lines of the C_2H molecule with the expected line strengths (Reitblat 1980). To test the local condition of the C_2H molecules, we fitted the main C_2H line with two Gaussian components at $31\,km\,s^{-1}$ and $64\,km\,s^{-1}$. Then, applied the same line widths and expected relative line ratios for the hyperfine lines. This resulted in a total of 12 Gaussian components (6 hyperfine lines $\times$ 2 Gaussian components). Fig. 4.5 shows the fitting results, including in total 12 Gaussian components. The combined Gaussian model profile is well consistent with the observed composite C_2H line profile. Therefore, we conclude that the obscuring gas is in this lines optically thin, following LTE conditions.

TABLE 4.4: Hyperfine lines of C_2H.

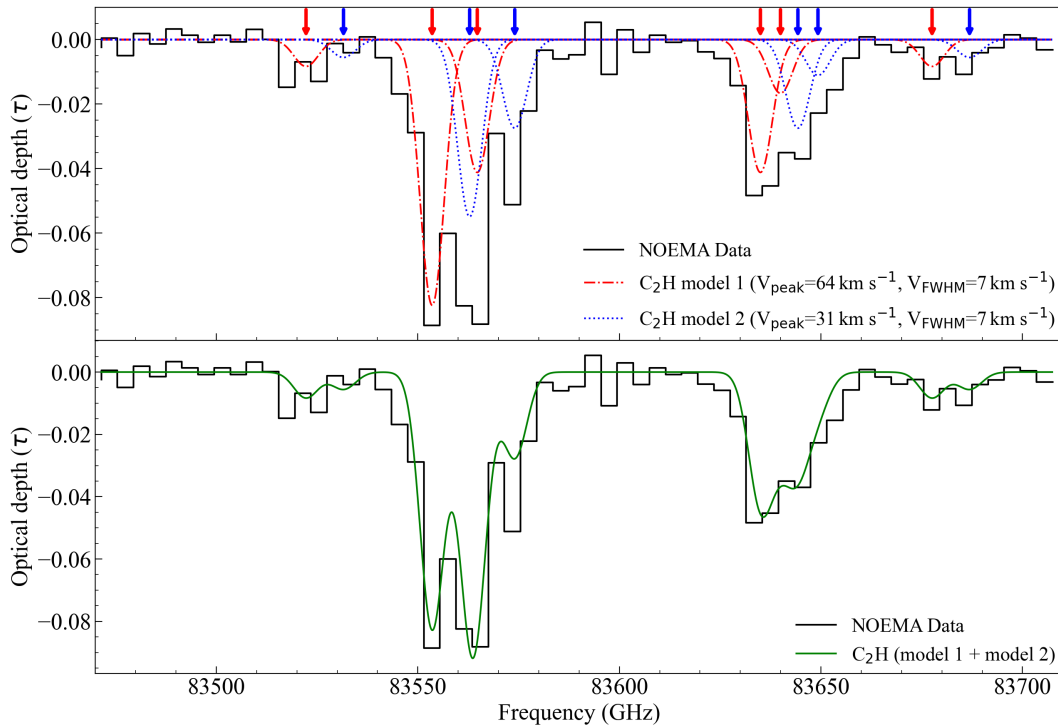| Molecule	Freq (GHz)	E_{low} (cm^{-1})	Transition	A (s^{-1})	I_{rel}
C_2H, $(N_{J,F})$	87.284105.	0.0015	$1_{3/2,1}$-$0_{1/2,1}$	2.59×10^{-7}	0.1
	87.316898	0.0015	$1_{3/2,2}$-$0_{1/2,1}$	1.53×10^{-6}	1.0
	87.328585	0.0000	$1_{3/2,1}$-$0_{1/2,0}$	1.27×10^{-6}	0.5
	87.401989	0.0015	$1_{1/2,1}$-$0_{1/2,1}$	1.27×10^{-6}	0.5
	87.407165	0.0015	$1_{1/2,0}$-$0_{1/2,1}$	1.53×10^{-6}	0.2
	87.446470	0.0000	$1_{1/2,1}$-$0_{1/2,0}$	2.61×10^{-7}	0.1

FIGURE 4.5: Hyperfine lines of C_2H **Top**: Superposed spectra of the observed C_2H lines and synthesized hyperfine C_2H lines. **Bottom**: Individual Gaussian components of the synthesized hyperfine C_2H lines

Column density: Molecular absorption lines allow us to measure the column density of the molecular absorbers along the line of sight. The relation between the optical depth of the absorption line and the column density of the obscuring medium is

$$N_{total} = \frac{8\pi v^3}{c^3} \frac{Q_{rot}(T_{ex})}{g_u} \frac{1}{A_{ul}} \exp\left(\frac{E_l}{kT_{ex}}\right) \left[1 - \exp\left(-\frac{hv}{kT_{ex}}\right)\right]^{-1} \int \tau d v, \qquad (4.2)$$

where v is the rest frequency of the transition, c is the speed of light, g_u is the statistical weight of the upper state, Q_{rot} is the rotational partition function, A_{ul} is the probability for spontaneous emission of the transition, E_l is the energy level of the lower state, k is the Boltzmann constant, h is the Planck constant, τ is the optical depth. The more detailed description for the column density calculation is addressed in Appendix A. The calculated total column densities of molecular absorption lines are listed in Table. 4.5. The kinetic temperature estimated by Eq. 4.1 was used as the excitation temperature, assuming LTE condition. Since the hyperfine lines of the C_2H molecule are thermalized, this is a reliable assumption. The hyperfine components of HCN, C_2H, and N_2H^+ molecules were summed in the column density calculations, as they are not resolved in the spectra.

TABLE 4.5: Column densities of molecular absorption lines.

Transition[a]	μ[b] (D)	S_{ul}[c]	3C 293 $\int \tau dv$ $(10^{-2}\,\mathrm{km\,s^{-1}})$	N_{tot}[d] $(10^{12}\,\mathrm{cm^{-2}})$	4C 31.04 $\int \tau dv$ $(10^{-2}\,\mathrm{km\,s^{-1}})$	N_{tot}[e] $(10^{12}\,\mathrm{cm^{-2}})$
$H^{13}CO^+$ J=1-0	3.90	1.00	480	252	<36	<57
$H^{13}CN$ J=1-0	2.99	1.00	183	166	<60	<59
SiO J=2-1	3.10	1.00	285	85	<32	<17
C_2H N=1-0 J=3/2-1/2	0.77	0.67	669	13326	161	5757
C_2H N=1-0 J=1/2-1/2	0.77	0.33	326	13184	<38	<2759
HCN J=1-0	2.99	1.00	5523	4771	2203	3415
HCO^+ J=1-0	3.90	1.00	9613	4791	3720	3326
HNC J=1-0	3.05	1.00	1964	1551	573	812
N_2H^+ J=1-0	3.40	1.00	559	337	<35	<38
^{13}CO J=1-0	0.11	1.00	320	463339	377	988302

Notes.: [a]Quantum numbers of the transition. [b]Dipole moments. [c] Relative line strengths. [d]T_{kin}=T_{ex}=28 K and [e]T_{kin}=T_{ex}=38 K were applied in total column density calculations.

Isotope and abundance ratios   Table. 4.6 shows the relative abundance ratios of several molecular species detected in 3C 293 and 4C 31.04 via absorption. For comparison, measurements from other astrophysical environments are also presented. Abundance ratios of $N(HCO^+)/N(H^{13}CO^+)$ and $N(HCN)/N(H^{13}CN)$ allowed us to

estimate the $^{12}C/^{13}C$ ratio in 3C 293 (18-28) and 4C 31.04 ($^{12}C/^{13}C < 56$). ^{12}C is rapidly produced by massive stars, whereas ^{13}C is predominantly synthesized by low-and intermediate stars in late evolutionary stages. Thus, low $^{12}C/^{13}C$ ratios are expected in early-type galaxies or aged regions, such as in the galactic center (Wilson & Rood 1994). Indeed, observational studies show that the $^{12}C/^{13}C$ ratio increases with distance from the galactic center of the Milky way. For the galactic center, $^{12}C/^{13}C$ ~24, ~30 at 5 kpc, and ~70 at 12 kpc (Langer & Penzias 1990; Henkel et al. 1994; Riquelme et al. 2010). Such a trend is also seen in nearby starburst galaxies NGC 253, NGC 1068, and NGC 4945 in the range from 30 to 67 (Tang et al. 2019; Martín et al. 2019). The nearby radio galaxy Cen A shows an $^{12}C/^{13}C$ ratio of 50 in the circumnuclear Disk (CND) (McCoy et al. 2017). The $^{12}C/^{13}C$ ratio measured in 3C 293 (18-28) is rather low and comparable with the molecular gas in the galactic center. This is consistent with the expected location of the obscuring gas in 3C 293.

The N(HCN)/N(HCO$^+$) ratio is significantly different between AGN and starburst galaxies, and such a trend is attributed to the different local environments, such as gas densities, temperature, and radiation fields (Krips et al. 2008; Imanishi et al. 2020). In particular, the HCN abundance relative to HCO$^+$ is enhanced in the vicinity of luminous AGN due to the presence of X-ray dominated regions (XDRs) (Imanishi et al. 2016; Saito et al. 2018). For typical galactic molecular clouds, the N(HCN)/N(HCO$^+$) ratio is also close to unity (Blake et al. 1987; Vogel & Welch 1983). The N(HCN)/N(HCO$^+$) ratios in 3C 293 and 4C31 04 are unity. The abundances of SiO, HNC, and N$_2$H$^+$ relative to HCN are comparable with the measurements from the extragalactic absorption system PKS 1830-211, which is a gravitational lens source with an intervening spiral galaxy. Therefore, the absorption lines analysis indicates the signature of AGN feedback on the chemical properties of the obscuring gas in 3C 293 and 4C31.04 is insignificant.

TABLE 4.6: Relative abundance ratios of molecular species detected in absorption.

Abundance ratio	3C 239	4C 31.04	PKS 1830-211 [a]	Cen A[b]	Hydra A[c]
HCO$^+$/H^{13}CO$^+$	28.9	< 56.4	21.2	71.0	-
HCN/H^{13}CN	18.9	< 59.9	36.3	-	-
HCN/HCO$^+$	1.0	1.0	1.7	0.6	0.3
HCN/SiO	56.1	< 200.9	40.5	-	-
HCN/HNC	3.1	4.21	3.0	3.5	0.7
HCN/N$_2$H$^+$	14.2	< 89.9	13.0	-	-

References: [a]Muller et al. (2011), [b] McCoy et al. (2017), and [c] Rose et al. (2020).

4.4   Discussion

4.4.1   The origin of molecular absorber in 3C 293

The NOEMA observations towards 3C 293 detected various molecular species, such as $H^{13}CN$, $H^{13}CO^+$, HCN, HCO^+, HNC, SiO, N_2H^+, C_2H, and ^{13}CO. The line centroids and line widths of different molecular species are similar, but a highly red-shifted $(200\,km\,s^{-1})$ faint absorption feature was only detected in the HCN and HCO^+ lines. This red-shifted feature corresponds to the weak CO absorption in the literature (Labiano et al. 2014). The red-shifted feature shows a narrow line width of a few tens of $km\,s^{-1}$, and thus it is more likely to represent an intervening molecular cloud, which is irrelevant to jet-ISM interaction. The most plausible origin of the main absorption feature is the circumnuclear disk in 3C 293. ALMA observations show a few kpc scale CO disk, surrounding the continuum radio jets. Deep CO absorption lines were detected at a red-shifted velocity of $50\,km\,s^{-1}$ with respect to the kinematic center of the CO disk (Labiano et al. 2014). This is consistent with the Doppler velocities of molecular absorption lines detected in our NOEMA observations. Fig. 4.6 shows the HST optical image of 3C 293 overlaid on the continuum radio jets. Clearly, a dust lane obscures the continuum radio jets. Therefore, we conclude that the molecular lines detected in the NOEMA observation have the same physical origin as the CO absorption, which is the tilted circumnuclear disk in 3C 293.
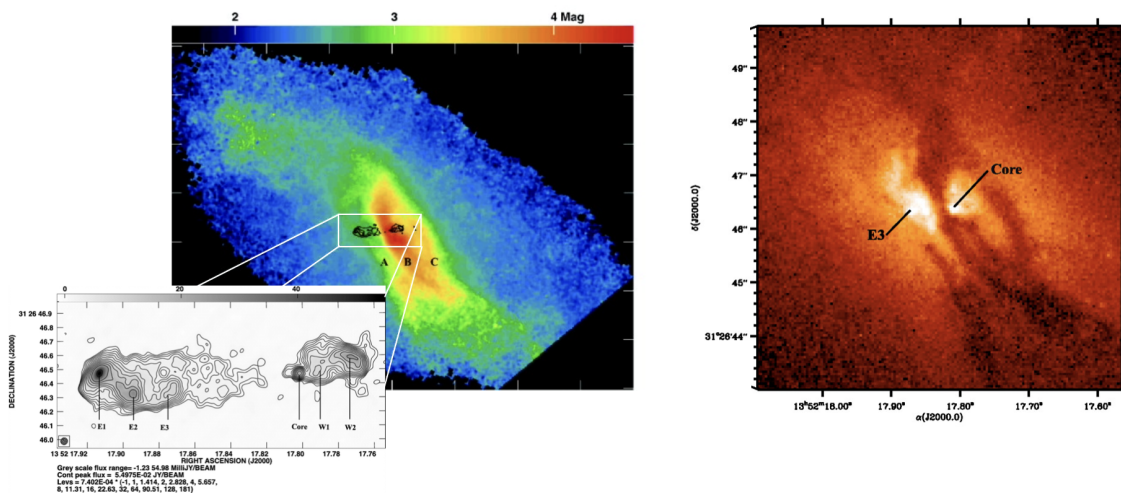

FIGURE 4.6: **Left**: R-H color map of 3C 293. The 5 GHz MERLIN continuum contours are overlaid on the map and zoomed at the left bottom corner. **Right**: HST R-band image of 3C 293. A dust lane obscures the radio core. Figure is taken from Martel et al. (1999); Floyd et al. (2006).

In addition to the comparison with the CO absorption, the physical properties constrained by absorption line ratios also hint at the origin of the molecular absorber. The kinematic temperature measured for the HCN and HNC absorption lines is

28 ± 2.5 K. This is lower than the typical kinetic temperature range observed in the Galactic center of the Milky way (50-100 K, Ao et al. 2013), and the temperature of warm Hydrogen gas observed in 3C 293 ($\sim$100 K) at infrared wavelengths (Ogle et al. 2010). A strong interaction between the radio jet and the molecular gas is thought to cause the warm H_2 emission in 3C 293, and thus the cold molecular gas (28 ± 2.5 K) detected in absorption seems not under the influence of the radio jet feedback. Abundance ratios of different molecular species also did not show a sign of AGN feedback, such as enhanced HCN and SiO abundances. The hyperfine C_2H lines following the relative line ratios expected in LTE condition indicate that the absorbing gas is not disturbed or excited by external shock or radiation. The low isotope ratio of $^{12}C/^{13}C$ (18-28) measured by HCN and HCO$^+$ isotopes indicates that the molecular absorber is not located in active star-forming regions, but resides at the aged region in the galactic center. Based on these measurements, we conclude that the molecular absorber in 3C 293 is located at the circumnuclear region at a moderate distance from the nucleus, where AGN feedback is insignificant.
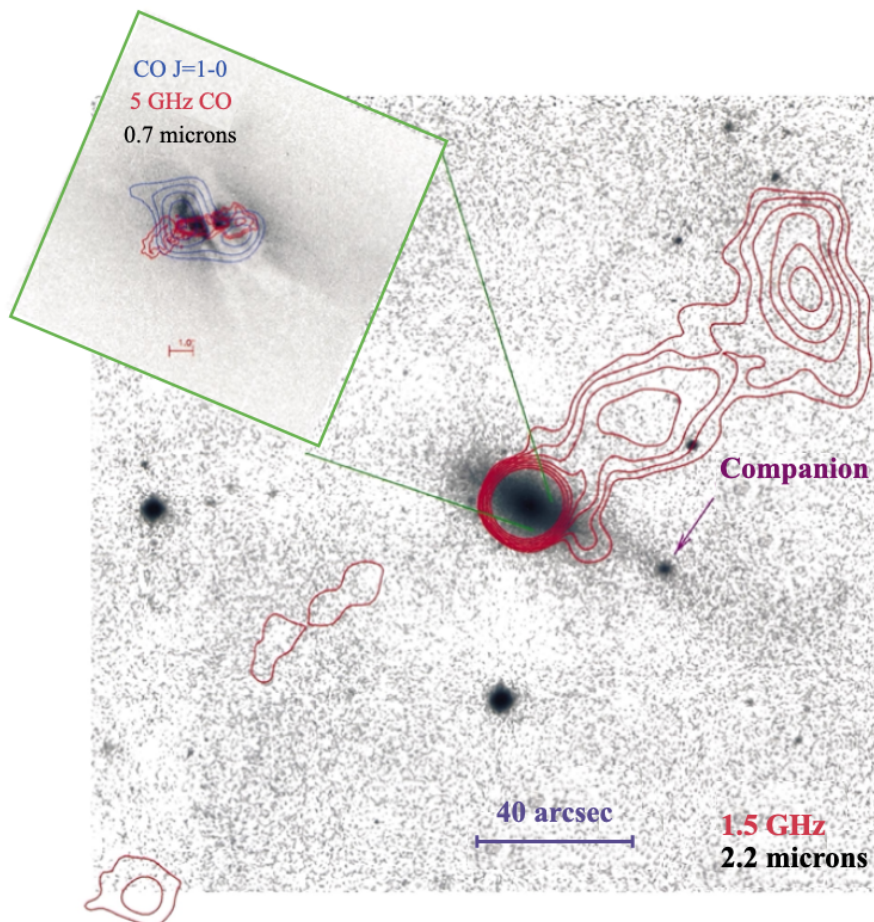

FIGURE 4.7: Radio continuum (1.5 GHz and 5 GHz) and spectral line (CO J=1-0) images are superposed on the near-infrared (2.17 um) image. The nearby galaxy is marked with the purple arrow. Figure is taken from Evans et al. (1999).

The substantial amount of circumnuclear gas in 3C 293 is supposed to be supplied by a recent gas-rich galaxy-galaxy merger or interaction (Machalski et al. 2016). The optical tail connecting 3C 293 and the nearby companion supports this scenario (see Fig. 4.7). The replenished gas is regarded as the main source of fueling materials, triggering AGN activity, but direct evidence is still pending (Evans et al. 1999; Martel et al. 1999). A more detailed diagnostic of the circumnuclear gas in 3C 293 is necessary to understand the origin of molecular gas and its role in forming the young radio jet in the core region.

4.4.2   Variability of absorption lines in 3C 293

3C 293 was observed with the IRAM 30-m telescope in Jul. 2019, and follow up NOMEA observations were conducted in Jan. 2020. Fig. 4.8 shows the comparison of the HCN, HCO⁺, and HNC J=1-0 absorption lines detected with the IRAM 30-m telescope and NOEMA. Two separated absorption peaks in the HCN and HNC lines are consistent at two epochs. The absorption depth of the HCN line is deeper in the NOEMA spectrum, but the HNC line shows similar depths. A drastic change is found in the HCO⁺ line. Line width is the same, but the absorption depth at velocity around $25 \, \text{km} \, \text{s}^{-1}$ is deeper by about $40 \, \%$ in the NOEMA spectrum. The significance of this change is above the 3σ limit. Such different line variabilities are puzzling. We can expect higher absorption depths in NOEMA observations due to its higher filling factor (i.e., small beam size) than for the 30-m IRAM telescope. However, the higher filling factor can not explain the distinct line variability found in different molecular species.

HCO⁺, HCN, and HNC molecules likely coexist in the same molecular clouds, but their relative abundance ratios can be different depending on their local environments. As the background continuum jet illuminates different parts of the intervening molecular clouds, inhomogeneous relative abundance ratios between HCO⁺ and HCN/HNC can cause distinct changes on their absorption line profile. Also, HCO⁺ absorption line is more sensitive than HCN and HNC due to its higher dipole moment (μ=3.90 D, 2.99 D, and μ=3.05 D for HCO⁺, HCN, and HNC, respectively). This can cause additional absorption features only seen in the HCO⁺ absorption line, but not in the HCN and HNC absorption lines. Indeed, two separate components found in the HCN and HNC lines are blended in the HCO⁺ line due to those additional absorption features. High-resolution observations resolving individual absorption features are required to clarify the physical mechanism responsible for the different variability between the HCO⁺ and HCN/HNC absorption lines in 3C 293.
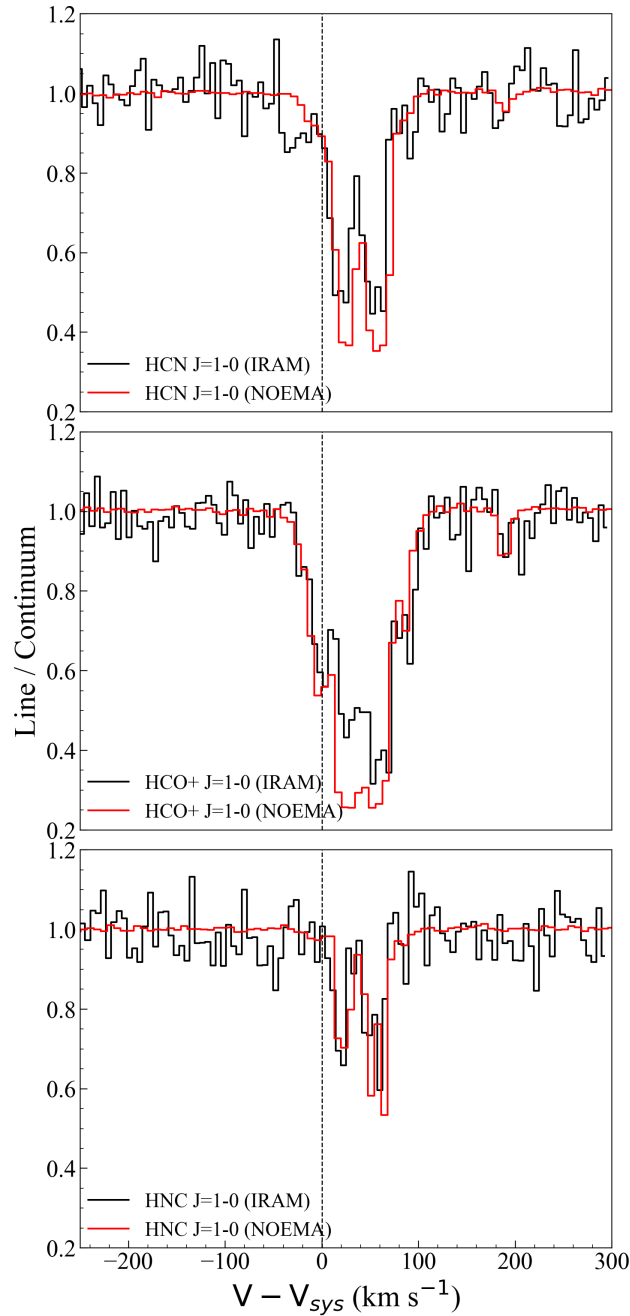
FIGURE 4.8: HCN, HCO⁺, and HNC J=1-0 spectra detected with the IRAM 30-m telescope and NOEMA. The time gap between two epochs is 6 months. The dotted vertical line marks the systemic velocity of 3C 293. The amplitude is normalized with the continuum flux.

4.4.3 The origin of molecular absorber in 4C 31.04

The previous spectral line VLBI observations towards 4C31.04 show the opacity distribution of the 21 cm H I absorption line (Conway & Blanco 1995; Struve & Conway 2012). The H I absorption line shows broad and narrow absorption features, which are separated by $200\,\mathrm{km\,s^{-1}}$ in the velocity axis. The broad absorption is dominant at the compact eastern jet, rather than at the faint and diffuse western jet (see Fig. 4.9).

The C_2H, HCN, HCO^+, HNC, and ^{13}CO absorption lines detected in 4C 31.04 show a broad absorption feature corresponding to the broad H I absorption, but the narrow absorption feature was not detected in molecular absorption lines. Our NOEMA observations did not spatially resolve the absorption features, but we speculate that the molecular absorbers are cospatial with the H I gas detected in absorption due to their similar Doppler velocities and line widths. The narrow absorption feature seen in the 21-cm H I line was not detected in molecular absorption lines. A steep spectral index makes the radio jet more faint and compact at 3 mm compared to the radio jet at 21 cm. Consequently, an illuminated region by the background continuum radio jet would be much smaller at 3 mm than 21 cm. This might result in the lack of a narrow absorption feature in molecular absorption lines at mm wavelengths.
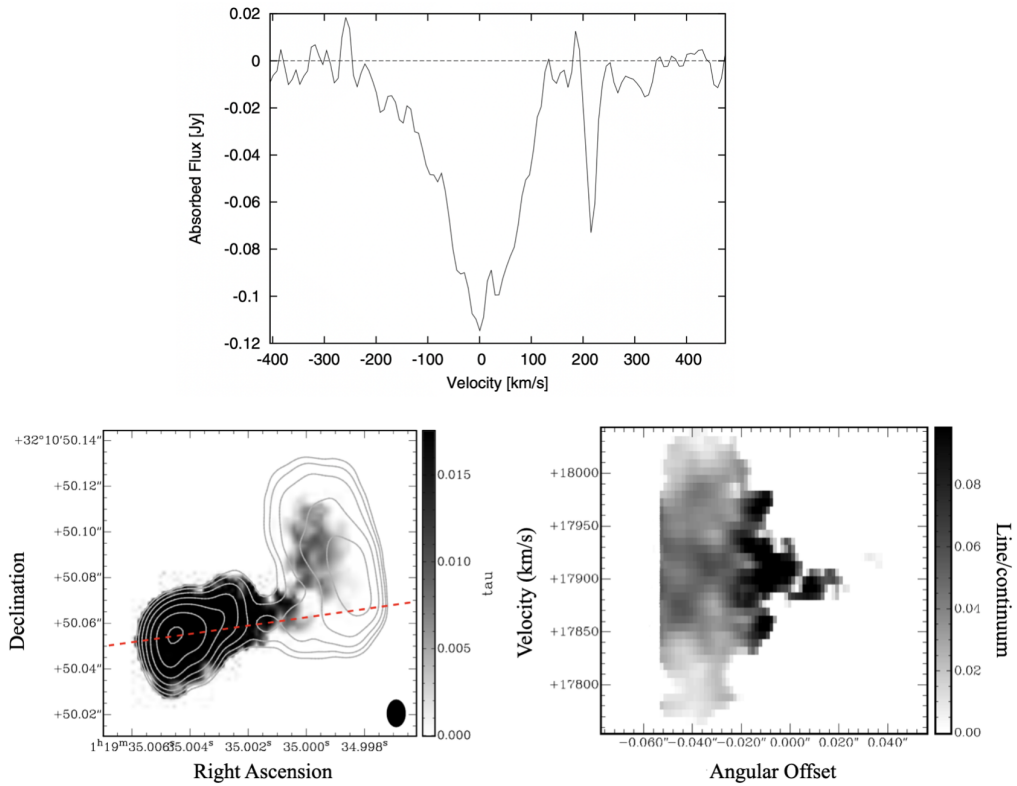
FIGURE 4.9: **Top**: Spectrum of H I absorption line in 4C 31.04. **Bottom left**: Opacity distribution of the H I absorption line on the continuum radio jet. The red dotted line indicates a slice for the position-velocity diagram. **Bottom right**: Position velocity diagram of the H I absorption along the sliced axis. The figure is taken from Struve & Conway (2012).

The line centroids of molecular absorption lines are blue-shifted by $\sim 150\,\mathrm{km\,s^{-1}}$ with respect to the systemic velocity of 4C 31.04. A simple interpretation is a molecular outflow driven by jet-ISM interaction. However, spatially resolved H_2 emission in the nuclear region of 4C 31.04 shows that the nuclear molecular disk is warped and has velocity offset of $150\,\mathrm{km\,s^{-1}}$ with respect to the systemic velocity of 4C 31.04 (Zovaro et al. 2019). This velocity offset is well consistent with the Doppler velocity of

our molecular absorption lines. Therefore, a proper interpretation of the blue-shifted absorption is a systemic velocity offset between the circumnuclear gas and the central engine rather than a jet-driven outflow. It is still unclear what causes such a velocity offset. Further high resolution observations are necessary to study the gas dynamics in the nuclear region of 4C31.04.

4.5   Conclusion

3C 293 and 4 C31.04 are known as young radio galaxies, harboring a dense ambient medium around their nuclei. We have detected in total 10 absorption lines in 3C 293, and 5 absorption lines in 4C31.04 at 3 mm. In particular, the SiO, C_2H, $H^{13}CN$, $H^{13}CO^+$, and N_2H^+ molecular lines are newly detected in absorption in 3C 293 without prominent molecular emission features. These results demonstrate the advantages of absorption line observations in detecting rare molecular species in the circumnuclear gas in radio AGN.

Line analysis using various molecular absorption features enabled us to constrain the physical and chemical properties of the obscuring gas and test the influence of the radio jet on its surroundings. Small Doppler shift velocities and narrow line widths of the molecular absorption lines in 3C 293 indicate that the molecular absorber is neither part of H I outflows driven by the radio jet nor part of the circumnuclear gas close to the central engine. Also, no strong signature of AGN feedback is seen by either HCN/HCO^+ abundance ratio (~1) or the kinetic temperature of the obscuring cloud ($28 \pm 2.5\,K$). Thus, we conclude that the kpc scale galactic disk is the source of molecular absorption lines detected in 3C 293. Absorption line observations towards 4C 31.04 detected a blue-shifted (~$150\,km\,s^{-1}$) feature. It is interpreted as the result of a systemic velocity offset between the circumnuclear disk and the central engine instead of a molecular outflow driven by radio jet feedback. The molecular absorber seems to be located in front of the eastern radio jet. The HCN/HCO^+ abundance ratio (~1) and kinetic temperature of the obscuring cloud ($38 \pm 2.5\,K$) indicates no imprint of the radio jet feedback on the obscuring gas.

Chapter 5

VLBI study of OH absorption lines in NGC 3079

Abstract This chapter presents a high-resolution study of the circumnuclear gas in the radio-quiet AGN NGC 3079. 6 GHz excited OH absorption lines were spatially resolved down to the sub-pc scale via spectral line VLBI observations using the European VLBI Network (EVN), including the Multi-Element Radio Linked Interferometer Network (e-MERLIN). The spatial distribution and kinematics of the OH absorber indicate a molecular outflow driven by a propagating radio jet component near the jet launching region. Ongoing jet-ISM interaction is also proved by the enhanced jet luminosity and significant jet deceleration. This study demonstrates how an infant radio jet interacts with the ambient medium and evolves in the environment of radio-quiet AGN NGC 3079.
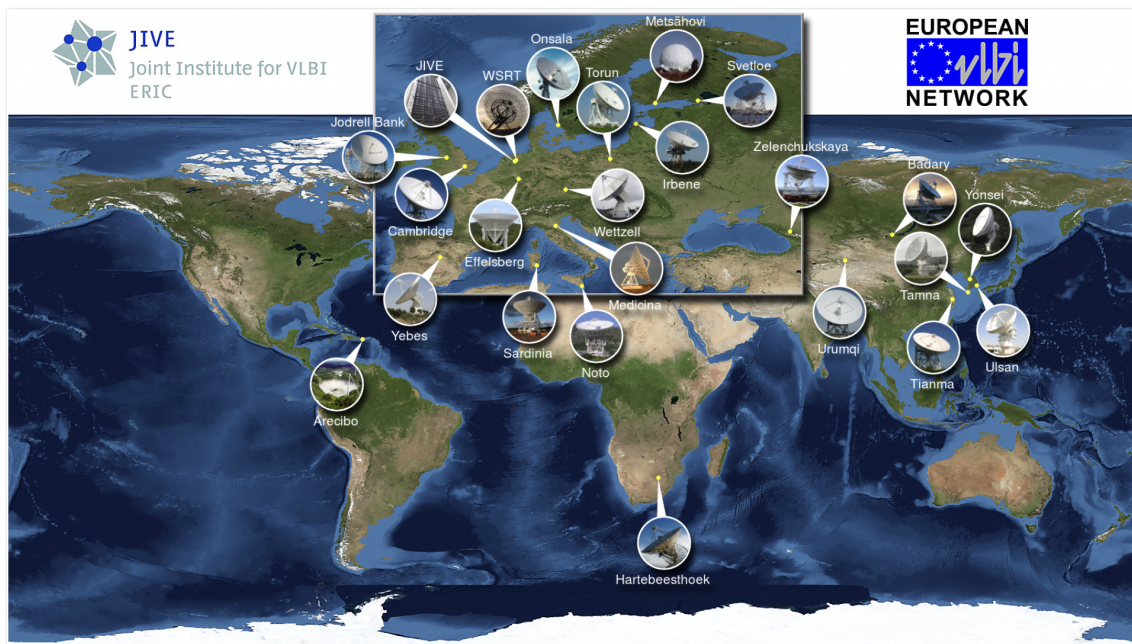
FIGURE 5.1: The location of EVN stations. It's operation is supported by the Joint Institute for VLBI ERIC (JIVE). (Credit: JIVE)

5.1 Introduction

An AGN jet outflow is capable of altering the physical properties of the surroundings, and this can affect galaxy formation and evolution. In radio-loud AGN, radio jets can heat the ambient medium up to large distances ($\sim$ up to a few hundred kpc), forming X-ray cavities. On the contrary, the signature of radio jet feedback in radio-quiet AGN is often confused with the energy output from ongoing star-formation or radiative AGN winds. In addition, the importance of jet feedback in radio-quiet AGN (e.g., Seyfert galaxies) has not been seriously considered due to the small scale ($\leq$ a few kpc) and low power of such jets. Interestingly, recent studies revealed jet-driven molecular outflows in some Seyfert galaxies from kpc to sub-kpc scales, but much is unknown about their initial conditions and development process (Oosterloo et al. 2017; Aalto et al. 2020). High-resolution VLBI observations which probe both the compact radio jet and its ambient medium via absorption provide a unique tool to study the circumnuclear gas interacting with the radio jet. The 1.4 GHz H I absorption has been used to probe jet-ISM interactions in radio AGN, but the angular resolution was limited by the low observing frequency (Schulz et al. 2018). Molecular absorption lines at higher frequencies offer better angular resolutions, and thus are promising to study the interaction between the radio jet and its ambient medium. This motivated us to image the OH absorption in the nuclear region and inner jet in the Seyfert galaxy NGC 3079.

NGC 3079 is a nearby Seyfert galaxy (16.0 Mpc, 1 mas=0.08 pc), exhibiting both AGN activity and active star formation. Kilo-parsec scale radio lobes and supper bubbles show energetic feedback from a radio jet or star-formation (Veilleux et al. 1994; Cecil et al. 2001; Sebastian et al. 2019). The SMBH mass was estimated to be $(2.39 \pm 0.06) \times 10^6 M_\odot$ (Davis et al. 2017). NGC 3079 is classified to be a radio-quiet AGN by its low radio loudness ($R \sim 3$, Taylor et al. 2005; Impellizzeri et al. 2008). Continuum cm-VLBI imaging revealed a parsec scale young radio jet and H_2O maser emission located in a disk (Middelberg et al. 2007; Kondratko et al. 2005). Blue-shifted molecular absorption lines hint at the presence of a molecular outflow, but solid evidence is pending due to lack of high-resolution observations towards the obscuring gas (Lin et al. 2016). The radio jet axis is not oriented perpendicular to the H_2O maser disk or circumnuclear disk and is also not aligned with the kpc-scale radio lobes. In the continuum, the individual jet components have sub-relativistic speeds or are stationary (Middelberg et al. 2007). 3D hydrodynamic simulations of the interaction of AGN jets with the surrounding ISM show that low-power and slow radio jets with inclined geometry with respect to the galactic disk are more efficiently coupled with the ISM (Mukherjee et al. 2016, 2018b). NGC 3079 harbours inclined and sub-relativistic radio jets in the nuclear region, and thus it is one of the ideal candidate
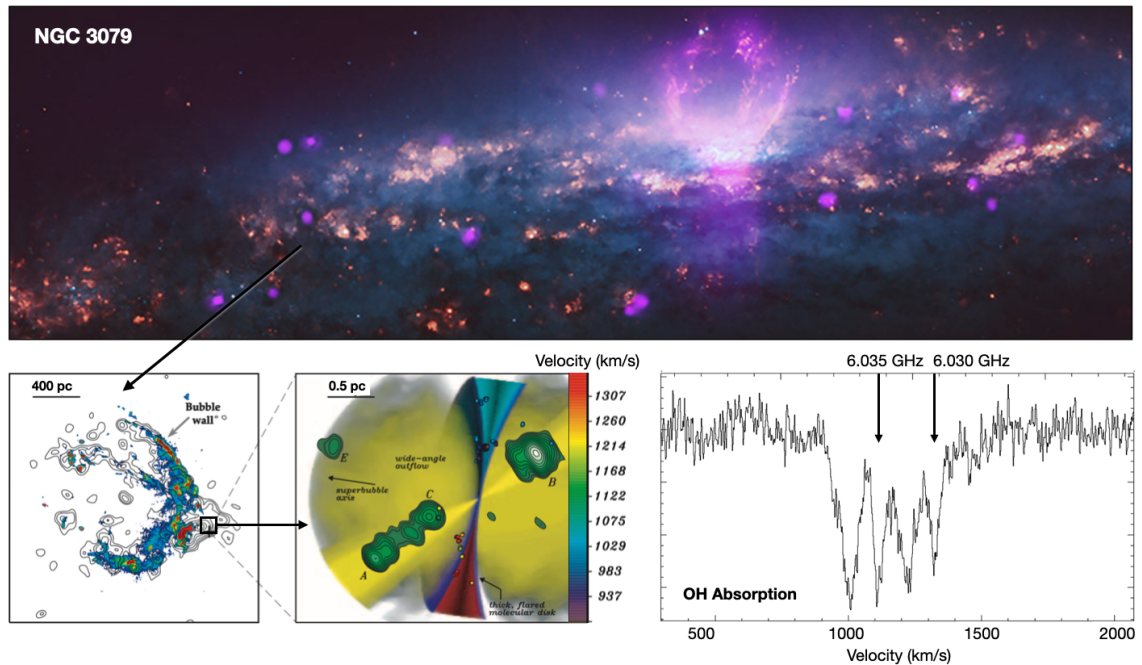
FIGURE 5.2: Multi-wavelength view of NGC 3079. **Top:** The super bubbles observed at optical and X-rays. **Bottom left:** Hα + [N II] (color contour) and X-ray (black contour) images of the super bubble. **Bottom middle**: Sub-parsec structure of the radio jets and H$_2$O maser disk. **Bottom right:** 6 GHz OH absorption lines detected against the continuum radio jet. Figures are taken from Li et al. (2019); Kondratko et al. (2005).

to study an initial phase of jet-ISM interaction. Previous spectral VLBI observations of the 1.6 GHz OH absorption line successfully demonstrated the feasibility of OH absorption imaging in the jet, but the angular resolution (FWHM~70 mas) was not sufficient to resolve the OH absorption features on the individual jet components (Hagiwara et al. 2004). Here our new study aims at imaging the 6 GHz OH absorption lines detected with the 100-m Efflesberg telescope via follow-up VLBI observations with an improved angular resolution by a factor of ~40 (FWHM$\simeq$ 1.6 mas). Such high angular resolution observations are suited to spatially resolve and locate the OH absorption and its possible connection with the propagating inner radio jet.

5.2 Observations and data reduction

The VLBI observations towards NGC 3079 were carried out at 6 GHz on Oct 31 2019 with the EVN, including e-Merlin. In total, twenty telescopes participated in the observations. Target transitions are 6.035 GHz and 6.030 GHz OH lines in absorption against the continuum jet of NGC 3079. Eight intermediate frequencies (IFs) were used, each with a bandwidth of 32 MHz, resulting in a total bandwidth of 256 MHz. Both right and left hand circular polarization feeds were used at most of the EVN stations. Only two IFs with a bandwidth of 64 MHz were used at the e-Merlin stations.

The data were correlated with the EVN software correlator at JIVE (SFXC) with 512 channels for each IF, which provides a velocity resolution of $3\,\mathrm{km\,s^{-1}}$ for the target transitions. The total observing time was about 8 hrs. The nearby calibrator 0954+556 was observed every 30 min for bandpass calibration. The data reduction was performed using the Astronomical Image Processing System (AIPS) software. The imaging and self-calibration were done with the Difmap package (Shepherd 1997). First, antenna gains and system temperatures (Tsys) were applied after flagging bad data points. Nominal Tsys values were assumed for the e-Merlin stations due to the lack of Tsys measurements. Then, we followed the standard calibration procedure for spectral-line data, which includes amplitude gain, instrumental delay, ionospheric delay, parallactic angle, band-pass shape, multi-band delay (i.e., fringe-fitting), and Doppler shift calibrations. For continuum imaging, the calibrated data were averaged over an integration time of 20 s and over frequency channels, avoiding sharp band-edges about 1 MHz for each IF. The averaged data were further processed in Difmap for phase and amplitude self-calibration and imaging using the CLEAN method. For 6 GHz OH absorption line imaging, several channels were averaged to increase imaging sensitivity by using the AIPS task UVLSF, which resulted in a spectral resolution of $13\,\mathrm{km\,s^{-1}}$. The established continuum model from Difmap was applied for the self-calibration of the spectral line data, and the clean process was iterated in each channel to detect the absorption features on the continuum images. All cleaned channel maps were combined by the AIPS task MCUBE. Detailed imaging process is described in §2.3.2.

5.3   Results

5.3.1   Continuum image

Fig 5.3 shows the 6 GHz continuum image of NGC 3079. The continuum image consists of four separated components A, B, C, and D. These components are consistent with the previous 5 GHz and 15 GHz images shown by Middelberg et al. (2007) (hereafter M07). The peak intensity is $46\,\mathrm{mJy\,beam^{-1}}$, and the rms noise level is $0.05\,\mathrm{mJy\,beam^{-1}}$. The high brightness temperatures of the continuum components $(1\text{-}51 \times 10^7 K)$ indicate that the continuum is synchrotron emission from the AGN jet. The recovered VLBI flux density in the EVN observations was 145.2 mJy, which is 67% of the total flux density (217.0 mJy) observed with 100-m Effelsberg telescope. The time gap between the Effelsberg and EVN observations is 10 months. The continuum components are aligned at a position angles 126.2° (A-C-B) and 87.3° (B-D). These position angles are consistent with the previous measurements in M07. The A

component shows extended structure with a narrow gap between the A and C components. The B component is known to be stationary from phase referencing VLBI observations in M07.
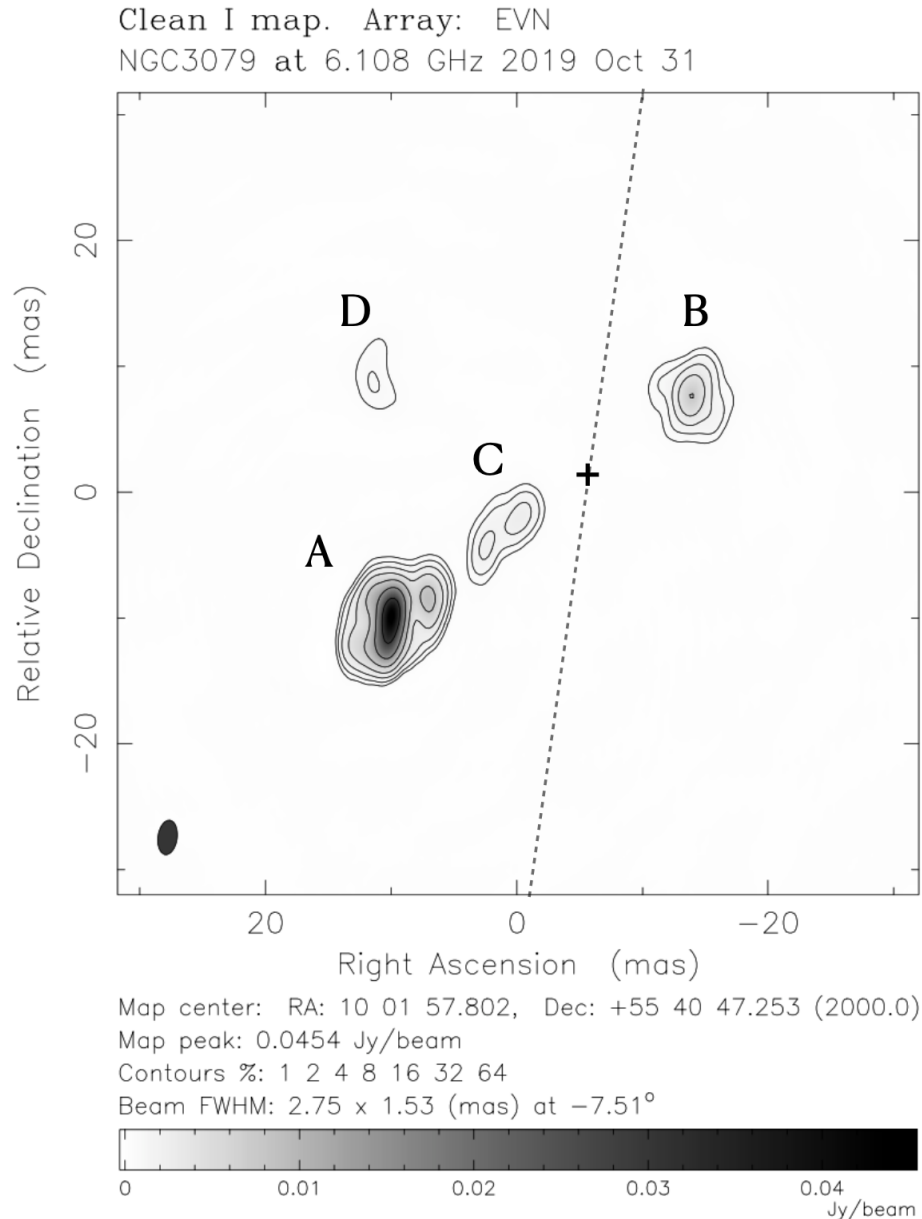

FIGURE 5.3: 6.0 GHz self-calibrated image of NGC 3079. Four separate continuum components are labeled with A, B, C, and D. The peak flux density is 46 mJy/beam, and the lowest contour is at 1% of the peak flux with subsequent contours increasing by factors of 2. The dashed line indicates the position angle of the H_2O maser disk (PA = 82°). The dynamical center of the H_2O maser disk is marked with a cross.

The B component was used as the reference position to measure the angular distance between the others. The angular distances between A-B (29.7 mas) and B-D (25.3 mas) were measured by Gaussian fittings on the intensity profiles along the

position angles, connecting two continuum components (see Fig. 5.4). Fig 5.5 shows the angular distance variation between A-B and B-D components measured at 5 GHz (2000-2006) in the literature and at 6 GHz in this study (Irwin & Seaquist 1988; Trotter et al. 1998; Sawada-Satoh et al. 2000; Kondratko et al. 2005; Middelberg et al. 2007). Different observing frequencies might affect the relative separation measurements due to the opacity shift effect caused by frequency dependent optical depths (Lobanov 1998). Comparing the relative component separations at 5 GHz, 15 GHz, and 22 GHz, the higher frequencies show a larger angular distance of about 0.40±0.35 and 0.60±0.35 mas between 5-15 GHz and 5-22 GHz, respectively (M07). Under the assumption of energy equipartition condition in the jet, the amount of opacity shift is given by Martí-Vidal et al. (2013).

$$\Delta\alpha = \Omega\left(\frac{1}{\nu_1} - \frac{1}{\nu_2}\right). \tag{5.1}$$

where the Ω is the normalized core shift, ν_1, and ν_2 are the observing frequencies. The estimated core shift between 5-6 GHz was less than 0.10 mas. Therefore, in the following we disregard it. This value was included in the positional error.

The increments of the angular distance are +1.83±0.3 mas (A-B) and -0.49±0.3 mas (B-D) over 15 years. The B and D components seem to be stationary or the D component is slightly moving towards the D component. The proper motion of the A component with respect to the B component is translated into 0.129±0.03 mas/yr (0.034 c). The apparent jet speed of the A component has been diminished by a factor of ~2.5 compared to the previous measurement between 1999-2002 (M07). Interestingly, the flux density of the A component has roughly doubled, but the flux densities of the B and D components were nearly constant.
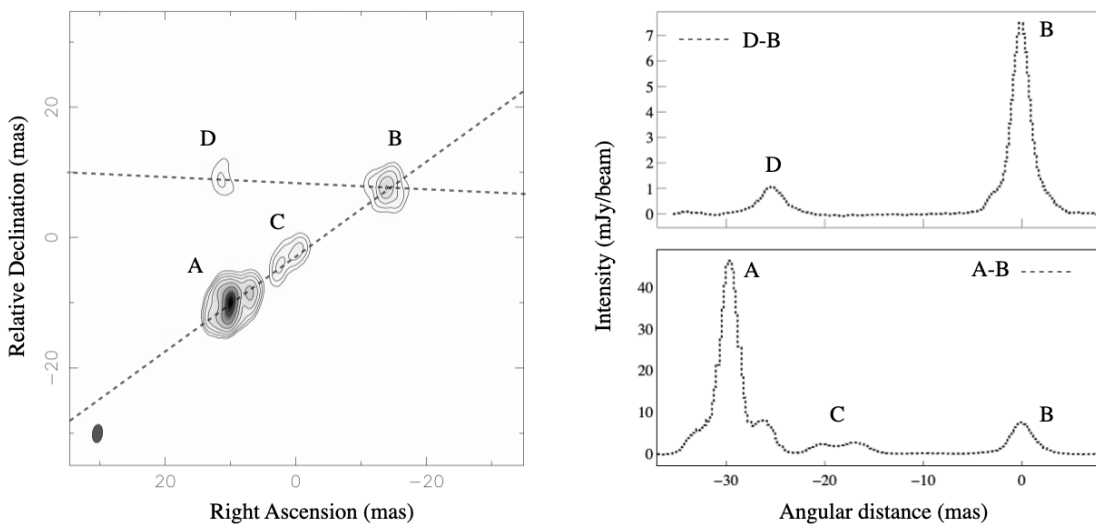

FIGURE 5.4: The location of the continuum components. **Left:** Slices along the B-D and B-A components. **Right**: Intensity profiles along the two slices.
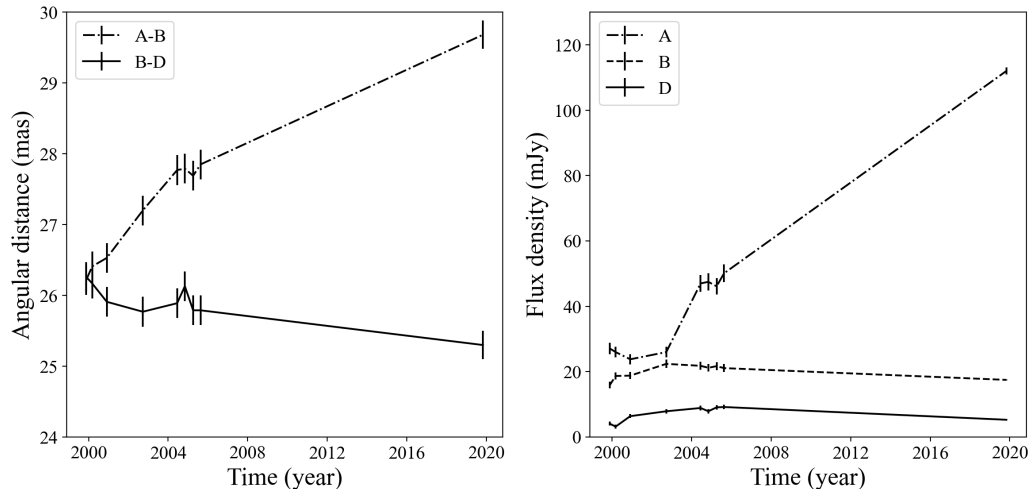
FIGURE 5.5: Variation of the continuum jets. **Left**: Variation of the angular distance between the continuum components. **Right**: Variation of the flux density of each continuum component.

5.3.2   6 GHz excited OH absorption lines

In the EVN observations we detected the 6.030 GHz and 6.035 GHz OH absorption lines. Fig 5.6 shows the comparison of the 6 GHz OH absorption lines detected with the 100-m Effelsberg telescope and the EVN. The amplitudes were normalized and the spectrum of the EVN observation was obtained towards the A component. 6 GHz OH absorption lines from the EVN observations reached up to 20.5 % of the continuum flux density, which is about two times deeper than the peak OH absorption (9.5 %) in the Effelsberg observations. The higher filling factor achieved by the small VLBI beam size of the EVN is a likely cause for the deeper OH absorption depths. The systemic velocity of NGC 3079 has been estimated from H I (1123 km s^{-1}), H$_2$O maser (1125 km s^{-1}), CO and HCN disk (1147 km s^{-1}) (Irwin & Seaquist 1991; Koda et al. 2002; Kondratko et al. 2005; Lin et al. 2016). In the following we adopt 1147 km s^{-1} as the systemic velocity of NGC 3079. From this we obtain Doppler velocities of the two OH absorption features at -29 km s^{-1} (hereafter C1) and -130 km s^{-1} (hereafter C2), respectively. The C2 component shows broader line widths and deeper absorption depths than C1. Fig 5.7 shows the spatial distribution of the two OH absorption features. The C2 (V$_{peak}$:-130 km s^{-1}) is located at the A component, and the C1 (V$_{peak}$:-29 km s^{-1}) was detected at the A and B components. If the absorbing gas is a part of the circumnuclear disk, red-shifted absorption is expected at the A component, considering the direction in which the disk rotates when being imaged by CO and HCN observations (Koda et al. 2002; Lin et al. 2016). Therefore, the most likely explanation of the blue-shifted OH absorption at the A component is a molecular outflow driven by the radio jet.
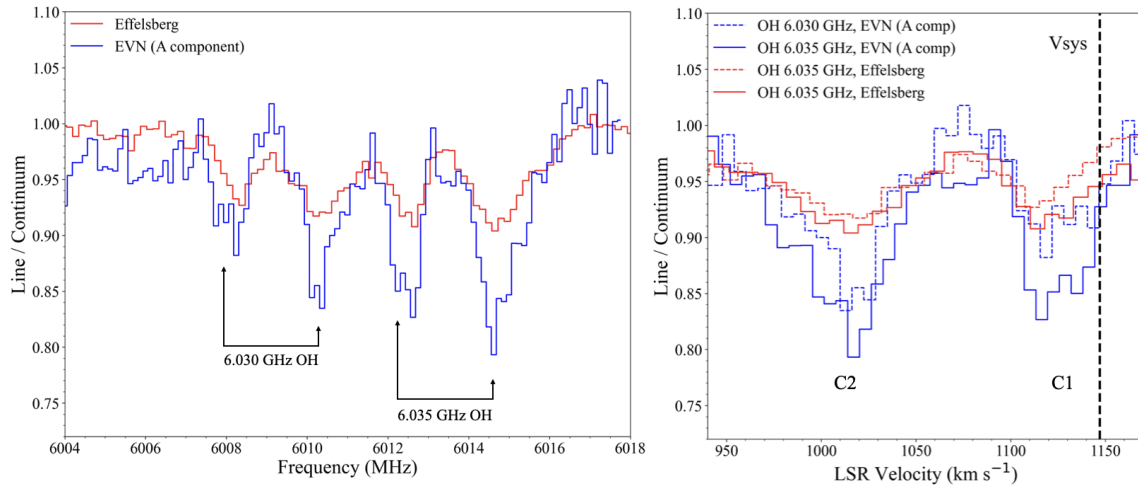
FIGURE 5.6: **Left**: Comparison of the 6 GHz OH absorption lines from the Effelsberg and the EVN observations in Dec 2018, and Oct 2019, respectively. The EVN spectrum was observed towards the A component. **Right**: 6.035 GHz and 6.030 GHz OH absorption lines aligned in the velocity axis. The systemic velocity of NGC 3079 (1147 km s^{-1}) is marked by a dotted line.
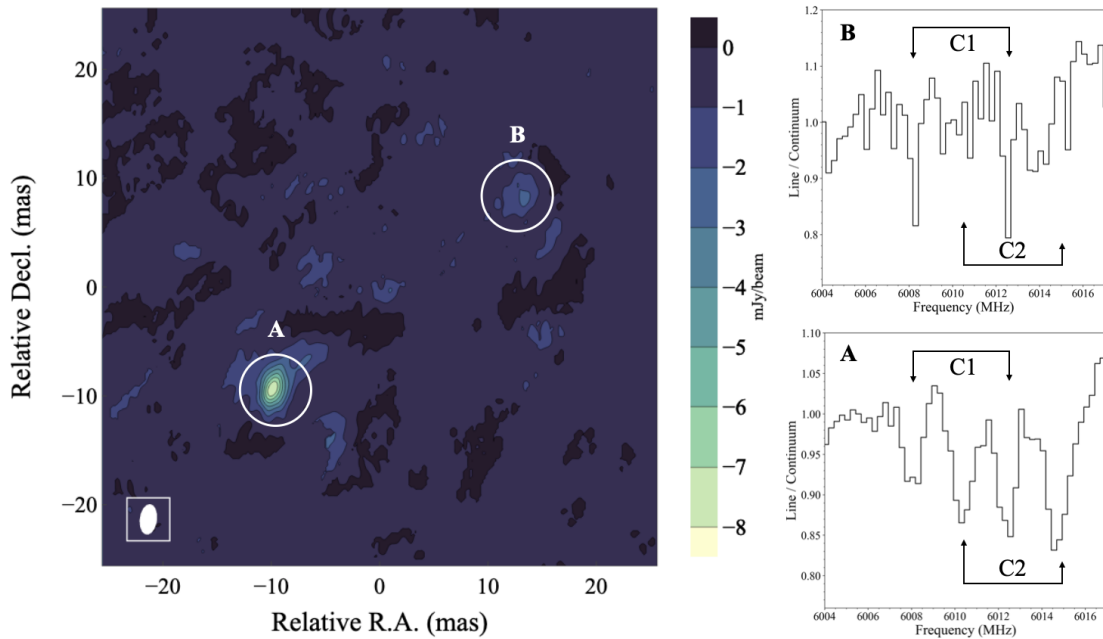

FIGURE 5.7: **Left**: Spatial distribution of the 6 GHz OH absorption lines. **Right**: Averaged OH absorption spectra towards the A and B continuum components. The C2 (V$_{peak}$:-130 km s^{-1}) and (V$_{peak}$:-29 km s^{-1}) are detected towards A, but only the C1 component appears towards the B.

5.4 Discussion

5.4.1 The jet evolution

Unlike the relativistic and extended radio jets in radio-loud AGN, the radio jets in Seyfert galaxies are commonly sub-relativistic, and only extend to within the few pc scales in VLBI observations (Ulvestad et al. 1999; Reynolds et al. 2009). Similar jet properties are found in NGC 3079. The nature of the different radio jet properties in radio-loud and quiet AGN have been controversially discussed (see §1.1.4). According to the jet launching mechanisms suggested by Blandford & Znajek (1977); Blandford & Payne (1982), the spin of the SMBH and the accumulated magnetic field strength are crucial factors, determining the jet power. On the other hand, environmental effects have been also invoked to explain the different radio jet properties (Norman & Miley 1984; Middelberg et al. 2004; Perucho et al. 2017). The time monitoring of the jet components in NGC 3079 may be regarded as an effect of jet-ISM interaction on the jet evolution. The decreasing proper motion of the A component indicates a deceleration of the jet as it propagates outwards. The proper motion of the A component was $0.32 \, \text{mas/yr}$ ($0.083 \, c$) between 2000-2006, but it decreased to $0.13 \, \text{mas/yr}$ ($0.034 \, c$) between 2006-2019. The presence of blue-shifted absorption on the propagating jet component, and an increasing radio luminosity suggests strong jet-ISM interactions. If such a strong jet-ISM interaction continues, the radio jet propagation may stop within a few pc scale. In this context, the stationary jet components B and D are likely to be already halted by jet-ISM interactions. The dynamical age estimated by the jet proper motion is less than $200 \, \text{yr}$. In this scenario, the Seyfert galaxy NGC 3079 resembles a Compact Symmetric Object (CSO) source, whose jet is young, and whose jet propagation is hindered by its interaction with a dense ISM in the nuclear region.

5.4.2 The origin of OH absorption

The $6 \, \text{GHz}$ OH absorption lines detected in EVN observations likely originate from different parts of the intervening ISM. Possible origins of the obscuring OH clouds are the galactic ISM distant from the central region, the circumnuclear disk, or an immediate ambient medium of the radio jet. The velocity dispersion (i.e., line width) of quiescent galactic clouds is only a few km s^{-1}, and the column density is nearly homogeneous on scales of a few pc. The broad line width of the OH absorption (40-$80 \, \text{km s}^{-1}$) and notable variations of the absorption depths within the sub-pc scale jet components are inconsistent with absorption from the galactic ISM. Accumulated absorption over several ISM clouds at different line of sight velocities can form a broad line width, but this is unlikely in NGC 3079, due to the small beam size of

the EVN observations (0.25 pc) and the presence of a single broad absorption profile. Thus, we ruled out the galactic ISM as the origin of the OH absorption.

OH absorption near the systemic velocity (C1) can be explained by the absorption from the circumnuclear disk, but the blue-shifted OH absorption (C2) towards the A component is inconsistent with the rotation velocity of the circumnuclear disk. One of the plausible explanations for the blue-shifted absorption at the A component is a molecular outflow driven by jet-ISM interactions. This scenario is supported by several observational features. We find that the deceleration of the jet component is associated with an increase of its flux density. Jet-ISM interaction causes jet deceleration via momentum transfer from jet to the interacting medium. The compressed ambient medium by jet-ISM interaction increases the external pressure of the jet, which can result in a variation of the jet luminosity (Middelberg et al. 2007). The broader line width and higher column density of the blue-shifted OH absorption (C2) with respect to the non-outflow absorption (C1) manifests an increased local column density and velocity dispersion of the jet-driven outflows. Blue-shifted SiO and $H^{13}CN$ absorption lines detected at 3 mm from NOEMA observations extend up to 350 km s^{-1} with respect to the systemic velocity, which is also supporting the presence of molecular outflows (Lin et al. 2016).

5.4.3   Radio jet feedback

Observational studies using the ionized gas (O [III]) have shown prevalent AGN outflows in Seyfert galaxies, but the main driving force of the outflows has been controversially discussed (Harrison et al. 2014; Crenshaw et al. 2010; Woo et al. 2016). The correlation between the velocity dispersion of the nuclear ionized gas and the radio luminosity points towards jet driven outflows (Mullaney et al. 2013; Bae & Woo 2014). In addition, the collimated molecular outflows in the nuclear regions of Seyfert galaxies provide evidence for jet-driven outflows (Aalto et al. 2020; Fernández-Ontiveros et al. 2020b). On the other hand, Woo et al. (2016) claimed that the outflows in Seyfert galaxies are related to the accretion luminosity rather than the radio activity. In most previous studies, the radio luminosity has been used as the proxy of the radio activity in AGN, but the kinetic power of the radio jet can be a few orders of magnitudes higher than its radiative power. In addition, the correlation between the radio luminosity and jet power is not straightforward (Godfrey & Shabala 2016). Thus, studies of radio jet feedback solely based on radio luminosity might have large uncertainties.

The circumnuclear OH gas revealed by the EVN observations shows the onset of radio jet feedback in the Seyfert galaxy NGC 3079. The inclined young (≤ 200 yr) radio jet is rapidly decelerating within a few pc around the jet launching region by jet-ISM interaction. The kinematics of the OH absorption lines indicate molecular

outflows (V_{peak}:130 km s^{-1}) on the propagating jet component. The dynamical mass of the circumnuclear HCN disk was estimated to be $10^{9.3} M_{\odot}$ (Lin et al. 2016). The escape velocity at the radius of the HCN disk (112 pc) is 391 km s^{-1}. If the jet component A is confined within a few pc scales from the jet launching region, the jet-driven outflow found in OH absorption (130 km s^{-1}) is incapable of wiping out the circumnuclear gas. However, a bright ionized emission around 250 pc from the jet-launching region is well aligned with the radio jet axis (Cecil et al. 2001). We speculate that the previous episodic radio jet activities in NGC 3079 might affect its surroundings over the few hundred pc scale. Although the young radio jet component A is incapable of driving a strong outflow, it can facilitate AGN fueling by removing angular momentum from the rotating gas. Indeed, the molecular outflow propagates towards an opposite direction of the rotating circumnuclear disk. Consequently, the molecular outflow might help to disturb the circumnuclear disk, and increase its accretion rate. If the enhanced AGN activity is powerful enough to expel the circumnuclear gas, it will slow down the accretion rate and AGN activity. In this process, the relative geometry of radio jet and circumnuclear disk is an important factor, determining the significance of jet-ISM interaction (Mukherjee et al. 2018a).

5.5   Conclusion

The circumnuclear gas in NGC 3079 has been imaged using excited OH absorption lines towards the continuum radio jets. Two absorption features were detected at 6030 GHz and 6035 GHz. Comparison of the OH absorption depths with single-dish observations indicates a compact OH absorber, obscuring only a part of the continuum radio jet. The blue-shifted absorption is located only in front of the propagating jet component, whereas absorption around the systemic velocity was detected in both approaching and receding jets. The blue-shifted absorption is interpreted as a jet-driven outflow, considering the kinematics of the circumnuclear disk. The molecular outflow is incapable of wiping out the circumnuclear gas, but likely to facilitate AGN fueling by disrupting the circumnuclear gas. In combination with previous VLBI data, our analysis reveals a clear signature of jet deceleration combined with an increasing radio luminosity. These results demonstrate the implication of jet-ISM interaction on the jet evolution in NGC 3079.

Chapter 6

VLBI study of OH absorption lines in Cygnus A and NGC 4261

Abstract This chapter presents a high-resolution VLBI study of the circumnuclear gas in the radio-loud AGN Cygnus A and NGC 4261. OH gas surrounding the radio jets was searched in absorption with the High Sensitivity Array (HSA) and the EVN to test the Unified scheme of AGN and to check different fueling environments in a high and a low luminosity radio AGN. As a result, 13 GHz OH absorption lines were detected in Cygnus A. The spatially resolved OH absorbers in Cygnus A suggest molecular gas in front of the inner cm-VLBI jet, but not in front of the counter-jet. This indicates that the gas is not associated with the putative torus. In spite of clear OH absorption detections in previous single-dish observations, surprisingly no absorption feature was detected in NGC 4261. The nature of the molecular absorbers and nuclear environments of Cygnus A and NGC 4261 are discussed.
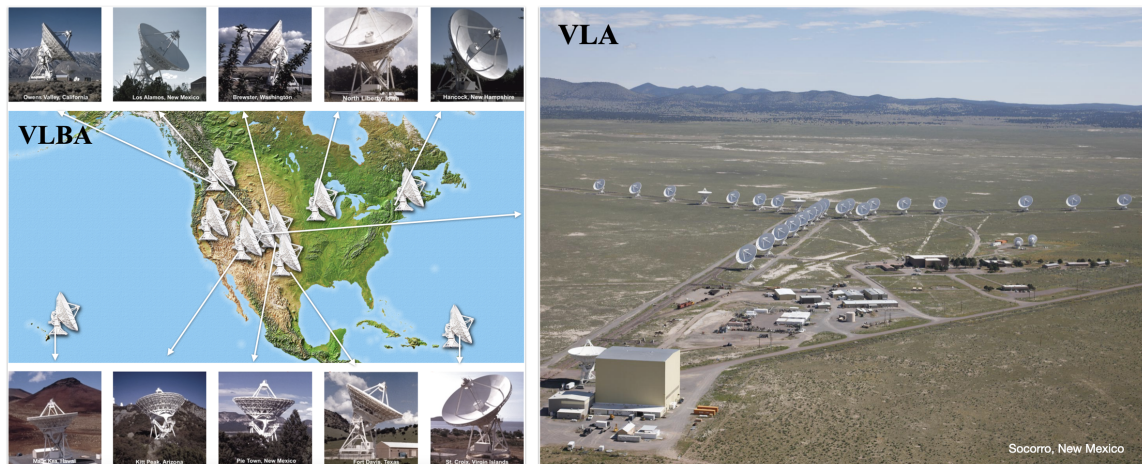
FIGURE 6.1: **Left**: The location of the VLBA stations. **Right**: The VLA located in New Mexico. The VLBA and VLA are operated by the National Radio Astronomy Observatory (NRAO). The phased VLA is a part of the High Sensitivity Array (HSA). Image credit: NRAO

6.1 Introduction

Extended powerful radio jets are found in AGN, which are hosted by massive elliptical galaxies. These sources are termed as radio-loud AGN, and they are classified into (Low-Excitation Radio Galaxies) LERG and (High-Excitation Radio Galaxies) HERG based on the accretion luminosity (see §1.2). Their physical connection with the large scale radio jet morphology (e.g., edge-darkened FR I type and edge-brightened FR II type) has been controversially discussed (Celotti et al. 1997; Ghisellini et al. 2014; Miraghaei & Best 2017; Macconi et al. 2020). For example, several studies argue that the jet morphology is intrinsically determined by different fueling flow properties in HERG (led by cold and condensed gas) and LERG (led by hot intergalactic gas) (Best & Heckman 2012; Heckman & Best 2014; Yuan & Narayan 2014) and by the parameters of the central black hole (Baum et al. 1995). On the contrary, studies focused on extrinsic factors attribute the radio jet dichotomy to different environments, such as jet-ISM interactions in a dense environment (Kaiser & Best 2007; Gendre et al. 2010, 2013; Wykes et al. 2015), magnetic instabilities (Tchekhovskoy & Bromberg 2016; Porth & Komissarov 2015), or Kelvin–Helmholtz instabilities (Perucho et al. 2010). However, the observational constraints are still too sparse to discriminate between the most plausible physical mechanisms responsible for the phenomenology in radio-loud AGN. The fueling material and matter content around the accretion disk is key to discern between distinct accretion flows in HERG and LERG. To do so, it implicitly requires high-resolution observations that can resolve the nuclear region at least down to the few pc scale.

High-resolution VLBI studies using the jet expansion profiles suggest different accretion environments near the accretion disk between HERG and LERG. HERG tend to have a thicker jet width and a larger transition distance of the jet shape compared to LERG. The surrounding environment formed by disk winds has been invoked as the possible causes of the different jet properties seen in HERG and LERG (Boccardi et al. 2021). A more direct observational probe for the ambient medium of the jet launching region can be obtained from spectral line VLBI observations towards molecular absorption lines against the bright radio jet. Spatially resolved molecular absorption lines can reveal the density, kinematics, temperature of the ambient gas along the jet, and thus can provide hints to the different accretion properties in HERG and LERG. Cygnus A and NGC 4261 are two representative nearby HERG and LERG radio AGN, respectively, and atomic or molecular absorption lines have been detected towards the radio jet (Impellizzeri 2008; Struve & Conway 2010), but their fine structure around the jet-launching region has not yet been revealed. This motivated us to conduct new high-sensitive VLBI observations of the excited OH absorption lines using the High-Sensitivity Array (HSA) and EVN.
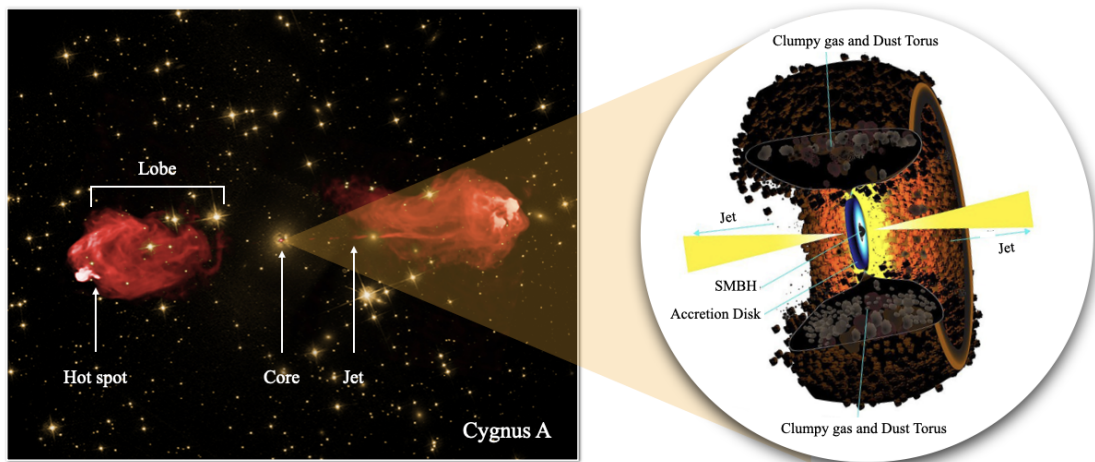
FIGURE 6.2: **Left**: The main structural components in a FR type II radio jet. **Right**: Sketch of the nuclear region of Cygnus A, as suggested in the Unified model of AGN. A toroidal dusty structure obscures the central engine. Image credit: NRAO

Cygnus A is a powerful (z=0.056, scale: ~1.07 pc mas^{-1}, (Stockton et al. 1994)) FR II radio galaxy, which is presumably undergoing a minor merger event (Canalizo et al. 2003). Fig 6.2 shows two edge-brightened radio lobes, and its putative nuclear structure as predicted from the Unified scheme of AGN (Antonucci 1993). Cygnus A is also a representative HERG (L_{bol} ~ 4× 10^{46} erg s^{-1} (Privon et al. 2012). For the estimated SMBH mass of $(2.5 \pm 0.7) \times 10^9 M_\odot$ (Tadhunter et al. 2003), the Eddington ratio is $\lambda_{Edd} = L_{bol}/L_{Edd} \geq 0.01$. The kinetic power of the jet estimated by the observed X-ray cocoon is an order of magnitude higher than the accretion luminosity (Ito et al. 2008). The nuclear region of Cygnus A is supposed to be highly obscured by some ambient gas. A buried BLR is detected from polarized optical emission (Ogle et al. 1997). The X-ray absorbing column density of N_H (1-4) × 10^{23} cm^{-2} also indicates a buried quasar in Cygnus A (Reynolds et al. 2015). The Spectral Energy Distribution (SED) model based on the mid-infrared observations suggests circumnuclear dust extending to 130 pc from the central engine (Privon et al. 2012). This putative obscuring structure is seen as diffuse extended radio continuum emission (Carilli et al. 2019). Further evidence for a compact absorber, which covers the inner counter-jet, but not the inner jet, comes from the frequency dependence of the jet-to-counter-jet ratio (Krichbaum et al. 1998; Bach 2004; Boccardi et al. 2016). Searches by Conway & Blanco (1995) failed to detect molecular absorption at 18-cm (OH) and at 6-cm (H_2CO). The lack of CO J=1-0 and J=2-1 absorption challenged the torus model for Cygnus A. However, the detection of CO+ absorption at 3-mm by Fuente et al. (2000) suggests radiatively excited molecular gas in the nuclear region. Previous absorption line experiments at 21-cm revealed two red-shifted absorption (narrow and broad) components in front of the VLBI core and counter-jet. However,

the physical connection between narrow and broad H I absorption components are unclear due to a large beam size (25 mas ~ 26 pc) (Struve & Conway 2010).
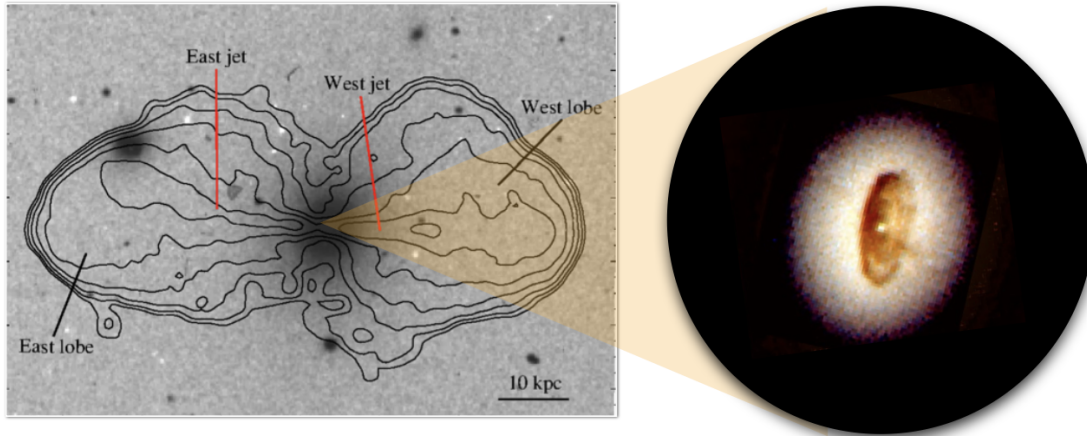

FIGURE 6.3: **Left**: Large scale morphology of a FR type I radio jet. **Right**: Obscuring structure in the nuclear region of NGC 4261 observed with the Hubble space telescope. The figures are taken from Kolokythas et al. (2015); Jaffe et al. (1993).

NGC 4261 is a nearby (z=0.00731, scale: ~0.15 pc mas^{-1}) FR I radio galaxy. Fig 6.3 shows its two edge-darkened radio lobes, and an optical HST image, unveiling a 100 pc scale disk of gas and dust in the nuclear region. The SMBH mass was estimated to be $(1.7 \pm 0.2) \times 10^9 M_\odot$ (Boizelle et al. 2021). NGC 4261 is a representative LERG with a low bolometric luminosity ($L_{bol} \sim 4 \times 10^{41}$ erg s^{-1} and Eddington ratio (λ_{Edd} = $L_{bol}/L_{Edd} \sim \sim 1 \times 10^{-5}$)(Eracleous et al. 2010). The X-ray observations indicate a heavily obscured nuclear region ($N_H \sim 8 \times 10^{23}$ cm^{-2}) (Zezas et al. 2005). NGC 4261 is one of the prime candidates to investigate in more detail the spatial structure of the circumnuclear disk or torus. ALMA observations show a circumnuclear disk with an inclination angle of 65°, from which a total gas mass of $1.12 \times 10^7 M_\odot$(Boizelle et al. 2021) is estimated. Previous VLBI observations indicate strong evidence for obscuring matter in front of the VLBI core and inner jet on sub-pc scales. Multi-frequency VLBI maps show a two-sided jet with a sub-pc scale emission gap between jet and counter-jet (Haga et al. 2015). The presence of significant free-free absorption from ionized gas in front of the jet is thought to cause this emission gap (Jones et al. 2001). Various absorption lines (H I, OH, and CO) have been detected at both cm- and mm-wavelengths (Jaffe & McNamara 1994; Impellizzeri 2008). The broad line width in OH absorption (up to 400 km s^{-1}) suggests that the obscuring gas is under strong gravitational influence from the SMBH or comes from a very turbulent environment. At 5 cm, the jet, core and counter-jet are bright enough to image the previously detected OH absorption by Impellizzeri (2008) via spectral line VLBI observations. A 22 GHz H$_2$O maser line was also detected in NGC 4261, but its spatial distribution

and physical connection with the OH absorption has not yet been studied (Wagner 2013).

6.2 VLBI observations

VLBI observations towards Cygnus A were carried out on 14 Dec. 2019 and 14 Feb. 2020 with the High Sensitive Array (HSA), including the Very Long Baseline Array (VLBA), phased Very Large Array (VLA), and 100 m Effelsberg telescope. The total observing time was about 14 hr in each session. Two nearby calibrators 2015+371 and 2005+403 were observed every 30 min for accurate bandpass calibration and fringe detection. The cycle time for the phase VLA was about 20 min. Target transitions were the OH $^2\Pi_{3/2}$ $J = 7/2$ $F = 3 - 3$ and $^2\Pi_{3/2}$ $J = 7/2$ $F = 4 - 4$ lines at 13.434 GHz and 13.441 GHz, respectively. The sky frequencies of the OH transitions were tuned by referring to the sky frequency of the 21 cm H I absorption line detected in Cygnus A (Struve & Conway 2010). The observations were made in dual polarization mode using four IFs, having 128 MHz bandwidth per IF. This resulted in a data rate of 2048 Mbps. The data were correlated with the VLBA-DiFX correlator at the National Radio Astronomy Observatory (NRAO) in Socorro, New Mexico. Correlation with 2048 channels per IF yielded a velocity resolution of 1.4 km s^{-1} for the target transitions.

VLBI observations towards NGC 4261 were carried out on 11 Jul. 2019 and 20 Oct. 2019 with the HSA (VLBA+Eff, at 13 GHz) and EVN (at 6 GHz), respectively. Target transitions were the OH $^2\Pi_{3/2}$ $J = 7/2$ $F = 3 - 3$, $^2\Pi_{3/2}$ $J = 7/2$ $F = 4 - 4$, $^2\Pi_{3/2}$ $J = 5/2$ $F = 2 - 2$, and $^2\Pi_{3/2}$ $J = 5/2$ $F = 3 - 3$ lines at 13.434, 13.441, 6.030 and 6.035 GHz, respectively. In the HSA observations, four IFs with a bandwidth of 128 MHz covered 256 MHz in dual polarization mode. The total observing time was 7 hr. 3C 273 was observed as a fringe finder and bandpass calibrator. The HSA data were correlated by the VLBA-DiFX correlator at the NRAO with 2048 channels per IF, resulting in a velocity resolution of 1.4 km s^{-1} for the target transition. In the EVN observations, 16 IFs were used with a bandwidth of 32 MHz per IF, resulting in a total bandwidth of 256 MHz in dual polarization mode. Only two IFs were used with a bandwidth of 64 MHz for e-Merlin stations. The data were correlated with the EVN Software Correlator (SFXC) at the Joint Institute for VLBI ERIC (JIVE) with 512 channels per IF, yielding a velocity resolution of 6 km s^{-1} for the target transition. The total observing time was 8 hr. 1156+295 and 3C 273 were observed for bandpass calibration and fringe detection.
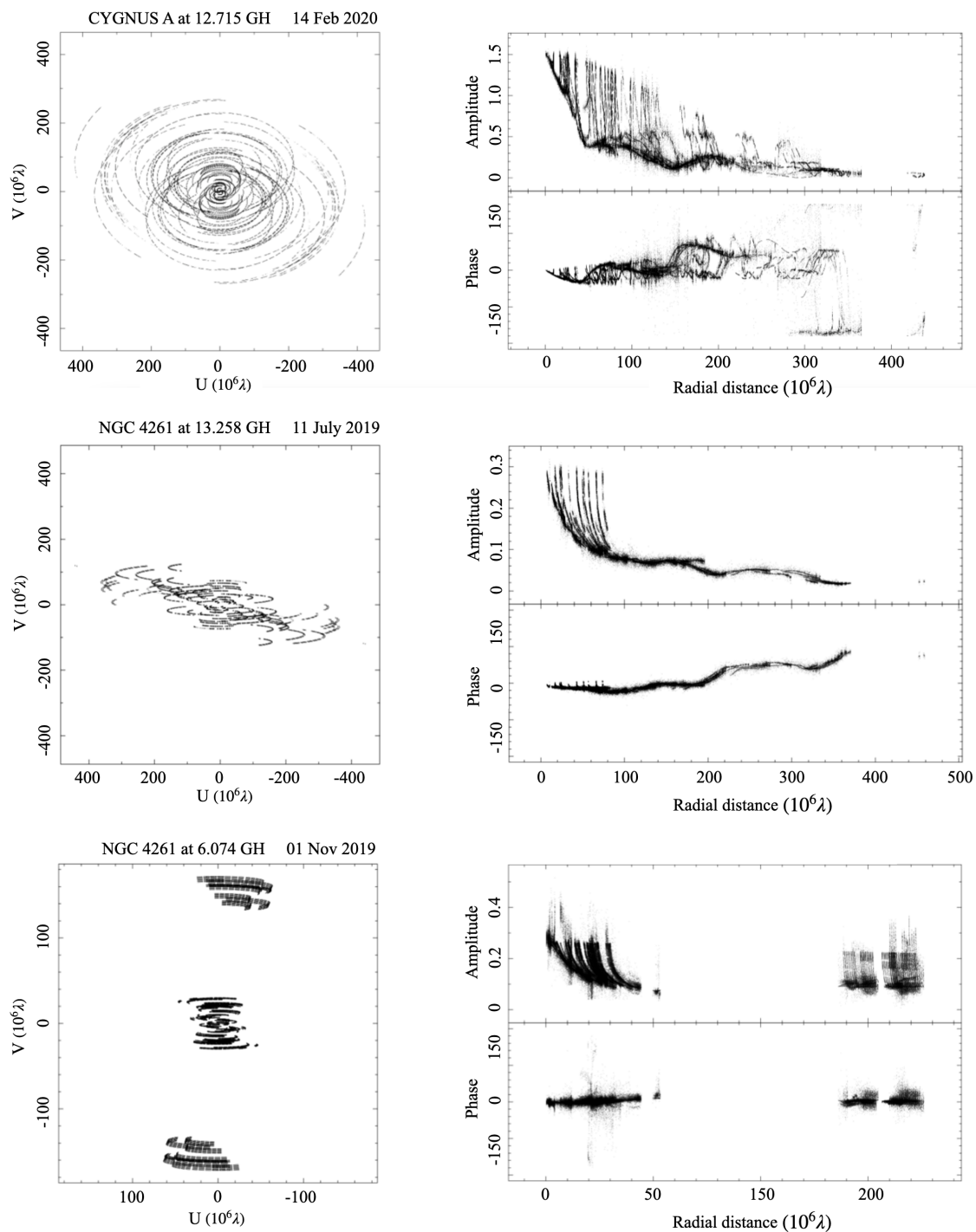
FIGURE 6.4: **Left**: UV coverage of the VLBI observations. Target sources and observing frequencies are labeled on the top. **Right**: Visibility amplitudes and phases over the range of UV distance.

6.3 Data reduction

Data reduction was implemented in two steps. First, a high fidelity continuum image was established using the averaged UV data over all IFs. Second, the continuum image was subtracted from the spectral channels, where absorption features are present or expected. The absorption components were cleaned in the residual map. In the Following, I describe the detailed process for imaging continuum and absorption images.

6.3.1 Continuum imaging

For continuum imaging, we implemented the standard data reduction process using tasks and procedures in AIPS. A priory amplitude calibration was made with the system temperatures and gain curves provided from the VLBI stations. Abnormal system temperatures were flagged or replaced with the normal values in nearby IFs or scans. Earth coordinate parameter, ionospheric delay, and parallactic angle corrections were made with the procedures VLBAUTIL. Different instrumental delays or phases among IFs were calibrated with fringe fitting on the bright calibrator. To calibrate the fluctuations of the delay and phase during the observations, global fringe fitting on the target source was implemented. We iterated this process several times to find the optimal parameters and the best reference antenna. For bandpass calibration, either total power or cross power spectra of the nearby bright calibrator were used. To increase the sensitivity of the visibility samples, the calibrated data was averaged with a time interval of 20 s and over IFs, avoiding sharp band-edges. Then, the UV data were extracted in uvfits format for imaging. Based on the Hybrid mapping method, clean and self-calibration were performed repetitively in Difmap. This allowed us to establish the continuum images with high dynamic range and fidelity.

6.3.2 Absorption line imaging

First, Doppler corrections for the target transitions were performed. We adopt z=0.056 (Struve & Conway 2010) to calculate the systemic velocity of Cygnus A. The heliocentric reference frame was used for the velocity calculations. The crucial part in absorption line imaging is to subtract the continuum data from the spectral data, which contain the absorption lines against the continuum emission. The continuum subtraction can be done either in the Fourier space (i.e., visibility based) or image domain (i.e., pixel based). The continuum subtraction in Fourier space is reliable when the absorption depth is deep enough for linear fitting. In case of the HSA observation data towards Cygnus A, the absorption depths of OH lines were too low to implement the continuum subtraction in Fourier space. Also, the existence of two

adjacent OH lines was not suitable for applying the linear fitting method. Thus, the continuum subtraction was made in the image domain. The spectral line data were self-calibrated with the established continuum model in continuum imaging, and the absorption features were cleaned in the residual map with the same imaging parameters and clean windows used in the continuum imaging. The spectral line sensitivity was not enough to obtain an individual channel map for the OH absorption line. Therefore, we integrated the whole channels over 13.434 GHz and 13.441 GHz OH lines, and imaged the total intensity map of the OH absorption. These absorption images were normalized by the continuum images to measure the optical depths.

6.4 Results

6.4.1 Continuum images of Cygnus A and NGC 4261

Fig. 6.5 and 6.6 show the continuum images and intensity profiles along the jet axis. The peak flux densities, rms levels, and beam sizes are listed in Table. 6.1. The 13 GHz continuum images of Cygnus A are obtained with a time gap of two months. A two-sided radio jet morphology is seen with a PA of 105° in Fig. 6.5. The peak intensity was slightly increased in the second observation, but the intensity profiles are consistent. A bending structure towards south is found at a distance of 2 mas from the radio core on the eastern jet. This bending structure has been detected in high-frequency observations together with a narrowing jet width (Boccardi et al. 2016). The SMBH is supposed to be located at the western jet, at an offset of 0.7-1.0 mas east of the 15 GHz radio core (Bach 2004; Boccardi et al. 2016).

NGC 4261 shows two-sided jets at 13 GHz and 6 GHz. The position angle of the jet is nearly parallel to the east-west direction. A sharp emission drop is seen at a distance of 0.8 mas from the radio core on the western jet. This emission trough was not resolved in the 6 GHz continuum image due to the elongated large beam along the jet axis. The gap has been detected in previous multi-frequency VLBI studies, and strong free-free absorption was measured at the gap (Jones et al. 2000; Haga et al. 2015).

TABLE 6.1: Parameters of the continuum observations of Cygnus A and NGC 4261.

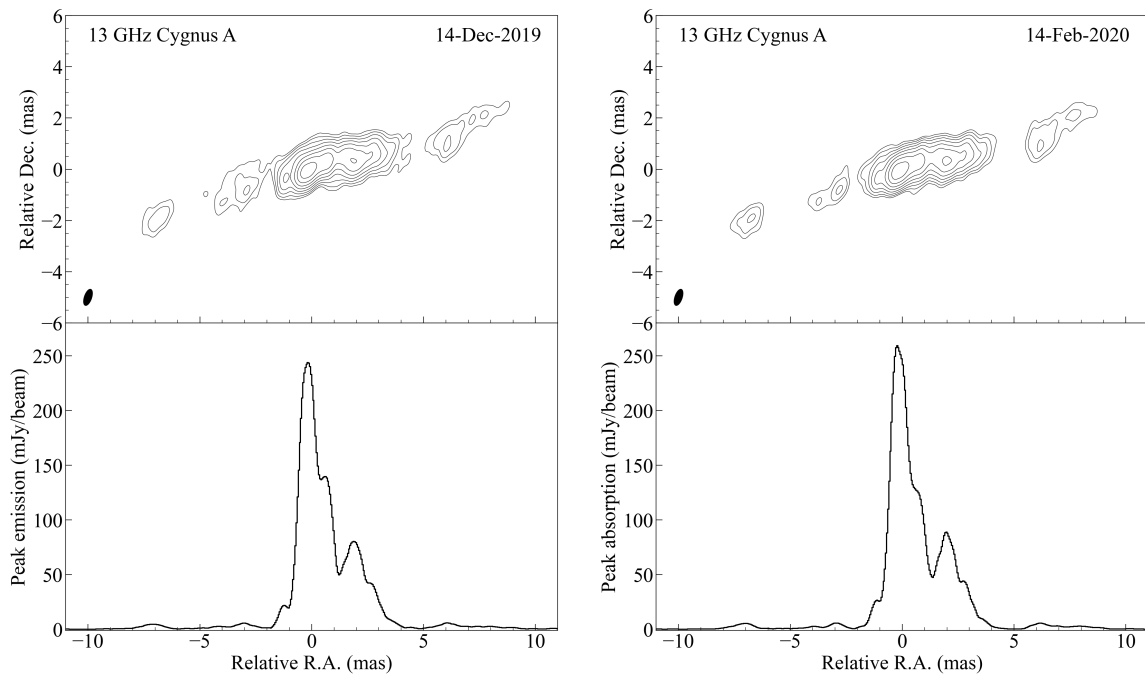| Frequency (GHz)	Target	Epoch (dd-mm-yyyy)	Array	Beam, PA mas, degree	Peak (mJy)	Total (mJy)	rms (mJy)
13	Cygnus A	14-12-2019	VLBA+VLA+Ef	0.67x0.32,-22.8	244.3	1487.7	0.13
13	Cygnus A	14-02-2020	VLBA+VLA+Ef	0.67x0.32,-20.1	259.1	1495.1	0.13
13	NGC 4261	11-07-2019	VLBA+Ef	2.04x0.31,-12.2	69.9	291.5	0.05
6	NGC 4261	20-10-2019	EVN+e-Merlin	5.03x1.36,79.6	165.3	265.3	0.20

FIGURE 6.5: Continuum images of Cygnus A **Top**: 13 GHz continuum image observed with the HSA. Contour levels are 0.5, 1, 2, 4, 8, 16, 32, 64 % of the peak flux density. **Bottom**: Peak intensity profile along the jet axis.
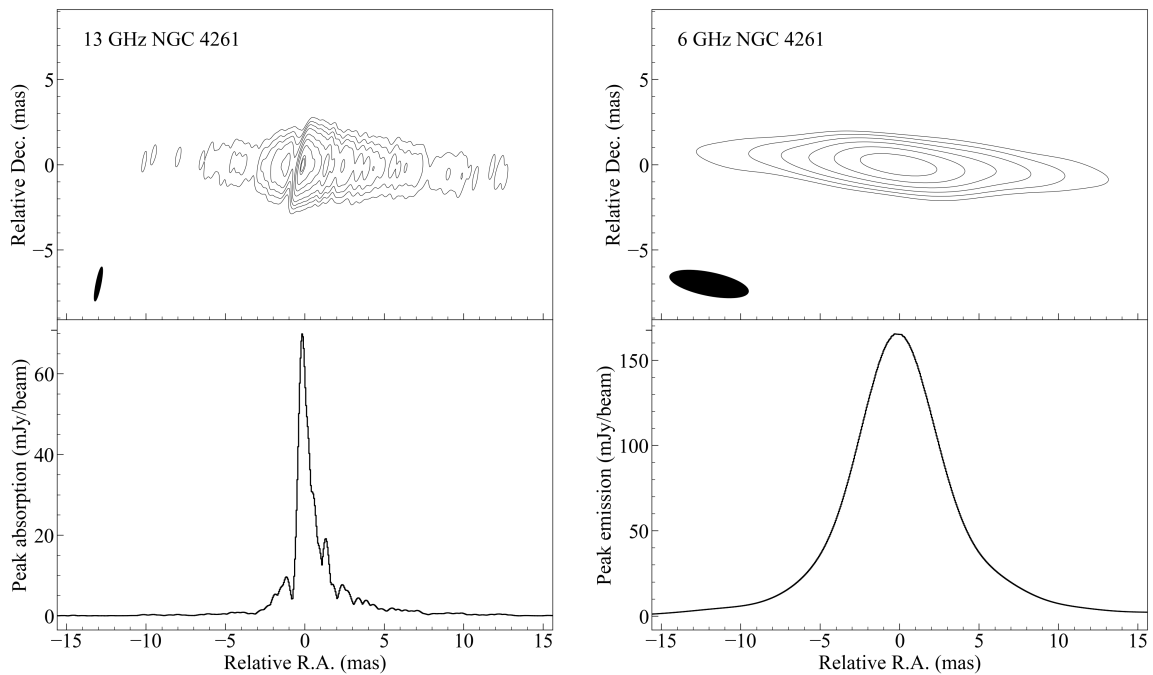

FIGURE 6.6: Continuum images of NGC 4261 **Top**: 13 GHz and 6 GHz continuum images observed with the HSA and EVN. Contour levels are 2, 4, 8, 16, 32, 64 % of the peak flux density. **Bottom**: Peak intensity profile along the jet axis.

6.4.2   13 GHz OH absorption lines in Cygnus A

Fig. 6.7 shows the results of OH absorption line observations towards Cygnus A. 13.434 GHz and 13.441 GHz OH absorption lines were detected at the two epochs (14 Dec. 2019 and 14 Feb. 2020). The spectral line sensitivities relative to the continuum levels are 0.023 % and 0.019 % with a velocity resolution of $5.9\,\mathrm{km\,s^{-1}}$ at two epochs, respectively. The 13.434 GHz and 13.441 GHz OH absorption lines are redshifted with respect to the systemic velocity and are well aligned around $180\,\mathrm{km\,s^{-1}}$ with a line width of $42\text{-}75\,\mathrm{km\,s^{-1}}$. Absorption peaks are 0.2-0.4 % of the continuum levels, and the resultant signal to noise ratio of the absorption detection is ≥ 10. At the velocities lower than the peak velocity ($\leq 196\,\mathrm{km\,s^{-1}}$), the line profile is broader than on the opposite side ($\geq 196\,\mathrm{km\,s^{-1}}$). Some absorption line variability is seen in two spectra obtained with a time gap of two months. The absorption peak was slightly weaker, but the line profile became flatter. These changes were found in both 13.434 GHz and 13.441 GHz OH absorption lines. The integrated optical depths of the OH absorption lines are summarized in Table. 6.2. The absorption peak of the 13.441 GHz OH absorption is 1.6-1.7 times deeper than the 13.341 GHz absorption.
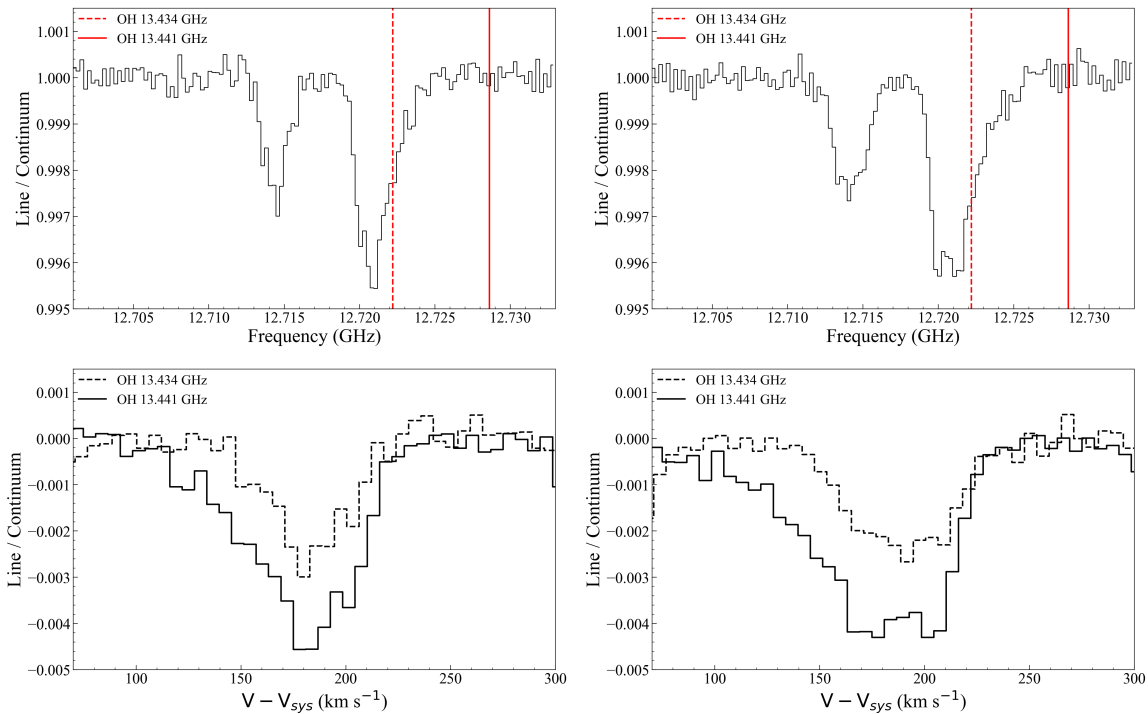
FIGURE 6.7: 13 GHz OH absorption lines in Cygnus A. **Top**: 13 GHz spectra of Cygnus A. The expected sky frequencies of the 13 GHz OH absorption lines at the systemic velocity of Cygnus A are marked with red lines. **Bottom**: 13.434 GHz and 13.441 GHz OH absorption lines aligned along the velocity axis. Velocities were calculated, referring the heliocentric reference frame.

TABLE 6.2: Parameters of 13 GHz OH absorption lines in Cygnus A.

Target	Date	OH transition[a]	Freq[b] (MHz)	ΔV[c] (km s^{-1})	V_0[d] (km s^{-1})	Peak[e] $10^{-2}\tau$	$\int \tau dv$[f] (10^{-2} km s^{-1})
Cygnus A	14-12-2019	$^2\Pi_{3/2}$, $J = 7/2\, F = 3 - 3$	12722.2	42	183	0.26	1.15
		$^2\Pi_{3/2}$, $J = 7/2\, F = 4 - 4$	12728.6	60	180	0.42	2.68
Cygnus A	14-02-2020	$^2\Pi_{3/2}$, $J = 7/2\, F = 3 - 3$	12722.2	57	189	0.25	1.53
		$^2\Pi_{3/2}$, $J = 7/2\, F = 4 - 4$	12728.6	75	179	0.43	3.30

Notes.: [a] Quantum numbers of the transition. [b] Sky frequency of the target transition (i.e., red-shifted 13.434 GHz and 13.441 GHz OH lines). [c] Line width (FWHM). [d] Doppler velocity. [f] Peak optical depth. [f] Integrated optical depth.

6.4.3   6 GHz and 13 GHz OH absorption lines in NGC 4261

The 13 GHz HSA and 6 GHz EVN observations did not detect OH absorption lines in NGC 4261. In the integrated cross power spectrum, the spectral line sensitivities were 0.7 % (0.4 mJy) and 1.9 % (1.2 mJy) of the continuum levels at 13 GHz and 6 GHz with a velocity resolution of 11.2 km s^{-1} and 6.2 km s^{-1}, respectively. We also searched for the 6 GHz OH absorption lines in the cross-power spectra with different baselines and integration times, but no clear absorption feature was identified. However, 6.030 GHz and 6.035 GHz OH absorption lines were detected with the 100-m Effelsberg telescope in 2004 (Impellizzeri 2008). The absorption peak of the 6 GHz OH line was about 1 % of the continuum flux density (absorption~13 mJy, continuum~1320 mJy). Although the EVN observations achieved a higher spectral line sensitivity than the previous single-dish observations (EVN: 1.4 mJy, Eff: 2.3 mJy), the sensitivity for absorption line detection was diminished due to an about four times lower VLBI flux density (~265 mJy) than in the single-dish observations (~1320 mJy). 13 GHz OH absorption lines were searched for the first time towards NGC 4261, and we obtained an upper limit of the absorption depth 2.1 % (3 σ) (see Fig. 6.8).
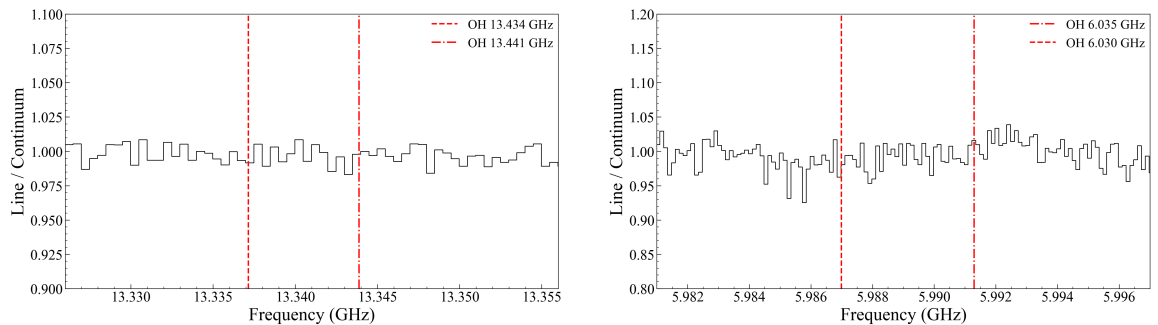

FIGURE 6.8: **Left**: 13 GHz spectrum of NGC 4261 obtained from the HSA observations. **Right**: 13 GHz spectrum obtained from the EVN observations. Expected sky frequencies of 13 GHz and 6 GHz OH absorption lines at the systemic velocity of NGC 4261 were marked with red lines.

6.4.4   The spatial distribution of the 13 GHz OH absorption in Cygnus A

Fig. 6.9 shows the 13 GHz OH absorption feature overlaid on the continuum image of Cygnus A. The absorption feature is seen around the radio core, and no significant morphological changes are found between the two epochs. The peak OH absorption intensities are 2.0-2.4 mJy/beam. More detailed zoom-in images are presented in Fig. 6.10 with the peak intensity profiles of the continuum and OH absorption. The position angle of the jet was adjusted parallel to the right ascension axis for a better visual inspection. The absorption feature is not extended, and its size is comparable to the synthesized beam size. The peak absorption depth is 1.1.-1.3 % of the continuum levels, and is located at the western jet. The angular separation between the continuum peak and absorption peak is about 0.3 mas, which translates to 0.3 pc in projected physical scale.
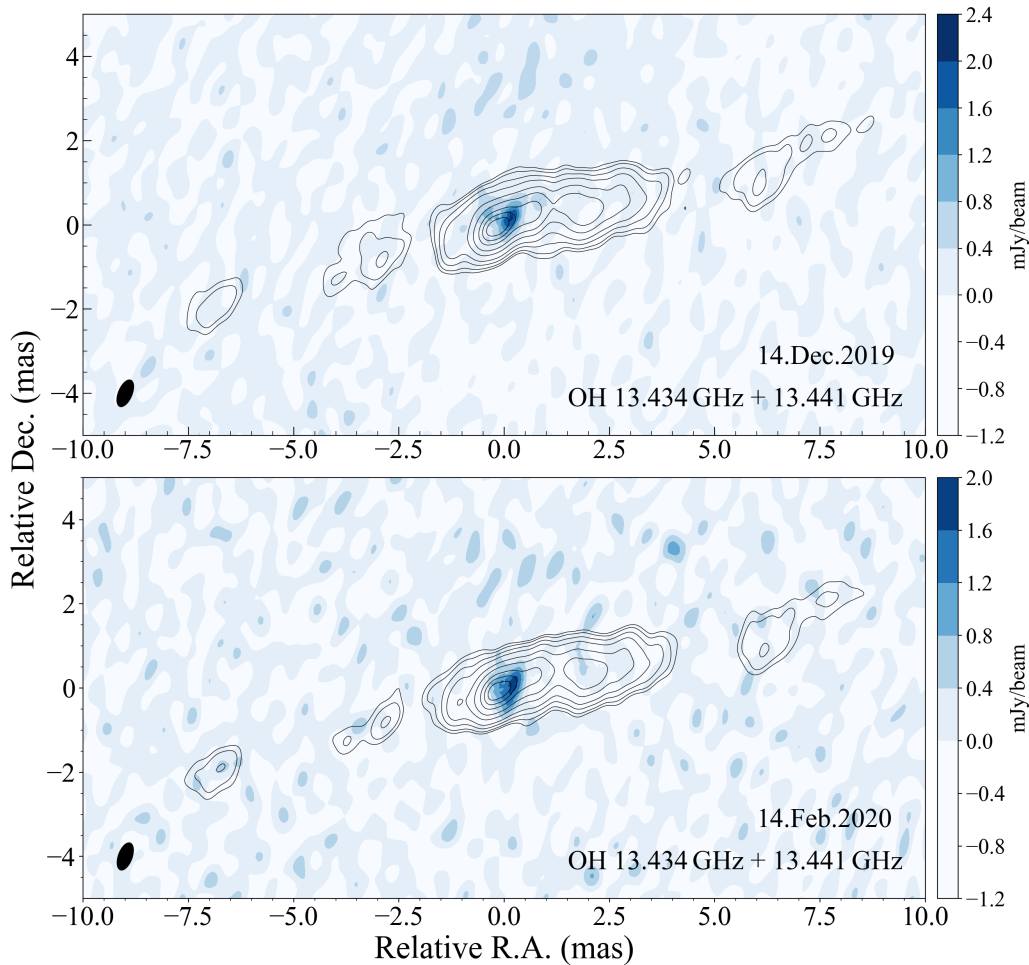
FIGURE 6.9: Images of 13 GHz OH absorption in Cygnus A. Both the 13.434 GHz and 13.441 GHz OH absorption lines were integrated. The background blue contour indicates the absolute OH absorption in the unit of mJy/beam. The black contour levels for the continuum maps are the same as in Fig. 6.5.
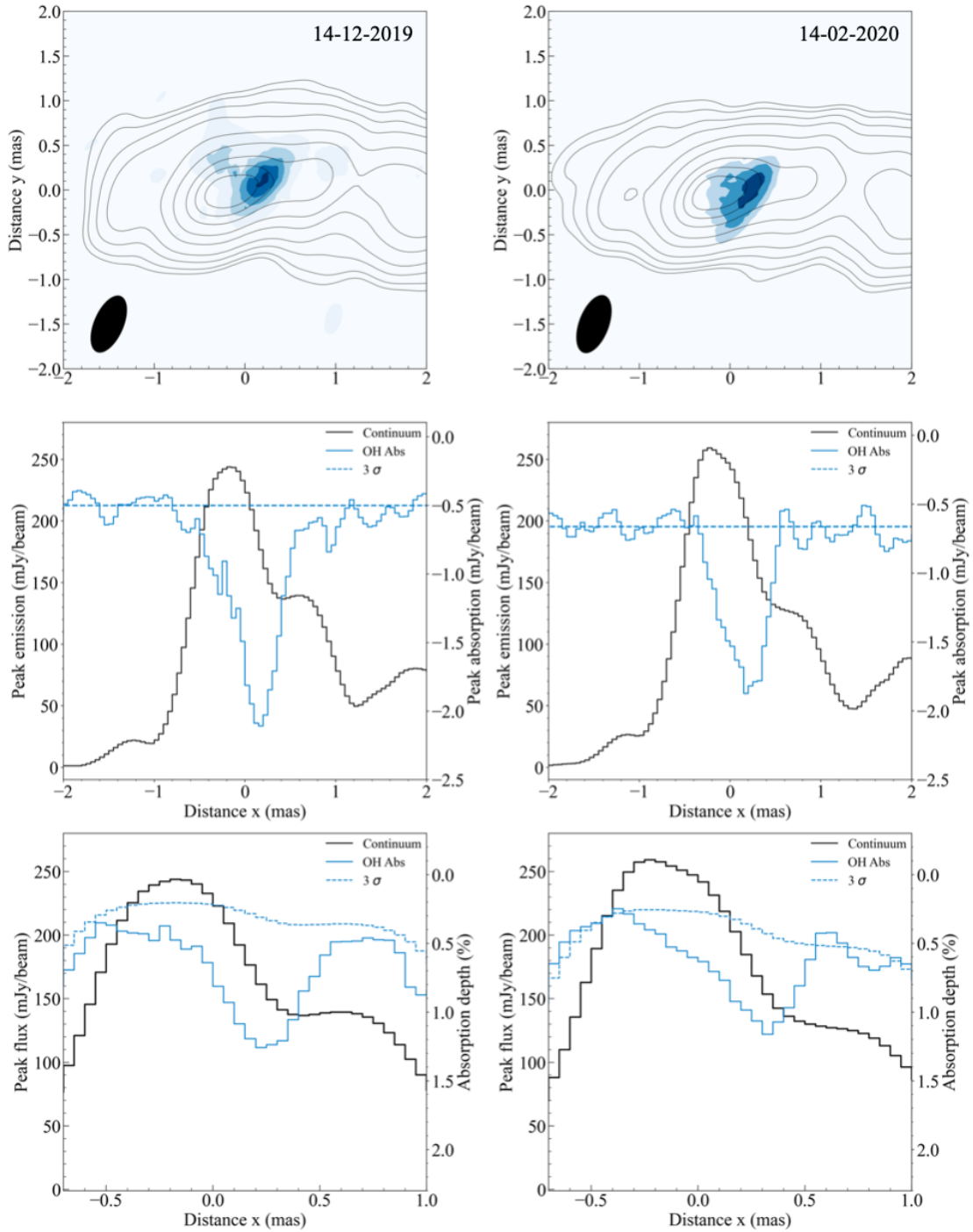
FIGURE 6.10: **Top:** Spatial distribution of OH absorption overlaid on the continuum image. **Middle:** Continuum and OH absorption profiles along the jet. **Bottom:** Zoom-in profiles of continuum and relative OH absorption depth along the jet axis of Cygnus A.

6.5 Discussion

6.5.1 Physical properties of the OH absorber in Cygnus A

Virial mass of the OH clouds: Molecular absorption can be caused by any obscuring clouds lying along the line of sight. For instance, absorption lines from the intervening galactic clouds in radio AGN show a line width of a few $km\,s^{-1}$ with composite velocity components (Muller & Guélin 2008; Rose et al. 2020). However, this is not the case for the 13 GHz OH absorption detected in Cygnus A. The absorbing gas is very compact (r<1 pc), and has a broad (FWHM:~75km s^{-1}) line width. As an alternative scenario, we assumed a single spherical clumpy cloud close to the circumnuclear region, and estimated the mass of the OH cloud using the Virial theorem. If the measured line width is caused by internal motion of the gas cloud with radius R, the virial mass of the cloud M_{Vir} is given by

$$M_{Vir} = \frac{R\sigma^2}{G}. \tag{6.1}$$

where the σ is the velocity dispersion, and G is the gravitational constant. The estimated Virial mass is $10^{5.6-5.8}$ $M_\odot$ adopting the measured line width of 60-75 km s^{-1}, and a cloud radius of 0.65 pc estimated from the 13 GHz OH absorption map (see Fig. 6.11).
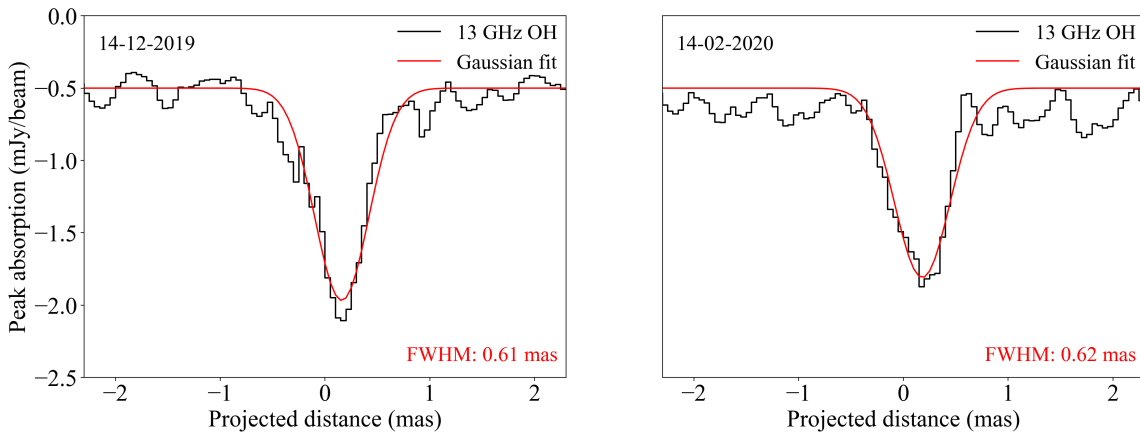
FIGURE 6.11: Size measurement of the 13 GHz OH absorption feature. The sliced OH absorption along the jet axis is presented with black dotted line at two epochs. The red solid line indicates Gaussian fitting.

Kinematics and location of the OH clouds: The H_2 molecular disk in Cygnus A shows a Keplerian rotation curve (Tadhunter et al. 2003). If the red-shifted OH absorption (180-190 km s^{-1}) originates from the rotating gas cloud in the Keplerian disk, the radial distance R_r and the rotation velocity of the OH clouds V_{rot} are given

by $R_r=R_{proj}/\cos(\theta)$ and $V_{rot}=V_{radi}/\cos(\theta)$, where R_{proj} is the projected distance between the SMBH and the OH cloud, V_{radi} is the radial velocity of the OH cloud, and θ is the projection angle along the line of sight. The projection angle θ can be calculated by the Kepler equation

$$cos(\theta) = \sqrt[3]{\frac{R_{proj}V_{radi}^2}{M_{SMBH}G}}. \tag{6.2}$$

The SMBH mass is $2.5\times 10^9 M_\odot$(Tadhunter et al. 2003), and the V_{radi} is $185\,\mathrm{km\,s^{-1}}$. The R_{proj} is the summation of the projected distance between the radio core-SMBH and the radio core-OH cloud. The angular distance between the 13 GHz radio core and the SMBH was estimated to be 1.0 mas using the jet opacity shift measurements in the literature (Boccardi 2015). The angular distance between the 13 GHz radio core and the OH absorption peak is 0.4 mas. Thus, a linear distance of 1.5 pc (1.4 mas) was adopted for R_{proj}. From the Eq. 6.2, the calculated projection angle is 80.3 °, which yields $R_r=8.9\,\mathrm{pc}$, and $V_{rot}= 1098\,\mathrm{km\,s^{-1}}$. Fig. 6.12 shows the projected distance and radial velocity along the projection angles. The Keplerian model provides reliable physical parameters of the OH clouds, but the rotation axis of the OH clouds (perpendicular to the jet) deviates from the rotation axis of the H_2 molecular disk (parallel to the jet). An alternative scenario explaining the red-shifted OH clouds is a fueling flow falling into the central engine. Indeed, high resolution H_2 observations detected an infalling gas cloud with a red-shifted velocity of ~200 km s^{-1} (Bellamy & Tadhunter 2004). Its projected distance from the infrared nucleus was ~1.35 kpc, thus the OH absorber at a projected distance of 1.5 pc might represent already progressed fueling gas. In this case, only the lower limits of the radial distance and velocity can be constrained for the OH absorber. Fig. 6.14 shows two possible scenarios, explaining the kinematics of the red-shifted OH absorption.
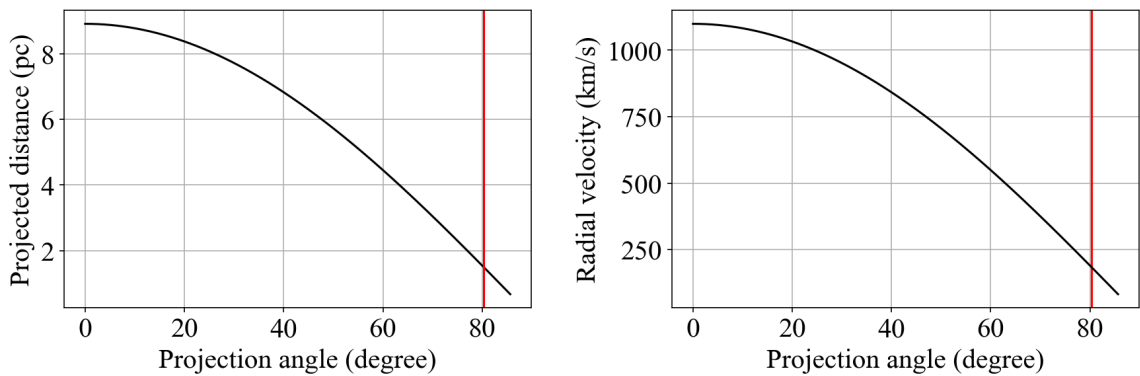

FIGURE 6.12: **Left**: The projected distance between the SMBH and the OH clouds with the projection angle. The projection angle is **Right**: The radial velocity of the OH clouds with the projection angle. The calculated projection angle was marked with the red vertical line.
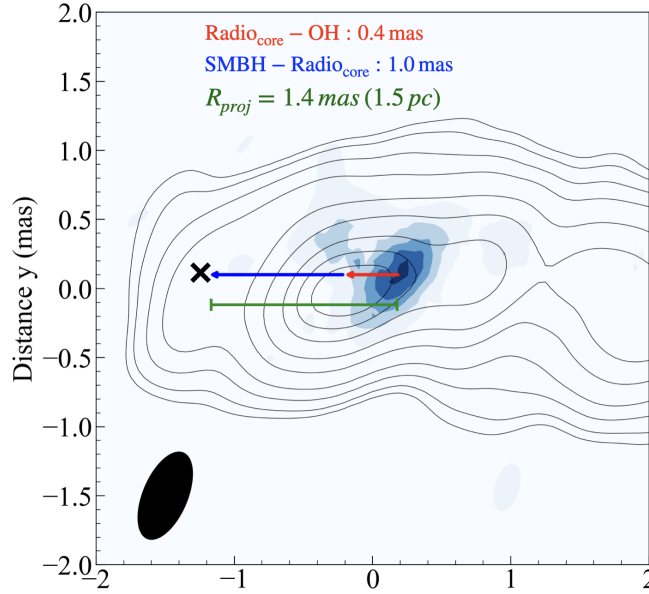
FIGURE 6.13: Projected distance between the OH cloud and the SMBH in Cygnus A. The angular distance between the peak continuum-OH absorption peak and the peak continuum-SMBH are marked with the red and blue arrows, respectively. The synthesized beam size is denoted on the left corner.
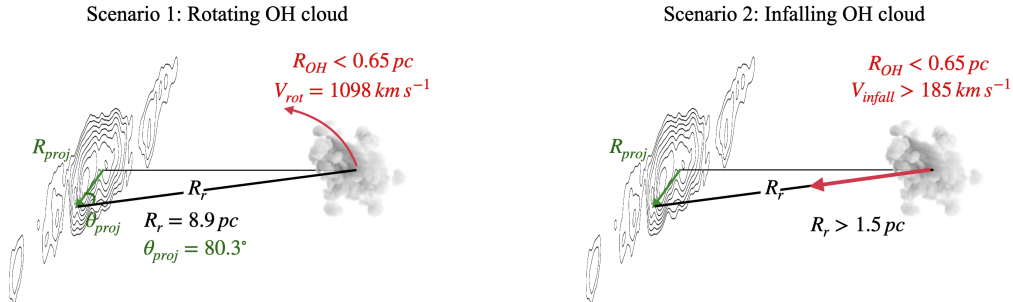

FIGURE 6.14: **Left**: A schematic view of the rotating OH clouds following the Keplerian motion. The estimated projection angle is $80.3\,°$. **Right**: A schematic view for the infalling OH clouds.

Line ratio and column densities: The OH J=7/2 state is situated at a high energy level around $290\,K$, thus its Λ-doubling transitions are suited for tracing molecular gas in a harsh environment. Indeed, $^2\Pi_{3/2}$, J = 7/2 OH transitions have been detected in ultra-compact H II regions via MASER emission or absorption (Matthews et al. 1986; Baudry & Desmurs 2002). The 13 GHz absorption features found in Cygnus A is the first extragalactic detection of the OH $^2\Pi_{3/2}$, J = 7/2 Λ-doubling transitions. A separation of the two absorption features in frequency axis corresponds to the expected frequency separation between the OH $^2\Pi_{3/2}$, J = 7/2 F=4-4 and F=3-3 transitions. Thus, the detected absorption features are interpreted as the two OH transitions rather than two velocity components.

Two hyperfine OH transitions at 13.441 GHz and 13.434 GHz allow us to constrain the physical conditions of the obscuring OH clouds. Under LTE conditions the expected line ratio of the F=4-4 (13.441 GHz) and F=3-3 (13.434 GHz) transition is 1.3 (35:27). However, the observed line ratios (1.61-1.72) were ~20 % higher than the expected line ratio. An external shock or a strong radiation field could lead to offsets of the OH level populations from LTE, and this leads to either increased F=4-4 absorption or decreased F=3-3 absorption. Matthews et al. (1986) suggested that 84.5 μm infrared rotational line from $^2\Pi_{3/2}$, J = 7/2 to $^2\Pi_{3/2}$, J = 5/2 state affects the OH J=7/2 hyperfine level populations via line overlaps effect (see Fig. 6.15). This mechanism is likely to work in the nuclear region of Cygnus A. The excited OH clouds radiate strong infrared emission, and it might disturb the hyperfine level populations of the J=7/2 state via the line overlaps effect (Guilloteau et al. 1981, 1984; Matthews et al. 1986). Consequently, the optical depths of the 13.441 GHz and 13.434 GHz transitions would deviate from the expected values under LTE condition. Observations of excited OH transition at low-J states (J=5/2 or 3/2) are necessary to test different line ratios of the OH Λ-doubling transitions. Also, they will allow us to estimate the rotational temperature of the OH cloud.

The column density of the OH absorption lines was estimated by using the following equations introduced by Guilloteau et al. (1984).

$$n\left(J,\ F\right) = 4\pi \sqrt{\frac{\pi}{\ln 2}} \frac{k}{h\nu} \left(\frac{\nu}{c}\right)^3 \frac{1}{(2F+1)\,A} \Delta v \ \cdot \tau\left(J,\ F\right) T_{\text{ex}}\left(J,\ F\right) \qquad (6.3)$$

where $n\left(J,\ F\right)$ is the column density in the lower level of each hyperfine line (J, F), k is the Bolzman constant, h is the Planck constant, ν is the line frequency, c is the speed of light, A is the Einstein coefficient, and Δv is the line width, τ is the peak optical depth, and T_{ex} is the excitation temperature. With the two main lines, the total column density in the rotational state J is given by

$$N\left(J\right) = 2\left\{(2J)\,n\left(J,\ J-\frac{1}{2}\right) + (2J+2)\,n\left(J,\ J+\frac{1}{2}\right)\right\}. \qquad (6.4)$$

The estimated column density of the N(OH) J=7/2 state is 2.9-3.8$\times 10^{13}$cm^{-2}/T$_{\text{ex}}$. If we apply the dust temperature of the nuclear dust in Cygnus A ($\sim$150 K) as the rotational temperature (Radomski et al. 2002), we obtain a total column density N(OH)$\simeq$(2.0-2.5) $\times 10^{14}$cm^{-2}/T$_{\text{ex}}$. Further estimation of the column density of molecular hydrogen using the OH/H$_2$ abundance ratio of 10^{-7} (Nguyen et al. 2018) yields the total column density of N(H$_2$)$\simeq$(2.0-2.5)$\times 10^{21}$cm^{-2}/T$_{\text{ex}}$. By adopting the rotational temperature as the excitation temperature (150 K), the estimated column density is N(H$_2$)$\simeq$(3-3.7)$\times 10^{23}$cm^{-2}. This value is comparable to the measurement from the X-ray observations N(H$_2$)$\simeq$(1-4)$\times 10^{23}$cm^{-2}.
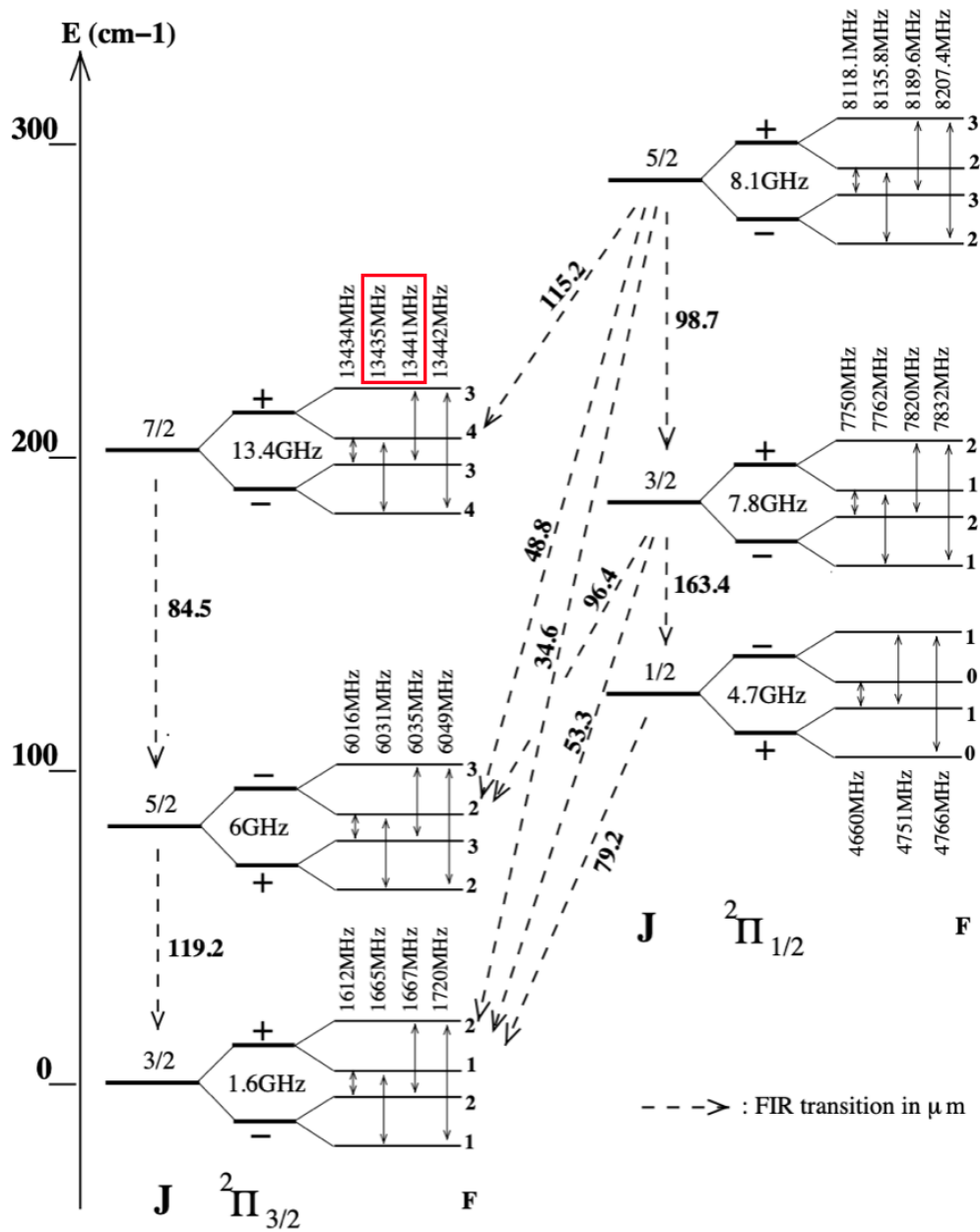
FIGURE 6.15: Energy levels of OH. **J** is the rotational energy level. $^2\Pi_{3/2}$ and $^2\Pi_{1/2}$ are spin-orbit splitting. **F** is the resultant of Λ-doubling and hyperfine splitting. Two 13 GHz OH transitions detected in Cygnus A are marked with the red box. Infrared rotational transitions are marked with the dotted arrow. The figure is taken from Desmurs et al. (2002).

6.5.2 Molecular torus in Cygnus A

The 'Unified Scheme' of AGN suggests a universal view of the different classes of AGN through orientation-dependence. A putative toroidal dusty structure, termed 'Torus', could hide the nuclear region depending on its inclination relative to an observer (Antonucci 1993; Urry & Padovani 1995). Over the last decade, torus models and phenomenological studies have suggested a variety of parameters for this circumnuclear structure, depending on the AGN property (i.e., AGN luminosity, accretion rate, BH mass). Recent studies with ALMA reveal molecular tori in nearby Seyfert galaxies (García-Burillo et al. 2014; Combes et al. 2019), but the detailed geometry and kinematics of these tori still remain unclear due to their compact size (scales < a few pc). Cygnus A is the archetypal type 2 radio-loud AGN, harboring an obscured BLR in the core region (Ogle et al. 1997). Thus, it is the prime candidate to scrutinize a putative Torus suggested by the Unified model. An elongated structure resolved by the VLA extends over a few hundred pc scales (Carilli et al. 2019). It indicates a diffuse obscuring structure completely covering the nuclear region, but the spectral index analysis using multi-frequency VLBI images suggested a much more compact and dense obscuring structure within a few pc scale (Bach 2004). The obscuring material could be a clumpy cloud comprising a diffuse torus or more compact nuclear structure surrounding the AGN, such as NLR or infalling gas fueling the central engine. The spatially resolved OH absorption lines now give a hint for the nature of the obscuring structure. In Fig. 6.10, the absorption depths of the 13 GHz OH lines are not uniform along the continuum jet. Instead, absorption is very localized on a sub-pc scale. This compact obscuring structure contradicts the classical torus model. Moreover, the absorption peak is not located on the counter-jet side, where also a dense ionized material is detected via free-free absorption (Bach 2004; Boccardi et al. 2016). The ionized gas is close to the accretion disk, and a continuation of the dusty disk or torus is expected in the same region. However, the obscuring molecular gas in Cygnus A seems not to be aligned with the accretion disk. This implies a more complex kinematics and structure of the circumnuclear gas, rather than a continuous toroidal structure perpendicular to the jet axis. Such complicated kinematics of the circumnuclear gas was also reported in the nearby AGN NGC 1068. High-resolution ALMA observations of the circumnuclear gas in NGC 1068 revealed two pc scale disk components rotating in opposite directions (Impellizzeri et al. 2019). The physical origin of the counter-rotating gas is yet unclear. The interaction between two inner disks is supposed to significantly increase the accretion rate.
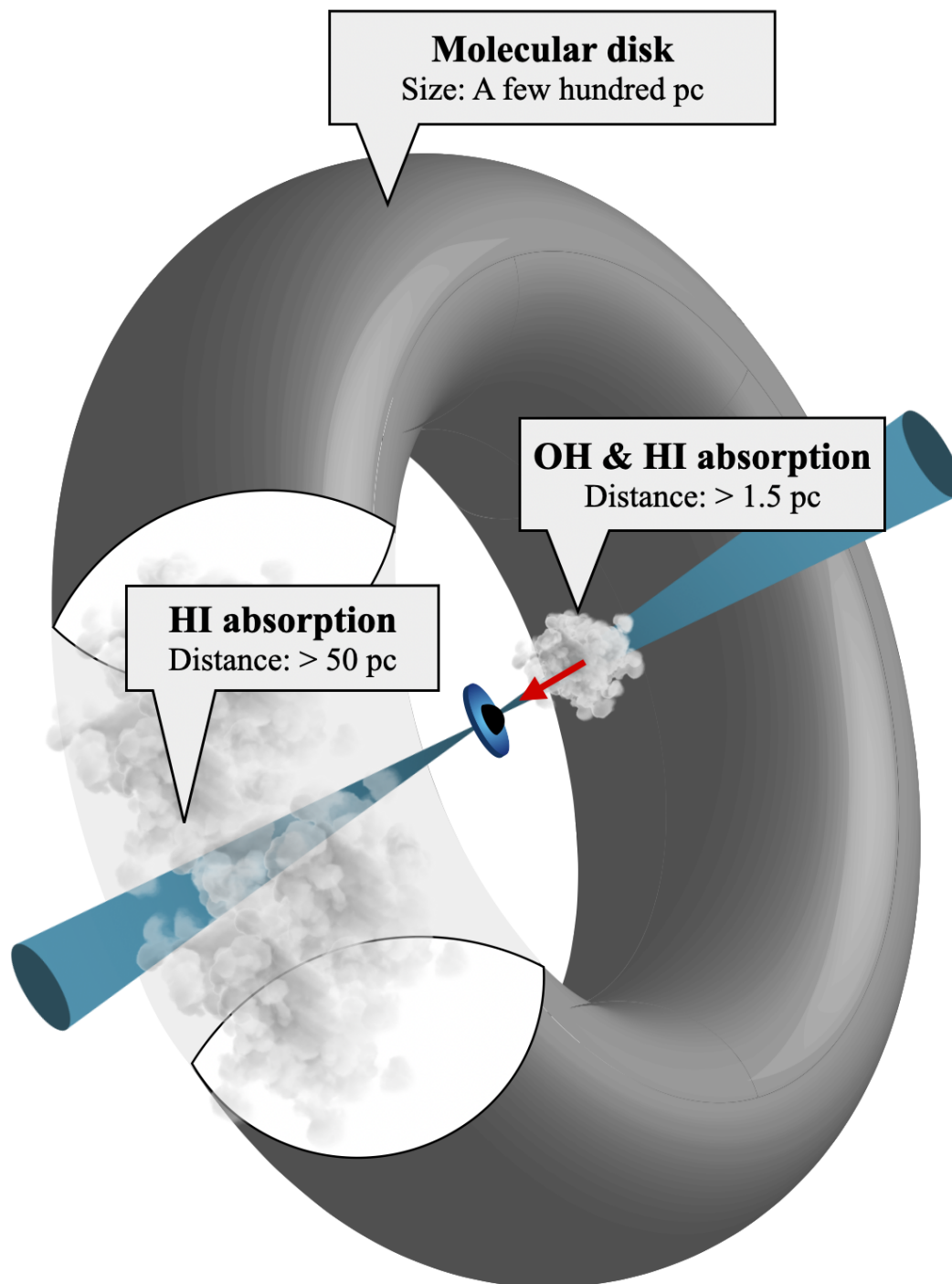
FIGURE 6.16: A diagram of the nuclear region of Cygnus A. The locations of H I and OH absorption are presented with the putative H_2 nuclear disk. Broad H I absorption is present in front of the counter-jet at the projected distance of ~50 pc, and the line centroid is close to the systemic velocity. The H I and OH absorption in front of the inner jet is red-shifted by about $185 \, \mathrm{km \, s^{-1}}$ and located at a projected distance of 1.5 pc.

6.5.3   The lack of OH absorption in NGC 4261

Previous single-dish observations detected 6 GHz OH absorption lines in NGC 4261 (Impellizzeri 2008), but our VLBI observations did not detect any 6 GHz and 13 GHz OH absorption lines. The lack of OH absorption in VLBI observations can be explained as follows. First, OH absorption caused by extended OH clouds in front of the radio lobes can only be seen in single-dish observations, but not in VLBI. The beam size of the 100-m Effelsberg telescope is large enough (~100 arc-second) to cover extended continuum emission from the radio lobes and OH absorption from intervening molecular clouds (see left bottom panel in Fig. 6.18). Instead, only the compact and bright radio core remains in VLBI observations, and hence OH absorption from the extended radio lobes cannot be detected.

On the other hand, the CO circumnuclear disk detected by ALMA suggests OH absorbers in front of the radio core, but not the radio lobes (see Fig. 6.17 and Fig. 6.18). For a compact OH absorber in front of the radio core, more deep and prominent OH absorption is expected in VLBI observations compared to the previous single-dish OH detection. However, this expectation is not consistent with our results. A possible explanation for the lack of OH absorption in VLBI observations is the variability of absorption caused by the motion of the obscuring gas and the continuum radio jet. On VLBI scales, the continuum jet is extended along the east-west direction, and the jet width is smaller than 1 pc. Assuming an OH cloud moving along the north-south direction with a velocity of $1000 \, \mathrm{km \, s^{-1}}$, the crossing time of the jet is about 300 yr (jet width: 0.3 pc). Meanwhile, the apparent speed of the background radio jet is 0.5 c (Piner et al. 2001). Consequently, the absorption depth of OH absorption and the line profile could be highly variable depending on the alignment between the background jet and the intervening OH clouds.
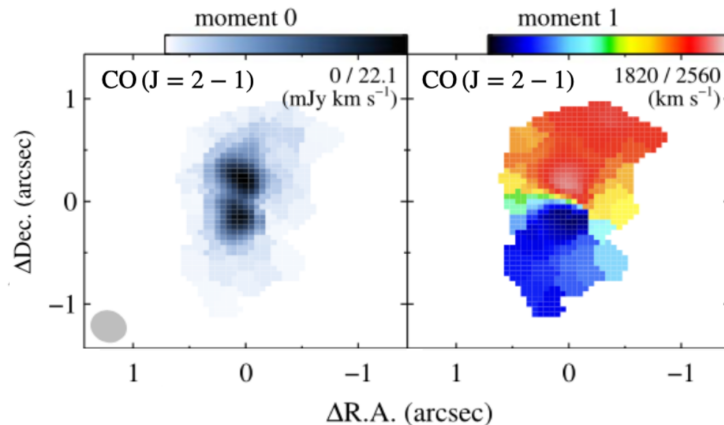

FIGURE 6.17: Moment 0 and 1 maps of CO *J*=2-1 emission from the circumnuclear disk in NGC 4261. The figure is taken from Boizelle et al. (2021).

Those two possible scenarios, explaining the lack of OH absorption in our VLBI observations towards NGC 4261, can be tested via sub-arcsecond resolution observations using a connected array, such as the VLA. With such a moderate angular resolution, we can discriminate whether the 6 GHz OH absorption originates from the radio lobes or the radio core. If the 6 GHz OH absorption is dominant at the radio core, monitoring VLBI observations are desirable to study its physical connection with the AGN fueling or feedback processes.
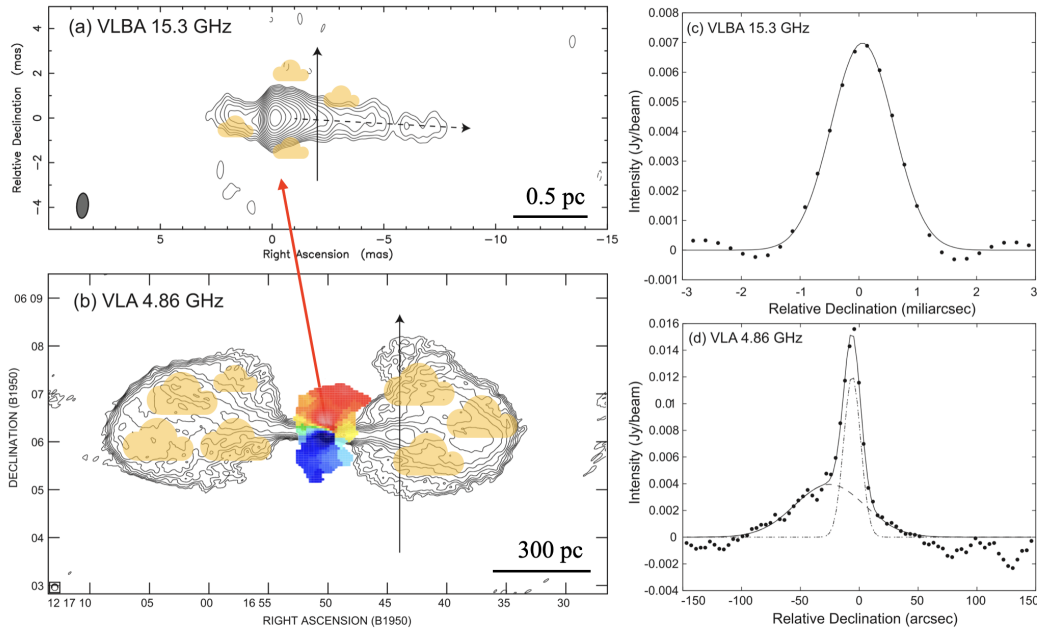
FIGURE 6.18: **Left**: 4.8 GHz and 15 GHz continuum radio jets in NGC 4261 imaged by the VLA and the VLBA, respectively. The CO disk image is overlaid on the VLA continuum image. Putative OH absorbers in front of radio lobes (left bottom) and radio core (left top) are illustrated yellow. **Right**: The jet profiles along the black solid lines in the continuum map. The figures are taken from Nakahara et al. (2018); Boizelle et al. (2021)

6.5.4 Accretion modes in Cygnus A and NGC 4261

Circumnuclear gas is an important observational probe to discriminate accretion modes responsible for the different AGN luminosities and radio jet properties in radio-loud AGN. A dichotomy of radio-loud AGN (LERG and HERG) is found in the AGN mass (i.e., host galaxy stellar mass) range $10^{10.5-11.7}\,M_\odot$, and the fraction of HERG in radio-loud AGN increases with the presence of a cold gas reservoir (Janssen et al. 2012). Higher accretion rates and jet powers in HERG than LERG have been attributed to a radiatively efficient accretion mode fed by cold gas. On the contrary, the radiatively inefficient hot gas accretion mode is expected in LERG (Best & Heckman 2012) (also see §1.2.2). However, observational evidence for the different accretion modes in LERG and HERG is still pending. Cygnus A and NGC 4261 are

archetypal radio-loud AGN with distinct AGN luminosity (HERG and LERG) and radio jet properties (FR II and FR I). Thus, the kinematics and physical properties of the circumnuclear gas near the jet launching region are crucial to reveal the physical connection between accretion modes and the radio-loud AGN dichotomy.

Circumnuclear gas has been detected in both Cygnus A and NGC 4261. Previous H I absorption line observations towards Cygnus A show absorption features of broad (FWHM~ $231 \,\mathrm{km\,s^{-1}}$) and narrow (FWHM~$30 \,\mathrm{km\,s^{-1}}$) Gaussian components. The centroid of the broad and narrow lines are red-shifted by about $116 \,\mathrm{km\,s^{-1}}$ and $186 \,\mathrm{km\,s^{-1}}$, with respect to the systemic velocity measured by optical and infrared emission lines. A large beam size (FWHM~25 mas) at 21-cm marginally located the narrow absorption feature on the radio core and the broad absorption feature on the counter-jet side separated by about 40 mas from the radio core. It is yet unclear whether those components are dynamically connected or separated. Comparable Doppler velocities (180-190 $\mathrm{km\,s^{-1}}$) and locations between the 13 GHz OH absorption and the narrow H I absorption suggest their similar physical origin. The red-shifted velocity indicates an inward motion from the rotating disk. Indeed, a rotating sub-kpc scale disk observed at near-infrared wavelengths shows a velocity of ~$100 \,\mathrm{km\,s^{-1}}$ at a few hundred pc from the core region (Tadhunter et al. 2003). Therefore, we conclude that the red-shifted OH absorption line is not part of the rotating disk, instead it is more likely to trace a fueling flow near the accretion disk. The presence of OH gas in a highly excited state (J=7/2, T_{ex}=290 K) also implies that the obscuring gas is close to the central engine. For NGC 4261, a thin circumnuclear disk suggested by H I observations was confirmed by CO disk observation using ALMA (van Langevelde et al. 2000; Boizelle et al. 2021). The amount of nuclear gas estimated by the CO disk ($1.1\times10^{7} M_{\odot}$) is around 1 % of the SMBH mass ($1.6\times10^{9} M_{\odot}$). The presence of molecular gas inflow or outflow in the nuclear region has not been reported, but a thin accretion disk was suggested by a sharp free-free absorption seen on the counter-jet (Jones et al. 2001). If molecular gas is located at the same region, it might support the presence of a thin disk formed by cold gas accretion. As a LERG, such an accretion mode is inconsistent with the appearance of NGC 4261, thus it is crucial to prove the presence of molecular gas near the free-free absorption region. In our VLBI experiments, OH absorption was not detected, thus we were not able to test the presence of molecular gas around the emission gap in the continuum jet. This might indicate a lack of cold gas near the core region, which is consistent with the expected accretion mode in LERG. However, this could be just due to insufficient sensitivity of our spectral line VLBI observations. Since absorption is suited for detecting a weak peculiar gas motion deviated from the rotating disk (Nagai et al. 2019; Kameno et al. 2020), further high sensitivity absorption line observations are needed to discern the nature of the continuum emission gap, and the accretion mode in NGC 4261.

6.6 Conclusion

Excited OH absorption lines in the radio-loud AGN Cygnus A and NGC 4261 were searched to study their distinct accretion environments. The 13 GHz HSA observations towards Cygnus A detected OH absorption lines at two epochs with little variability. The absorption features were spatially resolved on the continuum jet image. The estimated size of the absorption cloud is 0.65 pc. The OH gas was not seen on the counter-jet side, where strong free-free absorption is found. Instead, the absorption peak is located on the jet side separated from the SMBH about 1.4 mas (1.5 pc) in the projected distance. We suggest rotating or infalling circumnuclear gas as the possible origin of the OH absorber detected in Cygnus A. The absorption line intensity ratios probe the non-LTE environment of the OH absorbers. To constrain in more detailed physical and chemical properties of the circumnuclear gas, further observations of low-J OH transitions or absorption from other molecular species are necessary.

13 GHz and 6 GHz OH absorption line observations towards NGC 4261 were conducted with the HSA and EVN. We obtained upper limits for the opacity of 0.7 % and 1.9 % of the continuum levels for the compact radio core. Two possible scenarios were suggested to explain the 6 GHz OH absorption detection in single-dish observations, but not in our VLBI experiments. The lack of compact OH clouds near the jet launching region is consistent with the expected accretion mode in LERG, but relative motions between compact OH absorbers and continuum radio jets also can result in variability and the lack of OH absorption. Further absorption line observations using connected arrays and monitoring VLBI observations are necessary to discern the nature of OH absorption in NGC 4261.

Chapter 7

Summary and future outlook

7.1 Summary

This thesis focuses on circumnuclear gas in radio AGN to study the physical connections between the radio jets and their surroundings. The circumnuclear gas obscuring the bright continuum radio jet in radio AGN was studied using molecular absorption. Absorption line observations were conducted using single-dish (100-m Effelsberg and 30-m IRAM telescopes), connected element interferometers (NOEMA), and VLBI (HSA and EVN+e-Merlin) facilities, covering a broad range of resolutions (a few hundred pc down to sub-pc) and wavelength ranges (from cm to mm). The paragraphs below summarize the key findings and the implications of the molecular absorption line studies presented in this thesis.

Single-dish absorption line surveys: OH, HCN, and HCO$^+$ absorption lines were searched towards 41 radio AGN using single-dish telescopes at cm and mm wavelengths. As a result, the cm-absorption line survey using the 100-m Effelsberg telescope detected both H$_2$O MASER emission and OH absorption lines in NGC 3079 and NGC 1052. The line profiles of the 23 GHz OH absorption and 22 GHz H$_2$O MASER are very similar in NGC 1052, which implies a common physical origin of the H$_2$O MASER and obscuring OH clouds. In contrast to this, NGC 3079 shows different line profiles between 6 GHz OH absorption and 22 GHz H$_2$O MASER lines. A possible molecular outflow is suggested by the blue-shifted ($130 \, \mathrm{km \, s^{-1}}$) OH absorption. This scenario was tested by follow-up high-resolution VLBI observations. A line survey using the 30-m IRAM telescope detected HCO$^+$, HCN, and HNC absorption lines at 3 mm in 3C 293. Two red-shifted narrow absorption features at ~$20 \, \mathrm{km \, s^{-1}}$ and ~$55 \, \mathrm{km \, s^{-1}}$ seem to occur in the intervening circumnuclear disk.

The low detection rates in single-dish absorption surveys is attributed to technical hindrances (e.g., RFI, beam dilution) and broad line widths (comparable to standing waves in the telescope). Observing nearby continuum and bandpass calibrators of similar flux density as the target is essential to validate real absorption features in single-dish absorption surveys.

Interferometric absorption line survey: Interferometric observations were conducted towards two known absorption line systems 3C 293 and 4C 31.04. The main goal of this study was to demonstrate the capability of interferometric absorption line observations, avoiding the technical obstacles from single dish observations (e.g., RFI and standing waves), and to characterize the physical properties of the molecular absorbers using absorption lines from more molecular species seen in a spectral window of wider bandwidth. As a result, spectral line scans at 3 mm using the NOEMA interferometer detected HCN, HCO^+, HNC, $H^{13}CN$, $H^{13}CO^+$, ^{13}CO, SiO, C_2H, and N_2H^+ in 3C 293, and HCN, HCO^+, HNC, ^{13}CO, C_2H in 4C 31.04. The newly detected molecular species allow us to constrain the physical and chemical properties of the circumnuclear gas in 3C 293 and 4C 31.04 in more detail. As a result, we did not find strong evidence for radio jet feedback on the obscuring gas for these two AGN.

VLBI OH absorption line study towards NGC 3079: The composite 6 GHz OH absorption lines detected in the radio-quiet AGN NGC 3079 were spatially resolved by the EVN observations on sub-pc scales. A blue-shifted absorption feature was located in front of the propagating jet but not on the receding jet. This can be interpreted as a jet-driven outflow in NGC 3079. A higher column density and broader line width for the blue-shifted absorption component manifests the impact of jet-ISM interactions on the surroundings. A shock induced by jet-ISM interaction is likely to compress the ambient medium, which increases the local density and velocity dispersion of the ambient OH clouds. The presence of jet-ISM interaction is further supported by the observed variations in the jet properties. The jet luminosity of the interacting jet component has been increasing, and its apparent jet-speed has been decreasing over the last decade. In contrast, other jet components located further upstream remain stationary and stay at the same luminosity. These results show how the ambient medium can affect jet propagation and evolution.

The VLBI OH absorption line study towards Cygnus A and NGC 4261: OH absorption line observations towards the two radio-loud AGN NGC 4261 (3C 270) and Cygnus A were conducted to test if a different fueling environments between a HERG and a LERG may be present. 13 GHz OH absorption lines were detected in Cygnus A. The red-shifted absorption (190 km s^{-1}) feature was located in front of the radio jet instead of the counter-jet. This proves the presence of molecular gas in the nuclear region of Cygnus A but also contradicts the classical torus model, in which absorption would be more prominent on the counter-jet side. For NGC 4261, which is another well-known radio-galaxy showing evidence of circumnuclear absorption by a torus, the expected 13 GHz and 6 GHz OH absorption lines were not detected, despite a previous 6 GHz OH absorption detection with the Effelsberg telescope. The lack

of OH VLBI absorption in NGC 4261 is attributed to time variability of molecular absorption caused by the motion of OH clouds and/or in the continuum radio jet. Further interferometric absorption line observations may be necessary to clarify the nature of the OH absorption in NGC 4261 and its relation to the putative torus.

7.2 Future outlook

The studies presented in this thesis probe the physical properties of the circumnuclear gas in a small number of radio AGN using the absorption line technique. Although dense molecular gas is expected in the vicinity of the central engine, the number of objects for which molecular absorption actually was detected, still remains puzzling small. At present it is unclear, if this is due to the lack of molecular gas, higher excitation levels not probed by the current frequency coverage, or a gas distribution deviating from the widely accepted Unified Scheme/torus model. Further studies on larger source samples may be necessary to better characterize the circumnuclear gas in the various types of radio AGN. A pressing task is to find more molecular absorbers in radio AGN, which are suitable for centimeter and/or millimeter broad band radio interferometry, eg. with the SMA, NOEMA and ALMA and for follow-up studies using high frequency VLBI. High-sensitive interferometric absorption line measurements shall allow us to access the circumnuclear gas in many more sources and over a wider range of AGN types. With newly identified molecular absorption systems through interferometric observations, further spectral line scans can be carried out to detect known molecular species at higher excitation levels and also other molecules in the obscuring gas. As presented in Chapter 4, a spectral line analysis using various molecular species can effectively constrain the physical quantities of the obscuring gas. With those constraints, we are able to discriminate the nature of obscuring gas. VLBI observations of absorption systems showing a broader line width (up to hundreds of km s^{-1}) and/or a highly Doppler-shifted line velocities will be particular promising for the study of the spatial gas distribution on sub-pc scales and to figure out the physical connection of the circumnuclear gas with the jet outflow (AGN jet feedback) and accretion inflow (AGN fueling).

In the future, upcoming next-generation radio interferometers such as the (Next Generation Very Large Array) ngVLA and (next-generation Event Horizon Telescope) ngEHT, and Square Kilometre Array (SKA) will likely offer a remarkably improved capability for spectral line observations in terms of spectral window coverage, and sensitivity compared to current radio interferometers. This will bring significant advancements for the search of new absorption systems and/or rare molecular species. With a higher sensitivity and further optimized bandpass shapes, also not so bright continuum radio jets and absorption with broader lines widths could be targeted.

Meantime, the advanced infrared interferometer Very Large Telescope Interferometer (VLTI) will provide high-resolution images of dust continuum emission and molecular absorption lines in the vicinity of the central engine. Thus, a combined study using radio and infrared interferometers will help to better clarify the still controversial inner structure of AGN by unveiling the spatial distribution and kinematics of gas and dust near the central engine.

Bibliography

Aalto, S., Falstad, N., Muller, S., et al. 2020, A&A, 640, A104

Aditya, J. N. H. S. & Kanekar, N. 2018, MNRAS, 473, 59

Alam, S., Albareti, F. D., Allende Prieto, C., et al. 2015, ApJS, 219, 12

Alatalo, K., Lacy, M., Lanz, L., et al. 2015, ApJ, 798, 31

Alexander, D. M. & Hickox, R. C. 2012, New A Rev., 56, 93

Allen, J. T., Hewett, P. C., Maddox, N., Richards, G. T., & Belokurov, V. 2011, MNRAS, 410, 860

Allen, S. W., Dunn, R. J. H., Fabian, A. C., Taylor, G. B., & Reynolds, C. S. 2006, MNRAS, 372, 21

Alonso-Herrero, A., Pereira-Santaella, M., García-Burillo, S., et al. 2018, ApJ, 859, 144

An, T. & Baan, W. A. 2012, ApJ, 760, 77

Antonucci, R. 1993, ARA&A, 31, 473

Antonucci, R. R. J. & Miller, J. S. 1985, ApJ, 297, 621

Ao, Y., Henkel, C., Menten, K. M., et al. 2013, A&A, 550, A135

Asada, K., Nakamura, M., Doi, A., Nagai, H., & Inoue, M. 2014, ApJ, 781, L2

Asmus, D. 2019, MNRAS, 489, 2177

Asmus, D., Hönig, S. F., & Gandhi, P. 2016, ApJ, 822, 109

Audibert, A., Combes, F., García-Burillo, S., et al. 2019, A&A, 632, A33

Baan, W. A., Haschick, A., & Henkel, C. 1992, AJ, 103, 728

Bach, U. 2004, PhD thesis, Rheinischen Friedrich-Wilhelms-Universität Bonn

Baczko, A. K., Schulz, R., Kadler, M., et al. 2019, A&A, 623, A27

Baczko, A. K., Schulz, R., Kadler, M., et al. 2016, A&A, 593, A47

Bae, H.-J. & Woo, J.-H. 2014, ApJ, 795, 30

Baldwin, J. A., Phillips, M. M., & Terlevich, R. 1981, PASP, 93, 5

Baronchelli, L. 2020, PhD thesis, Ludwig-Maximilians-Universität München

Barvainis, R. 1993, ApJ, 412, 513

Baudry, A. & Desmurs, J. F. 2002, A&A, 394, 107

Baum, S. A., Zirbel, E. L., & O'Dea, C. P. 1995, ApJ, 451, 88

Belfiore, F., Maiolino, R., Maraston, C., et al. 2016, MNRAS, 461, 3111

Bellamy, M. J. & Tadhunter, C. N. 2004, MNRAS, 353, 105

Bennett, A. S. 1962, MmRAS, 68, 163

Best, P. N. & Heckman, T. M. 2012, MNRAS, 421, 1569

Beswick, R. J., Peck, A. B., Taylor, G. B., & Giovannini, G. 2004, MNRAS, 352, 49

Bhatnagar, S. & Cornwell, T. J. 2004, A&A, 426, 747

Bîrzan, L., McNamara, B. R., Nulsen, P. E. J., Carilli, C. L., & Wise, M. W. 2008, ApJ, 686, 859

Blake, G. A., Sutton, E. C., Masson, C. R., & Phillips, T. G. 1987, ApJ, 315, 621

Blandford, R. D. & Payne, D. G. 1982, Monthly Notices of the Royal Astronomical Society, 199, 883

Blandford, R. D. & Payne, D. G. 1982, MNRAS, 199, 883

Blandford, R. D. & Znajek, R. L. 1977, MNRAS, 179, 433

Boccardi, B. 2015, PhD thesis, Universität zu Köln

Boccardi, B., Krichbaum, T. P., Bach, U., et al. 2016, A&A, 585, A33

Boccardi, B., Krichbaum, T. P., Ros, E., & Zensus, J. A. 2017, A&A Rev., 25, 4

Boccardi, B., Perucho, M., Casadio, C., et al. 2021, A&A, 647, A67

Boizelle, B. D., Walsh, J. L., Barth, A. J., et al. 2021, ApJ, 908, 19

Bolli, P., Orlati, A., Stringhetti, L., et al. 2015, Journal of Astronomical Instrumentation, 4, 1550008

Bondi, H. 1952, MNRAS, 112, 195

Bonning, E. W., Shields, G. A., Salviander, S., Cheng, L., & Gebhardt, K. 2006, in American Astronomical Society Meeting Abstracts, Vol. 209, American Astronomical Society Meeting Abstracts, 34.05

Burbidge, G. R. 1956, ApJ, 124, 416

Buttiglione, S., Capetti, A., Celotti, A., et al. 2010, A&A, 509, A6

Canalizo, G., Max, C., Whysong, D., Antonucci, R., & Dahm, S. E. 2003, ApJ, 597, 823

Carilli, C. L., Perley, R. A., Dhawan, V., & Perley, D. A. 2019, ApJ, 874, L32

Cecil, G., Bland-Hawthorn, J., Veilleux, S., & Filippenko, A. V. 2001, ApJ, 555, 338

Celotti, A., Padovani, P., & Ghisellini, G. 1997, MNRAS, 286, 415

Chiaberge, M. & Marconi, A. 2011, MNRAS, 416, 917

Cicone, C., Brusa, M., Ramos Almeida, C., et al. 2018, Nature Astronomy, 2, 176

Cicone, C., Maiolino, R., Sturm, E., et al. 2014, A&A, 562, A21

Ciotti, L., Pellegrini, S., Negri, A., & Ostriker, J. P. 2017, ApJ, 835, 15

Clark, B. G. 1980, A&A, 89, 377

Claussen, M. J., Diamond, P. J., Braatz, J. A., Wilson, A. S., & Henkel, C. 1998, ApJ, 500, L129

Collier, J. D., Tingay, S. J., Callingham, J. R., et al. 2018, MNRAS, 477, 578

Combes, F. 2008, Ap&SS, 313, 321

Combes, F., García-Burillo, S., Audibert, A., et al. 2019, A&A, 623, A79

Conway, J. E. 1996, in Extragalactic Radio Sources, ed. R. D. Ekers, C. Fanti, & L. Padrielli, Vol. 175, 92

Conway, J. E. & Blanco, P. R. 1995, ApJ, 449, L131

Cornwell, T. J. & Evans, K. F. 1985, A&A, 143, 77

Cornwell, T. J. & Wilkinson, P. N. 1981, MNRAS, 196, 1067

Crenshaw, D. M., Kraemer, S. B., Schmitt, H. R., et al. 2010, AJ, 139, 871

Crummy, J., Fabian, A. C., Gallo, L., & Ross, R. R. 2006, MNRAS, 365, 1067

Curran, S. J., Whiting, M. T., Allison, J. R., et al. 2017, MNRAS, 467, 4514

Dallacasa, D., Orienti, M., Fanti, C., Fanti, R., & Stanghellini, C. 2013, MNRAS, 433, 147

Davis, B. L., Graham, A. W., & Seigar, M. S. 2017, MNRAS, 471, 2187

Desmurs, J. F., Baudry, A., Sivagnanam, P., & Henkel, C. 2002, A&A, 394, 975

Drinkwater, M. J., Combes, F., & Wiklind, T. 1996, A&A, 312, 771

Edge, D. O., Shakeshaft, J. R., McAdam, W. B., Baldwin, J. E., & Archer, S. 1959, MmRAS, 68, 37

Elitzur, M. 1992, ARA&A, 30, 75

Elitzur, M. & Ho, L. C. 2009, ApJ, 701, L91

Elitzur, M., Ho, L. C., & Trump, J. R. 2014, MNRAS, 438, 3340

Emonts, B. H. C., Morganti, R., Villar-Martín, M., et al. 2016, A&A, 596, A19

Endres, C. P., Schlemmer, S., Schilke, P., Stutzki, J., & Müller, H. S. P. 2016, Journal of Molecular Spectroscopy, 327, 95

Eracleous, M., Hwang, J. A., & Flohic, H. M. L. G. 2010, ApJS, 187, 135

Evans, A. S., Sanders, D. B., Surace, J. A., & Mazzarella, J. M. 1999, ApJ, 511, 730

Event Horizon Telescope Collaboration, Akiyama, K., Alberdi, A., et al. 2019, ApJ, 875, L1

Fabian, A. C. 2012, ARA&A, 50, 455

Fanaroff, B. L. & Riley, J. M. 1974, MNRAS, 167, 31P

Fanti, R. 2009, Astronomische Nachrichten, 330, 303

Fernández-Ontiveros, J. A., Dasyra, K. M., Hatziminaoglou, E., et al. 2020a, A&A, 633, A127

Fernández-Ontiveros, J. A., Dasyra, K. M., Hatziminaoglou, E., et al. 2020b, A&A, 633, A127

Fernández-Ontiveros, J. A., López-Gonzaga, N., Prieto, M. A., et al. 2019, MNRAS, 485, 5377

Ferrarese, L. & Ford, H. 2005, Space Sci. Rev., 116, 523

Ferrarese, L. & Merritt, D. 2000, ApJ, 539, L9

Fiore, F., Feruglio, C., Shankar, F., et al. 2017, A&A, 601, A143

Floyd, D. J. E., Perlman, E., Leahy, J. P., et al. 2006, ApJ, 639, 23

Fuente, A., Black, J. H., Martín-Pintado, J., et al. 2000, ApJ, 545, L113

Ganguly, R. & Brotherton, M. S. 2008, ApJ, 672, 102

Gao, F., Braatz, J. A., Reid, M. J., et al. 2017, ApJ, 834, 52

García-Burillo, S., Combes, F., Neri, R., et al. 2007, A&A, 468, L71

García-Burillo, S., Combes, F., Usero, A., et al. 2014, A&A, 567, A125

García-Burillo, S., Usero, A., Fuente, A., et al. 2010, A&A, 519, A2

Gaspari, M., Brighenti, F., & Temi, P. 2015, A&A, 579, A62

Gaspari, M., Ruszkowski, M., & Oh, S. P. 2013, MNRAS, 432, 3401

Gaspari, M., Temi, P., & Brighenti, F. 2017, MNRAS, 466, 677

Gaspari, M., Tombesi, F., & Cappi, M. 2020, Nature Astronomy, 4, 10

Gelderman, R. & Whittle, M. 1994, ApJS, 91, 491

Gendre, M. A., Best, P. N., & Wall, J. V. 2010, MNRAS, 404, 1719

Gendre, M. A., Best, P. N., Wall, J. V., & Ker, L. M. 2013, MNRAS, 430, 3086

Genzel, R., Eckart, A., Ott, T., & Eisenhauer, F. 1997, MNRAS, 291, 219

Ghisellini, G., Tavecchio, F., Maraschi, L., Celotti, A., & Sbarrato, T. 2014, Nature, 515, 376

Giroletti, M., Giovannini, G., Taylor, G. B., et al. 2003, A&A, 399, 889

Giustini, M., Cappi, M., Chartas, G., et al. 2011, A&A, 536, A49

Godfrey, L. E. H. & Shabala, S. S. 2016, MNRAS, 456, 1172

Gofford, J., Reeves, J. N., Turner, T. J., et al. 2011, MNRAS, 414, 3307

Goldsmith, P. F. & Langer, W. D. 1999, ApJ, 517, 209

Grasha, K., Darling, J., Bolatto, A., Leroy, A. K., & Stocke, J. T. 2019, ApJS, 245, 3

Gravity Collaboration, Sturm, E., Dexter, J., et al. 2018, Nature, 563, 657

Guilloteau, S., Baudry, A., Walmsley, C. M., Wilson, T. L., & Winnberg, A. 1984, A&A, 131, 45

Guilloteau, S., Lucas, R., & Omont, A. 1981, A&A, 97, 347

Gupta, N., Salter, C. J., Saikia, D. J., Ghosh, T., & Jeyakumar, S. 2006, MNRAS, 373, 972

Haardt, F., Maraschi, L., & Ghisellini, G. 1997, ApJ, 476, 620

Hacar, A., Bosman, A. D., & van Dishoeck, E. F. 2020, A&A, 635, A4

Haga, T., Doi, A., Murata, Y., et al. 2015, ApJ, 807, 15

Hagiwara, Y., Klöckner, H.-R., & Baan, W. 2004, MNRAS, 353, 1055

Harrison, C. M., Alexander, D. M., Mullaney, J. R., & Swinbank, A. M. 2014, MN-RAS, 441, 3306

Harrison, C. M., Costa, T., Tadhunter, C. N., et al. 2018, Nature Astronomy, 2, 198

Heckman, T. M. & Best, P. N. 2014, ARA&A, 52, 589

Henkel, C., Wilson, T. L., Langer, N., Chin, Y. N., & Mauersberger, R. 1994, Inter-stellar CNO Isotope Ratios, ed. T. L. Wilson & K. J. Johnston, Vol. 439, 72–88

Hernández-García, L., González-Martín, O., Masegosa, J., & Márquez, I. 2014, A&A, 569, A26

Herrnstein, J. R., Moran, J. M., Greenhill, L. J., et al. 1999, Nature, 400, 539

Ho, I. T., Kewley, L. J., Dopita, M. A., et al. 2014, MNRAS, 444, 3894

Ho, L. C. 2002, ApJ, 564, 120

Ho, L. C. & Peng, C. Y. 2001, ApJ, 555, 650

Högbom, J. A. 1974, A&AS, 15, 417

Holst, C., Zeimetz, P., Nothnagel, A., Schauerte, W., & Kuhlmann, H. 2012, Journal of Surveying Engineering, 138, 126

Hönig, S. F., Kishimoto, M., Gandhi, P., et al. 2010, A&A, 515, A23

Imanishi, M., Nakanishi, K., & Izumi, T. 2016, ApJ, 825, 44

Imanishi, M., Nguyen, D. D., Wada, K., et al. 2020, ApJ, 902, 99

Impellizzeri, C. M. V., Gallimore, J. F., Baum, S. A., et al. 2019, ApJ, 884, L28

Impellizzeri, C. M. V., Henkel, C., Roy, A. L., & Menten, K. M. 2008, A&A, 484, L43

Impellizzeri, V. 2008, PhD thesis, Rheinische Friedrich-Wilhelms-Universität Bonn

Irwin, J. A. & Seaquist, E. R. 1988, ApJ, 335, 658

Irwin, J. A. & Seaquist, E. R. 1991, ApJ, 371, 111

Ito, H., Kino, M., Kawakatu, N., Isobe, N., & Yamada, S. 2008, ApJ, 685, 828

Izumi, T., Kohno, K., Aalto, S., et al. 2016, ApJ, 818, 42

Jaffe, W., Ford, H. C., Ferrarese, L., van den Bosch, F., & O'Connell, R. W. 1993, Nature, 364, 213

Jaffe, W. & McNamara, B. R. 1994, ApJ, 434, 110

Janssen, R. M. J., Röttgering, H. J. A., Best, P. N., & Brinchmann, J. 2012, A&A, 541, A62

Jones, D. L., Wehrle, A. E., Meier, D. L., & Piner, B. G. 2000, ApJ, 534, 165

Jones, D. L., Wehrle, A. E., Piner, B. G., & Meier, D. L. 2001, ApJ, 553, 968

Kaastra, J. S., Kriss, G. A., Cappi, M., et al. 2014, Science, 345, 64

Kadler, M., Kerp, J., Ros, E., et al. 2004, A&A, 420, 467

Kaiser, C. R. & Best, P. N. 2007, MNRAS, 381, 1548

Kameno, S., Sawada-Satoh, S., Impellizzeri, C. M. V., et al. 2020, ApJ, 895, 73

Kellermann, K. I., Sramek, R., Schmidt, M., Shaffer, D. B., & Green, R. 1989, AJ, 98, 1195

Kerr, R. P. 1963, Phys. Rev. Lett., 11, 237

Koda, J., Sofue, Y., Kohno, K., et al. 2002, ApJ, 573, 105

Kohno, K., Nakanishi, K., Tosaki, T., et al. 2008, Ap&SS, 313, 279

Kolokythas, K., O'Sullivan, E., Giacintucci, S., et al. 2015, MNRAS, 450, 1732

Kondratko, P. T., Greenhill, L. J., & Moran, J. M. 2005, ApJ, 618, 618

Kormendy, J. & Ho, L. C. 2013, ARA&A, 51, 511

Kovalev, Y. Y., Lister, M. L., Homan, D. C., & Kellermann, K. I. 2007, ApJ, 668, L27

Krichbaum, T. P., Alef, W., Witzel, A., et al. 1998, A&A, 329, 873

Krips, M., Neri, R., García-Burillo, S., et al. 2008, ApJ, 677, 262

Kulkarni, G. & Loeb, A. 2012, MNRAS, 422, 1306

Kuo, C. Y., Braatz, J. A., Condon, J. J., et al. 2011, ApJ, 727, 20

Kutner, M. L. & Ulich, B. L. 1981, ApJ, 250, 341

Kuźmicz, A., Jamrozy, M., Kozieł-Wierzbowska, D., & Weżgowiec, M. 2017, MNRAS, 471, 3806

Labiano, A., García-Burillo, S., Combes, F., et al. 2014, A&A, 564, A128

Langer, W. D. & Penzias, A. A. 1990, ApJ, 357, 477

Larson, R. B. 1985, MNRAS, 214, 379

Lawrence, C. R., Zucker, J. R., Readhead, A. C. S., et al. 1996, ApJS, 107, 541

Lees, J. F., Knapp, G. R., Rupen, M. P., & Phillips, T. G. 1991, ApJ, 379, 177

Li, J.-T., Hodges-Kluck, E., Stein, Y., et al. 2019, ApJ, 873, 27

Lin, M.-Y., Davies, R. I., Burtscher, L., et al. 2016, MNRAS, 458, 1375

Liszt, H. & Lucas, R. 2004, A&A, 428, 445

Lo, K. Y. 2005, ARA&A, 43, 625

Lobanov, A. P. 1998, A&A, 330, 79

Lynden-Bell, D. & Rees, M. J. 1971, Monthly Notices of the Royal Astronomical Society, 152, 461

Ma, J., Maksym, W. P., Fabbiano, G., et al. 2021, ApJ, 908, 155

Macconi, D., Torresi, E., Grandi, P., Boccardi, B., & Vignali, C. 2020, MNRAS, 493, 4355

Machalski, J., Jamrozy, M., Stawarz, Ł., & Weżgowiec, M. 2016, A&A, 595, A46

Mahony, E. K., Morganti, R., Emonts, B. H. C., Oosterloo, T. A., & Tadhunter, C. 2013, MNRAS, 435, L58

Maloney, P. R., Begelman, M. C., & Rees, M. J. 1994, ApJ, 432, 606

Mangum, J. G. & Shirley, Y. L. 2015, PASP, 127, 266

Martel, A. R., Baum, S. A., Sparks, W. B., et al. 1999, ApJS, 122, 81

Martí-Vidal, I., Muller, S., Combes, F., et al. 2013, A&A, 558, A123

Martín, S., Kohno, K., Izumi, T., et al. 2015, A&A, 573, A116

Martín, S., Muller, S., Henkel, C., et al. 2019, A&A, 624, A125

Matthews, H. E., Baudry, A., Guilloteau, S., & Winnberg, A. 1986, A&A, 163, 177

Matthews, T. A. & Sandage, A. R. 1963, ApJ, 138, 30

McCoy, M., Ott, J., Meier, D. S., et al. 2017, ApJ, 851, 76

McNamara, B. R. & Nulsen, P. E. J. 2007, ARA&A, 45, 117

McNamara, B. R. & Nulsen, P. E. J. 2012, New Journal of Physics, 14, 055023

McNamara, B. R., Rohanizadegan, M., & Nulsen, P. E. J. 2011, ApJ, 727, 39

Melis, A., Concu, R., Trois, A., et al. 2018, Journal of Astronomical Instrumentation, 07, 1850004

Middelberg, E., Agudo, I., Roy, A. L., & Krichbaum, T. P. 2007, MNRAS, 377, 731

Middelberg, E., Roy, A. L., Nagar, N. M., et al. 2004, A&A, 417, 925

Miraghaei, H. & Best, P. N. 2017, MNRAS, 466, 4346

Miyoshi, M., Moran, J., Herrnstein, J., et al. 1995, Nature, 373, 127

Morganti, R., Fogasy, J., Paragi, Z., Oosterloo, T., & Orienti, M. 2013, Science, 341, 1082

Morganti, R., Oosterloo, T. A., Emonts, B. H. C., van der Hulst, J. M., & Tadhunter, C. N. 2003, ApJ, 593, L69

Morganti, R., Tadhunter, C. N., & Oosterloo, T. A. 2005, A&A, 444, L9

Mukherjee, D., Bicknell, G. V., Sutherland, R., & Wagner, A. 2016, MNRAS, 461, 967

Mukherjee, D., Bicknell, G. V., Wagner, A. Y., Sutherland, R. S., & Silk, J. 2018a, MNRAS, 479, 5544

Mukherjee, D., Wagner, A. Y., Bicknell, G. V., et al. 2018b, MNRAS, 476, 80

Mullaney, J. R., Alexander, D. M., Fine, S., et al. 2013, MNRAS, 433, 622

Muller, S., Beelen, A., Guélin, M., et al. 2011, A&A, 535, A103

Muller, S. & Guélin, M. 2008, A&A, 491, 739

Murray, N., Chiang, J., Grossman, S. A., & Voit, G. M. 1995, ApJ, 451, 498

Nagai, H., Onishi, K., Kawakatu, N., et al. 2019, ApJ, 883, 193

Nagao, T., Kawabata, K. S., Murayama, T., et al. 2004, AJ, 128, 109

Nakahara, S., Doi, A., Murata, Y., et al. 2018, ApJ, 854, 148

Narayan, R. & McClintock, J. E. 2012, MNRAS, 419, L69

Narayan, R. & Nityananda, R. 1986, ARA&A, 24, 127

Narayan, R. & Yi, I. 1994, ApJ, 428, L13

Nelson, C. H., Green, R. F., Bower, G., Gebhardt, K., & Weistrop, D. 2004, ApJ, 615, 652

Nenkova, M., Sirocky, M. M., Ivezić, Ž., & Elitzur, M. 2008, ApJ, 685, 147

Nguyen, H., Dawson, J. R., Miville-Deschênes, M. A., et al. 2018, ApJ, 862, 49

Nomura, M., Ohsuga, K., & Done, C. 2020, MNRAS, 494, 3616

Norman, C. & Miley, G. 1984, A&A, 141, 85

Ocaña Flaquer, B., Leon, S., Combes, F., & Lim, J. 2010, A&A, 518, A9

O'Dea, C. P. 1998, PASP, 110, 493

O'Dea, C. P., Baum, S. A., & Stanghellini, C. 1991, ApJ, 380, 66

Ogle, P., Boulanger, F., Guillard, P., et al. 2010, ApJ, 724, 1193

Ogle, P. M., Cohen, M. H., Miller, J. S., et al. 1997, ApJ, 482, L37

Oosterloo, T., Raymond Oonk, J. B., Morganti, R., et al. 2017, A&A, 608, A38

Padovani, P., Alexander, D. M., Assef, R. J., et al. 2017, A&A Rev., 25, 2

Page, K. L., Reeves, J. N., O'Brien, P. T., & Turner, M. J. L. 2005, Monthly Notices of the Royal Astronomical Society, 364, 195

Paragi, Z., Frey, S., Fejes, I., et al. 2000, PASJ, 52, 983

Penzias, A. A. & Burrus, C. A. 1973, ARA&A, 11, 51

Perucho, M., Bosch-Ramon, V., & Barkov, M. V. 2017, A&A, 606, A40

Perucho, M., Martí, J. M., Cela, J. M., et al. 2010, A&A, 519, A41

Peterson, B. M., Ferrarese, L., Gilbert, K. M., et al. 2004, ApJ, 613, 682

Petrucci, P. O., Ursini, F., De Rosa, A., et al. 2018, A&A, 611, A59

Pihlström, Y. M., Conway, J. E., & Vermeulen, R. C. 2003, A&A, 404, 871

Pihlström, Y. M., Vermeulen, R. C., Taylor, G. B., & Conway, J. E. 1999, ApJ, 525, L13

Piner, B. G., Jones, D. L., & Wehrle, A. E. 2001, AJ, 122, 2954

Popping, A. & Braun, R. 2008, A&A, 479, 903

Porth, O. & Komissarov, S. S. 2015, MNRAS, 452, 1089

Privon, G. C., Baum, S. A., O'Dea, C. P., et al. 2012, ApJ, 747, 46

Radomski, J. T., Piña, R. K., Packham, C., Telesco, C. M., & Tadhunter, C. N. 2002, ApJ, 566, 675

Reb, L., Fernández-Ontiveros, J. A., Prieto, M. A., & Dolag, K. 2018, MNRAS, 478, L122

Reber, G. 1944, ApJ, 100, 279

Reeves, J. N., O'Brien, P. T., & Ward, M. J. 2003, ApJ, 593, L65

Reitblat, A. A. 1980, Soviet Astronomy Letters, 6, 406

Reynolds, C., Punsly, B., Kharb, P., O'Dea, C. P., & Wrobel, J. 2009, ApJ, 706, 851

Reynolds, C. S. 2020, arXiv e-prints, arXiv:2011.08948

Reynolds, C. S., Lohfink, A. M., Ogle, P. M., et al. 2015, ApJ, 808, 154

Riechers, D. A., Weiß, A., Walter, F., & Wagg, J. 2010, ApJ, 725, 1032

Riquelme, D., Amo-Baladrón, M. A., Martín-Pintado, J., et al. 2010, A&A, 523, A51

Rose, T., Edge, A. C., Combes, F., et al. 2020, MNRAS, 496, 364

Ruan, J. J., Anderson, S. F., Eracleous, M., et al. 2019, ApJ, 883, 76

Russell, D. M., Gallo, E., & Fender, R. P. 2013, MNRAS, 431, 405

Ruze, J. 1966, Proceedings of the IEEE, 54, 633

Saito, T., Iono, D., Espada, D., et al. 2018, ApJ, 863, 129

Salpeter, E. E. 1964, ApJ, 140, 796

Sawada-Satoh, S., Byun, D.-Y., Lee, S.-S., et al. 2019, ApJ, 872, L21

Sawada-Satoh, S., Inoue, M., Shibata, K. M., et al. 2000, PASJ, 52, 421

Sawada-Satoh, S., Kameno, S., Nakamura, K., et al. 2008, ApJ, 680, 191

Schilizzi, R. T., Tian, W. W., Conway, J. E., et al. 2001, A&A, 368, 398

Schulz, R., Morganti, R., Nyland, K., et al. 2018, A&A, 617, A38

Schulz, R., Morganti, R., Nyland, K., et al. 2021, A&A, 647, A63

Sebastian, B., Kharb, P., O'Dea, C. P., Colbert, E. J. M., & Baum, S. A. 2019, ApJ, 883, 189

Seyfert, C. K. 1943, ApJ, 97, 28

Shakura, N. I. & Sunyaev, R. A. 1973, A&A, 500, 33

Shankar, F., Weinberg, D. H., & Miralda-Escudé, J. 2013, MNRAS, 428, 421

Shannon, C. 1949, Proceedings of the IRE, 37, 10–21

Shao, L. & Griffiths, P. R. 2007, Environmental Science & Technology, 41, 7054, pMID: 17993147

Shemmer, O., Brandt, W. N., Netzer, H., Maiolino, R., & Kaspi, S. 2008, ApJ, 682, 81

Shepherd, M. C. 1997, in Astronomical Society of the Pacific Conference Series, Vol. 125, Astronomical Data Analysis Software and Systems VI, ed. G. Hunt & H. Payne, 77

Sikora, M., Stawarz, Ł., & Lasota, J.-P. 2007, ApJ, 658, 815

Small, T. A. & Blandford, R. D. 1992, MNRAS, 259, 725

Stalevski, M., Tristram, K. R. W., & Asmus, D. 2019, MNRAS, 484, 3334

Stanghellini, C., O'Dea, C. P., Baum, S. A., et al. 1997, A&A, 325, 943

Stickel, M., Meisenheimer, K., & Kuehr, H. 1994, A&AS, 105, 211

Stockton, A., Ridgway, S. E., & Lilly, S. J. 1994, AJ, 108, 414

Storchi-Bergmann, T., Dall'Agnol de Oliveira, B., Longo Micchi, L. F., et al. 2018, ApJ, 868, 14

Struve, C. & Conway, J. E. 2010, A&A, 513, A10

Struve, C. & Conway, J. E. 2012, A&A, 546, A22

Sun, A.-L., Greene, J. E., Zakamska, N. L., et al. 2018, MNRAS, 480, 2302

Tadhunter, C., Marconi, A., Axon, D., et al. 2003, MNRAS, 342, 861

Tang, X. D., Henkel, C., Menten, K. M., et al. 2019, A&A, 629, A6

Taylor, V. A., Jansen, R. A., Windhorst, R. A., Odewahn, S. C., & Hibbard, J. E. 2005, ApJ, 630, 784

Tchekhovskoy, A. & Bromberg, O. 2016, MNRAS, 461, L46

Thompson, A. R., Moran, J. M., & Swenson, George W., J. 2017, Interferometry and Synthesis in Radio Astronomy, 3rd Edition

Thorne, K. S. 1974, ApJ, 191, 507

Tielens, A. G. G. M. 2010, The Physics and Chemistry of the Interstellar Medium

Titarchuk, L. 1994, ApJ, 434, 570

Tombesi, F., Cappi, M., Reeves, J. N., et al. 2010, A&A, 521, A57

Tortosa, A., Bianchi, S., Marinucci, A., Matt, G., & Petrucci, P. O. 2018, A&A, 614, A37

Tremblay, G. R., Oonk, J. B. R., Combes, F., et al. 2016, Nature, 534, 218

Trotter, A. S., Greenhill, L. J., Moran, J. M., et al. 1998, ApJ, 495, 740

Trump, J. R., Impey, C. D., Kelly, B. C., et al. 2011, ApJ, 733, 60

Tully, R. B., Courtois, H. M., Dolphin, A. E., et al. 2013, AJ, 146, 86

Ulvestad, J. S., Wrobel, J. M., Roy, A. L., et al. 1999, ApJ, 517, L81

Urry, C. M. & Padovani, P. 1995, PASP, 107, 803

Usero, A., García-Burillo, S., Fuente, A., Martín-Pintado, J., & Rodríguez-Fernández, N. J. 2004, A&A, 419, 897

Valente, G., Marongiu, P., Navarrini, A., et al. 2016, in Millimeter, Submillimeter, and Far-Infrared Detectors and Instrumentation for Astronomy VIII, ed. W. S. Holland & J. Zmuidzinas (SPIE)

van der Wolk, G., Barthel, P. D., Peletier, R. F., & Pel, J. W. 2010, A&A, 511, A64

van Dishoeck, E. F. 2018, IAU Symposium, 332, 3

van Gorkom, J. H., Knapp, G. R., Ekers, R. D., et al. 1989, AJ, 97, 708

van Langevelde, H. J., Pihlström, Y. M., Conway, J. E., Jaffe, W., & Schilizzi, R. T. 2000, A&A, 354, L45

Veilleux, S., Cecil, G., Bland-Hawthorn, J., et al. 1994, ApJ, 433, 48

Venturi, T., Pearson, T. J., Barthel, P. D., & Herbig, T. 1993, A&A, 271, 65

Venturi, T. & Taylor, G. B. 1999, AJ, 118, 1931

Vermeulen, R. C., Pihlström, Y. M., Tschager, W., et al. 2003, A&A, 404, 861

Vogel, S. N. & Welch, W. J. 1983, ApJ, 269, 568

Wagner, J. 2013, A&A, 560, A12

Wang, J., Fabbiano, G., Elvis, M., et al. 2011, ApJ, 736, 62

Willett, K. W., Stocke, J. T., Darling, J., & Perlman, E. S. 2010, ApJ, 713, 1393

Williams, D. R. A., McHardy, I. M., Baldi, R. D., et al. 2017, MNRAS, 472, 3842

Wilson, T. L. & Rood, R. 1994, ARA&A, 32, 191

Winkel, B., Kraus, A., & Bach, U. 2012, A&A, 540, A140

Woo, J.-H., Bae, H.-J., Son, D., & Karouzos, M. 2016, ApJ, 817, 108

Woods, D. T., Klein, R. I., Castor, J. I., McKee, C. F., & Bell, J. B. 1996, ApJ, 461, 767

Wu, F., An, T., Baan, W. A., et al. 2013, A&A, 550, A113

Wykes, S., Hardcastle, M. J., Karakas, A. I., & Vink, J. S. 2015, MNRAS, 447, 1001

Yuan, F. & Narayan, R. 2014, ARA&A, 52, 529

Zezas, A., Birkinshaw, M., Worrall, D. M., Peters, A., & Fabbiano, G. 2005, ApJ, 627, 711

Zovaro, H. R. M., Sharp, R., Nesvadba, N. P. H., et al. 2019, MNRAS, 484, 3393

Appendix A

Column density measurements

Column density is a basic measurement to analysis chemical and physical properties of interstellar medium. This appendix provides a general expression to calculate the column density of molecules from absorption line observations. Column density calculations presented in this appendix follow the description in Mangum & Shirley (2015).

A.1 Radiative transfer

The radiative transfer equation describes the propagation of radiation through a medium. A simplified radiative equation includes emission and absorption, which is given by

$$\frac{dI_\nu}{ds} = -\kappa_\nu I_\nu + j_\nu \tag{A.1}$$

where I_ν is the specific intensity, s is the path of the light along the line of sight, k_ν and j_ν are the absorption and emission coefficients, respectively. In a simple two-level system with upper and lower states, the absorption and emission coefficients are

$$\kappa_\nu = \frac{h\nu}{4\pi} \left(n_l B_{lu} - n_u B_{ul} \right) \phi_\nu \tag{A.2}$$

$$j_\nu = \frac{h\nu}{4\pi} A_{ul} n_u \tag{A.3}$$

where h is the Planck constant, ν is the rest frequency of the transition, Einstein coefficient A_{ul} is the transition probability of spontaneous emission, B_{lu} is the transition probability of absorption, and B_{ul} is the transition probability of stimulated emission, ϕ_ν is the line profile of the transition. n_l and n_u are the number densities of molecules in upper and lower energy levels of the transition J_ν, respectively. In thermal equilibrium state, the relation between level populations and the Einstein coefficients is

$$n_l B_{lu} J_\nu \phi_\nu = n_u A_{ul} + n_u B_{ul} J_\nu \phi_\nu. \tag{A.4}$$

The integral of the specific intensity I_ν defines J_ν, which is

$$J_\nu = \frac{1}{4\pi} \int I_\nu d\Omega. \tag{A.5}$$

The level populations of molecules are described by the Boltzmann distribution

$$\frac{n_u}{n_l} = \frac{g_u}{g_l} \exp\left(-\frac{h\nu}{kT}\right) \tag{A.6}$$

where g_u and g_l are the statistical weights of the upper and lower energy levels. h is the Planck constant, ν is the rest frequency of the transition, k is the Boltzmann constant, and T is the temperature. At temperature T, radiation field is decribed by

$$B_\nu(T) = \frac{2h\nu^3}{c^2} \left[\exp\left(\frac{h\nu}{kT}\right) - 1\right]^{-1} \tag{A.7}$$

By applying Eq. A.7 and Eq. A.6 on Eq. A.4, we obtain

$$A_{ul} = \frac{2h\nu^3}{c^2} B_{ul} \tag{A.8}$$

$$g_l B_{lu} = g_u B_{ul}. \tag{A.9}$$

The absorption coefficient κ_ν in Eq. A.2 is then given by

$$\kappa_\nu = \frac{c^2}{8\pi\nu^2} \frac{g_u}{g_l} n_l A_{ul} \left(1 - \frac{g_l n_u}{g_u n_l}\right) \phi_\nu. \tag{A.10}$$

The optical depth τ_ν ($d\tau_\nu = \kappa_\nu ds$) describes the amount of accumulated absorption along the line of sight. Integral of Eq. A.10 along the path length ds gives the optical depth

$$\begin{aligned}
\tau_\nu &= \frac{c^2}{8\pi\nu^2} \frac{g_u}{g_l} A_{ul} \phi_\nu \int n_l(s') \left(1 - \frac{g_l n_u(s')}{g_u n_l(s')}\right) ds \\
&= \frac{c^2}{8\pi\nu^2} \frac{g_u}{g_l} A_{ul} \phi_\nu N_l \left[1 - \exp\left(-\frac{h\nu}{kT_{ex}}\right)\right].
\end{aligned} \tag{A.11}$$

The column density of molecules in a certain energy level N_l is

$$N_l = \frac{8\pi\nu^3}{c^3} \frac{g_l}{g_u} \frac{1}{A_{ul}} \left[1 - \exp\left(-\frac{h\nu}{kT_{ex}}\right)\right]^{-1} \int \tau d\nu. \tag{A.12}$$

In case of rotational transitions, the rotatinoal partition function Q_{rot} describes the fraction of molecular population at a certain energy level E_l. Therefore, the total column density of molecules can be derived by

$$N_{total} = Q_{rot} \frac{N_l}{g_l} \exp\left(\frac{E_l}{kT_{ex}}\right). \tag{A.13}$$

In summary, the measured integrated optical depth of a molecular absorption line is translated to the total column density as follow

$$N_{total} = \frac{8\pi\nu^3}{c^3} \frac{Q_{rot}(T_{ex})}{g_u} \frac{1}{A_{ul}} \exp\left(\frac{E_l}{kT_{ex}}\right) \left[1 - \exp\left(-\frac{h\nu}{kT_{ex}}\right)\right]^{-1} \int \tau d\nu \tag{A.14}$$

- ν = rest frequency of the transition
- c = speed of light
- g_u = statistical weight of the upper state
- g_l = statistical weight of the lower state
- Q_{rot} = rotational partition function
- A_{ul} = probability for spontaneous emission of the transition
- E_l = Energy level of the lower state
- k = Boltzmann constant
- h = Planck constant
- τ = optical depth

The optical depth correction factor suggested by Goldsmith & Langer (1999) provides more general column density calculation, including optically thick cases. The correction is given by

$$N_{tot} = N_{tot}^{thin} \frac{\tau}{1 - \exp(-\tau)}. \tag{A.15}$$

A.2 Partition function

The partition function of rotational transitions is

$$Q_{rot} = \sum_i g_i \exp\left(-\frac{\mathrm{E}_i}{kT}\right) \tag{A.16}$$

where g_i is the degeneracy of individual energy level E_i. For linear molecules, the partition function is

$$Q_{rot} \simeq \sum_{J=0}^{\infty} (2J+1) \exp\left(-\frac{hB_0 J(J+1)}{kT}\right) \tag{A.17}$$

For symmetric and asymmetric molecules with rotational constants A_0, B_0, and C_0, the approximation to the rotational partition function is

$$Q_{rot} \simeq \sum_{J=0}^{\infty} \sum_{K=-J}^{J} g_k g_I (2J+1) \exp\left(-\frac{h\left[B_0 J(J+1) + s_0 K^2\right]}{KT}\right) \tag{A.18}$$

where g_K is the degeneracy associated with the internal quantum number K and g_I is the nuclear spin degeneracy. $s_0 = A_0 - B_0$ for a prolate symmetric molecule and $s_0 = C_0 - B_0$ for an oblate symmetric molecule.

A.3 Integrated optical depth

Integrated optical depth is an important measurement from molecular absorption line observations. An optical depth is given by

$$\tau = -\ln\left(1 - \frac{1}{f_c}\frac{I_{obs}}{I_{cont}}\right) \tag{A.19}$$

where f_c is filling factor, which indicates the fraction of the continuum emission covered by the intervening molecular absorbers. I_{obs} is the amplitude of absorption, and I_{cont} is the amplitude of the background continuum emission. An integral over the the absorption line profile yields the integrated optical depth. For instance, the integrated optical depth of an absorption line with a single Gaussian profile is given by

$$\int \tau \, d\nu = \frac{1}{2}\sqrt{\frac{\pi}{\ln 2}} \tau_{peak} \Delta \nu \tag{A.20}$$

where τ_{peak} is the peak optical depth, and $\Delta \nu$ is the Full Width at Half power Maximum (FWHM) in the unit of $\mathrm{km\,s^{-1}}$.

Personal Acknowledgements

Funding, Data, and Software Acknowledgements

Erklärung

Ich versichere, dass ich die von mir vorgelegte Dissertation selbständig angefertigt, die benutzten Quellen und Hilfsmittel vollständig angegeben und die Stellen der Arbeit –einschließlich Tabellen, Karten und Abbildungen –, die anderen Werken im Wortlaut oder dem Sinn nachentnommen sind, in jedem Einzelfall als Entlehnung kenntlich gemacht habe; dass diese Dissertation noch keiner anderen Fakultät oder Universität zur Prüfung vorgelegen hat; dass sie –abgesehen von unten angegebenen Teilpublikationen– noch nicht veröffentlicht worden ist, sowie, dass ich eine solche Veröffentlichung vor Abschluss des Promotionsverfahrens nicht vornehmen werde. Die Bestimmungen der Promotionsordnung sind mir bekannt. Die von mir vorgelegte Dissertation ist von Prof. Dr. Andreas Eckart und Prof. Dr. J. Anton Zensus betreut worden.

08.12.2021 Dongjin Kim

Lebenslauf

Persönliche Daten

Dongjin Kim

Geburtsdatum :   18. September 1989
Geburtsort :   Seoul, Republik Korea
Staatsangehörigkeit :   Republik Korea

Anschrift

Max-Planck-Institut für Radioastronomie
Auf dem Hügel 69
53121 Bonn, Deutschland
Email : dongjin@mpifr-bonn.mpg.de

Ausbildung

2018–2021   Doktorand an der Univeristät zu Köln und dem
            Max-Planck-Institut für Radioastronomie in Bonn
            Stipendium der International Max Planck Research School (IMPRS)
            for Astronomy and astrophysics
            wiss. Betreuer   Prof. Dr. J. Anton Zensus,
                                  Prof. Dr. Andreas Eckart, und
                                  Dr. Thomas P. Krichbaum
            Titel: *"Circumnuclear Gas in Radio AGN Revealed by Molecular
                    Absorption"*

2016-2018   Forscher, Center for Galaxy Evolution Research, Seoul, Republik Korea

2014-2016   M.Sc. in Astronomie, Yonsei University, Seoul, Republik Korea
            wiss. Betreuer   Prof. Dr. Se-Hyung Cho
                                  Prof. Dr. Suk-Jin Yoon
            Title: *"VLBI and single-dish monitoring of SiO and H2O masers
            around the semi-regular variable star R Crateris"*

2009-2011   Militärdienst, Seoul, Republik Korea

2008-2014   B.Sc in Physik, Kyung Hee University, Seoul, Republik Korea

Unterschrift _____